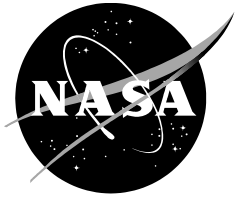


NASA/TM—2018—219895



Aerodynamics and Aeroacoustic Sources of a Coaxial Rotor

Natasha Lydia Schatzman
Ames Research Center
Moffett Field, California

November 2018

NASA STI Program ... in Profile

Since its founding, NASA has been dedicated to the advancement of aeronautics and space science. The NASA scientific and technical information (STI) program plays a key part in helping NASA maintain this important role.

The NASA STI program operates under the auspices of the Agency Chief Information Officer. It collects, organizes, provides for archiving, and disseminates NASA's STI. The NASA STI program provides access to the NTRS Registered and its public interface, the NASA Technical Reports Server, thus providing one of the largest collections of aeronautical and space science STI in the world. Results are published in both non-NASA channels and by NASA in the NASA STI Report Series, which includes the following report types:

- **TECHNICAL PUBLICATION.** Reports of completed research or a major significant phase of research that present the results of NASA Programs and include extensive data or theoretical analysis. Includes compilations of significant scientific and technical data and information deemed to be of continuing reference value. NASA counterpart of peer-reviewed formal professional papers but has less stringent limitations on manuscript length and extent of graphic presentations.
- **TECHNICAL MEMORANDUM.** Scientific and technical findings that are preliminary or of specialized interest, e.g., quick release reports, working papers, and bibliographies that contain minimal annotation. Does not contain extensive analysis.
- **CONTRACTOR REPORT.** Scientific and technical findings by NASA-sponsored contractors and grantees.

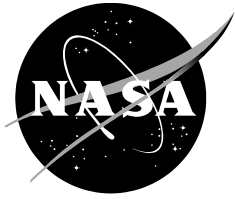
- **CONFERENCE PUBLICATION.** Collected papers from scientific and technical conferences, symposia, seminars, or other meetings sponsored or co-sponsored by NASA.
- **SPECIAL PUBLICATION.** Scientific, technical, or historical information from NASA programs, projects, and missions, often concerned with subjects having substantial public interest.
- **TECHNICAL TRANSLATION.** English-language translations of foreign scientific and technical material pertinent to NASA's mission.

Specialized services also include organizing and publishing research results, distributing specialized research announcements and feeds, providing information desk and personal search support, and enabling data exchange services.

For more information about the NASA STI program, see the following:

- Access the NASA STI program home page at <http://www.sti.nasa.gov>
- E-mail your question to help@sti.nasa.gov
- Phone the NASA STI Information Desk at 757-864-9658
- Write to:
NASA STI Information Desk
Mail Stop 148
NASA Langley Research Center
Hampton, VA 23681-2199

NASA/TM—2018—219895



Aerodynamics and Aeroacoustic Sources of a Coaxial Rotor

Natasha Lydia Schatzman
Ames Research Center
Moffett Field, California

National Aeronautics and
Space Administration

Ames Research Center
Moffett Field, CA 94035-1000

November 2018

ACKNOWLEDGMENTS

I would like to thank my husband, Dr. David M. Schatzman, for all of his love and dedication. You have been my support system throughout this process, and your advice has helped me along the way. Special thanks to my parents, James and Lydia Barbely, for supporting my educational goals. My grandmother, Mrs. Lydia Zakrewsky, has shown me that it takes hard work and courage to succeed—thank you. Thank you to my brothers, Eric and Allen Barbely, for guiding me into engineering as a young lady. A special thank you to my sisters, Crystal Bowen and Erin Barbely, for your patience and guidance. Thank you Crystal Bowen and Eric Barbely for being my support system in Atlanta and being there when I needed you the most. Thank you Katie Pope for being my best friend and supporter over the years. Thank you Meredith Segall and Tammy Baier for guidance during my years at NASA. Thank you to all of my friends and family not mentioned. Thank you to my coworkers and teachers at NASA Ames Research Center, the U.S. Army Aviation Development Directorate, and the Georgia Institute of Technology who have given me professional development advice to help better my future.

This work is dedicated to Dr. Wel Chong “Ben” Sim.

Available from:

NASA STI Support Services
Mail Stop 148
NASA Langley Research Center
Hampton, VA 23681-2199
757-864-9658

National Technical Information Service
5301 Shawnee Road
Alexandria, VA 22312
webmail@ntis.gov
703-605-6000

This report is also available in electronic form at

<http://ntrs.nasa.gov>

Contents

1	Summary	1
2	Introduction and Background	3
2.1	Literature Survey	3
2.2	Scope and Objectives	6
2.3	Coaxial Rotor Aerodynamic Features	6
2.4	Coaxial Rotor Aerodynamic Acoustic Sources	7
2.4.1	Thickness noise	8
2.4.2	Loading noise	8
2.4.3	HSI noise	8
3	2D Simulation of Blade Crossings	9
3.1	2D Representation and Assumptions	9
3.2	Potential Flow Simulation	10
3.2.1	Computational set up	10
3.2.2	Potential flow simulation results	10
3.3	Incompressible and Compressible Flow Simulation	12
3.3.1	Computational setup	12
3.3.2	OVERFLOW 2.2k	15
3.4	Simulation Setup	15
3.4.1	Simulation test conditions	19
3.5	Isolated Airfoil Mach Sweep	22
3.6	Two Airfoils Crossing: Circulation, Thickness, and Compressibility Effects	22
3.6.1	Two airfoils crossing: circulation	26
3.6.2	Two airfoils crossing: thickness	26
3.6.3	Two airfoils crossing: compressibility	27
3.7	Viscosity, Shed Vorticity, and Downwash Effects	31
3.7.1	Isolated airfoil	36
3.7.2	Two airfoils crossing	43
3.7.3	Single train of eight airfoils	43
3.7.4	Two trains of eight airfoils crossing	47
3.8	Modern Coaxial and Single Rotor Design Comparison: Hover	47
3.9	Summary	53
4	3D Coaxial Rotor Simulation	54
4.1	Rotor Unstructured Navier-Stokes (RotUNS) Performance Validation	54
4.1.1	CAMRAD II	55
4.2	Harrington Single Rotor 1 (HS1) and Coaxial Rotor 1 (HC1)	55
4.2.1	Geometry description	55
4.3	HS1 Hover Performance	57
4.4	HC1 Hover Performance	57
4.4.1	Rotor vertical separation distance variation	59
4.5	HS1 and HC1 Forward Flight Performance	61
4.6	Pressure Distribution Above and Below Rotor	62
4.6.1	Wake dissipation effects	68
4.7	Comparison of 2D and 3D Results	68

4.8	Summary	73
5	Blade Crossing and BVI Location Identification	73
5.1	Blade Crossing Location Identification	73
5.2	BVI Location Identification	75
5.3	Single Rotor BVI Location Identification	75
5.4	Coaxial Rotor Blade Crossing and BVI Location Identification	82
5.5	Summary	84
6	Acoustic Prediction: Thickness and Loading Noise	84
6.1	Aerodynamics Loads	84
6.2	Acoustic Predictions	88
6.2.1	PSU-WOPWOP version 3.4.3	88
6.2.2	Observer locations	88
6.2.3	Modern single rotor acoustic predictions	91
6.2.4	Modern coaxial rotor acoustic predictions	91
6.2.5	Modern single versus coaxial rotor acoustic predictions	92
6.3	Summary	101
7	Conclusions	101
8	Future work	106
	References	107

List of Figures

1	Coaxial rotorcraft aerodynamic complexities.	3
2	3D representation of a coaxial rotor simulated in 2D as two airfoils moving past each other.	9
3	a) Pictorial representation of two airfoils moving past each other modeled by a source, sink, and vortex; b) mathematical model of an individual source, vortex, and sink; and c) simulation of a combined source, vortex, and sink for an isolated airfoil. . . .	11
4	VITS simulation of two airfoils crossing, c_l versus distance to overlap in chords ($M = 0.25$, $\alpha = 9.8^\circ$, and $S/c = 4.0$ ($S = 2.0$ ft, $c = 0.5$ ft)).	12
5	Simulation of two airfoils: a) before, b) at, and c) after time of crossing. Vorticity contour shown using velocity vectors, downwash not simulated ($M = 0.25$, $\alpha = 9.8^\circ$, and $S/c = 4.0$ ($S = 2.0$ ft, $c = 0.5$ ft)).	13
6	Change in lift of two NACA 0012 airfoils crossing (when compressibility is not dominating): a) before and b) after.	14
7	OVERFLOW 2.2k simulation with grid adaption for an NACA 0012 isolated airfoil at $\alpha = 7^\circ$	16
8	Inviscid and viscid simulations of an isolated airfoil (a) through d)), two airfoils crossing (e) through h)), a single train of eight airfoils (i) through l)), and two trains of eight airfoils crossing (m) through p)).	17
9	Coefficient of thrust versus coefficient of power for modern coaxial rotor in hover.	19
10	Simulated test condition variables.	20
11	Viscid isolated NACA 0012 airfoil at $\alpha = 7^\circ$ with a chord of 0.50 ft, Mach number variation for a) c_l and c_d , and b) C_P versus x/c	23
12	C_P flow-field contours for Mach number variation for an isolated NACA 0012 airfoil at $\alpha = 7^\circ$, and $M =$ a) 0.10, b) 0.30, c) 0.50, d) 0.60, e) 0.70, f) 0.80, g) 0.90, h) 1.0, and i) 1.1.	24
13	Two NACA 0012 airfoils crossing for a) c_z , b) c_x , and c) c_m versus distance to overlap ($M = 0.5$ ($V_{tip} = 560$ ft/s), $\alpha = -7^\circ$, 0° , and 7° , and $S/c = 4.0$ ($S = 2.0$ ft, $c = 0.5$ ft)).	26
14	Two NACA 0012 airfoils crossing for a) c_z , b) c_x , and c) c_m versus distance to overlap ($M = 0.9$ ($V_{tip} = 1,005$ ft/s), $\alpha = -7^\circ$, 0° , and 7° , and $S/c = 4.0$ ($S = 2.0$ ft, $c = 0.5$ ft)).	27
15	Comparison of two NACA 0001 and NACA 0012 airfoils crossing for a) c_z , b) c_x , and c) c_m versus distance to overlap ($M = 0.5$ ($V_{tip} = 560$ ft/s), $\alpha = 0^\circ$, and $S/c = 4.0$ ($S = 2.0$ ft, $c = 0.5$ ft)).	28
16	Comparison of two NACA 0001 and NACA 0012 airfoils crossing for a) c_z , b) c_x , and c) c_m versus distance to overlap ($M = 0.9$ ($V_{tip} = 1,005$ ft/s), $\alpha = 0^\circ$, and $S/c = 4.0$ ($S = 2.0$ ft, $c = 0.5$ ft)).	28
17	Comparison of two NACA 0001 and NACA 0012 airfoils crossing for a) c_z , b) c_x , and c) c_m versus distance to overlap ($M = 0.5$ ($V_{tip} = 560$ ft/s), $\alpha = 3^\circ$, and $S/c = 4.0$ ($S = 2.0$ ft, $c = 0.5$ ft)).	29
18	Comparison of two NACA 0001 and NACA 0012 airfoils crossing for a) c_z , b) c_x , and c) c_m versus distance to overlap ($M = 0.9$ ($V_{tip} = 1,005$ ft/s), $\alpha = 3^\circ$, and $S/c = 4.0$ ($S = 2.0$ ft, $c = 0.5$ ft)).	29
19	Two NACA 0012 airfoils crossing for a) c_z , b) c_x , and c) c_m versus distance to overlap ($M = 0.5$ ($V_{tip} = 560$ ft/s), $\alpha = 7^\circ$, and $S/c = 2.0, 4.0$, and 6.0 ($c = 0.5$ ft)). . . .	30

20	Two NACA 0012 airfoils crossing for a) c_z , b) c_x , and c) c_m versus distance to overlap ($M = 0.9$ ($V_{tip} = 1,005$ ft/s), $\alpha = 7^\circ$, and $S/c = 2.0, 4.0,$ and 6.0 ($c = 0.5$ ft)).	30
21	Two NACA 0012 airfoils crossing for a) c_z , b) c_x , and c) c_m versus distance to overlap ($M = 0.5, 0.7, 0.9, 1.0,$ and 1.2 ($V_{tip} = 560, 780, 1005, 1116,$ and 1340 ft/s), $\alpha = 0^\circ$, and $S/c = 4.0$ ($S = 2.0$ ft, $c = 0.5$ ft)).	31
22	Mach contour of two airfoils crossing a) before, b) at, and c) after overlap ($M = 1.2,$ $\alpha = 0^\circ$, and $S/c = 4.0$ ($S = 2.0$ ft, $c = 0.5$ ft)).	32
23	Mach contour of two airfoils crossing a) before, b) at, and c) after overlap ($M = 0.90,$ $\alpha = 0^\circ$, and $S/c = 4.0$ ($S = 2.0$ ft, $c = 0.5$ ft)).	33
24	VITS (inviscid) and OVERFLOW (inviscid) calculations of two airfoils and two trains of eight airfoils crossing, c_l versus distance to overlap in chords ($M = 0.25,$ $\alpha = 9.8^\circ,$ $S/c = 4.0$ ($S = 2.0$ ft, $c = 0.5$ ft), and $D/c = 33.51$).	34
25	Multiple airfoil simulation illustration at time of overlap of <i>UA4</i> and <i>LA4</i>	35
26	Viscid airfoil simulation, two trains of eight airfoils crossing (<i>UA4/LA4</i>) with downwash, c_z versus distance to overlap ($M = 0.25,$ $\alpha = 9.8^\circ,$ $V_i = 31$ ft/s, $S/c = 4.0$ ($S = 2.0$ ft, $c = 0.5$ ft), and $D/c = 33.51$).	36
27	Viscid and inviscid isolated airfoil, two airfoils crossing at time of overlap (<i>UA/LA</i>), single train of eight airfoils (<i>A4</i>), and two trains of eight airfoils crossing (<i>UA4/LA4</i>) with and without downwash, c_z versus distance to overlap ($M = 0.25,$ $\alpha = 9.8^\circ,$ $V_i = 31$ ft/s, $S/c = 4.0$ ($S = 2.0$ ft, $c = 0.5$ ft), and $D/c = 33.51$).	37
28	Viscid isolated airfoil, two airfoils crossing at time of overlap (<i>UA/LA</i>), single train of eight airfoils (<i>A4</i>), and two trains of eight airfoils crossing (<i>UA4/LA4</i>) with and without downwash, c_x versus distance to overlap ($M = 0.25,$ $\alpha = 9.8^\circ,$ $V_i = 31$ ft/s, $S/c = 4.0$ ($S = 2.0$ ft, $c = 0.5$ ft), and $D/c = 33.51$).	38
29	Viscid isolated airfoil, two airfoils crossing at time of overlap (<i>UA/LA</i>), single train of eight airfoils (<i>A4</i>), and two trains of eight airfoils at crossing (<i>UA4/LA4</i>) with and without downwash, c_m versus distance to overlap ($M = 0.25,$ $\alpha = 9.8^\circ,$ $V_i = 31$ ft/s, $S/c = 4.0$ ($S = 2.0$ ft, $c = 0.5$ ft), and $D/c = 33.51$).	39
30	Isolated airfoil, two airfoils crossing at time of overlap (<i>UA/LA</i>), single train of eight airfoils (<i>A4</i>), and two trains of eight airfoils crossing (<i>UA4/LA4</i>) for an inviscid no downwash (a), e), i), and m)); inviscid with downwash (b), f), j), and n)); viscoid no downwash (c), g), k), and o)); and viscoid with downwash (d) h) i) and p)) simulation, C_P contour ($M = 0.25$ ($V_{tip} = 280$ ft/s), $\alpha = 9.8^\circ,$ $V_i = 31$ ft/s, and $S/c = 4.0$ ($S = 2.0$ ft, $c = 0.5$ ft)).	40
31	Isolated NACA 0012 airfoil C_P contour for a) viscoid, no downwash, b) viscoid with downwash, c) inviscid, no downwash, and d) inviscid with downwash simulation ($M = 0.25$ ($V_{tip} = 280$ ft/s), $\alpha = 9.8^\circ,$ and $V_i = 31$ ft/s). Note: abrupt changes in contour levels are due to changing grid densities and numerical issues.	41
32	An isolated NACA 0012 airfoil wake y-vorticity contour for a) viscoid, no downwash, b) viscoid with downwash, c) inviscid, no downwash, and d) inviscid with downwash simulation ($M = 0.25$ ($V_{tip} = 280$ ft/s), $\alpha = 9.8^\circ,$ and $V_i = 31$ ft/s).	42
33	Viscid flow-field C_P contour of two NACA 0012 airfoils crossing a) before, b) at, and c) after, with downwash ($M = 0.25$ ($V_{tip} = 280$ ft/s), $\alpha = 9.8^\circ,$ $V_i = 31$ ft/s, and $S/c = 4.0$ ($S = 2.0$ ft, $c = 0.5$ ft)).	44
34	Two NACA 0012 airfoils y-vorticity contour after time of crossing for a) viscoid, no downwash, b) viscoid with downwash, c) inviscid, no downwash, and d) inviscid with downwash simulation ($M = 0.25$ ($V_{tip} = 280$ ft/s), $\alpha = 9.8^\circ,$ $V_i = 31$ ft/s, and $S/c = 4.0$ ($S = 2.0$ ft, $c = 0.50$)).	45

35	Results for an isolated airfoil and the upper airfoil of the two airfoils crossing case: a) c_z , b) Γ , and c) $-d\Gamma/dt$. Horizontal axis is distance to overlap for the upper airfoil (UA) (HC1: $M = 0.47$ ($V_{tip} = 500$ ft/s), $\alpha = 7^\circ$, and $S/c = 6.21$ ($S = 2.33$ ft, $c = 0.375$ ft)).	46
36	Y-vorticity contours for A4 (4th airfoil in a train of eight airfoils) for a) viscid no downwash, b) viscid with downwash, c) inviscid no downwash, and d) inviscid with downwash simulation ($M = 0.25$, $\alpha = 9.8^\circ$, $V_i = 31$ ft/s, and $D/c = 33.51$).	48
37	Viscid calculations with downwash for an isolated airfoil, two airfoils crossing, a single train of eight airfoils crossing (A4), and two trains of eight airfoils crossing (UA4 and LA4), c_z versus distance to overlap ($M = 0.25$, $\alpha = 9.8^\circ$, $V_i = 31$ ft/s, $S/c = 4.0$ ($S = 2.0$ ft, $c = 0.5$ ft), and $D/c = 33.51$).	49
38	Y-vorticity contour with downwash viscid simulation of a) two airfoils (UA/LA) crossing, and b) two trains of eight airfoils crossing after time of overlap of upper and lower airfoil four (UA4/LA4) ($M = 0.25$, $\alpha = 9.8^\circ$, $V_i = 31$ ft/s, $S/c = 4.0$ ($S = 2.0$ ft, $c = 0.5$ ft), and $D/c = 33.51$).	50
39	2D representation of a modern single rotor in hover: a) Δc_l and b) Δc_d versus distance to overlap ($r/R = 0.25$ through 1.00). Results shown for airfoil four (A4).	51
40	2D representation of a modern coaxial rotor in hover: a) Δc_l and b) Δc_d for UA4, and c) Δc_l and d) Δc_d for LA4, versus distance to overlap ($r/R = 0.25$ through 1.00). Results shown for airfoil four (A4).	52
41	HS1 and HC1 blade planform geometry as modeled in RotUNS.	56
42	Performance of HS1 [13] in hover compared to BEMT, CAMRAD II, and RotUNS calculations.	57
43	Performance of HC1 [13] in hover compared to BEMT, CAMRAD II, and RotUNS with and without grid adaption calculations.	58
44	Thrust ratio versus rotor separation distance in hover comparing HC1 RotUNS rotor disk model calculations and Ramasamy's experimental data [9] for twisted and untwisted blades.	60
45	Measured performance of HS1 and HC1 [16] in forward flight compared to CAMRAD II and RotUNS calculations.	61
46	HS1 flow-field absolute pressures: a) below and above rotor, and b) time history (one revolution) at $r/R = 0.85$ in hover. RotUNS lifting-line (discrete blade) rotor model calculations.	64
47	HC1 comparison of absolute pressure above and below upper and lower rotors at non-overlap. RotUNS lifting-line (discrete-blade) rotor model calculations are presented for hover.	65
48	HC1 comparison of absolute pressure above and below upper and lower rotors at overlap. RotUNS lifting-line (discrete-blade) rotor model calculations are presented for hover.	66
49	Time history (one revolution) at $r/R = 0.85$ for absolute pressure below and above U2 (upper rotor blade two) and L1 (lower rotor blade one) in hover.	67
50	HC1 flow-field absolute pressures below and above rotor at two instances when blades are not overlapped, for a) upper rotor, where $U1, U2 = 0^\circ, 180^\circ$, and b) lower rotor, where $L1, L2 = 90^\circ, 270^\circ$. RotUNS forward flight lifting-line (discrete-blade) rotor model calculations in forward flight ($\mu = 0.12$).	69

51	HC1 flow-field absolute pressures below and above rotor at two instances when blades are overlapped, for a) upper rotor, where $U1, U2 = 225^\circ, 45^\circ$, and b) lower rotor, where $L1, L2 = 45^\circ, 225^\circ$. RotUNS forward flight lifting-line (discrete-blade) rotor model calculations in forward flight ($\mu = 0.12$).	70
52	HC1 flow-field absolute pressures above lower rotor blades where $L1, L2 = 90^\circ, 270^\circ$ for a) forward flight, and b) hover. RotUNS lifting-line (discrete-blade) rotor model calculations.	71
53	Comparison between 2D OVERFLOW and 3D RotCFD modern coaxial rotor in hover at $r/R = 0.90$ for upper rotor blade one (U1), lower rotor blade one (L1), upper airfoil four (UA4), and lower airfoil four (LA4) (OVERFLOW conditions: $M = 0.564, \alpha = 5.8^\circ, S/c = 4.0$ ($S = 2.0$ ft, $c = 0.5$ ft), and $D/c = 75.4$ ft. RotCFD conditions: $V_{tip} = 700$ ft/s, $\alpha = 5^\circ, S/c = 4.0$ ($S = 2.0$ ft, $c = 0.5$ ft), $C_T = 0.004, C_P = 0.0003$, and $\theta_U/\theta_L = 9^\circ$).	72
54	RABBIT's predictions for a six-bladed coaxial rotor blade crossing time and locations ($V_{tip} = 625$ ft/s, $\mu = 0.10, S = 2.0$ ft, and $\alpha_s = 7.00^\circ$).	74
55	RABBIT's blade crossing predictions for three unconventional coaxial configurations.	76
56	Pictorial representation of a blade tip vortex formation and the trailed and shed vorticity in wake.	77
57	Rotor tip vortex wake displacement for a) X/R , b) Y/R , and c) Z/R	78
58	RABBIT output for single rotor case study.	79
59	RABBIT and Sim et al. case study comparison of blade azimuth angle versus r/R locations.	80
60	RABBIT and Sim et al. case study comparison of a) impulse factor versus azimuth angle, and b) normalized $\frac{\partial F}{\partial t}$ versus azimuth angle for r/R locations.	81
61	RABBIT blade crossing and lower rotor BVI predictions for a six-bladed (three upper/three lower) coaxial rotor ($V_{tip} = 625$ ft/s, $\mu = 0.0867, S = 2.0$ ft, $\chi_{TTP} = 89.6^\circ, C_T = 0.0025$, and $\alpha_S = 10.00^\circ$).	83
62	RABBIT versus CAMRAD II predictions for a six-bladed coaxial (three upper/three lower) rotor wake comparison at time of 0.786 revolutions (U_{ref}) ($V_{tip} = 625$ ft/s, $\mu = 0.0867, S = 2.0$ ft, $\chi_{TTP} = 89.6^\circ, C_T = 0.0025$, and $\alpha_S = 10.00^\circ$).	85
63	RABBIT versus CAMRAD II predictions for a six-bladed coaxial (three upper/three lower) rotor blade crossing time and BVI lower rotor locations for U_{ref} at time of a) 0.000, b) 0.786, c) 0.847, and d) 1.000 revolutions ($V_{tip} = 625$ ft/s, $\mu = 0.0867, S = 2.0$ ft, $\chi_{TTP} = 89.6^\circ, C_T = 0.0025$, and $\alpha_S = 10.00^\circ$).	86
64	RABBIT modern coaxial lower rotor BVI predictions for U_{ref} for a) impulse factor versus azimuth angle, and b) normalized $\frac{\partial F}{\partial t}$ versus azimuth angle for r/R locations ($V_{tip} = 625$ ft/s, $\mu = 0.0867, S = 2.0$ ft, $\chi_{TTP} = 89.6^\circ, C_T = 0.0025$, and $\alpha_S = 10.00^\circ$).	87
65	Rotor blade loading with and without tip loss.	88
66	Stacked 2D OVERFLOW results for modern single rotor in hover without tip loss: a) F_X , b) F_Y , and c) F_Z , and with tip loss d) F_X , e) F_Y , and f) F_Z	89
67	Stacked 2D OVERFLOW results for modern coaxial rotor in hover: upper rotor a) F_X , b) F_Y , and c) F_Z , and lower rotor d) F_X , e) F_Y , and f) F_Z	90
68	Rotor source noise directivity.	92
69	Elevation acoustic directivity in hover for modern single rotor acoustic pressure time history. Loading and total noise, left (red) y-axis; thickness noise, right (blue) y-axis.	93
70	Elevation acoustic directivity in hover for modern single rotor frequency spectrum.	94

71	Azimuthal acoustic directivity in hover for modern single rotor acoustic pressure time history. Loading and total noise, left (red) y-axis; thickness noise, right (blue) y-axis.	95
72	Azimuthal acoustic directivity in hover for modern single rotor frequency spectrum.	96
73	Elevation acoustic directivity in hover for modern coaxial rotor acoustic pressure time history. Loading and total noise, left (red) y-axis; thickness noise, right (blue) y-axis.	97
74	Elevation acoustic directivity in hover for modern coaxial rotor frequency spectrum.	98
75	Azimuthal acoustic directivity in hover for modern coaxial rotor acoustic pressure time history. Loading and total noise, left (red) y-axis; thickness noise, right (blue) y-axis.	99
76	Azimuthal acoustic directivity in hover for modern coaxial rotor frequency spectrum.	100
77	Modern single and coaxial rotor in hover. Thickness noise time history comparison for observers 1 through 10.	103
78	Modern single and coaxial rotor in hover. Loading noise time history comparison for observers 1 through 10.	104
79	Modern single and coaxial rotor in hover. Total noise time history comparison for observers 1 through 10.	105

List of Tables

1	Computational investigations of coaxial rotors in hover (h) and forward flight (ff).	5
2	Atmospheric conditions for 2D OVERFLOW simulations.	16
3	Simulated rotor design parameters 3D and 2D analog.	18
4	List of isolated airfoil OVERFLOW simulations.	20
5	List of two airfoils crossing OVERFLOW simulations.	21
6	List of single train of eight airfoils OVERFLOW simulations.	21
7	List of two trains of eight airfoils OVERFLOW simulations.	22
8	Conditions for 2D OVERFLOW simulations for two airfoils crossing.	25
9	2D representation of a coaxial and single rotor r/R location.	49
10	HS1 and HC1 parameters [13].	56
11	HC1 hover RotUNS rotor disk model control inputs (* denotes grid adaption (GA)).	59
12	HC1 hover RotUNS rotor disk model control inputs for varying separation distance.	60
13	HS1 forward flight RotUNS inputs using CAMRAD II control settings [41].	62
14	HC1 forward flight RotUNS inputs using CAMRAD II control settings [41].	62
15	CAMRAD II and RotUNS percent error difference for HS1 and HC1 experimental data.	63
16	Operating conditions for single rotor case study.	79
17	Modern single and coaxial rotor observer locations.	91
18	Modern coaxial and single rotor noise sources and differences for observers 1 through 10.	102

Nomenclature

Symbol	Description
A_i	airfoil i
B_1	single rotor blade one
B_2	single rotor blade two
c	chord (ft)
c_0	speed of sound in undisturbed medium (ft/s)
c_l	coefficient of 2D sectional lift
c_{l_α}	2D lift curve slope
c_d	coefficient of 2D sectional drag
c_x	coefficient of 2D sectional force in the horizontal direction
c_z	coefficient of 2D sectional force in the vertical direction
C_P	rotor power coefficient
C_T	rotor thrust coefficient
D	rotor diameter (ft)
dS	element of the rotor blade surface (ft)
h	miss distance (ft)
\bar{I}	BVI impulse factor
$L1$	lower rotor blade one
$L2$	lower rotor blade two
LA_i	lower airfoil blade i
Li	lower rotor blade i
l_i	components of local force intensity that acts on the fluid, $l_i = P_{ij} n_j$
l_r	$l_i \hat{r}_i$
\dot{l}_r	$\dot{l}_i \hat{r}_i$
\vec{M}	vector of local source Mach number with respect to a frame fixed to the undisturbed medium, with components M_i
M	$ \vec{M} $
M_{tip}	tip Mach number
M_r	Mach number of source in radiation direction, $M_i \hat{r}_i$
\dot{M}_r	$\dot{M}_i \hat{r}_i$, where $\dot{M}_i = \frac{\partial M}{\partial \tau}$
N_b	number of blades (per rotor)
\hat{n}	unit outward pointing normal vector to rotor blade surface, with components \hat{n}_i
P_{ij}	compressive stress tensor
P	rotor power (hp)
p'	acoustic pressure in undisturbed medium
Q	torque (lb_f -ft)
R	rotor radius (ft)
r	distance between source and observer (ft)
r/R	dimensionless radial position
r	spanwise radial position (ft)
\hat{r}	unit vector in the radiation direction, with components \hat{r}_i

T	rotor thrust (lb_f)
t	observer time (s)
T_U	upper rotor thrust (lb_f)
T_L	lower rotor thrust (lb_f)
UA_i	upper airfoil blade i
U_i	upper rotor blade i
V	forward flight velocity (ft/s)
V_i	downwash, induced inflow (ft/s)
V_b	translating blade velocity (ft/s)
v_n	local normal velocity of rotor blade (ft/s)
\dot{v}_n	$\dot{v}_i \hat{n}_i$
$v_{\dot{n}}$	$v_i \dot{\hat{n}}_i$
V_{tip}	rotor blade rotational speed at tip (ft/s)
\bar{X}	shape function
\vec{x}	observer location vector with x , y , and z components (ft)
\vec{y}	source location vector with x , y , and z components (ft)
Z	vertical distance between rotors or airfoils (ft)
α	airfoil angle of attack (deg), positive pitch up
α_S	blade pitch angle (deg), positive pitch up
Γ	vortex strength
$\bar{\Gamma}$	vortex strength factor
γ	blade vortex interaction angle (deg)
$\frac{\partial F}{\partial t}$	time rate of change of loading
κ_{int}	coaxial rotor induced power interference factor
λ_i	inflow (ft/s)
μ	advance ratio (V/V_{tip})
ω	rotor angular velocity (rad/s)
ρ_0	density in medium (slugs/ft ³)
σ	rotor solidity, $\frac{N_b c R}{\pi R^2}$
τ	source time (s)
θ_S	single rotor collective pitch angle (deg)
θ_L	lower rotor collective pitch angle (deg)
θ_U	upper rotor collective pitch angle (deg)
θ_{1cU}	upper rotor lateral cyclic pitch (deg)
θ_{1cL}	lower rotor lateral cyclic pitch (deg)
θ_{1sU}	upper rotor longitudinal cyclic pitch (deg)
θ_{1sL}	lower rotor longitudinal cyclic pitch (deg)
χ_{TPP}	wake skew angle(deg)

Subscripts

ISO	isolated airfoil
i	blade and airfoil number counter (1, 2, 3, 4, ...)
L	loading noise component (Pa)
ret	quantity is evaluated at the retarded time, $\tau = t + \frac{r}{c}$
T	thickness noise component (Pa)

Abstract

Vehicles with coaxial, contra-rotating rotor (CACR) systems are being considered for a range of applications, including those requiring high speed and operation in urban environments. Community and environmental noise impact is likely to be a concern in these applications. Design parameters are identified that effect the fundamental aerodynamics and fluid dynamic features of a CACR system in hover, vertical, and edgewise flight. Particular attention is paid to those features affecting thickness, loading, blade vortex interaction (BVI), and high-speed impulsive (HSI) noise. Understanding the fluid dynamic features is a precursor to studying the aeroacoustics of a coaxial rotor. Rotor performance was computed initially using a Navier-Stokes solver with prescribed blade section aerodynamic properties, and the results were validated against generic experimental test cases. The fluid dynamics of blade interactions was simplified and broken into a two-dimensional (2D) blade crossing problem, with crossing locations and velocity fields from the rotor results. Two trains of eight airfoils passing were simulated to understand the effects due to shed vorticity. The airfoils are displaced vertically by a distance equivalent to the typical spacing between the upper and lower rotors of a coaxial system. A 2D potential flow code and 2D OVERFLOW compressible-flow Navier-Stokes solver were used to investigate the complex coaxial rotor system flow field. One challenge of analyzing the CACR system is the difficulty of envisioning all of the possible interactions and their possible locations as flight conditions and rotor designs change. A calculation tool was developed to identify time and location of blade overlap. The tool was then integrated with a wake aerodynamics model to identify locations and instances of upper rotor tip vortex interaction with a lower rotor blade. This tool enables rapid identification of different types of BVI based on relative rotor orientation. Specific aerodynamic phenomena that occur for each noise source relevant to CACR systems are presented, along with computational tools to predict these occurrences.

1 Summary

Vehicles with coaxial, contra-rotating rotor (CACR) systems are being considered for a range of applications, including those requiring high speed and operation in urban environments. Community and environmental noise impact is likely to be a concern in these applications. Design parameters are identified that affect the fundamental aerodynamics and fluid dynamic features of a CACR system in hover, vertical, and edgewise flight. Particular attention is paid to those features affecting noise sources. These sources include thickness, loading, blade vortex interaction (BVI), and high-speed-impulsive (HSI) noise. Understanding the fluid dynamic features is a precursor to studying the aeroacoustics of a coaxial rotor.

A literature survey has been completed, listing theoretical, computational, and experimental studies relevant to CACR systems. Because of the lack of information regarding the flow field and acoustics of a CACR system compared to single rotor systems, this study investigated the aerodynamic and aeroacoustic sources of a CACR system by investigating each noise source independently. The impact of thickness, circulation, compressibility, viscosity, downwash, and shed vorticity of a CACR system are compared to a single rotor system and the rotor noise sources are identified.

Two blades passing in close proximity can cause strong compressibility effects that can have a profound impact on noise generation. Prior to examining the complex three-dimensional (3D) flow field of a coaxial rotor in detail, two airfoils traveling in opposite directions were simulated. Furthermore, two trains of eight airfoils passing were simulated to understand the effects due to shed vorticity, and a vertical velocity was simulated representative of downwash. The airfoils are displaced vertically by a distance equivalent to the typical spacing between the upper and lower rotors of a coaxial system. A 2D potential flow code and the 2D OVERFLOW compressible-flow Navier-Stokes solver were used to investigate the complex coaxial rotor system flow field.

A 2D potential flow solver simulated two airfoils crossing, modeling the airfoil as a source, vortex, and sink. The simulation revealed that the lift of both the upper and lower airfoils increased before the crossing, followed by a decrease in lift after the crossing. Before the crossing, the upper airfoil experiences an increase in angle of attack because of the upwash from the lower airfoil. The angle of attack of the lower airfoil also increases because of the upwash from the upper airfoil, therefore both airfoils experience an increase in lift. The opposite occurs after the airfoils pass each other, where both the upper and lower airfoil experience a decrease in lift. This phenomenon is a circulation effect, which contributes to loading noise.

2D OVERFLOW was used to further investigate circulation, along with thickness, compressibility, viscosity, downwash, and shed vorticity in 2D. Airfoil thickness effects were explored by comparing three different separation distances at a constant low speed for a symmetrical airfoil; this eliminated the large effects of circulation and compressibility. Comparing the upper and lower airfoils revealed that at low and high speeds, thickness effects due to the airfoil were negligible, although a vertical separation distance greater than twice the chord is recommended to avoid thickness effects of one rotor on the other. Furthermore, two different airfoils were compared to understand thickness noise contributions due to airfoil shape. This comparison indicated that thickness noise for a CACR compared to a single rotor is negligible at vertical separation distances larger than twice the chord.

For two airfoils crossing, the flow field and aerodynamic forces for three angles of attack with the same symmetrical airfoil, speed, and vertical separation distance were simulated using OVERFLOW in order to eliminate any large effects due to airfoil thickness or compressibility. When comparing circulation at various angles of attack, an angle of attack greater or less than zero resulted in a change in lift, drag, and moment before and after the airfoils crossed, and therefore a change in loading noise.

HSI noise due to compressibility effects was investigated in 2D by performing a Mach sweep ($M = 0.5$ through 1.2), while keeping angle of attack, airfoil, and vertical separation distance constant. The higher the Mach number, the larger the change in lift, drag, and moment at the time of overlap. As Mach numbers neared 1.0 , a large change in drag and moment was observed because of compressibility and the formation of weak shocks. The formation of shocks leads to a possible rotor-rotor shock interaction. HSI noise can be reduced by ensuring the translating blade velocity does not exceed Mach numbers where possible rotor-rotor, shock-shock interactions can occur.

Simulations of an isolated airfoil, two airfoils crossing, a single train of eight airfoils, and two trains of eight airfoils were used to independently understand the effects of shed vorticity and downwash in 2D. An airfoil overlap/crossing results in deposited shed vorticity in the flow field because of the rapid change in aerodynamic forces. The addition of downwash resulted in an overall decrease in lift and moment, and an increase in drag. Computations of viscid and inviscid out-of-plane vorticity contours indicated that the deposited shed vorticity was pushed downward by the vertical downwash velocity, which, in turn, deposited shed vorticity from the upper airfoils that directly impacted the lower airfoils. Overall, shed vorticity effects can be avoided with reduced rotor RPM and increased horizontal and vertical separation distance.

A hovering modern single rotor and a modern coaxial rotor system were simulated in 3D by stacking 2D OVERFLOW calculations along the rotor span. Using the rotorcraft noise prediction code PSU-WOPWOP, OVERFLOW calculations were used as input to calculate thickness and loading noise. Compared to the modern single rotor, the modern coaxial rotor acoustic predictions revealed a minimal contribution to thickness noise as compared to loading noise, even though the modern coaxial rotor design had three additional blades. Blade crossing events (circulation) are the dominate contribution to total noise.

The 3D CACR performance analysis used momentum theory and the RotUNS Navier-Stokes solver. Calculations were compared with data for the hovering CACR Harrington rotor tested in the 1950s. The simulation was extended to forward flight using the lifting-line blade model in RotUNS. Steady hover calculations showed improved accuracy compared to blade element momentum theory (BEMT) using the ability of RotUNS to couple the rotor momentum disk to an incompressible Navier-Stokes flow solver. The pressure fields above, between, and below the coaxial rotor system computed by RotUNS were then examined for different azimuth positions of the upper and lower rotor blades; this confirmed results from the 2D OVERFLOW simulations.

One challenge of analyzing the CACR system is the difficulty of envisioning all of the possible interactions, and their possible locations, as flight conditions and rotor designs change. A calculation tool was developed to identify the time and location of blade overlap. The tool was then integrated with a wake aerodynamics model to identify locations and instances of upper rotor tip vortex interaction with a lower rotor blade. This tool enables rapid identification of different types of BVI based on relative rotor orientation. Specific aerodynamic phenomena that occur for each noise source relevant to a CACR system are presented.

2 Introduction and Background

Coaxial rotorcraft are finding increased use in civil and military applications, as well as in the small unmanned aerial vehicle (UAV) market. As with all rotorcraft, the rotor noise generated by a CACR system must be mitigated to minimize impact to the community. Unlike single-main-rotor helicopters, the CACR system results in aerodynamic interactions between the upper and lower rotor, especially their wakes, as shown in Figure 1. A literature survey of CACR research was performed, and gaps in research are highlighted and discussed.

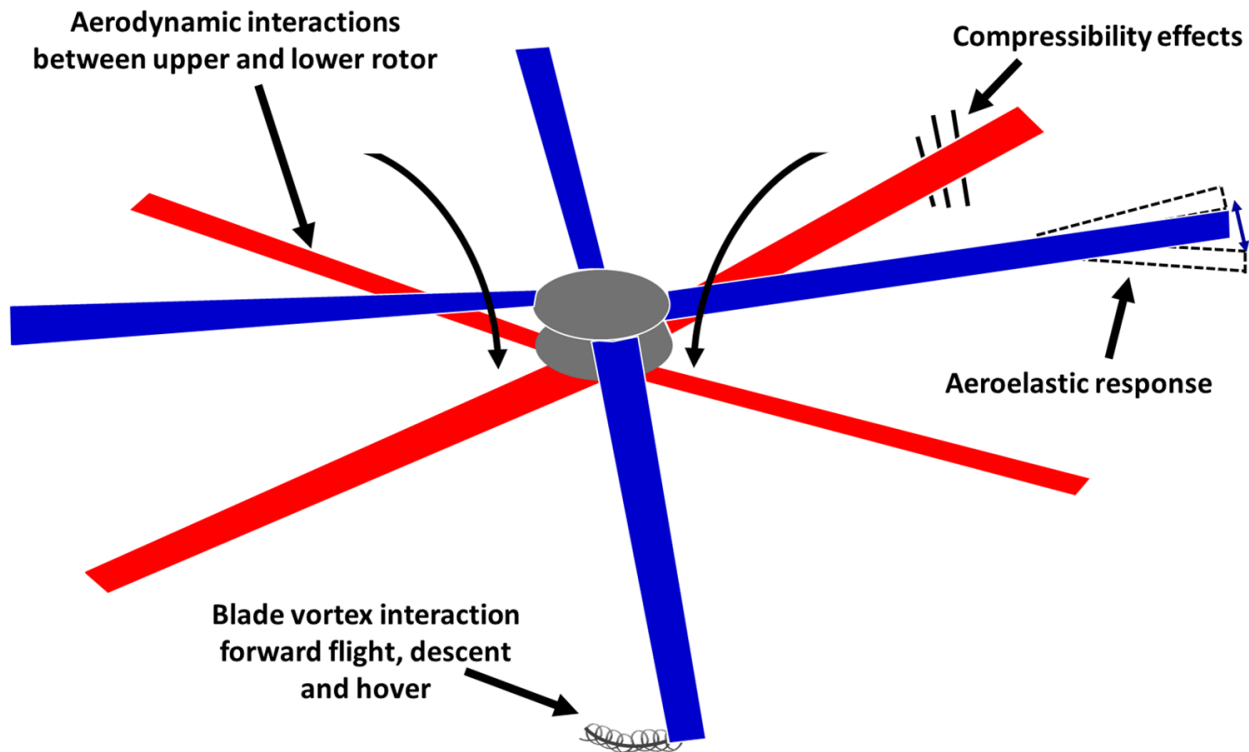


Figure 1. Coaxial rotorcraft aerodynamic complexities.

2.1 Literature Survey

Unlike single-main-rotor or tiltrotor configurations, there are limited analytical and experimental studies on CACR noise [1–6]. Studies on CACR performance are highlighted below. Coleman [7] provides a thorough summary of experimental and analytical studies of CACR through 1997. In the U.S., the first documented coaxial rotor test was a hover test by Taylor in 1950 [8] in the full-scale wind tunnel at NASA Langley Research Center. The CACR consisted of two 20-inch-diameter rotors, with two blades per rotor. The test objective was to visualize the flow through several (single, coaxial, tandem) rotor configurations with and without a ground plane present. A surprisingly small number of coaxial rotor hover experiments have been performed since the Taylor test, with the work by Ramasamy [9] being the most comprehensive. Ramasamy measured the performance of single, coaxial, tandem, and tiltrotor configurations using untwisted and twisted blade sets. The coaxial rotor system comprised two independent test rigs allowing performance measurements of the upper and lower rotors separately. Ramasamy provided a convenient summary of coaxial rotor

hover performance measurements prior to 2013, including those surveyed by Coleman. More recently, Cameron et al. [10] measured the performance of a single rotor and a coaxial rotor system using an 80-inch-diameter rotor with untwisted blades. Hub loads and blade deformation were also measured. Coaxial rotor measurements in forward flight are scarce compared to hover. Since 1997, the data from the Sikorsky X2 [11] flight test joins the handful of forward flight measurements included in the Coleman survey.

Analysis of coaxial rotor systems has progressed over the last decade thanks to improved modeling capabilities. Leishman and Ananthan [12] developed a BEMT model for coaxial rotors in hover and axial flight to design an optimum coaxial rotor for hover and used the Harrington data [13] to validate the model. Using momentum theory and the Harrington data, Leishman and Syal [14] developed expressions for the figure of merit for a coaxial rotor for four different operating conditions. Ho et al. [15] summarized some of the more recent validation studies of coaxial rotors. Analysis validations have relied primarily on the Harrington [13] and Dingeldein [16] large-scale coaxial rotor data. Although the Ramasamy data are for an approximately 4.3-foot-diameter coaxial rotor system, the individual rotor performance measurements are valuable for analysis validation. Ho et al. [15] used RCAS (a comprehensive rotorcraft analysis) to model the rotors used by Harrington and Ramasamy to compute coaxial rotor performance in hover and forward flight. Table 1 lists the validation studies discussed by Ho et al. [15], including the configurations modeled and the data set used for validation.

Using lift offset rotors in a coaxial rotor system has gained interest in recent years. Lift offset rotors maintain lift on the advancing side of the rotor disk in forward flight by eliminating the requirement for roll moment balance of the rotor. A very stiff hingeless rotor is used to carry the roll moment. By changing the angle of attack and loading distribution over the disk, the retreating side does not have to carry lift to balance the advancing side, so the retreating side does not have to approach stall. Lift offset is accomplished by varying the blade pitch distribution around the azimuth. Changing the lift vector location affects the overall performance; dynamic stall still occurs but not as severe because the location of the lift vector changes. The location of the lift offset rotor vector depends on the aerodynamics, which is controlled by varying the collective pitch (θ_0), lateral cyclic pitch (θ_{1c}), and longitudinal cyclic pitch (θ_{1s}). The collective pitch is the zeroth harmonic, and the lateral and longitudinal cyclic pitch are the first harmonic.

The idea of lift offset rotors has been crucial in enabling CACR vehicle designs for high-speed forward flight. The vehicle rolling moment is balanced by having contra-rotating rotors so that one rotor is always advancing on each side of the vehicle. However, each rotor is now likely to generate strong root moments requiring stiffer hub designs [17].

Kim and Brown [3,4,18,19] exercised their Vorticity Transport Model (VTM) analysis, and also predicted maneuverability performance of a lift-offset rotor using Harrington [13] and Dingeldein [16] data for validation and design. Kim and Brown [3,4] are one of the few studies on coaxial rotor noise.

Juhasz et al. [20] applied three aerodynamic models to simulate the McAlister et al. [21] model-scale coaxial rotor in hover. The three models include BEMT, a free-wake model, and computational fluid dynamics (CFD) using OVERFLOW2. A combination of the three methodologies was found to be the best approach to analyze the aerodynamics, though dependent on the level of detail desired. Schmaus and Chopra [22] developed a comprehensive analysis for a coaxial rotor for high advance ratios, using the code UMARC. The experimental rotor data from the University of Texas at Austin [10], along with data from the Harrington rotor 1 [13] and the XH-59A [23], were used for validation. Using the University of Texas rotor [10], the flight envelope for high advance ratios was defined for anticipated experimental tests.

Singh and Kang [24] performed computational simulations using a loosely coupled CFD (Helios)/CSD(RCAS) approach using a scaled-model coaxial rotor in hover from the University of Texas [10]. Results revealed that the interference between the upper and lower rotor required a computational structural dynamics (CSD) solver in order to have a robust trim convergence.

Walsh et al. [25, 26] performed computational aerodynamic and aeroacoustic predictions using RCAS and PSU-WOPWOP, respectively, for the XH-59A [23]. Thickness and loading noise were explored with emphasis on blade crossings and BVI for a variety of high-speed flight conditions.

The approach to explore a coaxial rotor in 2D, developed by the ongoing work of Schatzman (formerly Barbely) et al. [27–30] was pursued in recent papers by Singh and Friedmann [31, 32]. Using vortex discretized airfoils, Singh and Friedmann’s 2D simulations included effects of downwash and shed vorticity by using periodic boundaries. Furthermore, ongoing coaxial rotor computational and experimental research has been performed by the University of Maryland [33, 34] and the University of Texas at Austin [35], with a focus on rotor performance and blade flap bending moments, particularly with variation in lift offset.

Limited research regarding the fundamental aerodynamics specific to CACR systems was found. To build on the existing literature, performance and flow-field characteristics of the CACR system are explored herein to further understand the aerodynamics and acoustic sources. This work uses the hybrid-CFD analysis tool RotUNS for hover and forward flight performance predictions to compare against Harrington [13] and Dingeldein [16] data, as well as 2D OVERFLOW to understand various aerodynamic phenomena. The effect of the relative position of the upper and lower rotor blades on the flow field pressures near the rotor blades, which are important for acoustics, is studied. This exploration of the physics of coaxial aerodynamics adds to the computational work of Table 1.

Table 1. Computational investigations of coaxial rotors in hover (h) and forward flight (ff).

Citation	Flight condition	R (ft)	V_{tip} (ft/s)	N_b (per rotor)	Z/D	Data
Leishman and Ananthan 2006 [12]	h	12.5	500	2	0.095	[13]
	h	12.5	327, 392	2	0.080	[13]
Wachspress and Quackenbush 2006 [2]	h	1.25	400	4	0.105 - 0.5	[36]
	ff	26.0	740	3	0.095	[37]
McAlister et al. 2006 [21]	h	2.04	165	3	0.1 - 0.73	[21]
Bagai 2008 [11, 38]	h	13.2	620	4	N/A	[11]
	h	13.2	620	4	N/A	[11]
Ruzicka and Strawn 2008 [39]	h	2.04	165	3	0.1 - 0.73	[21]
Kim and Brown 2009 [3, 4, 18, 19]	h	12.5	500	2	0.095	[13]
	ff	12.5	469	2	0.095	[16]
Lim at al. 2009 [40]	h	12.5	500	2	0.095	[13]
	h	12.5	327, 392	2	0.080	[13]
	h	2.04	165	3	0.1 - 0.73	[21]
	h	18.0	650	3	0.0694	[23]
Johnson 2009 [41]	h	18.0	650	3	0.0694	[23]
	h	12.5	500	2	0.095	[13]
	h	12.5	327, 392	2	0.080	[13]
	ff	18.0	650	3	0.0694	[23]

	ff	12.5	469	2	0.095	[16]
Lakshminarayan and Baeder 2009 [43]	h	12.5	327, 392	2	0.080	[13]
	h	0.28	55 - 80	3	0.625	[42]
Juhasz et al. 2010 [20, 22]	h	12.5	500	2	0.095	[13]
	h	2.04	165	3	0.1 - 0.73	[21]
	ff	18.0	650	3	0.0694	[23]
	ff	2.04	165	3	0.1 - 0.73	[21]
Johnson et al. 2012 [17]	h	18.0	650	3	0.0694	[23]
	h	13.2	620	4	N/A	[11]
	ff	18.0	650	3	0.0694	[23]
	ff	13.2	620	4	N/A	[11]
Yeo and Johnson. 2013 [44]	h	18.0	650	3	0.0694	[23]
	ff	18.0	650	3	0.0694	[23]
Rajmohan et al. 2014 [45]	h	2.04	165	3	0.1 - 0.73	[21]
Ho et al. 2015 [15]	h	12.5	500	2	0.095	[13]
	h	12.5	327, 392	2	0.080	[13]
	h	2.17	182, 273	3	0.05 - 1.5	[9]
	h	2.15	180, 270	3	0.05 - 0.75	[9]
Schmaus and Chopra 2015 [22]	h	12.5	500	2	0.095	[13]
	h	18.0	650	3	0.0694	[23]
	h	3.83	573	2	0.060	[10]
Singh and Kang 2015 [24]	h	12.5	500	2	0.095	[13]
	h	3.83	573	2	0.060	[10]
Walsh 2016 [25]	ff	18.0	650	3	0.0694	[23]
Barbely et al. 2016 [27-30]	h	12.5	500	2	0.095	[13]
	ff	12.5	469	2	0.095	[16]
Singh and Friedmann 2017 [31, 32]	h	12.5	500	2	0.095	[13]
	h/ff	13.2	620	4	0.114	[11]
Bhagwat 2017 [15, 35, 46]	h/ff	3.33	623	2	0.068	[10, 35]
	h	2.17	182, 273	3	0.05 - 1.5	[9]
	h	2.15	180, 270	3	0.05 - 0.75	[9]

2.2 Scope and Objectives

The goal of this work is to develop an analysis approach to understand the aerodynamics and aeroacoustics of a CACR and their relation to noise generation sources. The results will identify primary rotor design parameters that affect noise to aid in forming low-noise CACR designs.

2.3 Coaxial Rotor Aerodynamic Features

A contra-rotating rotor brings new aerodynamic challenges, primarily the interactions between the upper and lower rotor. Specifically in hover and low-speed flight, the wake from the upper rotor impinges on the lower rotor blades and, therefore, affects the performance [14]. In high-speed forward flight, the possibility of shock formation occurs for each rotor and introduces the possibility

of shock-shock interactions between the rotors. In descent or climb, coaxial rotors complicate BVI occurrences, with the possibility of tip vortices from one rotor interacting with the other rotor [3].

2.4 Coaxial Rotor Aerodynamic Acoustic Sources

The Ffowcs Williams-Hawkings equation [47] extended Sir James Lighthill's acoustic analogy [48] to include turbulence and sound generation from surfaces that are in arbitrary motion. The Ffowcs Williams-Hawkings equation is used to predict acoustics for various rotor configurations. Equations 1 through 3 are known as Formulation 1A, which are the solutions of the Ffowcs Williams-Hawkings equation [49].

$$p'(\vec{x}, t) = p'_T(\vec{x}, t) + p'_L(\vec{x}, t), \quad (1)$$

where

$$4\pi p'_T(\vec{x}, t) = \int_{f=0} \left[\frac{\rho_0(\dot{v}_n + v_{\dot{n}})}{r |1 - M_r|^2} \right]_{ret} dS + \int_{f=0} \left[\frac{\rho_0 v_n (r \dot{M}_r + c M_r - c_0 M^2)}{r^2 |1 - M_r|^3} \right]_{ret} dS \quad (2)$$

$$4\pi p'_L(\vec{x}, t) = \frac{1}{c} \int_{f=0} \left[\frac{\dot{l}_r}{r |1 - M_r|^2} \right]_{ret} dS + \int_{f=0} \left[\frac{l_r - l_M}{r^2 |1 - M_r|^2} \right]_{ret} dS + \frac{1}{c} \int_{f=0} \left[\frac{l_r (r \dot{M}_r + c_0 M_r - c_0 M^2)}{r^2 |1 - M_r|^3} \right]_{ret} dS \quad (3)$$

A complete derivation and theoretical background of the Ffowcs Williams-Hawkings equation is presented by Brentner and Farassat [50]. A fundamental understanding of retarded time is important when predicting noise. The time at the source (τ) and time at the observer (t) are two different but dependent variables based on the distance (r) between the source (\vec{y}) and the observer (\vec{x}), and the speed of sound in the undisturbed medium (c_0). The source location (\vec{x}) is dependent on rotor radius (R), rotor velocity (ω), and τ . The relation is mathematically represented in equations 4 through 6.

$$t = \tau + \frac{r}{c_0} \quad (4)$$

where

$$r = |\vec{x} - \vec{y}| \quad (5)$$

$$\vec{y} = -R(\cos(\omega\tau), \sin(\omega\tau), 0) \quad (6)$$

The Ffowcs Williams-Hawkings equation consists of monopole, dipole, and quadrupole sources used to mathematically model the noise. Three categories of noise (thickness, loading, and HSI noise) are discussed below. Loading includes both steady and unsteady loading noise. Unsteady loading noise includes BVI, broadband, and blade-wake interaction (BWI) noise, along with other unsteady noise sources.

2.4.1 Thickness noise

A rotor blade continuously displaces the air while rotating. The displacement is due to the geometric shape of the blade. This effect is mathematically modeled as a monopole source and is referred to as thickness noise. A monopole source can be described as a sphere that repeatedly expands and contracts sinusoidally [51]. Thickness noise is predominately directed in the plane of the rotor or rotors [50]. For a coaxial rotor, the presence of two rotors in different locations will have two independent signals adding together linearly from two independent source locations. Compared to a single rotor, this rotor-rotor interaction gives rise to different aerodynamic flow behavior (air displacement) and emission directionality.

2.4.2 Loading noise

Loading noise can be both steady and unsteady. Within unsteady loading, BVI, and Broadband or BWI noise sources are particularly important for coaxial rotors.

In steady loading, the noise generated by steady aerodynamic forces is referred to as loading noise and is directed below the rotor [50]. This loading noise can be mathematically modeled as a dipole. A dipole source is a combination of two spheres expanding and contracting, 180° out of phase with each other [51].

For unsteady loading, coaxial rotors create new problems because of the rotor wake interaction, unlike the single main rotor. Crossings of the upper and lower rotor blades also generate unsteady loading occurrences.

A subset of unsteady loading is BVI, which is dependent on advance ratio, tip path plane, Mach tip number, and thrust [52], and whether the rotor is in ascent, descent, or forward flight. BVI noise occurs when the tip vortices interact with a rotor blade [53]. BVI noise is usually out-of-plane, directed down and forward for single main rotors; this is true for the CACR with the addition of other directions. The strength of each interaction depends on the tip vortex strength, the local interaction angle between the blade and vortex, and the vertical distance between the blade and vortex [54]. For coaxial rotors, the interaction between the lower rotor blade and the tip vortex from the upper rotor can create an additional interaction [3].

Analysis and prediction of rotor broadband noise has been performed, particularly by Brooks and Burley [55], but is not explored in this study.

2.4.3 HSI noise

HSI noise can occur at high rotational or forward flight speeds where transonic flow and severe shocks can form on the rotor blade. HSI noise is mathematically modeled as a quadrupole [50]. HSI noise is acoustically radiated in front of the rotor, similar to the thickness noise radiation direction.

The addition of another rotor creates a possible shock/rotor blade interaction between the upper and lower rotor, unlike a single rotor where the shock essentially has little or no interaction with another body or rotor. Although measurements of transonic flow over static airfoils have been conducted [56] and computationally predicted by many including Sengupta et al. [57], little or no work has been performed on coaxial rotor blade shock formation. With the lack of information

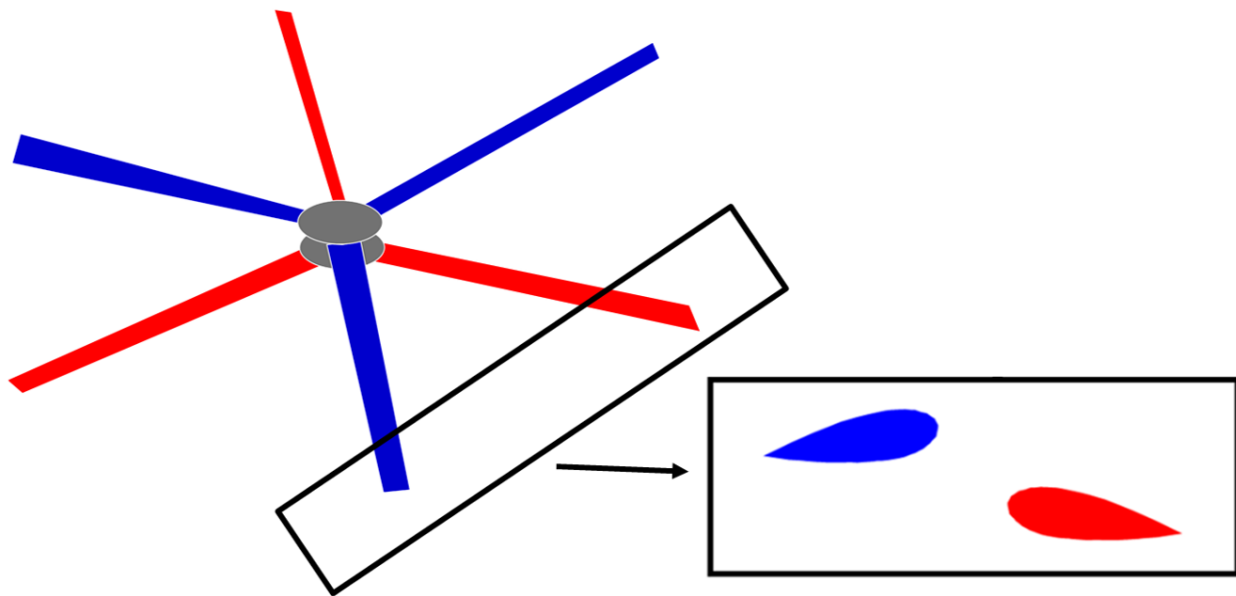


Figure 2. 3D representation of a coaxial rotor simulated in 2D as two airfoils moving past each other.

available, the idea of possible upper rotor shock and lower rotor shock interaction becomes worth exploring.

3 2D Simulation of Blade Crossings

On a coaxial rotor, each rotor operates in the induced flow field produced by the opposing rotor. This complicated flow field introduces additional aerodynamic and aeroacoustic effects compared to the single rotor. One of the effects is due to blade crossings or blade overlap. Figure 2 shows a visual representation of how this complex 3D problem of blades crossing can be deconstructed to a 2D problem by simulating the upper and lower blades as airfoils moving past each other in opposite directions.

The 2D simulations aided in understanding the effects of circulation, thickness, compressibility, viscosity, shed vorticity, and downwash for a coaxial rotor. Information from these aerodynamic effects provides insight into the aeroacoustic sources of thickness, loading, and HSI noise.

3.1 2D Representation and Assumptions

The first step towards understanding this complex 3D time-varying flow field was to model the coaxial rotor as a 2D potential flow simulation of two airfoils moving past each other. First, a simulation of two airfoils modeled as a source, vortex, and sink was computed to understand effects due to thickness and circulation. Next, a Navier-Stokes CFD tool was used to further investigate incompressible and compressible effects due to circulation, thickness, compressibility, shed vorticity, and downwash (inflow). Compared to the 3D model, the 2D representation did not capture spanwise flow, tip vortices, and curvature. However, 2D results were stacked to approximate the 3D solution in hover. Forward flight cases were not investigated in 2D for this analysis.

3.2 Potential Flow Simulation

A simplified, incompressible simulation was used to understand the change in lift at the time of airfoil crossing (or overlap). A vortex was used in this model to simulate the effect of circulation, and a source and sink were used to represent the body of the airfoil in order to simulate thickness effects. A low-speed incompressible flow is a realistic condition for inboard spanwise r/R locations.

3.2.1 Computational set up

The unsteady effects of two airfoils crossing in an incompressible flow ($M \leq 0.30$) were simulated using MATLAB software. This simplified model enabled the aerodynamic interactions at the time of an airfoil crossing to be easily analyzed. To model the unsteady effects for an incompressible flow, assumptions included 2D, inviscid, instantaneous reaction, and airfoil modeled using a source, vortex, and sink.

The upper and lower airfoils were each simulated using a source (leading edge), vortex (quarter-chord) and sink (trailing edge) as shown in Figure 3 a). The source and sink provide the ability to model thickness effects and the vortex model's circulation. Figure 3 b) shows a mathematical model of the individual sink, vortex, and source used to represent an airfoil. Figure 3 c) shows a simulated NACA 0012 airfoil at 9.8° angle of attack traveling at $M = 0.25$ using the source-vortex-sink model. The simulated airfoils are representative of an NACA 0012 with a chord of 0.5 ft. For the simulation of two airfoils crossing, the vertical separation distance was two chords. Since airfoil geometry was not fully modeled, only the change in angle of attack caused by the two airfoils crossing was analyzed.

3.2.2 Potential flow simulation results

The potential flow code VITS (Vortex Interaction Tracking Simulation) was developed to understand the aerodynamic behavior of airfoils crossing at a fixed vertical separation distance, where each airfoil is modeled as a source, vortex, and sink. VITS calculates c_l for each airfoil by using the Biot-Savart law and updating the airfoils vortex strength for each time step [58]. As the two airfoils approach each other, each airfoil induces a velocity on the other, resulting in a change in vortex strength. Figure 4 shows c_l versus distance to overlap for a flight condition of $M = 0.25$, $\alpha = 9.8^\circ$, and $S/c = 4.0$ ($S = 2.0$ ft, $c = 0.5$ ft) with no downwash for the upper and lower airfoils. The c_l of the upper (UA) and lower (LA) airfoils for VITS calculations sees an increase in lift before overlap followed by a decrease in lift after overlap. To understand the change in c_l before and after overlap, the flow field was analyzed.

Figure 5 shows the flow field from the VITS simulation in terms of vorticity, for two airfoils before, at, and after the time of crossing at a flight condition of $M = 0.25$, $\alpha = 9.8^\circ$, and $S/c = 4.0$ ($S = 2.0$ ft, $c = 0.5$ ft). To simplify the problem, downwash was not modeled for this simulation, but will be explored using OVERFLOW in a later section. As the two airfoils approach each other, the surrounding flow fields of each airfoil begin to interact. The interaction causes a symmetrical flow field before, at, and after time of overlap because of the absence of viscosity, resulting in an equal and opposite change in lift for the upper and lower airfoil. The resultant time history of the change in angle of attack (or lift) and induced velocity is visually explained in Figure 6. When compressibility is not dominating, the lift of both the upper and lower airfoil increases before the overlap, followed by a decrease in lift after the overlap. Before the overlap, the angle of attack of the upper airfoil increases because of the upwash from the lower airfoil. The angle of attack of the lower airfoil also increases due to the upwash from the upper airfoil. Therefore an increase in lift is experienced by both airfoils as depicted in Figure 6 a). The opposite occurs after the time

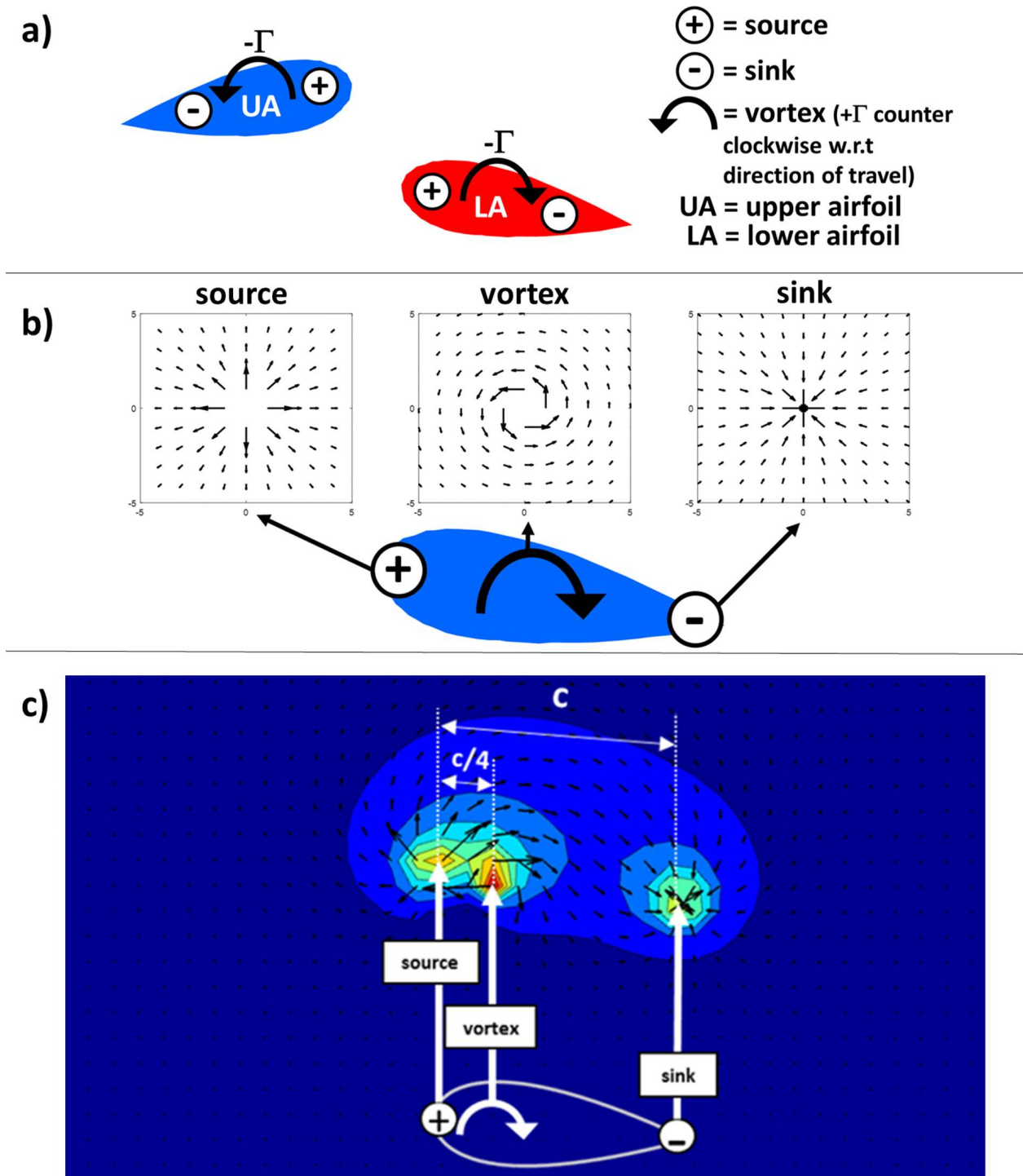


Figure 3. a) Pictorial representation of two airfoils moving past each other modeled by a source, sink, and vortex; b) mathematical model of an individual source, vortex, and sink; and c) simulation of a combined source, vortex, and sink for an isolated airfoil.

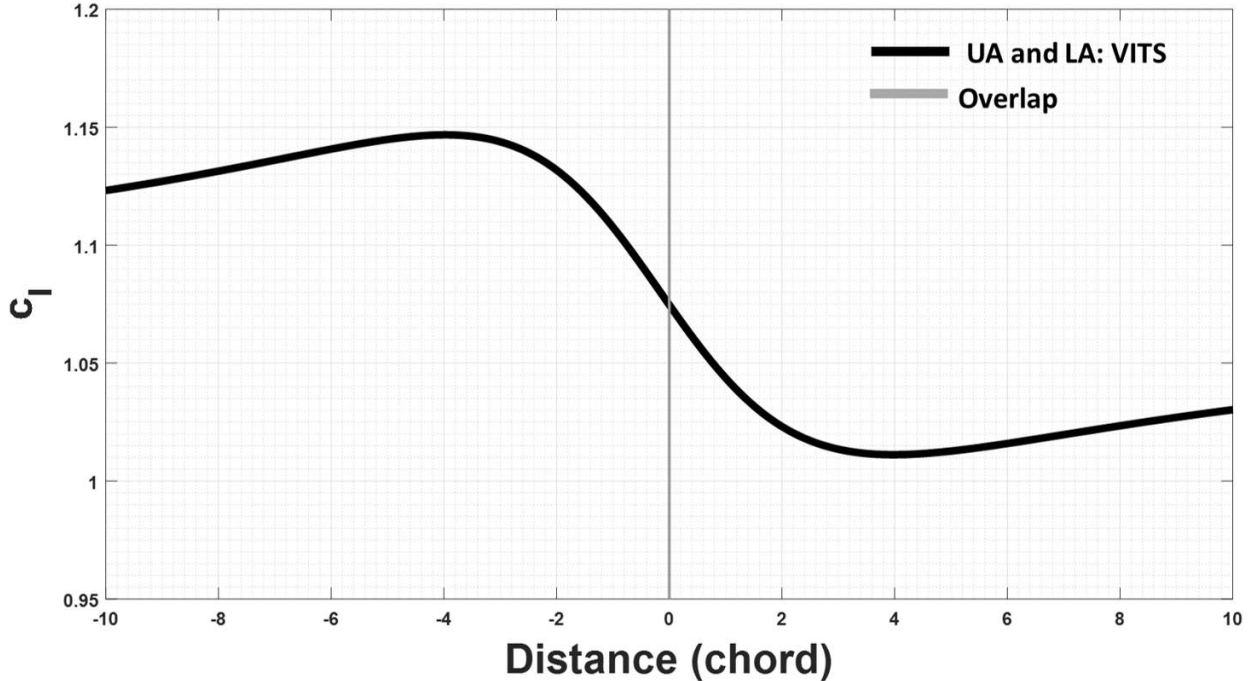


Figure 4. VITS simulation of two airfoils crossing, c_l versus distance to overlap in chords ($M = 0.25$, $\alpha = 9.8^\circ$, and $S/c = 4.0$ ($S = 2.0$ ft, $c = 0.5$ ft)).

of the overlap, where the lift for both the upper and lower airfoils decreases (see Fig. 6 b)). As the airfoils approach one another, the c_l of each airfoil changes because of the circulation effect of the other airfoil. A compressible flow solver is needed to further investigate the effects of viscosity, circulation, thickness, compressibility, downwash, and shed vorticity.

3.3 Incompressible and Compressible Flow Simulation

To capture all the aerodynamic effects of a coaxial rotor in 2D, a compressible Reynolds-Averaged Navier-Stokes solver was used to further investigate the aerodynamic sources. The computational setup, along with a detailed description of the solver, are discussed next. Initial calculations included Mach number variation of an isolated airfoil. Simulations of two airfoils crossing with variation of angle of attack, separation distance, Mach number, and airfoil thickness were compared to understand effects due to thickness, circulation, and compressibility. Furthermore, an isolated airfoil, two airfoils crossing, a single train of eight airfoils, and two trains of eight airfoils traveling in opposite directions were simulated to understand effects due to downwash and shed vorticity. Inviscid and viscous calculations were performed to help isolate the effects of downwash and shed vorticity.

3.3.1 Computational setup

The computational tool OVERFLOW 2.2k was selected because of availability and reputation to accurately calculate complex flow-field phenomena [59]. The improved computational tool aids in computing more precise, and compressible, flow-field calculations.

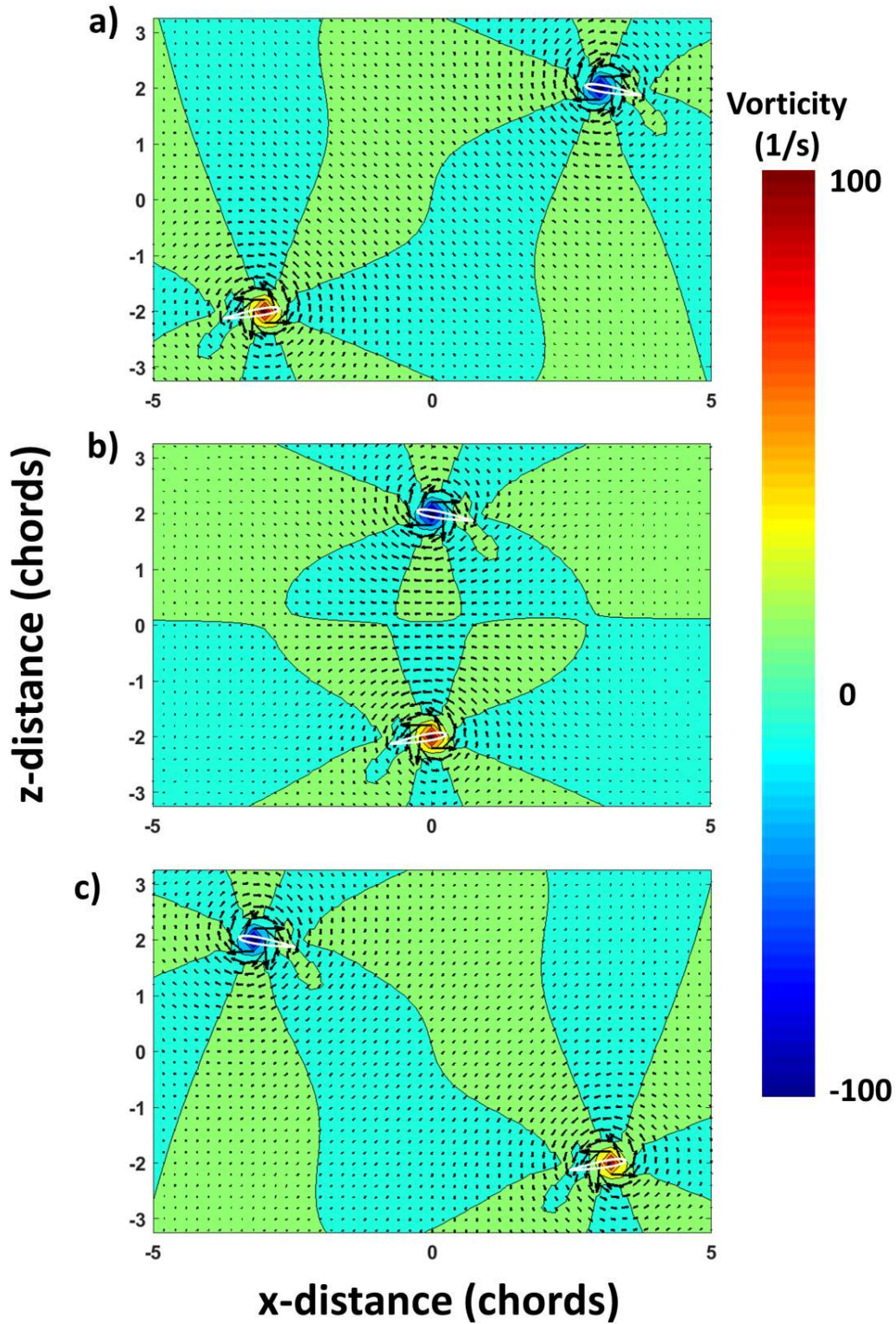
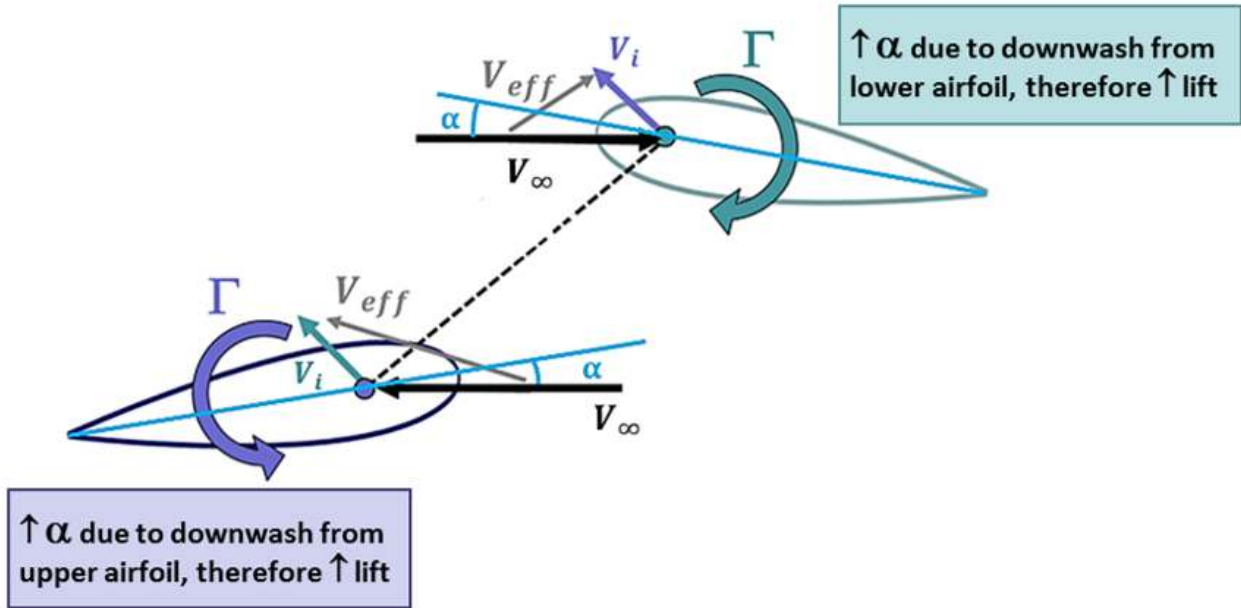


Figure 5. Simulation of two airfoils: a) before, b) at, and c) after time of crossing. Vorticity contour shown using velocity vectors, downwash not simulated ($M = 0.25$, $\alpha = 9.8^\circ$, and $S/c = 4.0$ ($S = 2.0$ ft, $c = 0.5$ ft)).

a)



b)

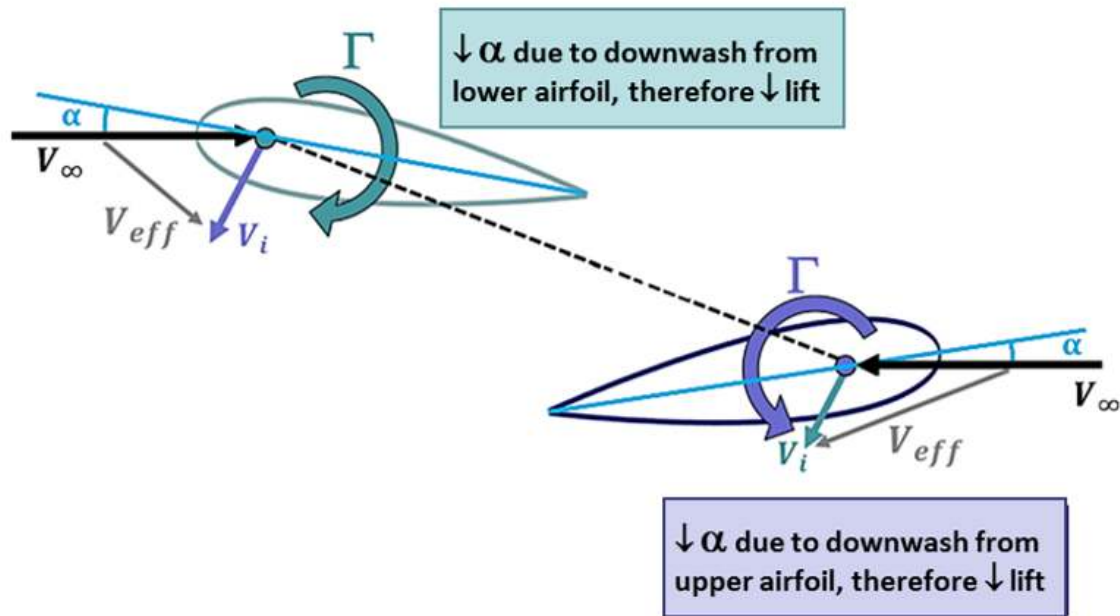


Figure 6. Change in lift of two NACA 0012 airfoils crossing (when compressibility is not dominating): a) before and b) after.

3.3.2 OVERFLOW 2.2k

OVERFLOW 2.2k [59], developed by NASA, is a compressible Reynolds-Averaged Navier-Stokes CFD analysis tool that uses structured, overset grids. This study used the OVERFLOW 2D configuration to model airfoils moving through a static background mesh. Over the course of the simulation, these airfoil(s) moved horizontally toward the origin at a speed representative of the tip speed of the coaxial rotor design. At the origin, they passed by each other to model a blade passage or “overlap.” The upper airfoil(s) were initially displaced 200 chord lengths to the right of the origin, while the lower airfoils were initially displaced 200 chord lengths to the left of the origin. This distance was chosen to give the flow sufficient time to reach a steady state before the airfoil grids reached the origin, where aerodynamic forces were constant over time. The airfoils were also displaced from the origin in the vertical direction by a distance that represented the rotor-rotor separation for the given coaxial design. This vertical separation was held constant for the entire simulation.

OVERFLOW 2.2k offers a wide variety of numerical schemes, turbulence models, and boundary conditions. All simulations in this study used a fifth-order accurate central difference spatial scheme with an ARC3D diagonalized Beam-Warming scalar pentadiagonal scheme for the left-hand side. Time marching was performed using a second-order dual time-stepping scheme. Turbulence was modeled using the Spalart-Allmaras one-equation turbulence model. Airfoil surfaces were modeled as viscous, adiabatic walls, and the edges of the computational domain were modeled using a characteristic condition that imposed a quiescent free stream at standard atmospheric conditions. A physical time step was chosen such that the airfoils moved 1/200th of a chord length for each time step. Each physical time step included 10 dual-time sub-iterations. These values ensured that sub-iteration convergence met or exceeded two orders of decrease in the residual at all times.

Airfoils were modeled using a set of identical body-fitted, curvilinear structured grids. These grids were an O-topology with 253 points around each airfoil and 65 points normal to the airfoil surface. The $y+$ value at the first point off the airfoil surface was less than one. These airfoil grids moved through a Cartesian background mesh that extended 1200 chords from the origin in the horizontal and vertical directions. Background grids can be refined based on an estimate of the solution error using overlapping Cartesian refinement grids (see Fig. 7). This grid adaption scheme ensured sufficient grid support for shed vorticity in the wake of the airfoils. All grids were modeled in 2D. Total grid sizes ranged from approximately 350,000 points for an isolated airfoil before grid adaption to approximately 11 million for an 8-airfoil simulation after grid adaption.

Forces and moments exerted on the airfoils were integrated from the pressure and viscous stress at the airfoil surface. These quantities were integrated and recorded periodically over the entire course of the simulation. The force in the vertical, z , direction is positive up and is equivalent to aerodynamic lift. The coefficient of z -force is abbreviated as c_z . The direction of force in the horizontal, x , direction is positive toward the airfoils’ trailing edge and is equivalent to aerodynamic drag. The coefficient of x -force is abbreviated c_x . The coordinate system origin is located at the quarter-chord of the airfoil, where the x direction is positive toward the airfoil’s trailing edge and the z direction is positive up. Atmospheric conditions for all 2D OVERFLOW simulations are shown in Table 2.

3.4 Simulation Setup

In order to understand the effects due to circulation, thickness, compressibility, shed vorticity, and downwash (inflow), multiple simulations were performed to study the effects independently. A complete pictorial list of the different types of simulations performed is shown in Figure 8.

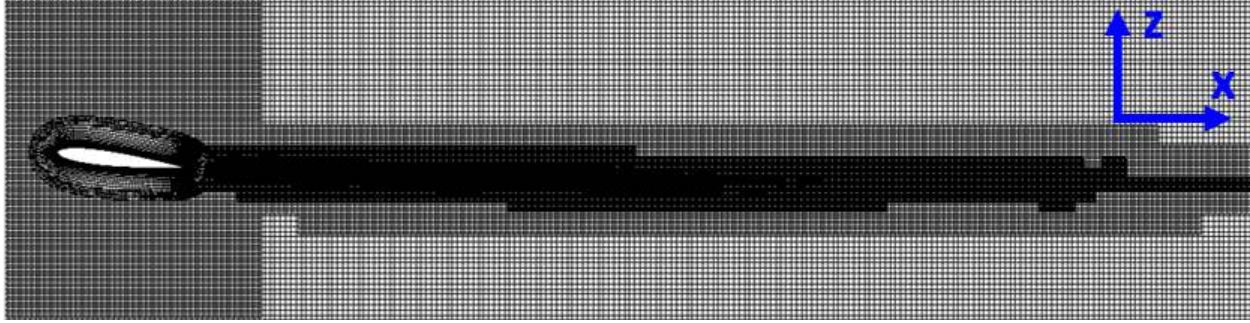


Figure 7. OVERFLOW 2.2k simulation with grid adaption for an NACA 0012 isolated airfoil at $\alpha = 7^\circ$.

Table 2. Atmospheric conditions for 2D OVERFLOW simulations.

Variable	Value	Units
pressure	2,118.17	(lb_f/ft^2)
viscosity	3.737×10^{-7} (viscous)	(slug/(s-ft))
density	0.002377	(slug/ft ³)
temperature	518.7	(R ^o)
speed of sound	1,116.46	(ft/s)

A viscid isolated airfoil was first simulated for a Mach number sweep as shown in Figure 8 c) to understand OVERFLOW settings and grid resolution. To explore effects due to circulation, thickness, and compressibility, two viscid airfoils crossing in opposite directions were simulated, as shown in Figure 8 g). An inviscid and viscous isolated airfoil were simulated and compared to understand the effect of viscous flow (Figs. 8 a) and c)). Downwash was simulated for both the inviscid and viscid isolated airfoil case to understand independent effects on a single airfoil for inflow (Figs. 8 b) and d)). Inviscid and viscid cases of two airfoils traveling in opposite directions were simulated to represent the blade crossing of a coaxial rotor (Figs. 8 e) and g)). Because of the presence of the inflow, downwash was applied for both the inviscid and viscid cases (Figs. 8 f) and h)). The effects due to shed vorticity were simulated by a single train of eight airfoils for both inviscid and viscous cases (Figs. 8 i) and k)). Downwash was simulated in the single train of eight airfoils for the inviscid and viscous case (Figs. 8 j) and l)). Two trains of eight airfoils traveling in opposite directions were simulated to represent a coaxial rotor for an inviscid and viscous case (Figs. 8 m) and o)). Downwash was simulated in the two trains of eight airfoils to model the inflow for both the inviscid and viscid case (Figs. 8 n) and p)). A pictorial of all shed vorticity simulations is shown in Figures 8 i) through p).

As previously mentioned in Chapter 1, the Harrington coaxial rotor 1 (HC1) was tested in a wind tunnel and the results have been used by many as a validation case [13]. For this study, a configuration was introduced that is representative of modern coaxial systems [41] and previously modeled by Barbely et al. [27–29]. The modern coaxial rotor design has three blades per rotor, a smaller rotor-rotor vertical separation distance, and faster tip speed compared to the HC1. Table 3 shows HC1 and modern coaxial rotor design parameters and the 2D analog.

The downwash was simulated by introducing a vertical velocity everywhere as shown in Figures 8 b), d), f), h), j), l), n), and p). The induced velocity (downwash) was calculated using a BEMT hover model for the modern rotor design as shown in Table 3. The results from the BEMT hover

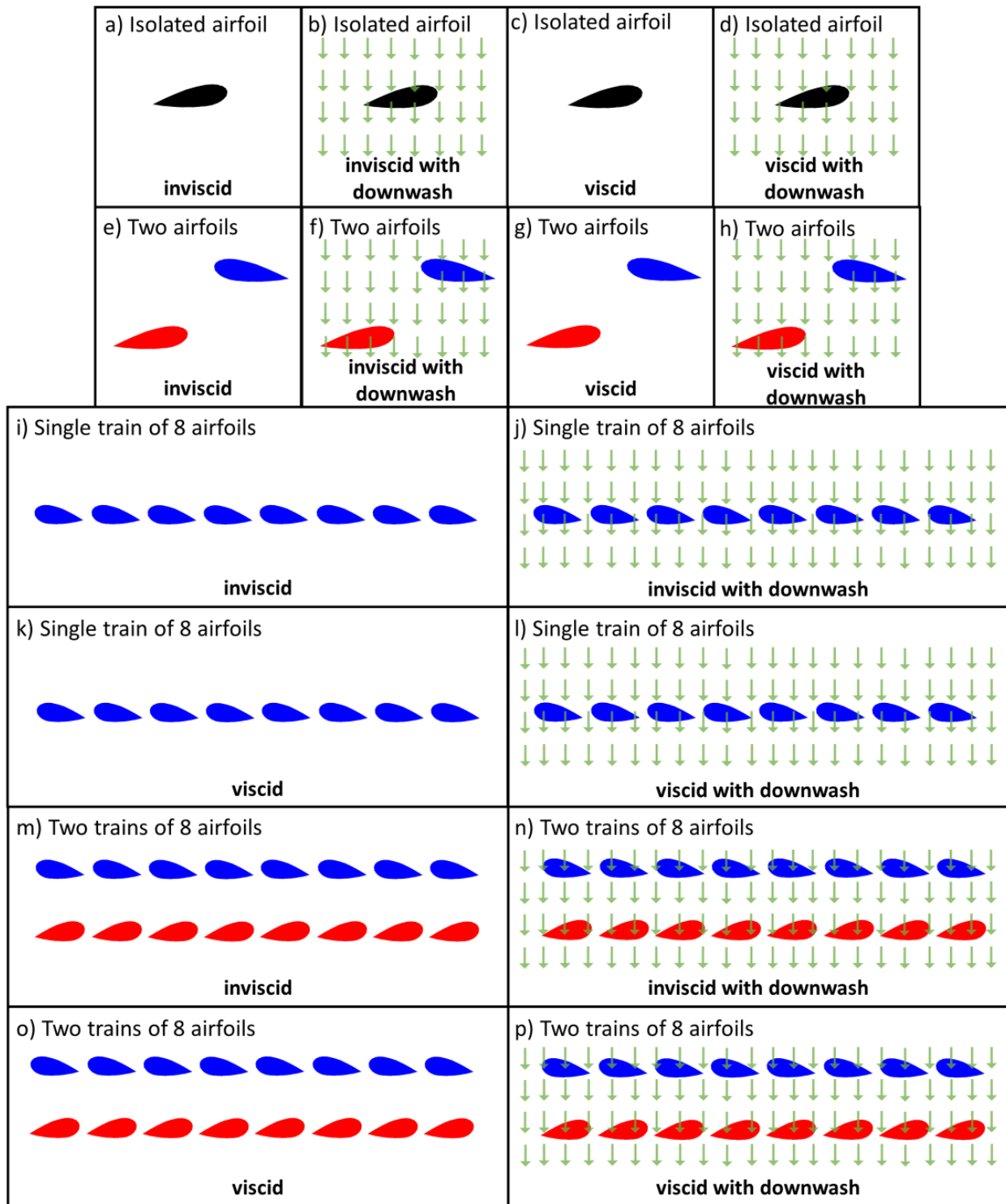


Figure 8. Inviscid and viscous simulations of an isolated airfoil (a) through d)), two airfoils crossing (e) through h)), a single train of eight airfoils (i) through l)), and two trains of eight airfoils crossing (m) through p)).

Table 3. Simulated rotor design parameters 3D and 2D analog.

2D rotor tip parameter	HC1	Modern	Coaxial rotor parameter	HC1	Modern
R , Radius (ft)	N/A	N/A	R , Radius (ft)	12.5	20
No. of airfoils (per train)	8	8	No. of blades (per rotor)	2	3
S , vertical separation between airfoils (ft)	2.33	2	S , rotor separation (ft)	2.33	2
D , horizontal separation between airfoils (ft)	39.27	41.9	D , horizontal separation (ft)	N/A	N/A
c , chord (ft)	0.375	0.5	c , chord (ft)	varying	0.5
Airfoil speed (ft/s)	500	700	V_{tip} , hover (ft/s)	500	700
M , Mach number	0.47	0.627	M , Mach number (M_{tip} for hover)	0.47	0.627
θ_{tw} , Linear twist (deg)	N/A	N/A	θ_{tw} , Linear twist (deg)	0	-8
α (deg)	7	5	α (deg)	N/A	N/A
θ_0 (deg)	N/A	N/A	θ_0 (deg)	7	0
Airfoils	NACA 0012 0012	NACA 0012 0012	Airfoils	varying	NACA 0012 0012

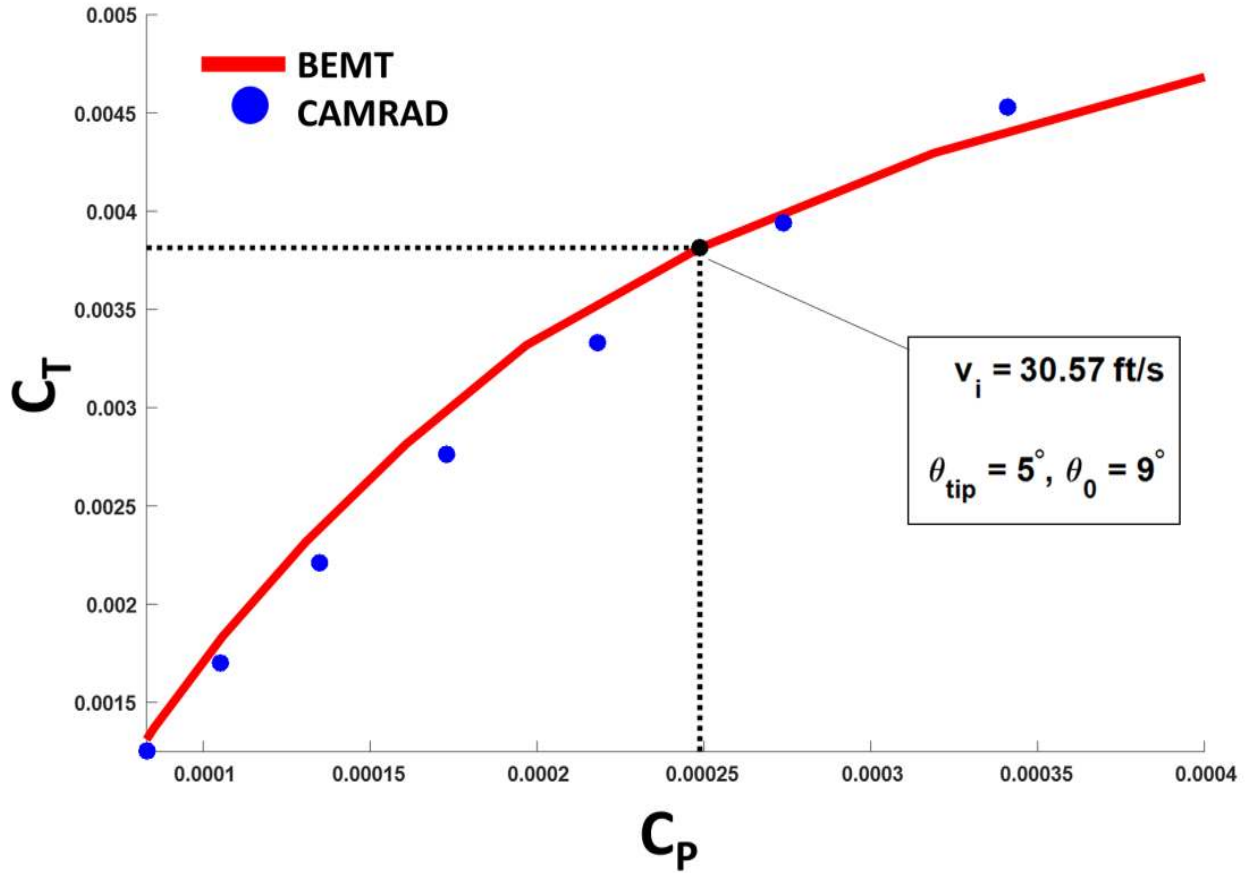


Figure 9. Coefficient of thrust versus coefficient of power for modern coaxial rotor in hover.

model were then compared to CAMRAD [60] as shown in Figure 9. The BEMT uses a coaxial interference-induced power factor from Leishman’s Case 4a [12]. Leishman’s Case 4a assumes that the rotors have balanced torque with the lower rotor operating in the slipstream of the upper rotor. The BEMT uses a C81 table and interpolates to find the correct C_l and C_d for the various span locations. For all downwash simulations, an induced velocity (V_i) of 31 ft/s was used from the modern rotor design BEMT results.

3.4.1 Simulation test conditions

Along with the various simulation setups, test conditions were varied to understand the effects of changing angle of attack (α), Mach number (M), airfoil thickness (NACA 0001/NACA 0012), vertical separation distance (S), and horizontal separation distance (D) (see Fig 10). Tables 4 through 7 provide a complete list of simulations for an isolated airfoil, two airfoils crossing, a single train of eight airfoils, and two trains of eight airfoils crossing. In Tables 4 through 7, an asterisk represents inviscid and viscid calculations, and simulations without an asterisk represent viscid-only calculations.

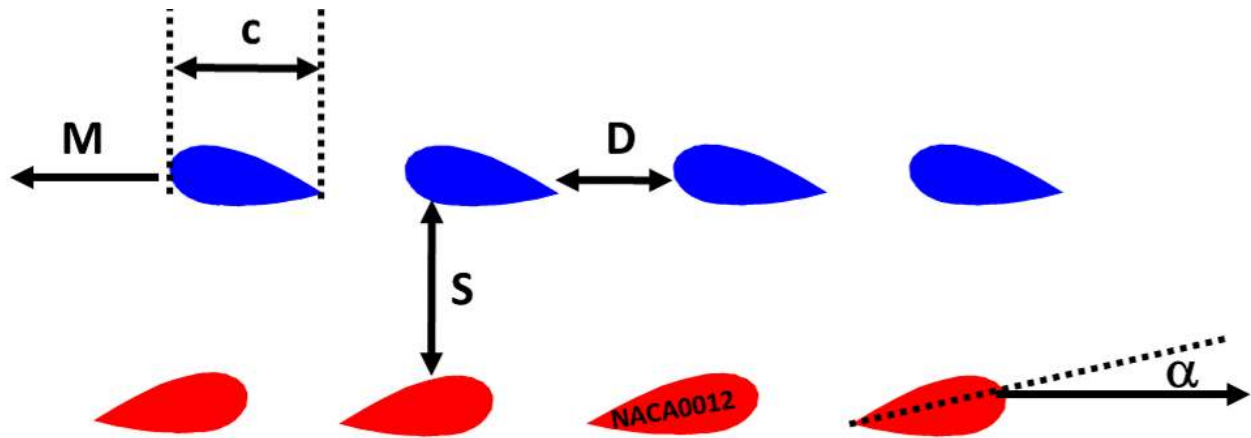


Figure 10. Simulated test condition variables.

Table 4. List of isolated airfoil OVERFLOW simulations.

Airfoil	M	S/c	D/c	α ($^{\circ}$)	V_i (ft/s)	Re #
NACA 0012*	0.25	N/A	N/A	9.8	31	8.90×10^5
NACA 0012*	0.25	N/A	N/A	9.8	0	8.90×10^5
NACA 0012	0.10	N/A	N/A	7.0	0	3.60×10^5
NACA 0012	0.20	N/A	N/A	7.0	0	7.10×10^5
NACA 0012	0.30	N/A	N/A	7.0	0	1.10×10^6
NACA 0012	0.40	N/A	N/A	7.0	0	1.40×10^6
NACA 0012	0.50	N/A	N/A	7.0	0	1.80×10^6
NACA 0012	0.60	N/A	N/A	7.0	0	2.10×10^6
NACA 0012	0.70	N/A	N/A	7.0	0	2.50×10^6
NACA 0012	0.75	N/A	N/A	7.0	0	2.70×10^6
NACA 0012	0.80	N/A	N/A	7.0	0	2.80×10^6
NACA 0012	0.90	N/A	N/A	7.0	0	3.20×10^6
NACA 0012	1.00	N/A	N/A	7.0	0	3.60×10^6
NACA 0012	1.10	N/A	N/A	7.0	0	3.90×10^6

Table 5. List of two airfoils crossing OVERFLOW simulations.

Airfoil	M	S/c	D/c	α ($^\circ$)	V_i (ft/s)	Re #
NACA 0012*	0.25	4	N/A	9.8	31	8.90×10^5
NACA 0012*	0.25	4	N/A	9.8	0	8.90×10^5
NACA 0012	0.50	4	N/A	-7.0	0	1.80×10^6
NACA 0012	0.50	4	N/A	0.0	0	1.80×10^6
NACA 0012	0.50	4	N/A	7.0	0	1.80×10^6
NACA 0012	0.90	4	N/A	-7.0	0	3.20×10^6
NACA 0012	0.90	4	N/A	0.0	0	3.20×10^6
NACA 0012	0.90	4	N/A	7.0	0	3.20×10^6
NACA 0012	0.50	2	N/A	7.0	0	1.80×10^6
NACA 0012	0.50	4	N/A	7.0	0	1.80×10^6
NACA 0012	0.50	6	N/A	7.0	0	1.80×10^6
NACA 0012	0.90	2	N/A	7.0	0	3.20×10^6
NACA 0012	0.90	4	N/A	7.0	0	3.20×10^6
NACA 0012	0.90	6	N/A	7.0	0	3.20×10^6
NACA 0012	0.20	4	N/A	0.0	0	7.10×10^5
NACA 0012	0.50	4	N/A	0.0	0	1.80×10^6
NACA 0012	0.70	4	N/A	0.0	0	2.50×10^6
NACA 0012	0.90	4	N/A	0.0	0	3.20×10^6
NACA 0012	1.00	4	N/A	0.0	0	3.60×10^6
NACA 0012	1.20	4	N/A	0.0	0	4.30×10^6
NACA 0012	0.50	4	N/A	0.0	0	1.80×10^6
NACA 0001	0.50	4	N/A	0.0	0	1.80×10^6
NACA 0012	0.90	4	N/A	0.0	0	3.20×10^6
NACA 0001	0.90	4	N/A	0.0	0	3.20×10^6
NACA 0012	0.50	4	N/A	3.0	0	1.80×10^6
NACA 0001	0.50	4	N/A	3.0	0	1.80×10^6
NACA 0012	0.90	4	N/A	3.0	0	3.20×10^6
NACA 0001	0.90	4	N/A	3.0	0	3.20×10^6

Table 6. List of single train of eight airfoils OVERFLOW simulations.

Airfoil	M	S/c	D/c	α ($^\circ$)	V_i (ft/s)	Re #
NACA 0012	0.08	N/A	11.14	11.9	0	3.00×10^5
NACA 0012	0.16	N/A	20.94	11.0	0	5.60×10^5
NACA 0012*	0.25	N/A	33.51	9.8	0	8.90×10^5
NACA 0012	0.31	N/A	41.89	9.0	0	1.10×10^6
NACA 0012	0.38	N/A	50.27	8.2	0	1.30×10^6
NACA 0012	0.47	N/A	62.83	7.0	0	1.70×10^6
NACA 0012	0.50	N/A	67.02	6.6	0	1.80×10^6
NACA 0012	0.53	N/A	71.21	6.2	0	1.90×10^6
NACA 0012	0.56	N/A	75.40	5.8	0	2.00×10^6
NACA 0012	0.60	N/A	79.59	5.4	0	2.10×10^6
NACA 0012	0.63	N/A	83.78	5.0	0	2.20×10^6

Table 7. List of two trains of eight airfoils OVERFLOW simulations.

Airfoil	M	S/c	D/c	α ($^\circ$)	V_i (ft/s)	Re #
NACA 0012	0.08	4	11.14	11.9	31	3.00×10^5
NACA 0012	0.16	4	20.94	11.0	31	5.60×10^5
NACA 0012*	0.25	4	33.51	9.8	31	8.90×10^5
NACA 0012	0.31	4	41.89	9.0	31	1.10×10^6
NACA 0012	0.38	4	50.27	8.2	31	1.30×10^6
NACA 0012	0.47	4	62.83	7.0	31	1.70×10^6
NACA 0012	0.50	4	67.02	6.6	31	1.80×10^6
NACA 0012	0.53	4	71.21	6.2	31	1.90×10^6
NACA 0012	0.56	4	75.40	5.8	31	2.00×10^6
NACA 0012	0.60	4	79.59	5.4	31	2.10×10^6
NACA 0012	0.63	4	83.78	5.0	31	2.20×10^6

3.5 Isolated Airfoil Mach Sweep

A Mach number sweep simulation was performed for Mach 0.10, 0.20, 0.30, 0.40, 0.50, 0.60, 0.70, 0.75, 0.80, 0.90, 1.00, and 1.10 for a viscid isolated NACA 0012 airfoil at $\alpha = 7^\circ$ with a chord of 0.50 ft (Table 4). Figure 11 a) shows the variation with Mach number for c_l and c_d . Figure 11 b) shows C_P versus nondimensional chord (x/c) for the same Mach number range. Coefficient of pressure (C_P) contours of the flow field of the isolated airfoil for $M =$ a) 0.10, b) 0.30, c) 0.50, d) 0.60, e) 0.70, f) 0.80, g) 0.90, h) 1.0, and i) 1.1 are shown in Figure 12.

An increase in c_d with increasing Mach number was observed in Figure 11 a), which is due to shocks and viscous forces increasing with Mach number [58]. As shocks move toward the trailing edge, the drag decreases because of the weakening of the trailing edge shocks.

From Mach 0.10 to 0.50, an increase in c_l was observed. From Mach 0.50 to 0.80, a decrease in c_l was observed in Figure 11 a); this decrease in c_l is because flow is supersonic over most of the lower surface and decelerated to subsonic speeds through a shock wave at the trailing edge, so lower surface pressures are lower than before Mach 0.50. The location of the shock wave can be determined from Figure 11 b). For example, at Mach 0.80 and 0.90, the shock was at $x/c = 0.35$ and 0.90, respectively. The formation of a shock wave on the upper surface became more apparent from the C_P behavior, as shown in Figure 11 b) and Figure 12 in comparison to Figure 11 a). As the Mach number increased further to 0.90, c_l increased because of the upper surface shock wave moving to the trailing edge, where the local Mach number was supersonic for most of the airfoil [58]. Beyond, Mach 1.0, the upper and lower shock have moved to the tail, creating a fishtail of shocks.

3.6 Two Airfoils Crossing: Circulation, Thickness, and Compressibility Effects

The effects due to circulation, thickness, and compressibility for a coaxial rotor blade crossing occurrence were simulated by two airfoils, separated vertically, traveling in opposite directions. The time of overlap is when the quarter-chord of each airfoil overlap. Because of the change in angle of attack at time of crossing, the notations c_l and c_d cannot be used. c_z is the force in the vertical direction at quarter-chord, and c_x is the force in the horizontal direction at quarter-chord. In general, c_l and c_d are in the wind axis, so the force direction changes based on angle of attack, whereas within OVERFLOW the vertical and horizontal force vectors are fixed (c_z and c_x). Various conditions were simulated for two airfoils crossing, each with a chord (c) of 0.5 feet; see Table 8.

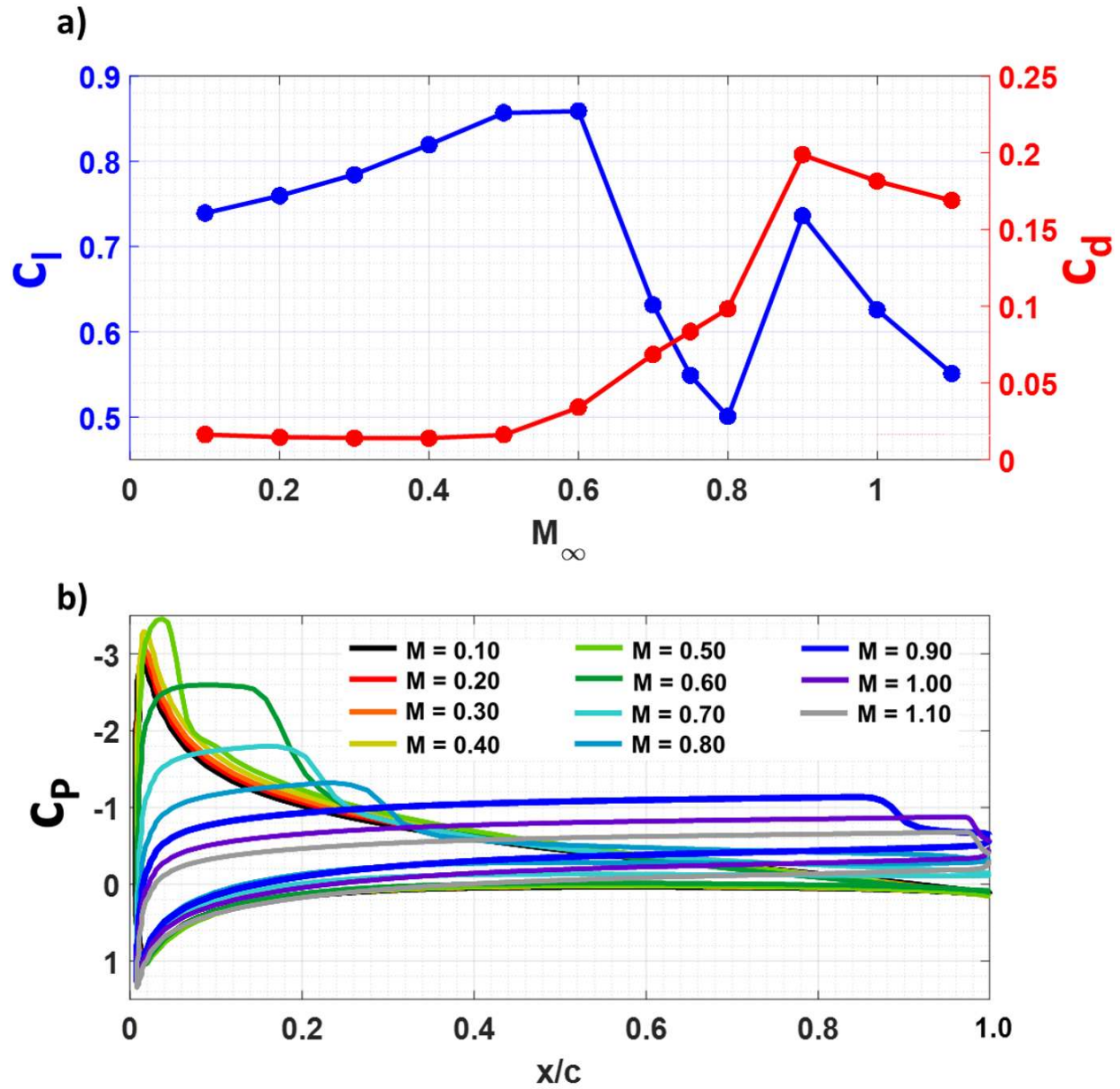


Figure 11. Viscid isolated NACA 0012 airfoil at $\alpha = 7^\circ$ with a chord of 0.50 ft, Mach number variation for a) c_l and c_d , and b) C_P versus x/c .

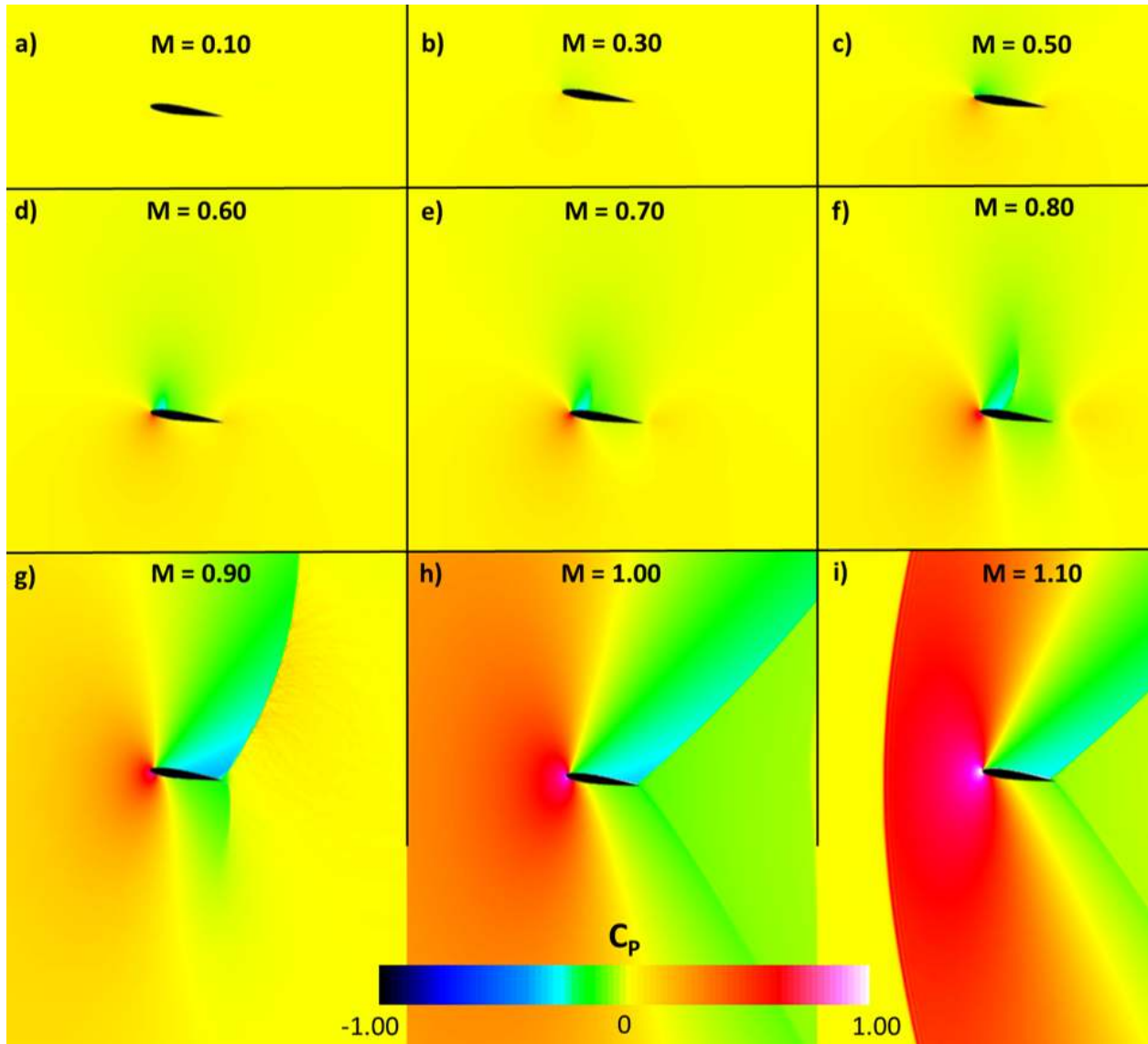


Figure 12. C_P flow-field contours for Mach number variation for an isolated NACA 0012 airfoil at $\alpha = 7^\circ$, and $M =$ a) 0.10, b) 0.30, c) 0.50, d) 0.60, e) 0.70, f) 0.80, g) 0.90, h) 1.0, and i) 1.1.

Table 8. Conditions for 2D OVERFLOW simulations for two airfoils crossing.

Airfoil	M	S (ft)	S/c	α ($^\circ$)	Re #
Low-speed: α variation					
NACA 0012	0.5	2	4	-7	1.78×10^6
NACA 0012	0.5	2	4	0	1.78×10^6
NACA 0012	0.5	2	4	7	1.78×10^6
High-speed: α variation					
NACA 0012	0.9	2	4	-7	3.20×10^6
NACA 0012	0.9	2	4	0	3.20×10^6
NACA 0012	0.9	2	4	7	3.20×10^6
Low-speed: S variation					
NACA 0012	0.5	1	2	7	1.78×10^6
NACA 0012	0.5	2	4	7	1.78×10^6
NACA 0012	0.5	3	6	7	1.78×10^6
High-speed: S variation					
NACA 0012	0.9	1	2	7	3.20×10^6
NACA 0012	0.9	2	4	7	3.20×10^6
NACA 0012	0.9	3	6	7	3.20×10^6
Mach variation					
NACA 0012	0.2	2	4	0	7.10×10^5
NACA 0012	0.5	2	4	0	1.78×10^6
NACA 0012	0.7	2	4	0	2.49×10^6
NACA 0012	0.9	2	4	0	3.20×10^6
NACA 0012	1.0	2	4	0	3.55×10^6
NACA 0012	1.2	2	4	0	4.26×10^6
Low-speed: Airfoil variation, $\alpha = 0^\circ$					
NACA 0012	0.5	2	4	0	1.78×10^6
NACA 0001	0.5	2	4	0	1.78×10^6
High-speed: Airfoil variation, $\alpha = 0^\circ$					
NACA 0012	0.9	2	4	0	3.20×10^6
NACA 0001	0.9	2	4	0	3.20×10^6
Low-speed: Airfoil variation, $\alpha = 3^\circ$					
NACA 0012	0.5	2	4	0	1.78×10^6
NACA 0001	0.5	2	4	0	1.78×10^6
High-speed: Airfoil variation, $\alpha = 3^\circ$					
NACA 0012	0.9	2	4	3	3.20×10^6
NACA 0001	0.9	2	4	3	3.20×10^6

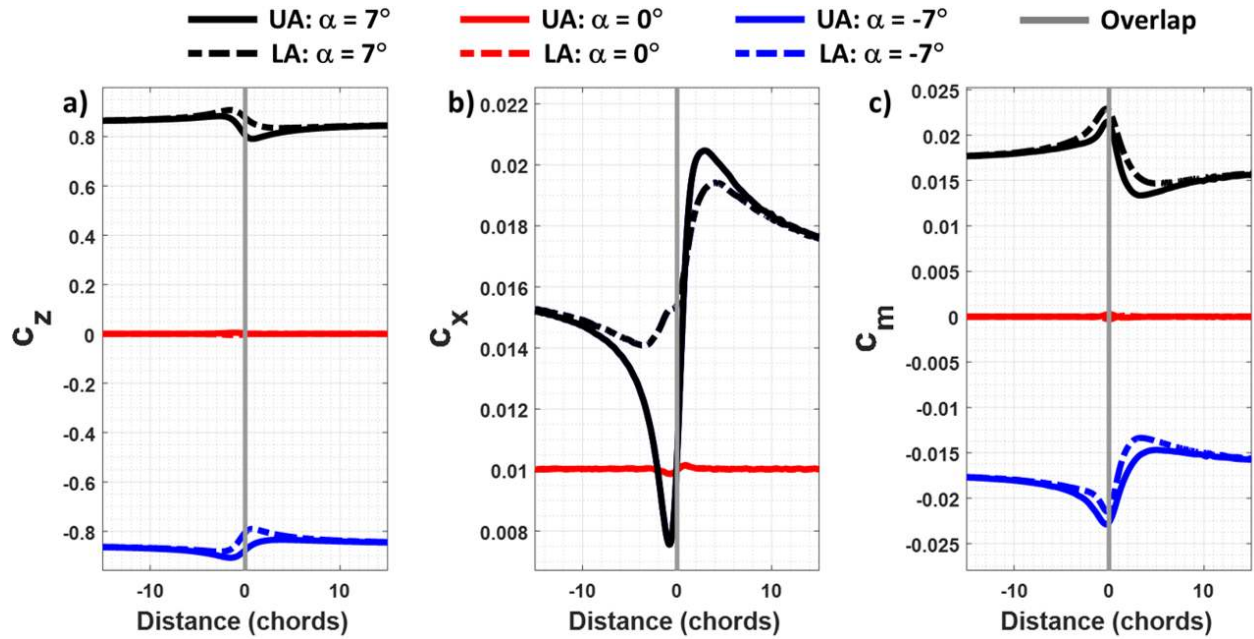


Figure 13. Two NACA 0012 airfoils crossing for a) c_z , b) c_x , and c) c_m versus distance to overlap ($M = 0.5$ ($V_{tip} = 560$ ft/s), $\alpha = -7^\circ, 0^\circ$, and 7° , and $S/c = 4.0$ ($S = 2.0$ ft, $c = 0.5$ ft)).

3.6.1 Two airfoils crossing: circulation

Effects due to circulation are caused by changes in the measure of rotation for a finite area of fluid. A change in α results in a change in circulation. To isolate effects due to circulation, airfoil thickness, separation distance, and Mach number were held constant.

For two NACA 0012 airfoils crossing at $M = 0.50$ and $S/c = 4.0$, angles of attack equal to -7° , 0° , and 7° were simulated (see Fig 13). An α of -7° and 7° shows an equal and opposite result for c_z and c_m , while for c_x , the results are equal. Minimum change between the upper and lower airfoil in c_z , c_x , and c_m is shown for $\alpha = 0^\circ$ compared to $\alpha = -7^\circ$ and 7° , which reveals that effects due to circulation are significant.

Similar comparisons were made for $M = 0.90$. Figure 14 shows two NACA 0012 airfoils crossing at $M = 0.90$ and $S/c = 4.0$, for angles of attack of -7° , 0° , and 7° . As shown for the low-speed case, an α of -7° and 7° gives an almost equal and opposite result for c_z and c_m , while for c_x , the results are equal. Large differences between the two speed cases could be due to compressibility effects.

3.6.2 Two airfoils crossing: thickness

Thickness effects are caused by the displacement of flow due to the geometry of the body and the location of bodies relative to each other. To isolate effects due to thickness, an NACA 0001 and an NACA 0012 were compared for 0° and 3° angle of attack for a low- and high-speed condition, while keeping all other variables constant. The NACA 0001 was used to simulate a flat plate. The NACA 0012 was selected even though current modern-day helicopters avoid thick airfoils; the NACA 0012 represents an extreme geometry. Vertical separation distance between airfoils was varied for a low- and high-speed condition.

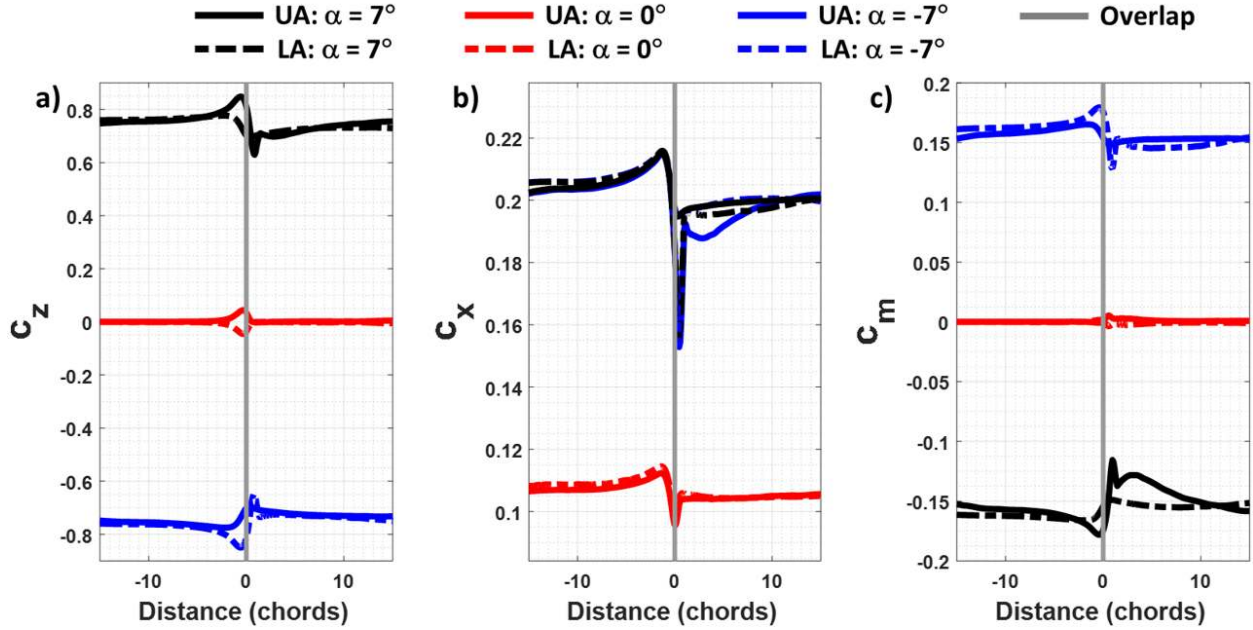


Figure 14. Two NACA 0012 airfoils crossing for a) c_z , b) c_x , and c) c_m versus distance to overlap ($M = 0.9$ ($V_{tip} = 1,005$ ft/s), $\alpha = -7^\circ, 0^\circ$, and 7° , and $S/c = 4.0$ ($S = 2.0$ ft, $c = 0.5$ ft)).

The c_z , c_x , and c_m of two NACA 0001 and two NACA 0012 airfoils crossing versus distance to overlap are shown in Figure 15. The conditions for both airfoil calculations were $M = 0.5$ ($V_{tip} = 560$ ft/s), $\alpha = 0^\circ$, and $S/c = 4.0$ ($S = 2.0$ ft, $c = 0.5$ ft). Although changes in c_z , c_x , and c_m are observed in Figure 15 comparing the two airfoils, the magnitude of the aerodynamic forces for each airfoil is small. A similar comparison of the same airfoils, but for $\alpha = 3^\circ$, is shown in Figure 17; in this case effects due to circulation dominate because of the increase in angle of attack. The aerodynamic forces shown in Figure 15 are orders of magnitude fewer than the forces shown in Figure 17, supporting the conclusion that circulation effects dominate thickness effects.

For $M = 0.90$, a comparison of two NACA 0001 and two NACA 0012 airfoils crossing is shown in Figure 16. As previously concluded from Figure 15, minimal changes in c_z , c_x , and c_m at time of overlap are observed because of thickness effects. Differences between the loads of the two speed cases are due to compressibility effects. A similar comparison is made for $\alpha = 3^\circ$ (Fig. 18), where effects due to circulation and compressibility dominate.

Separation distance between airfoils was varied for two NACA 0012 airfoils crossing for $M = 0.5$ ($V_{tip} = 560$ ft/s) and $\alpha = 7^\circ$. Figure 19 shows results for $S/c = 2.0, 4.0$, and 6.0 ($c = 0.5$ ft). An increase in S/c resulted in a decrease in c_z , c_x , and c_m in the interaction transient. For these cases, effects due to circulation ($\alpha = 7^\circ$) and airfoil thickness are present. The same comparison is made for a high-speed case ($M = 0.9$ ($V_{tip} = 1,005$ ft/s)), as shown in Figure 20.

3.6.3 Two airfoils crossing: compressibility

The magnitude of compressibility effects depends on Mach number. As the flow over an airfoil approaches Mach 1.0, the onset of shocks form. In order to explore effects due to compressibility, the Mach number is varied for two airfoils traveling in opposite directions with fixed angle of attack and vertical separation distance.

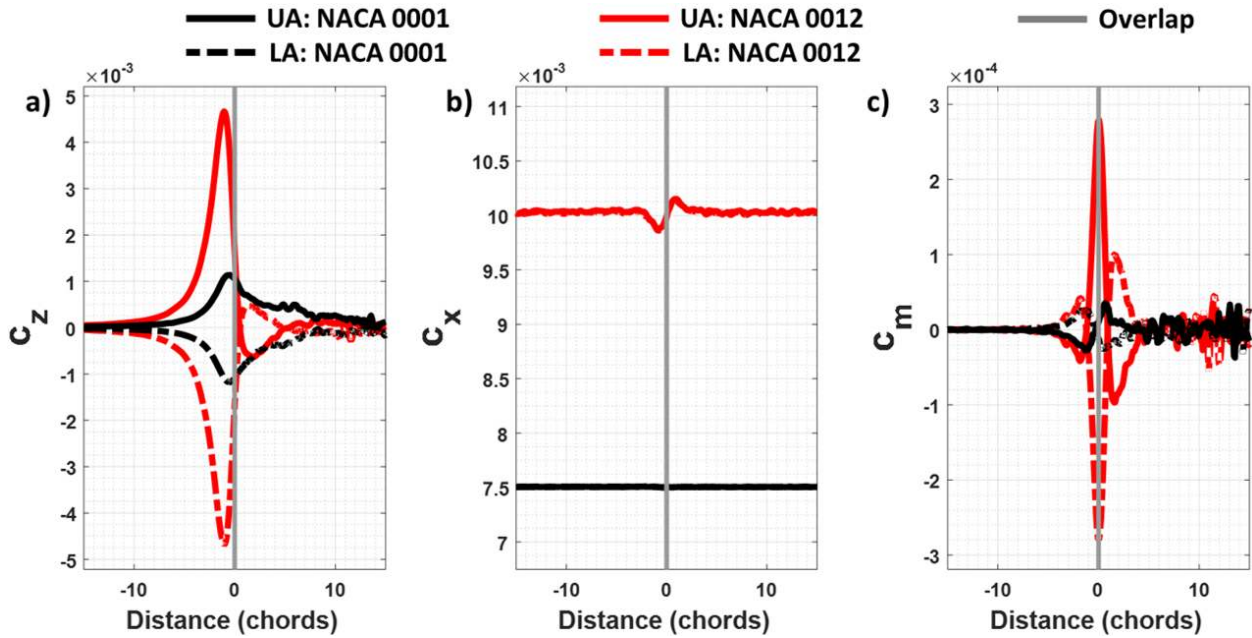


Figure 15. Comparison of two NACA 0001 and NACA 0012 airfoils crossing for a) c_z , b) c_x , and c) c_m versus distance to overlap ($M = 0.5$ ($V_{tip} = 560$ ft/s), $\alpha = 0^\circ$, and $S/c = 4.0$ ($S = 2.0$ ft, $c = 0.5$ ft)).

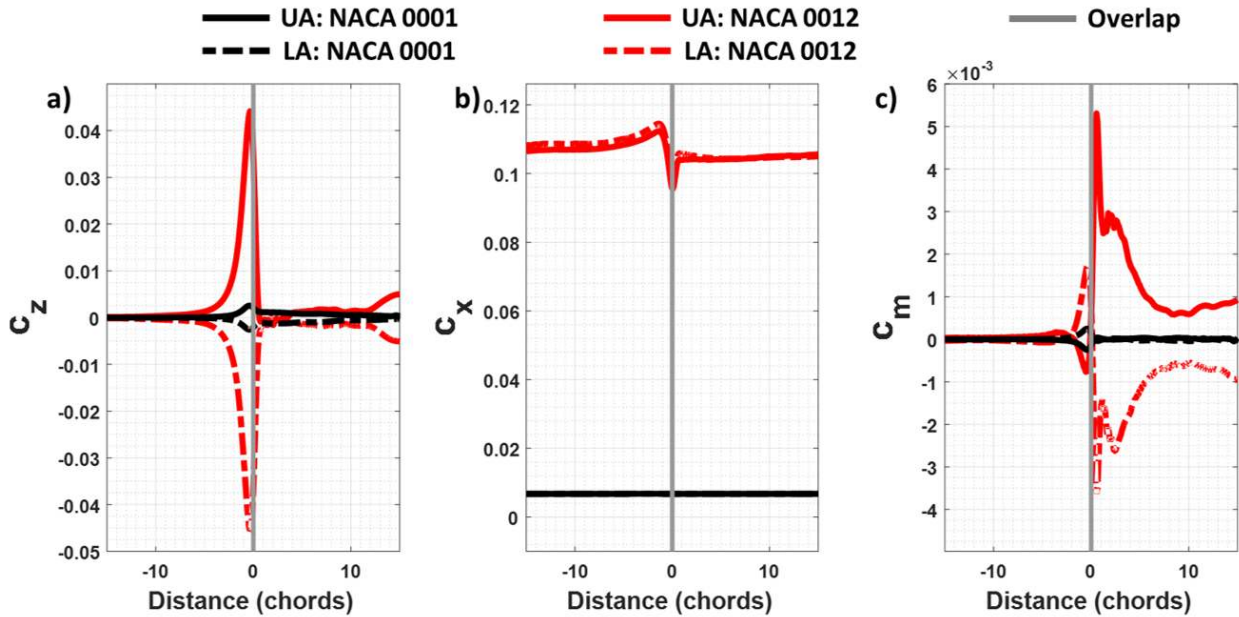


Figure 16. Comparison of two NACA 0001 and NACA 0012 airfoils crossing for a) c_z , b) c_x , and c) c_m versus distance to overlap ($M = 0.9$ ($V_{tip} = 1,005$ ft/s), $\alpha = 0^\circ$, and $S/c = 4.0$ ($S = 2.0$ ft, $c = 0.5$ ft)).

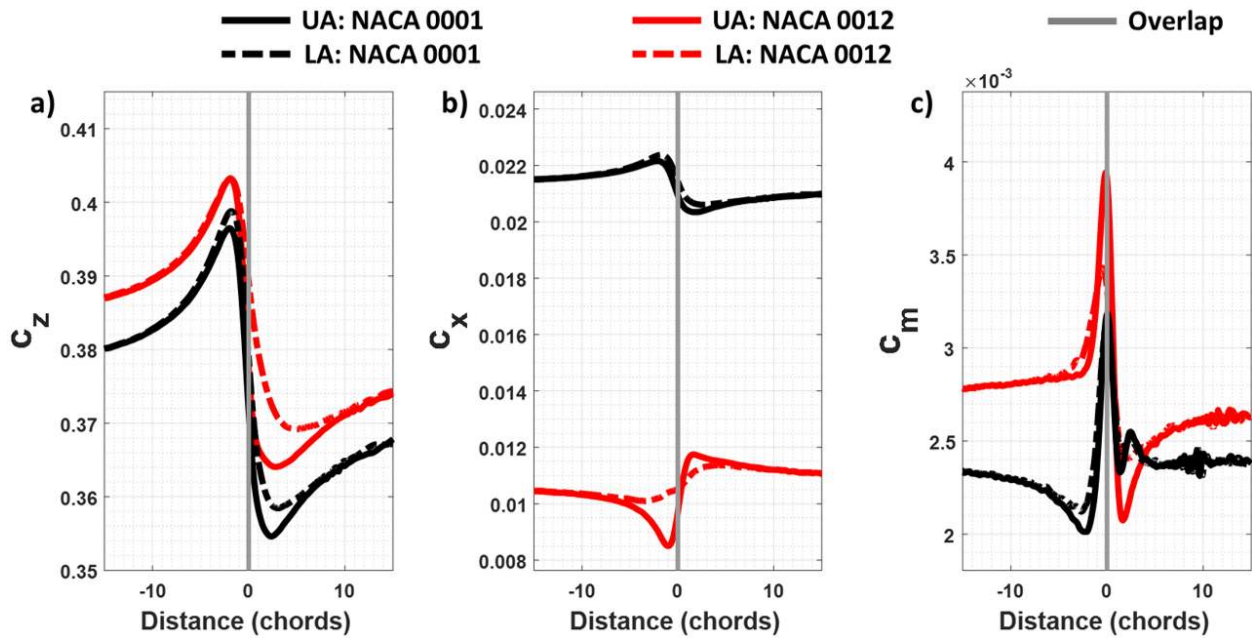


Figure 17. Comparison of two NACA 0001 and NACA 0012 airfoils crossing for a) c_z , b) c_x , and c) c_m versus distance to overlap ($M = 0.5$ ($V_{tip} = 560$ ft/s), $\alpha = 3^\circ$, and $S/c = 4.0$ ($S = 2.0$ ft, $c = 0.5$ ft)).

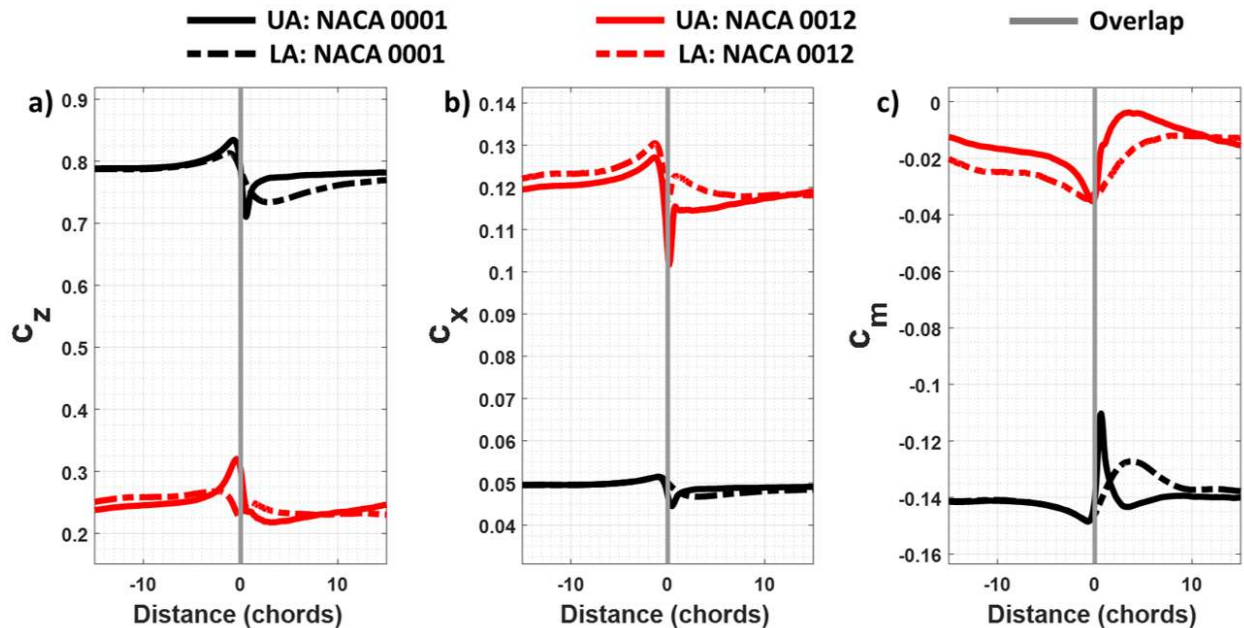


Figure 18. Comparison of two NACA 0001 and NACA 0012 airfoils crossing for a) c_z , b) c_x , and c) c_m versus distance to overlap ($M = 0.9$ ($V_{tip} = 1,005$ ft/s), $\alpha = 3^\circ$, and $S/c = 4.0$ ($S = 2.0$ ft, $c = 0.5$ ft)).

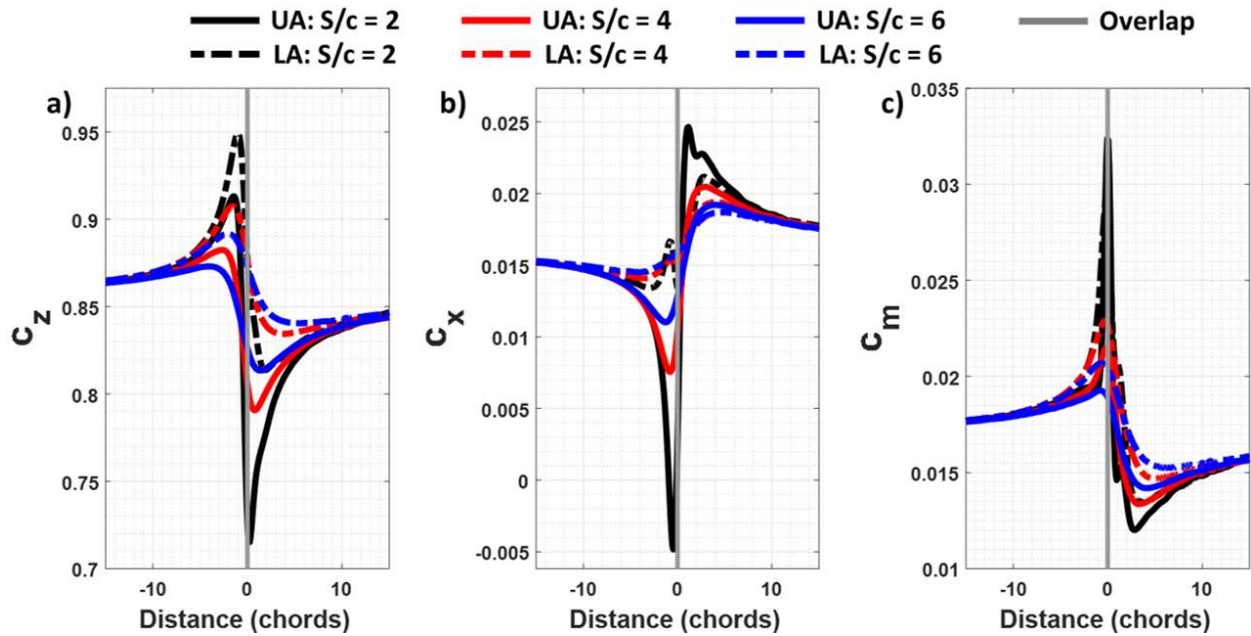


Figure 19. Two NACA 0012 airfoils crossing for a) c_z , b) c_x , and c) c_m versus distance to overlap ($M = 0.5$ ($V_{tip} = 560$ ft/s), $\alpha = 7^\circ$, and $S/c = 2.0, 4.0,$ and 6.0 ($c = 0.5$ ft)).

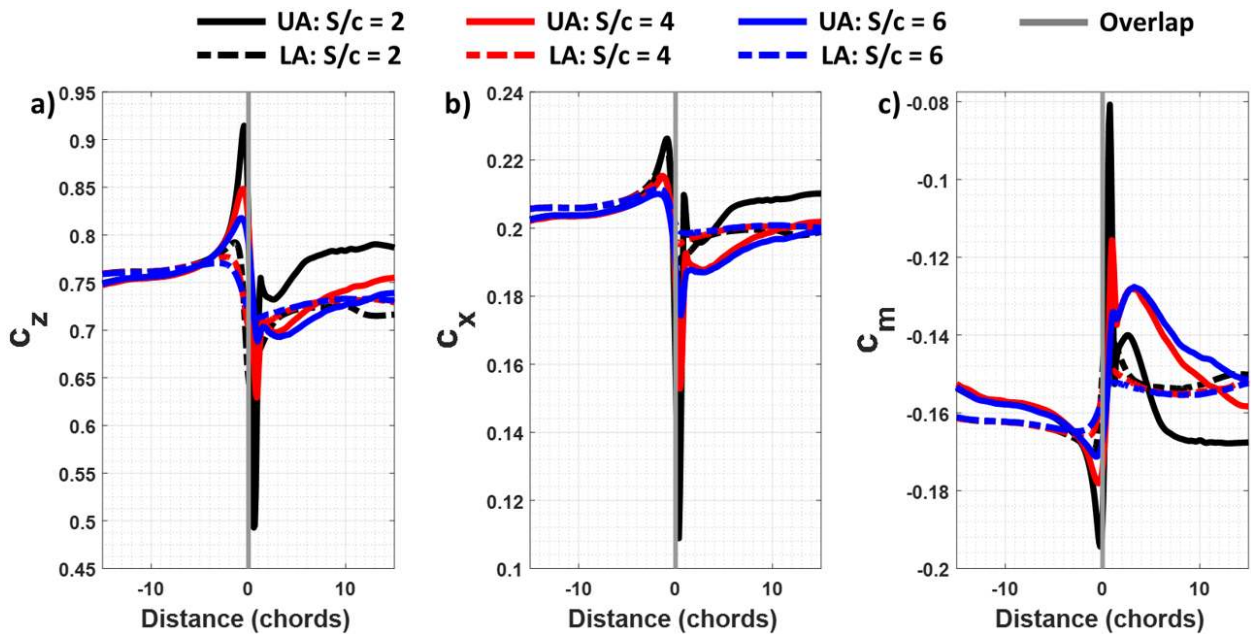


Figure 20. Two NACA 0012 airfoils crossing for a) c_z , b) c_x , and c) c_m versus distance to overlap ($M = 0.9$ ($V_{tip} = 1,005$ ft/s), $\alpha = 7^\circ$, and $S/c = 2.0, 4.0,$ and 6.0 ($c = 0.5$ ft)).

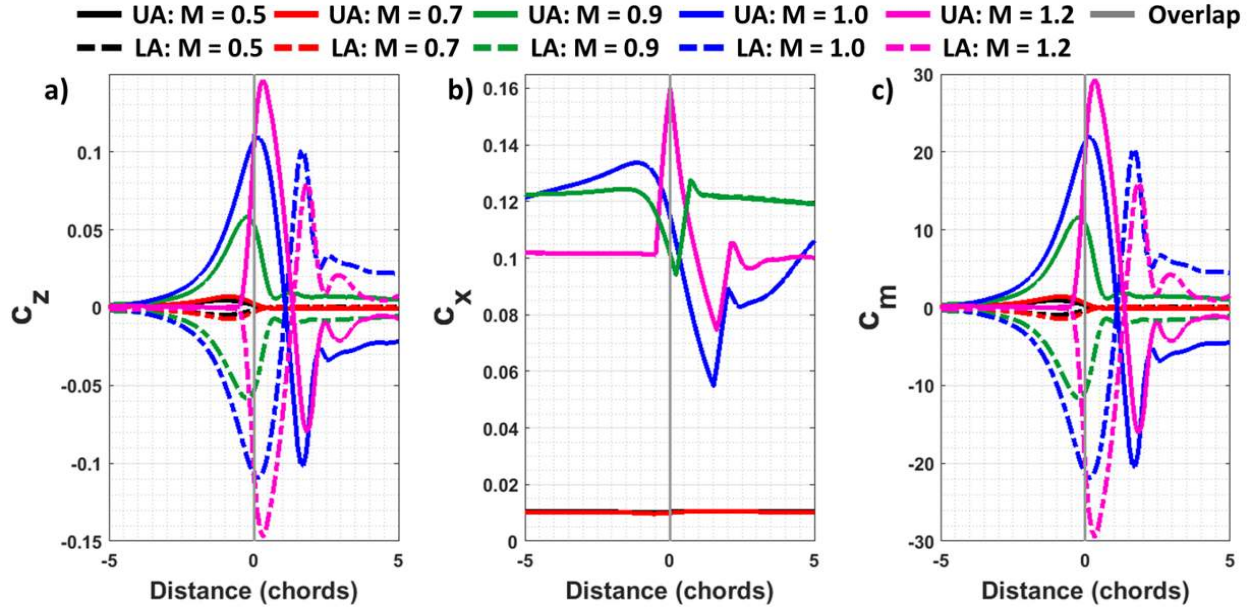


Figure 21. Two NACA 0012 airfoils crossing for a) c_z , b) c_x , and c) c_m versus distance to overlap ($M = 0.5, 0.7, 0.9, 1.0,$ and 1.2 ($V_{tip} = 560, 780, 1005, 1116,$ and 1340 ft/s), $\alpha = 0^\circ$, and $S/c = 4.0$ ($S = 2.0$ ft, $c = 0.5$ ft)).

Figure 21 shows c_z , c_x , and c_m for a Mach sweep of 0.50 to 1.2 for two NACA 0012 airfoils crossing. Even though helicopters avoid high-speed-flight regimes, Mach numbers above 0.90 are compared to explore the design domain for educational purposes. The angle of attack of both airfoils was $\alpha = 0^\circ$, and $S/c = 4.0$ ($S = 2.0$ ft, $c = 0.5$ ft). An angle of attack of 0 is used to eliminate circulations effects, though a NACA 0012 still includes thickness effects. A large increase in lift, drag, and moment is seen as the Mach number reaches 0.90, where weak shocks begin to form.

Figure 22 shows the Mach contour of two airfoils crossing a) before, b) at, and c) after overlap for Mach 1.2. As the two airfoils approach each other (Fig. 22 a)), a bow shock is formed in front of each airfoil. At the time of overlap (Fig. 22 b)), the shocks from each airfoil coincide and a shock-airfoil interaction occurs. After time of overlap (Fig. 22 c)), the shock-airfoil interaction continues, where the lower surface of the upper airfoil is impacted by the upper surface shock of the lower airfoil, and vice versa for the lower airfoil.

Today's helicopters avoid high Mach numbers, although a high Mach number of 0.9 is a more realistic case for today's coaxial rotors. Figure 23 shows the Mach contour of two airfoils crossing a) before, b) at, and c) after overlap for Mach 0.9. Figure 23 also shows a shock-airfoil interaction but with weaker shocks. As the angle of attack increases, so does the strength of the shocks, therefore resulting in unsteady aerodynamics.

3.7 Viscosity, Shed Vorticity, and Downwash Effects

The two airfoils traveling in opposite directions demonstrated the effects of circulation, thickness, and compressibility for a coaxial rotor, but lacked any treatment of the rotor wake, because of multiple blades. Viscous effects due to shed vorticity and downwash are discussed by comparing the aerodynamic flow field of an isolated airfoil, two airfoils crossing, a single train of eight air-

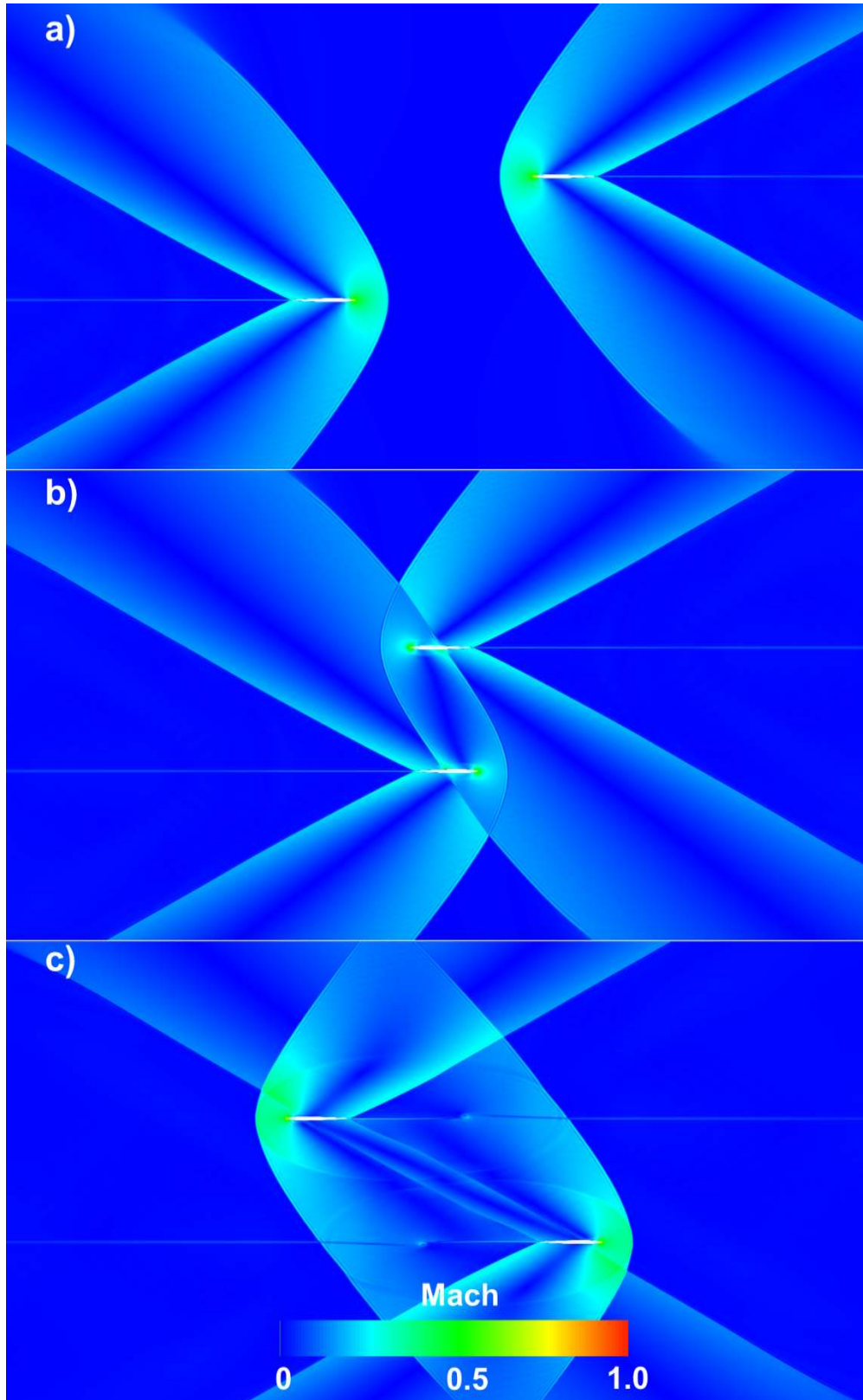


Figure 22. Mach contour of two airfoils crossing a) before, b) at, and c) after overlap ($M = 1.2$, $\alpha = 0^\circ$, and $S/c = 4.0$ ($S = 2.0$ ft, $c = 0.5$ ft)).

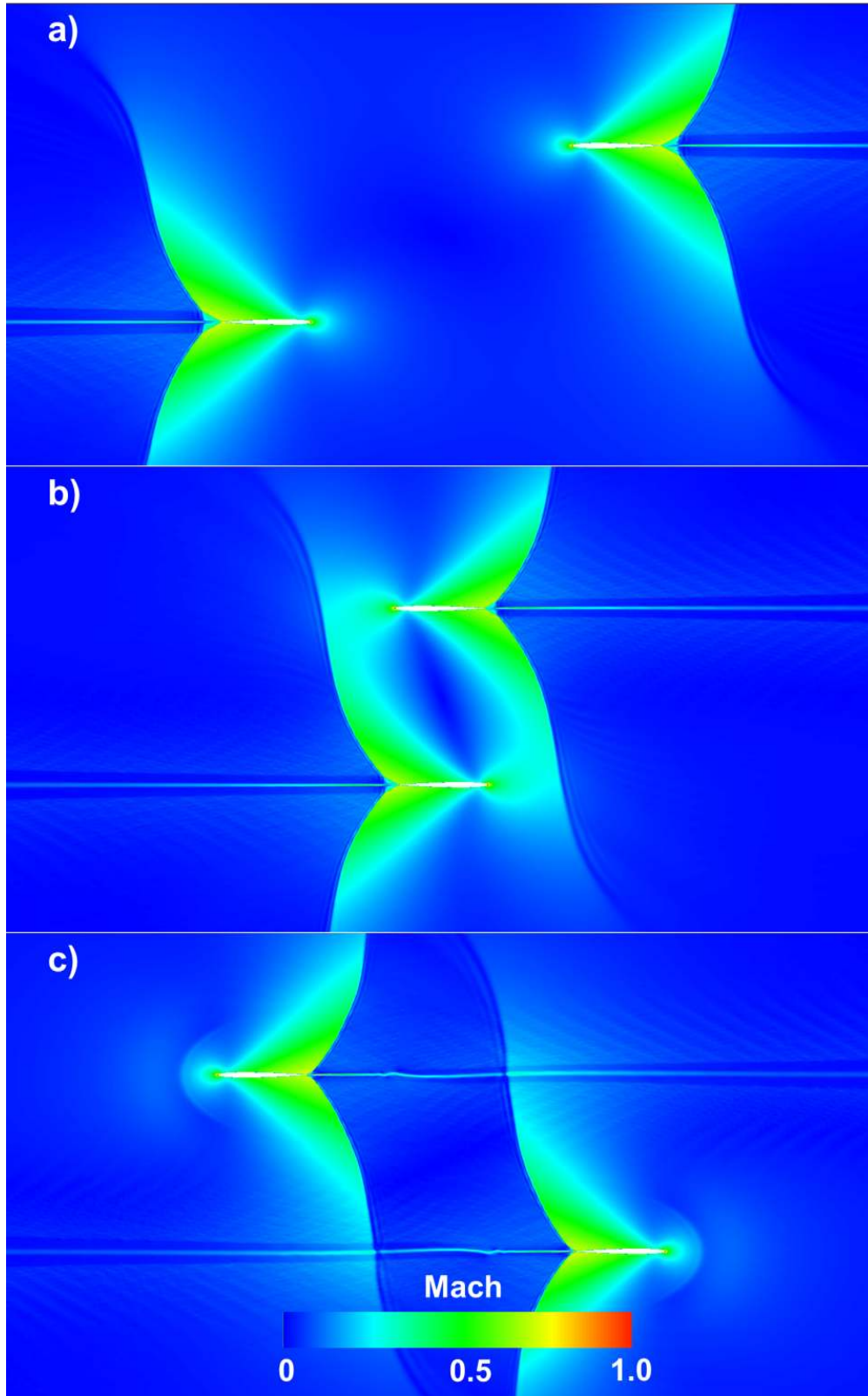


Figure 23. Mach contour of two airfoils crossing a) before, b) at, and c) after overlap ($M = 0.90$, $\alpha = 0^\circ$, and $S/c = 4.0$ ($S = 2.0$ ft, $c = 0.5$ ft)).

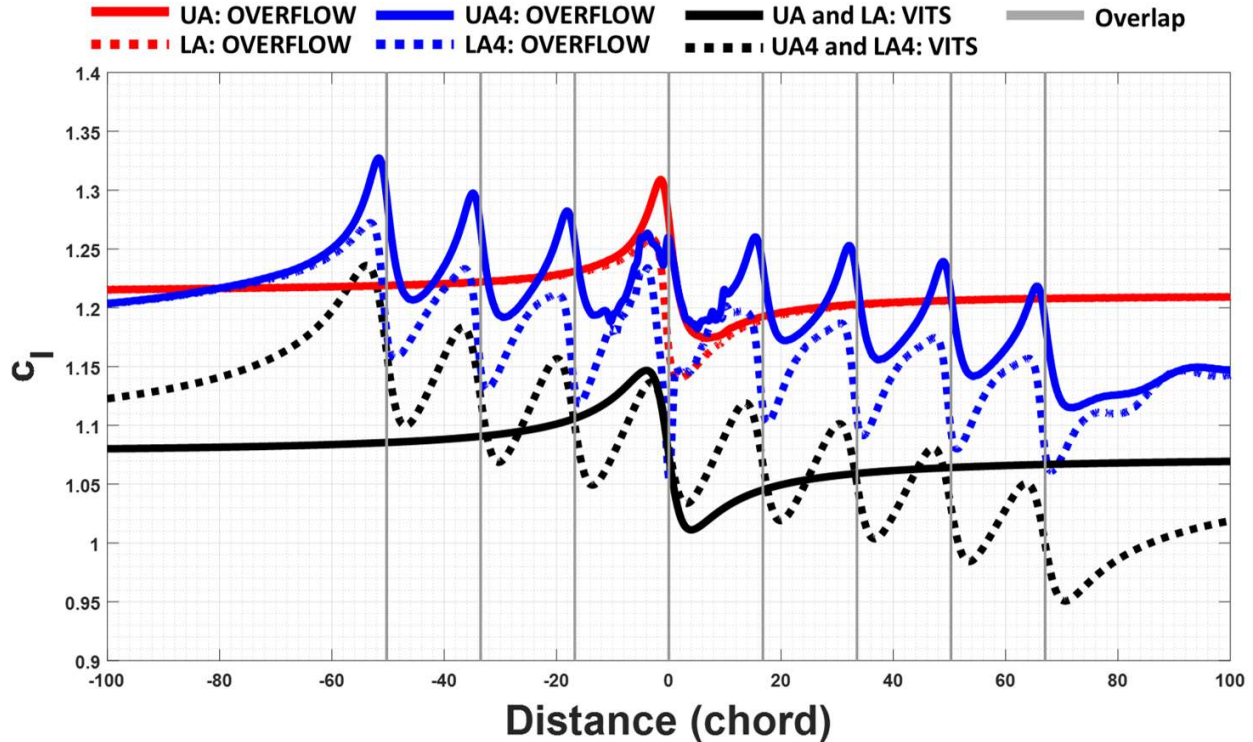


Figure 24. VITS (inviscid) and OVERFLOW (inviscid) calculations of two airfoils and two trains of eight airfoils crossing, c_l versus distance to overlap in chords ($M = 0.25$, $\alpha = 9.8^\circ$, $S/c = 4.0$ ($S = 2.0$ ft, $c = 0.5$ ft), and $D/c = 33.51$).

foils, and two trains of eight airfoils crossing. Inviscid calculations are performed to reveal further information that may not be easily discerned from viscous calculations.

As previously shown in Figures 4 and 5, two airfoils crossing investigated circulation effects. VITS was further used to investigate shed vorticity by simulating a train of eight airfoils traveling in opposite directions; results are compared to OVERFLOW simulations as shown in Figure 24. Comparing VITS simulations for UA/LA and $UA4/LA4$, the addition of airfoils resulted in a change in lift for $UA4$ and $LA4$ because of the circulation and crossing interaction of the surrounding airfoils; this was accounted for by using the Biot-Savart law [58]. Because of the difference in airfoil modeling, inviscid OVERFLOW calculations resulted in higher lift compared to the inviscid VITS potential calculations. OVERFLOW models the geometry, while VITS uses a source, vortex, and sink to represent an airfoil. The flight condition and geometry used to explore viscosity, shed vorticity, and downwash effects are based on a modern rotor design at a span location of $r/R = 0.40$, where $M = 0.25$, $\alpha = 9.8^\circ$, $S/c = 4.0$ ($S = 2.0$ ft, $c = 0.5$ ft), and $D/c = 33.51$ (see Table 9).

Deposited shed vorticity was not represented in the VITS calculations. To explore the effect of shed vorticity, OVERFLOW y -vorticity contours are shown. Inviscid flow-field disturbances dissipate at a slow rate, therefore the shed vorticity can be preserved and further analyzed. Each effect and simulation is discussed and compared in terms of c_z , c_x , and c_m versus distance to airfoil overlap, coefficient of pressure contour (C_P), and y -vorticity contour.

The vertical separation distance of the two airfoils is equal to the horizontal distance between the two rotors of a coaxial rotor. To model the blade phase angle in 2D, the distance between two airfoils (e.g., $UA3$ and $UA4$) was set to the circumferential distance between adjacent blade tips (or

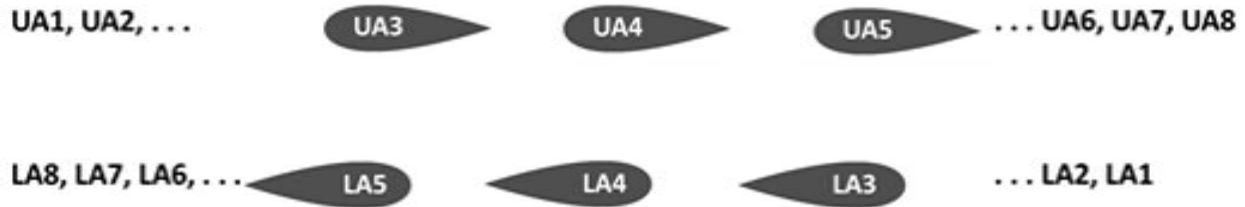


Figure 25. Multiple airfoil simulation illustration at time of overlap of $UA4$ and $LA4$.

specified r/R location) of the modeled rotor (see Fig. 10). A total of eight airfoils were simulated, and the fourth airfoil in the trains ($UA4$ and $LA4$) was chosen to ensure that the aerodynamics influence from the airfoils ahead and behind were captured. Further investigation regarding the total number of airfoils is necessary to ensure a converged solution for the middle airfoil in the train and was not performed in this study.

Two trains of eight airfoils traveling in opposite directions were simulated to investigate the effect of blade crossing, shed vorticity, and downwash as depicted in Figures 8 m), n), o), and p). Figure 25 shows a train of eight airfoils representing the upper rotor blades and eight airfoils representing the lower rotor blades. Airfoils are labeled by vertical position (upper or lower) and horizontal position. For example, upper airfoil four and lower airfoil four are labeled $UA4$ and $LA4$, respectively. Figure 25 shows the positions of a multiple airfoil simulation when $UA4$ and $LA4$ are overlapped (the quarter-chord location of each airfoil coincide). The full time history for the multiple viscous airfoil simulation $UA4$ and $LA4$ over time with labeled crossings ($M = 0.25$, $\alpha = 9.8^\circ$, $V_i = 31$ ft/s, $S/c = 4.0$ ($S = 2.0$ ft, $c = 0.5$ ft), and $D/c = 33.51$) is shown in Figure 26. By the time $UA4$ and $LA4$ overlap, $UA4$ has already overlapped with $LA1$ through $LA3$, and $LA4$ has overlapped with $UA1$ through $UA3$.

Figure 27 shows a viscous and inviscid isolated airfoil, two airfoils crossing at time of overlap (UA/LA), single train of eight airfoils ($A4$), and two trains of eight airfoils crossing ($UA4/LA4$) with and without downwash for c_z versus distance ($M = 0.25$, $\alpha = 9.8^\circ$, $V_i = 31$ ft/s, $S/c = 4.0$ ($S = 2.0$ ft, $c = 0.5$ ft), and $D/c = 33.51$). Figures 28 and 29 show c_x and c_m versus distance for the same conditions for viscous simulations only. For the same conditions, the flow field in terms of C_P contour is shown in Figure 30 for the isolated airfoil, a single train of eight airfoils, two airfoils crossing at time of overlap, and two trains of eight airfoils crossing at time of overlap for $UA4$ and $LA4$. The C_P contour reveals a clear difference between the isolated airfoil (Figs. 30 a) through d)) and the single train of airfoils (Figs. 30 i) through l)) compared to the simulations with crossing events (Figs. 30 e) through h) and m) through p)) where the flow fields of the oncoming airfoil(s) coincide. Further investigation of the flow field is performed to understand the effects of downwash and shed vorticity.

The effect of viscosity for all of the different simulations (isolated airfoil, single train of eight airfoils, two airfoils crossing at the time of overlap, and two trains of eight airfoils crossing at time of overlap) whether downwash was present or not, showed an increase in c_z versus distance (Fig. 27) for the inviscid simulations compared to the viscous simulations. Lift is higher for the inviscid calculations because of the absence of a boundary layer. Inviscid solutions for c_x and c_m are negligible because of the absence of viscosity and are not shown in Figures 28 and 29.

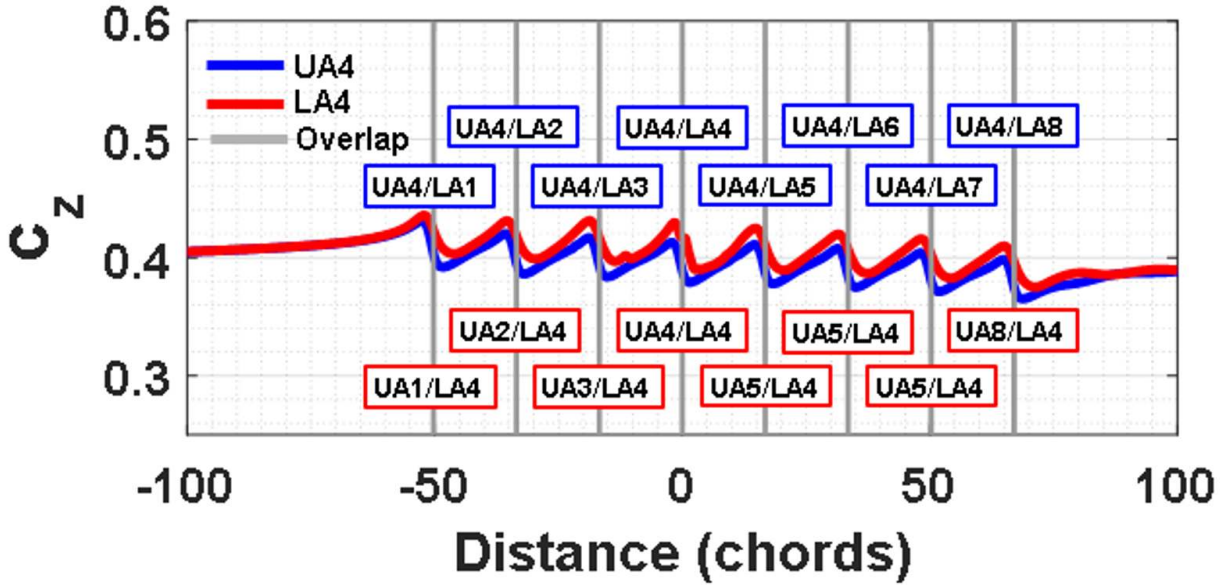


Figure 26. Viscid airfoil simulation, two trains of eight airfoils crossing ($UA4/LA4$) with downwash, c_z versus distance to overlap ($M = 0.25$, $\alpha = 9.8^\circ$, $V_i = 31$ ft/s, $S/c = 4.0$ ($S = 2.0$ ft, $c = 0.5$ ft), and $D/c = 33.51$).

3.7.1 Isolated airfoil

As shown in Figures 27 through 29 for an isolated airfoil, a larger lift is observed for inviscid calculations compared to viscous calculations. For an isolated airfoil, C_P and y-vorticity contour is shown in Figures 31 and 32 for a) viscid, no downwash, b) viscid with downwash, c) inviscid, no downwash, and d) inviscid with downwash simulation ($M = 0.25$ ($V_{tip} = 280$ ft/s), $\alpha = 9.8^\circ$, and $V_i = 31$ ft/s).

The pressure above the viscid and inviscid isolated airfoils without downwash (Figs. 31 a) and c)) is lower compared to the simulations with downwash (Figs. 31 b) and d)), while below the inviscid airfoils without downwash the pressure is larger compared to the simulations with downwash; as a result, lift for viscid and inviscid airfoils without downwash is greater. The simulated downwash decreased overall lift for the inviscid and viscid solution and increased drag for the viscid simulation. Comparing the flow field of the viscid and inviscid airfoils without downwash (Figs. 31 a) and c)) little information between the two simulations can be discussed, therefore the y-vorticity contour of the flow field is analyzed.

The y-vorticity contour further reveals the differences between the inviscid and viscid simulations with downwash (Figs. 32 b) and d)) and without downwash (Figs. 32 a) and c)). The inviscid and viscid simulations with downwash show a downward y-vorticity at the trailing edge of the airfoil pattern compared to the simulation without downwash, which is due to the vertical velocity (V_i) of 31 ft/s. Viscid solutions have a higher y-vorticity because of the presence of a boundary layer (viscosity). Furthermore, the addition of downwash decreases lift, and the vertical velocity decreases the angle of attack causing a decrease in lift, while drag and moment are increased.

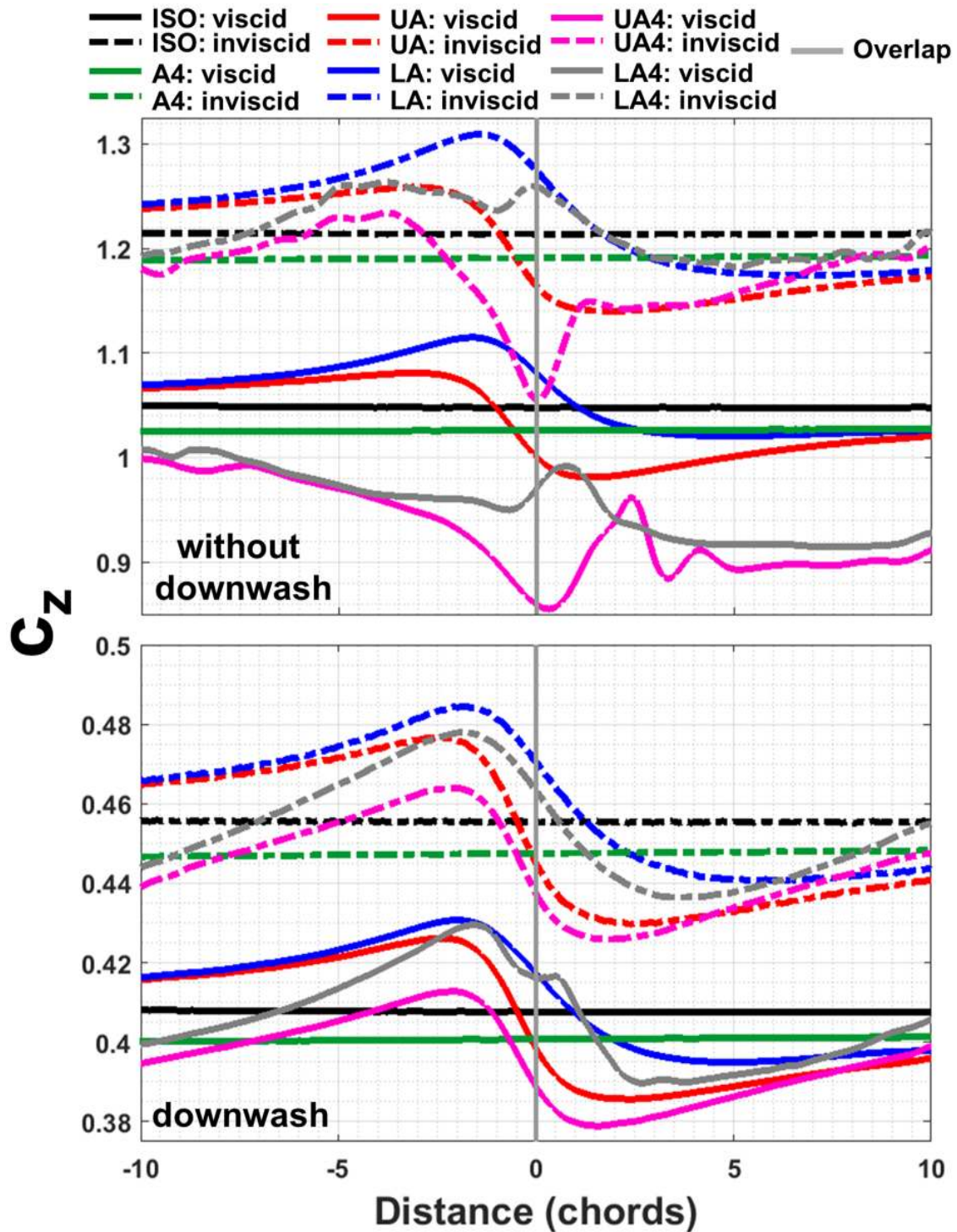


Figure 27. Viscid and inviscid isolated airfoil, two airfoils crossing at time of overlap (UA/LA), single train of eight airfoils ($A4$), and two trains of eight airfoils crossing ($UA4/LA4$) with and without downwash, c_z versus distance to overlap ($M = 0.25$, $\alpha = 9.8^\circ$, $V_i = 31$ ft/s, $S/c = 4.0$ ($S = 2.0$ ft, $c = 0.5$ ft), and $D/c = 33.51$).

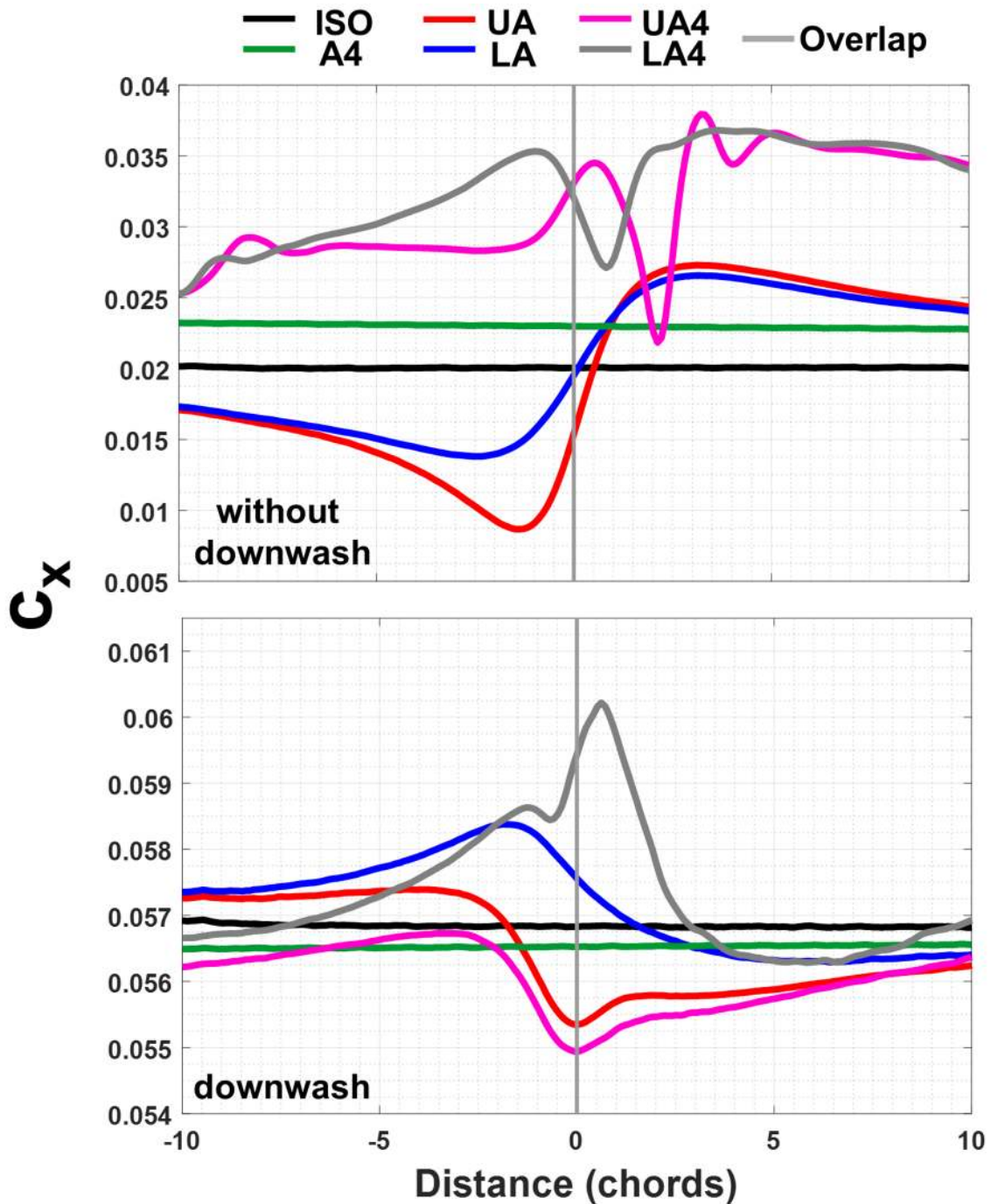


Figure 28. Viscid isolated airfoil, two airfoils crossing at time of overlap (UA/LA), single train of eight airfoils ($A4$), and two trains of eight airfoils crossing ($UA4/LA4$) with and without downwash, c_x versus distance to overlap ($M = 0.25$, $\alpha = 9.8^\circ$, $V_i = 31$ ft/s, $S/c = 4.0$ ($S = 2.0$ ft, $c = 0.5$ ft), and $D/c = 33.51$).

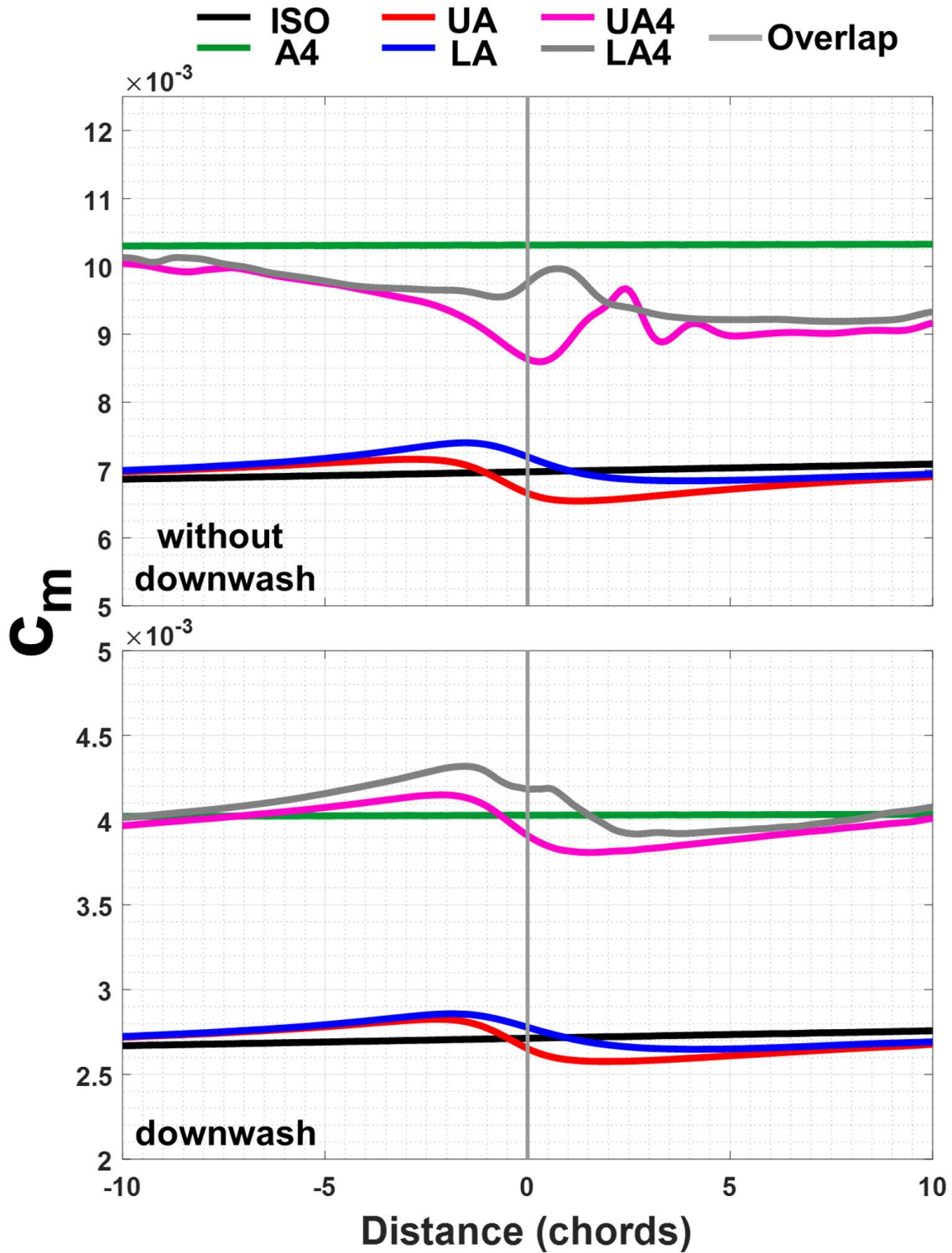


Figure 29. Viscid isolated airfoil, two airfoils crossing at time of overlap (UA/LA), single train of eight airfoils ($A4$), and two trains of eight airfoils at crossing ($UA4/LA4$) with and without downwash, c_m versus distance to overlap ($M = 0.25$, $\alpha = 9.8^\circ$, $V_i = 31$ ft/s, $S/c = 4.0$ ($S = 2.0$ ft, $c = 0.5$ ft), and $D/c = 33.51$).

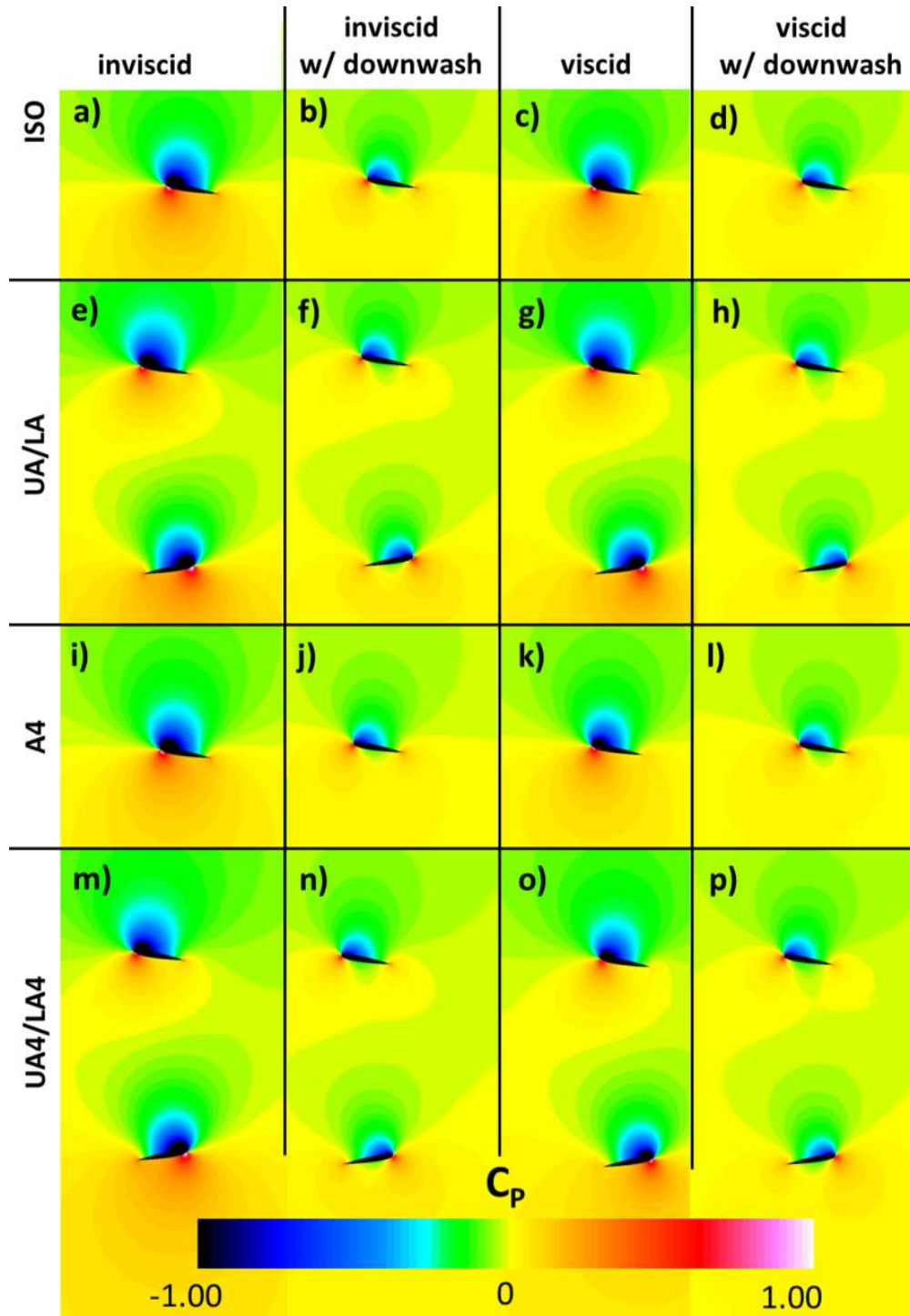


Figure 30. Isolated airfoil, two airfoils crossing at time of overlap (UA/LA), single train of eight airfoils ($A4$), and two trains of eight airfoils crossing ($UA4/LA4$) for an inviscid no downwash (a), (e), i), and m)); inviscid with downwash (b), f), j), and n)); viscid no downwash (c), g), k), and o)); and viscid with downwash (d), h), l), and p)) simulation, C_P contour ($M = 0.25$ ($V_{tip} = 280$ ft/s), $\alpha = 9.8^\circ$, $V_i = 31$ ft/s, and $S/c = 4.0$ ($S = 2.0$ ft, $c = 0.5$ ft)).

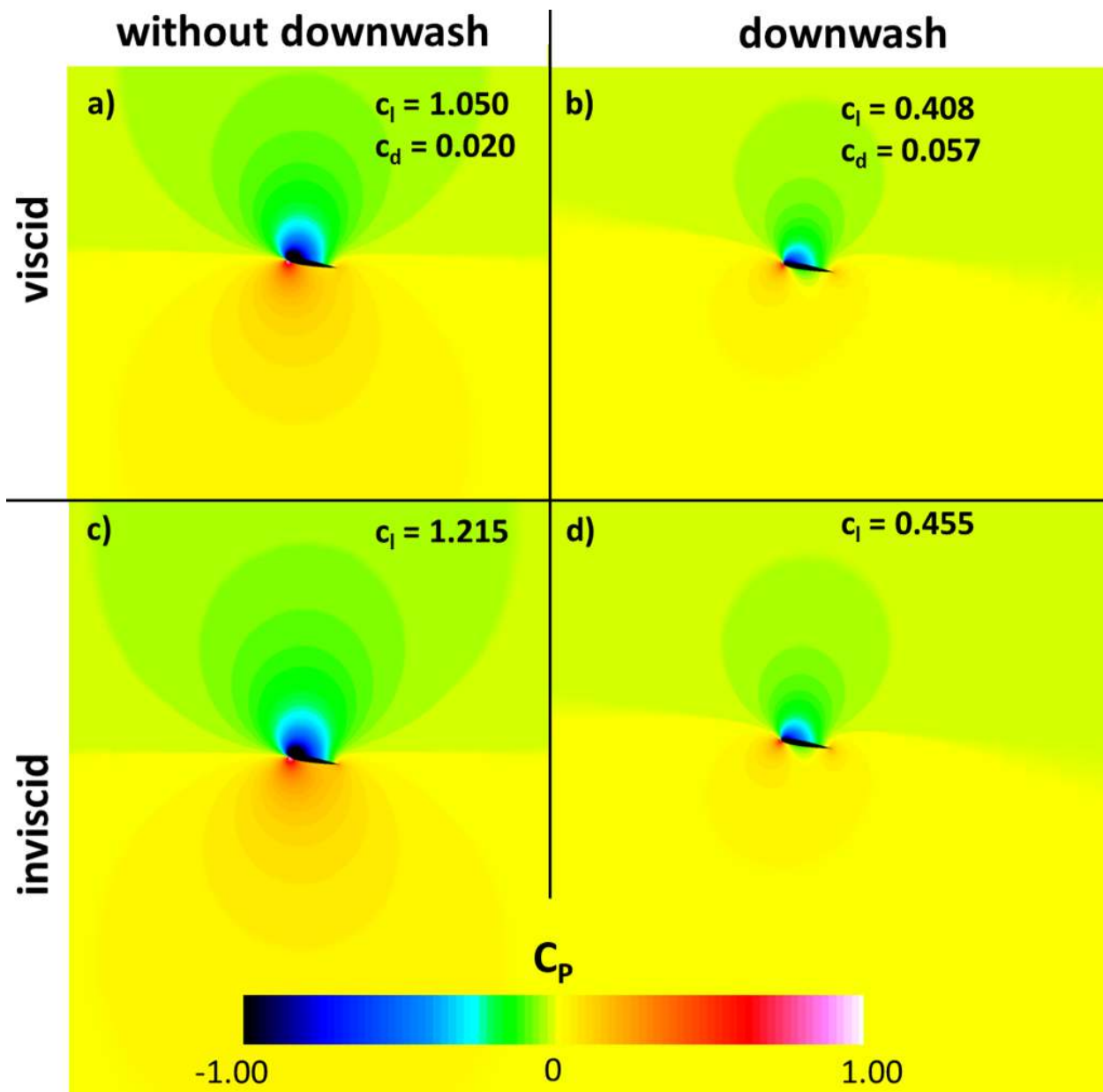


Figure 31. Isolated NACA 0012 airfoil C_p contour for a) viscous, no downwash, b) viscous with downwash, c) inviscid, no downwash, and d) inviscid with downwash simulation ($M = 0.25$ ($V_{tip} = 280$ ft/s), $\alpha = 9.8^\circ$, and $V_i = 31$ ft/s). Note: abrupt changes in contour levels are due to changing grid densities and numerical issues.

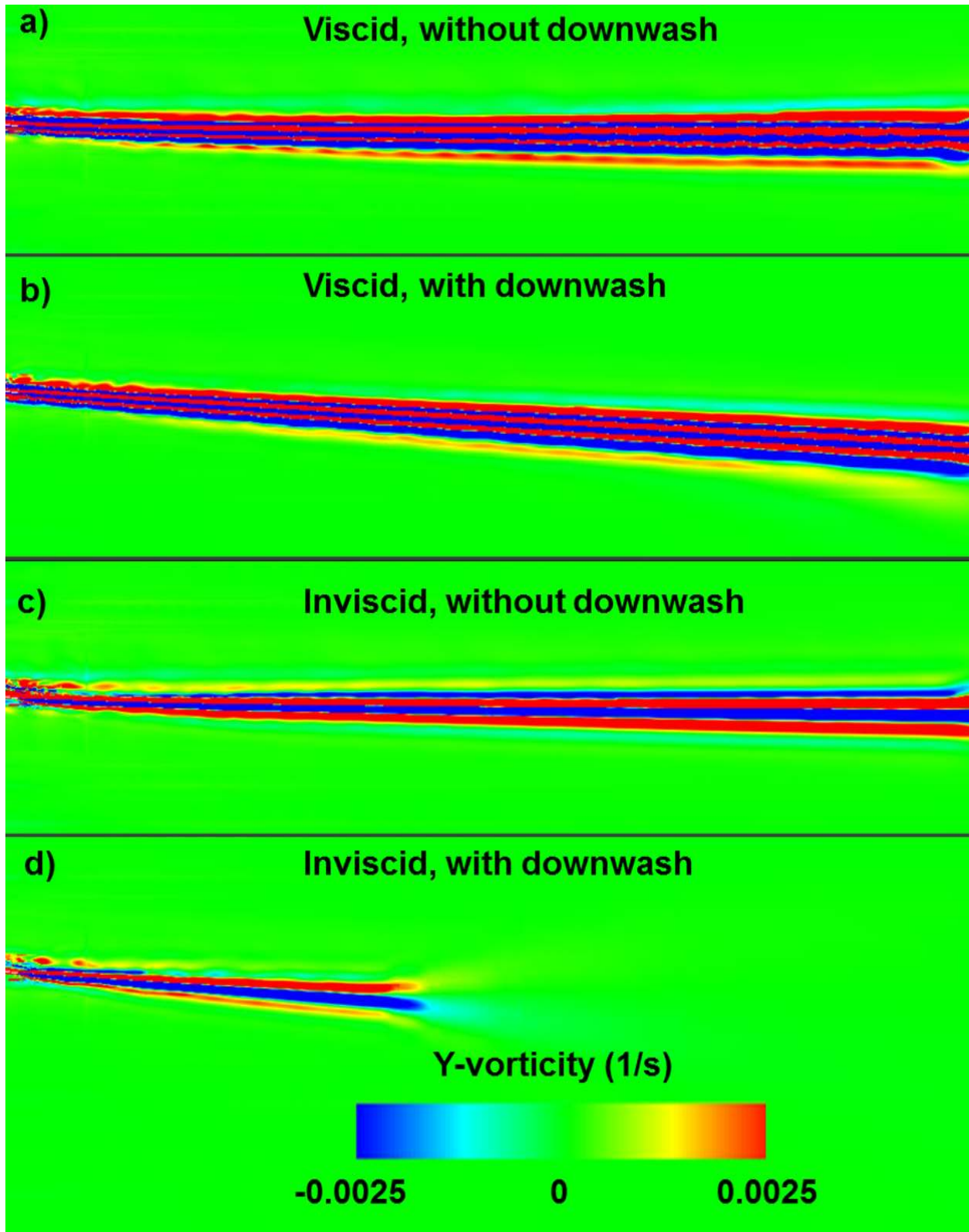


Figure 32. An isolated NACA 0012 airfoil wake y-vorticity contour for a) viscous, no downwash, b) viscous with downwash, c) inviscid, no downwash, and d) inviscid with downwash simulation ($M = 0.25$ ($V_{tip} = 280$ ft/s), $\alpha = 9.8^\circ$, and $V_i = 31$ ft/s).

3.7.2 Two airfoils crossing

A second airfoil traveling in the opposite direction was added to the isolated airfoil simulation. Compared to the isolated airfoil results, all simulations of two airfoils crossing show a change in c_z , c_x , and c_m before and after time of overlap (Figs. 27 through 29). The change in c_z , c_x , and c_m is caused by the interaction of the flow fields of each airfoil. Viscid flow-field C_P contours for two NACA airfoils crossing before, at, and after, with downwash, are shown in Figure 33 ($M = 0.25$ ($V_{tip} = 280$ ft/s), $\alpha = 9.8^\circ$, $V_i = 31$ ft/s, and $S/c = 4.0$ ($S = 2.0$ ft, $c = 0.5$ ft)). As previously shown in Figures 5 and 33, as the two airfoils approach each other, the flow fields between the two airfoils start to interact, which results in a change in angle of attack of both airfoils because of the induced velocity (see Fig. 6).

Figure 34 shows vorticity contours of the flow field of two NACA 0012 airfoils after time of crossing. Viscid and inviscid results are shown, with and without a vertical velocity imposed ($M = 0.25$ ($V_{tip} = 280$ ft/s), $\alpha = 9.8^\circ$, and $V_i = 31$ ft/s). Similar to the isolated airfoil (Fig. 32), the vorticity behind the airfoil travels downward because of the imposed vertical velocity (Figs. 34 b) and d)).

The effect of shed vorticity is highlighted after the airfoils cross each other at the location of overlap, as shown in Figure 34. Inviscid calculations with and without downwash reveal deposited vorticity at the location of overlap (Figs. 34 c) and d)), while viscous solutions are harder to see because of the presence of viscosity (Figs. 34 a) and b)). The addition of downwash reduces the angle of attack for each airfoil, resulting in less shed vorticity in the overlap region.

3.7.3 Single train of eight airfoils

The change in airfoil circulation with time ($-d\Gamma/dt$) was calculated from the airfoil lift time history in order to investigate shed vorticity. The circulation calculations were first performed for an isolated airfoil and the upper airfoil (UA) of a two airfoils crossing simulation, as shown in Figure 35 (HC1: $M = 0.47$ ($V_{tip} = 500$ ft/s), $\alpha = 7^\circ$, and $S/c = 6.21$ ($S = 2.33$ ft, $c = 0.375$ ft)). The horizontal axis is the chord distance to overlap; negative and positive values correspond to before and after airfoil overlap, respectively. The vertical gray line is the location where the quarter-chord of the upper and lower airfoils overlap. The c_z results are converted to circulation (Γ) (Fig. 35 b)), and then the negative time derivative of circulation is computed to obtain shed vorticity ($-d\Gamma/dt$) (Fig. 35 c)). The circulation is negated to satisfy Kelvin's circulation theorem (conservation of body forces), and the derivative of circulation is taken with respect to time (distance) because of the time-varying loads. There is an increase in shed vorticity beginning about 10 chords before overlap, peaking just before overlap, and then decreasing back to 0 approximately 10 chords after overlap. In order to simulate the effect of shed vorticity, a train of airfoils was modeled to investigate the impact of deposited shed vorticity on an airfoil in the middle of the train (analogous to a rotor with multiple blades).

When airfoils are added ahead or behind an isolated airfoil, each airfoil encounters the wakes of the preceding airfoils. Rapid changes in airfoil lift and drag, due to wake interactions, result in shed vorticity deposited into the fluid medium. Any ensuing airfoils that impinge on these shed vortices are susceptible to additional airload fluctuations.

A single train of eight airfoils was simulated to investigate the effect of shed vorticity as depicted in Figures 8 i), k), j), and l). A train of eight airfoils was chosen to ensure that there was sufficient aerodynamic influence from airfoils preceding and following the airfoil of interest. The fourth airfoil in the train was selected for analysis and is noted as A4.

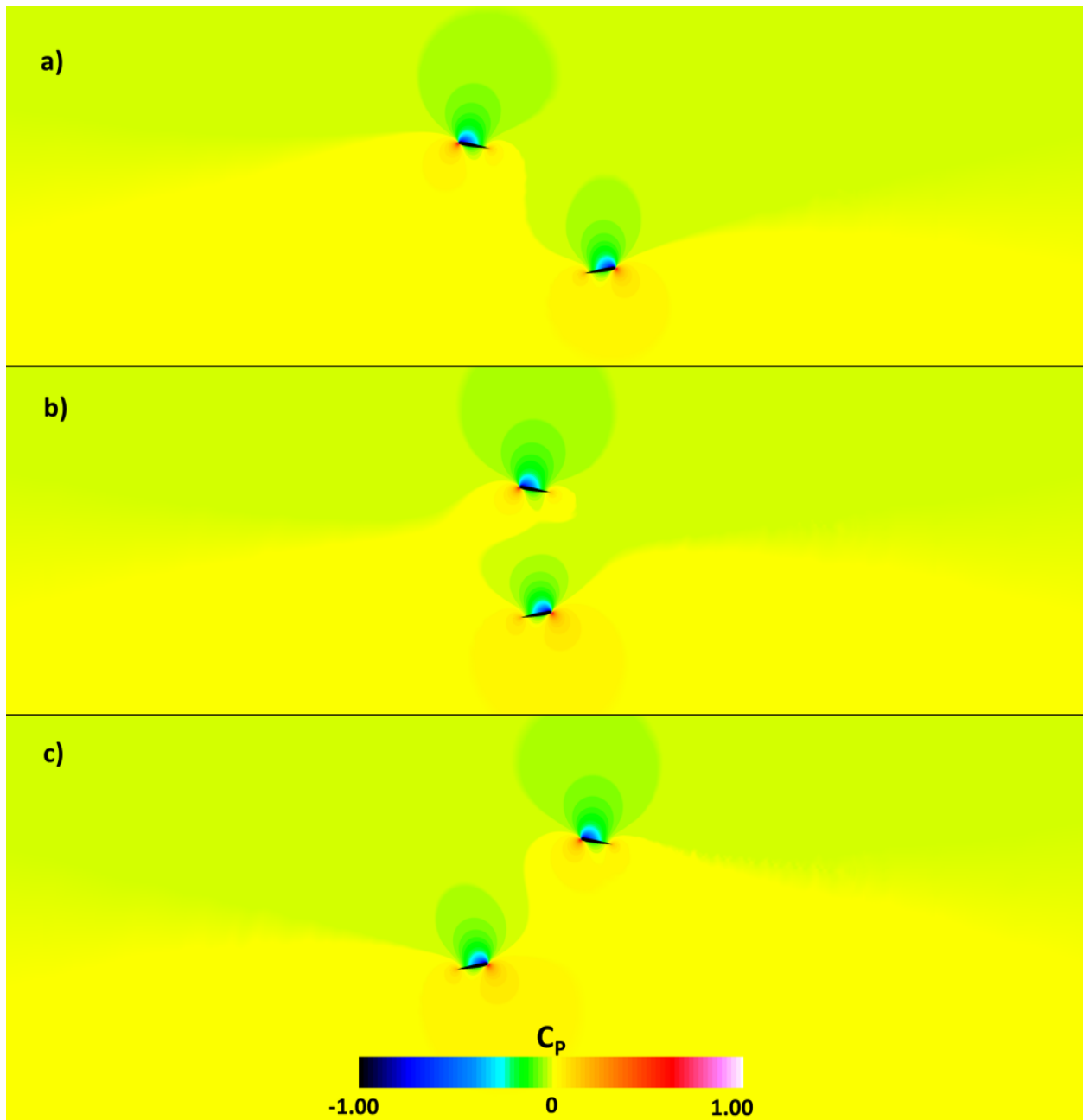


Figure 33. Viscid flow-field C_p contour of two NACA 0012 airfoils crossing a) before, b) at, and c) after, with downwash ($M = 0.25$ ($V_{tip} = 280$ ft/s), $\alpha = 9.8^\circ$, $V_i = 31$ ft/s, and $S/c = 4.0$ ($S = 2.0$ ft, $c = 0.5$ ft)).

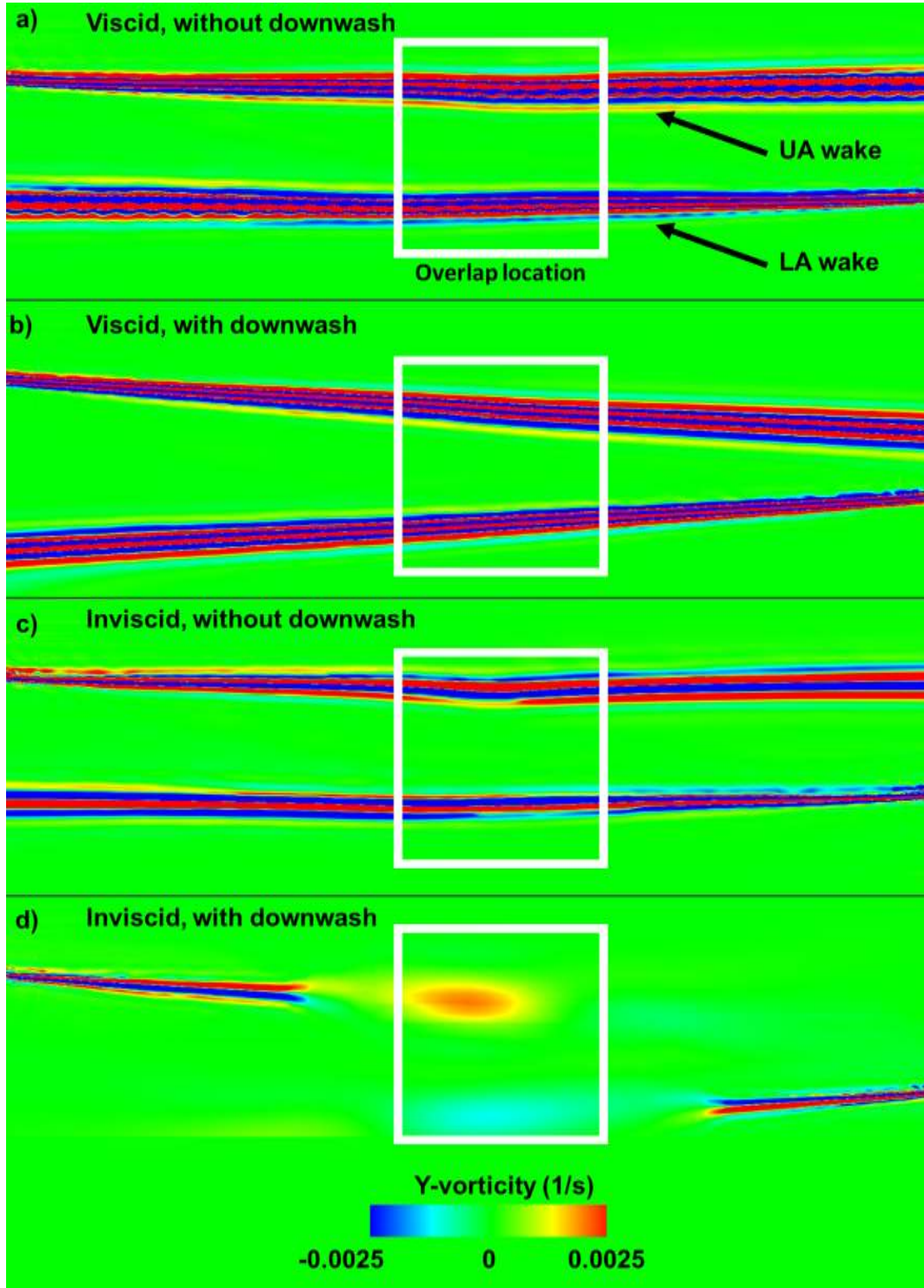


Figure 34. Two NACA 0012 airfoils y-vorticity contour after time of crossing for a) viscid, no downwash, b) viscid with downwash, c) inviscid, no downwash, and d) inviscid with downwash simulation ($M = 0.25$ ($V_{tip} = 280$ ft/s), $\alpha = 9.8^\circ$, $V_i = 31$ ft/s, and $S/c = 4.0$ ($S = 2.0$ ft, $c = 0.50$)).

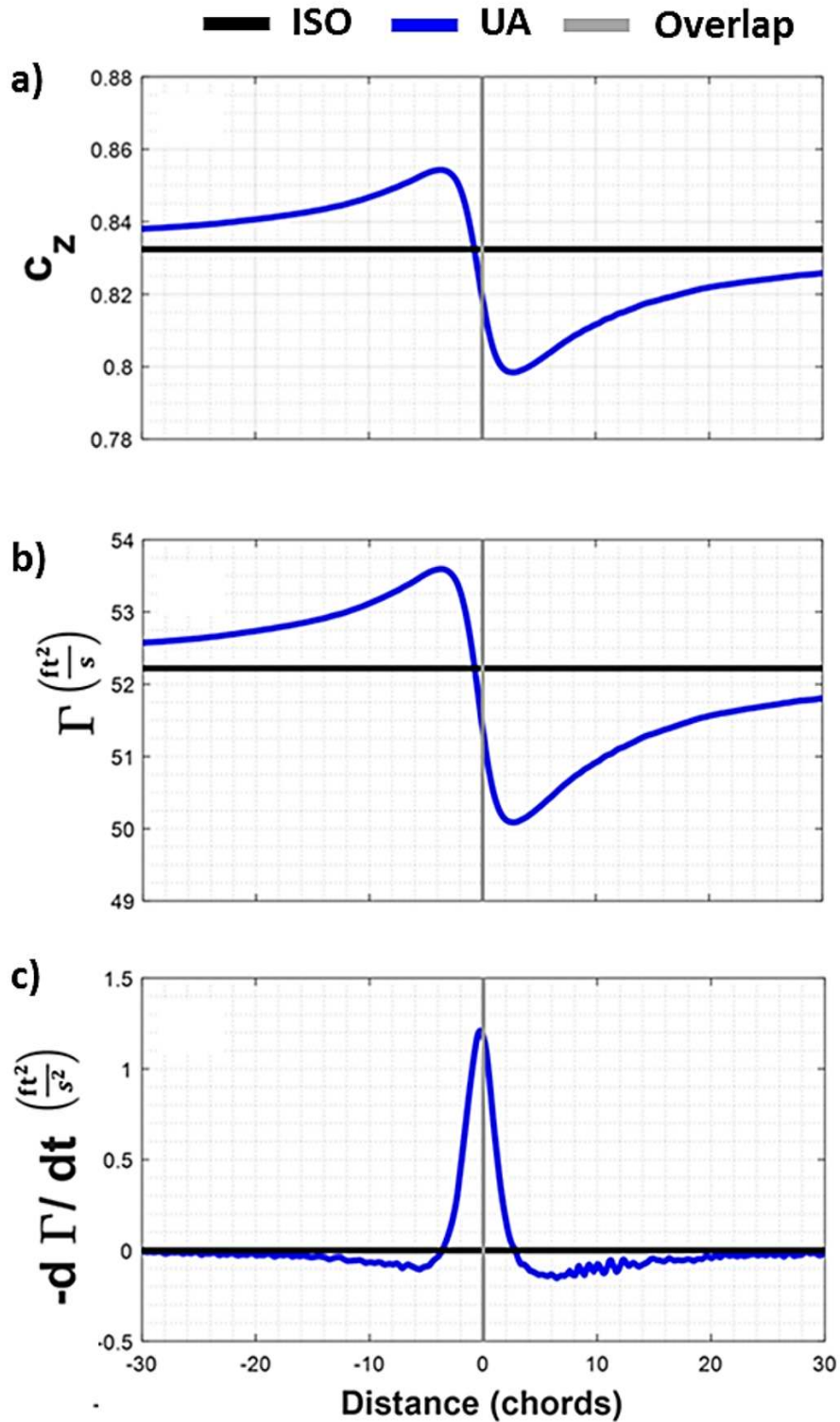


Figure 35. Results for an isolated airfoil and the upper airfoil of the two airfoils crossing case: a) c_z , b) Γ , and c) $-d\Gamma/dt$. Horizontal axis is distance to overlap for the upper airfoil (UA) (HC1: $M = 0.47$ ($V_{tip} = 500 \text{ ft/s}$), $\alpha = 7^\circ$, and $S/c = 6.21$ ($S = 2.33 \text{ ft}$, $c = 0.375 \text{ ft}$)).

Comparing $A4$ to the isolated airfoil, the difference in c_z shows an overall small decrease in lift for all inviscid and viscid calculations with and without downwash (Fig. 27), while a small increase in viscid c_x calculations is observed (Fig. 28). An overall increase in viscid c_m calculations is observed for $A4$ compared to the isolated airfoil simulations with and without downwash (Fig. 29).

Vorticity contours for $A4$ are shown in Figures 36. The wakes from the airfoils preceding $A4$ are clearly shown in Figures 36 a), b), and c), whereas in Figure 36 d) the wakes are not seen. The presence of downwash pushes the wake from the preceding two airfoils ($A2$, $A3$) ahead of $A4$ into proximity of $A4$ (Fig. 36 b)); the wake is not seen in the inviscid simulation (Fig. 36 d)) because of the absence of viscosity.

3.7.4 Two trains of eight airfoils crossing

The final configuration studied was two eight-airfoil trains. The addition of the second train should capture all effects explored thus far: circulation, thickness, compressibility, viscosity, and downwash. The fourth airfoils of the upper and lower trains, $UA4$ and $LA4$, respectively, were analyzed. The two airfoils, $UA4$ and $LA4$, experienced lower lift, higher drag, and higher moment compared to the case of two airfoils (UA , LA) crossing, with and without downwash (Figs. 27 through 29). As $UA4$ and $LA4$ encounter an overlap, the deposited shed vorticity builds on the previously deposited shed vorticity from overlapping occurrences, resulting in lower lift, higher drag, and higher moment.

A comparison of the UA/LA and $UA4/LA4$ vorticity fields with downwash is shown in Figures 38 a) and b), respectively. The addition of airfoils further complicates the flow. Although the downwash pushes the wake and deposited shed vorticity downward, in Figure 38 b) the oncoming lower airfoil ($LA4$) encounters the wake of $UA3$. Figure 37 shows c_z versus distance to overlap of $UA4$ and $LA4$, where $UA4$ and $LA4$ are overlapping $LA1-LA8$ and $UA1-UA8$, respectively. Figure 37 also shows viscid calculations with downwash for an isolated airfoil (ISO), two airfoils crossing (UA , LA), and a single train of eight airfoils crossing ($A4$). Comparing $UA4$ and $LA4$ to the other simulations, the mean lift decreases after each overlapping occurrence. The decrease in lift is due to the deposited shed vorticity.

3.8 Modern Coaxial and Single Rotor Design Comparison: Hover

Comparisons were made between a modern single rotor and a coaxial rotor to highlight aerodynamic differences (see Table 3 for 2D analog). A single train of eight airfoils was used to simulate a single rotor in hover, as shown in Figure 8 i). Two trains of eight airfoils were used to simulate the modern coaxial rotor in hover (Fig. 8 p)).

For a constant chord of 0.5 ft, Table 9 shows the 2D representation of a coaxial and single rotor based on radial span r/R location. A varying horizontal distance spacing (D/c), twist (θ_{tw}), and α were used based on spanwise location. A downwash of 31 ft/s was applied to the coaxial rotor simulation, as shown in Figure 9, with a rotor separation distance of 2.0 ft.

The modern single rotor in hover 2D representation for airfoil four ($A4$), a) Δc_l and b) Δc_d , versus distance to overlap, is shown in Figure 39. The mean value of c_l and c_d is subtracted from c_l and c_d to get Δc_l and Δc_d . The modern coaxial rotor in hover 2D representation for $UA4$, a) Δc_l and b) Δc_d , and for $LA4$, c) Δc_l and d) Δc_d , versus distance to overlap is shown in Figure 40. Spanwise locations for the modern single and coaxial rotors include r/R locations of 0.25, 0.40, 0.50, 0.60, 0.75, 0.80, 0.85, 0.90, 0.95, and 1.00.

Comparing Figures 39 and 40, there is a clear difference in the Δc_l and Δc_d between the modern single and coaxial rotors. The modern single rotor does not change over time, whereas

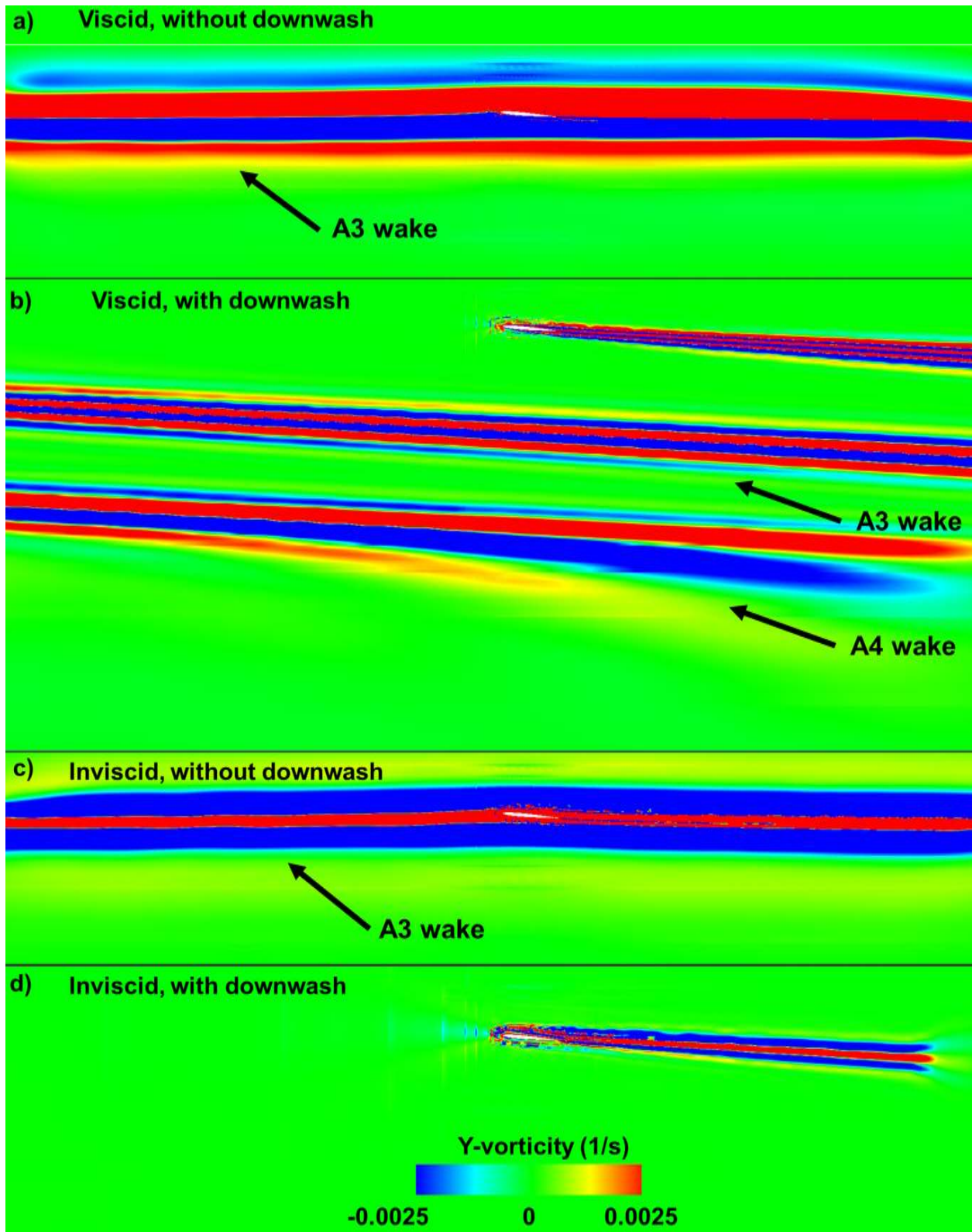


Figure 36. Y-vorticity contours for A4 (4th airfoil in a train of eight airfoils) for a) viscous no downwash, b) viscous with downwash, c) inviscid no downwash, and d) inviscid with downwash simulation ($M = 0.25$, $\alpha = 9.8^\circ$, $V_i = 31$ ft/s, and $D/c = 33.51$).

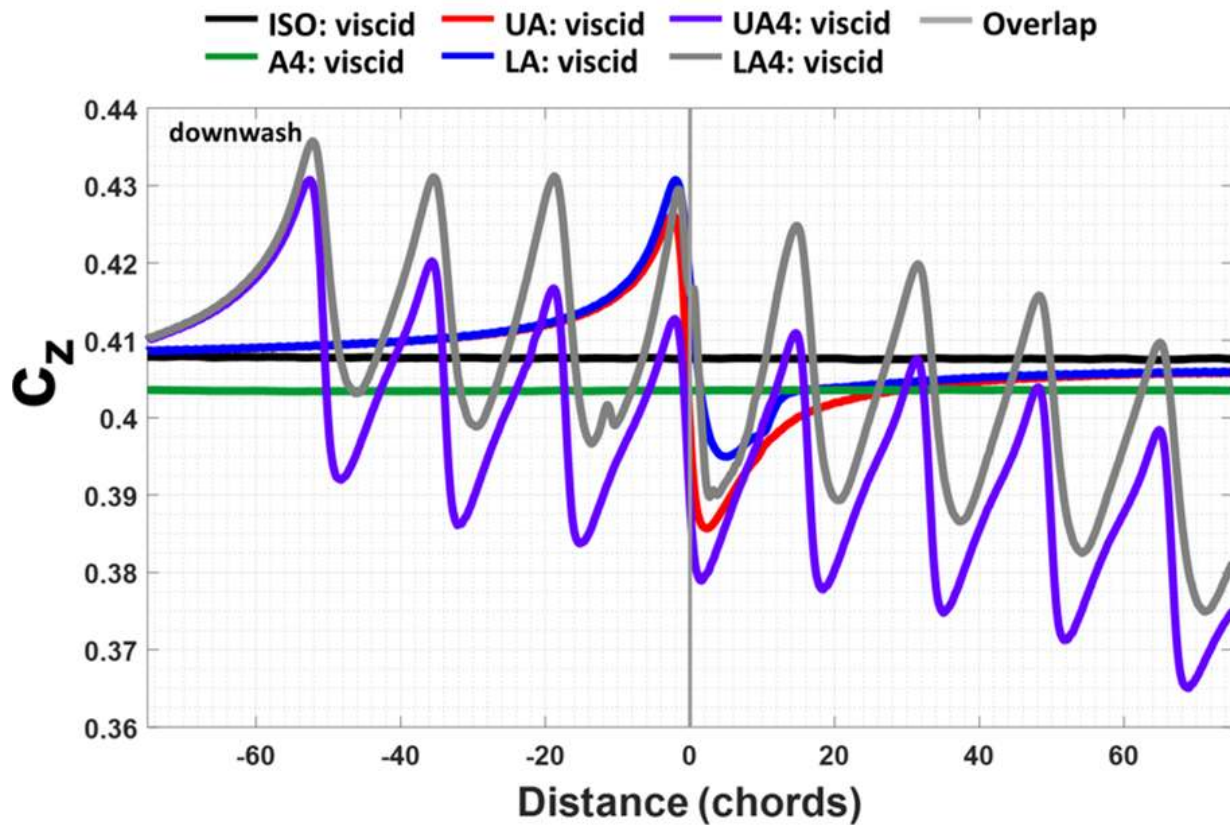


Figure 37. Viscid calculations with downwash for an isolated airfoil, two airfoils crossing, a single train of eight airfoils crossing (*A4*), and two trains of eight airfoils crossing (*UA4* and *LA4*), c_z versus distance to overlap ($M = 0.25$, $\alpha = 9.8^\circ$, $V_i = 31$ ft/s, $S/c = 4.0$ ($S = 2.0$ ft, $c = 0.5$ ft), and $D/c = 33.51$).

Table 9. 2D representation of a coaxial and single rotor r/R location.

r/R	R (ft)	D/c	$V_{r/R}$ (ft/s)	M	θ_{tw} ($^\circ$)	α ($^\circ$)	$Re \#$
0.13	2.7	11.142	93	0.083	4.94	11.94	3.0×10^5
0.25	5.0	20.944	175	0.157	4.00	11.00	5.6×10^5
0.40	8.0	33.510	280	0.251	2.80	9.80	8.9×10^5
0.50	10.0	41.888	350	0.313	2.00	9.00	1.1×10^6
0.60	12.0	50.265	420	0.376	1.20	8.20	1.3×10^6
0.75	15.0	62.832	525	0.470	0.00	7.00	1.7×10^6
0.80	16.0	67.021	560	0.502	-0.40	6.60	1.8×10^6
0.85	17.0	71.209	595	0.533	-0.80	6.20	1.9×10^6
0.90	18.0	75.398	630	0.564	-1.20	5.80	2.0×10^6
0.95	19.0	79.587	665	0.596	-1.60	5.40	2.1×10^6
1.00	20.0	83.776	700	0.627	-2.00	5.00	2.2×10^6

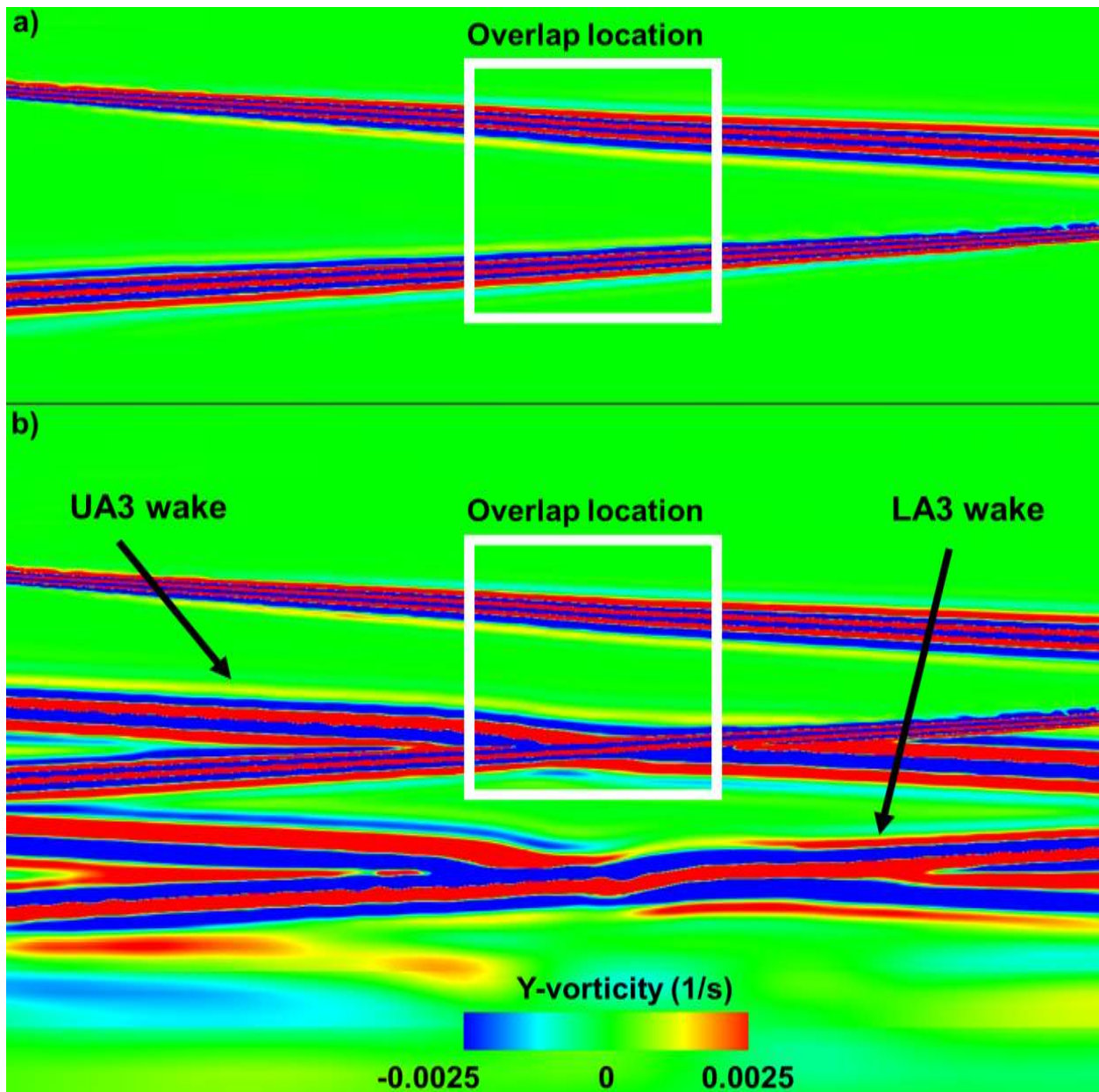


Figure 38. Y-vorticity contour with downwash viscid simulation of a) two airfoils (UA/LA) crossing, and b) two trains of eight airfoils crossing after time of overlap of upper and lower airfoil four ($UA4/LA4$) ($M = 0.25$, $\alpha = 9.8^\circ$, $V_i = 31$ ft/s, $S/c = 4.0$ ($S = 2.0$ ft, $c = 0.5$ ft), and $D/c = 33.51$).

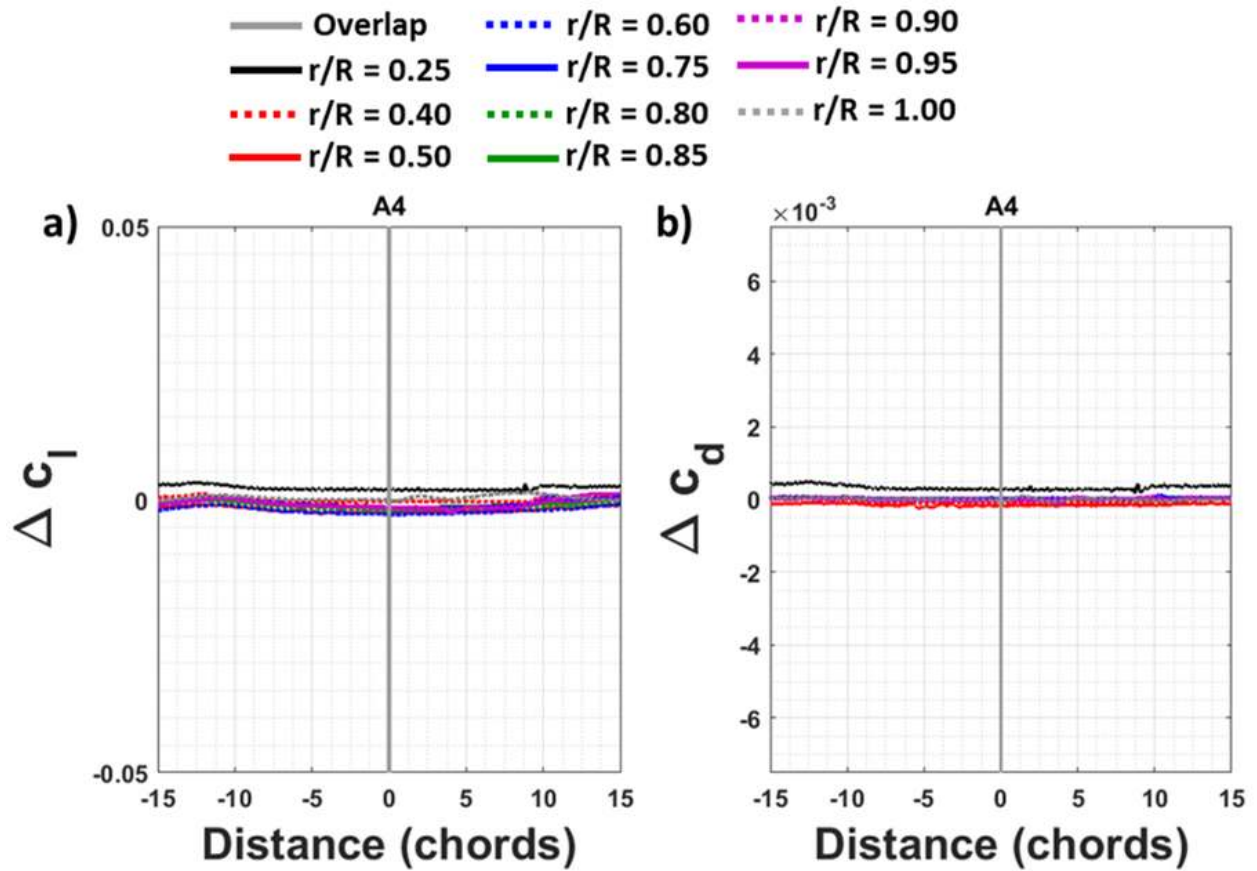


Figure 39. 2D representation of a modern single rotor in hover: a) Δc_l and b) Δc_d versus distance to overlap ($r/R = 0.25$ through 1.00). Results shown for airfoil four (A4).

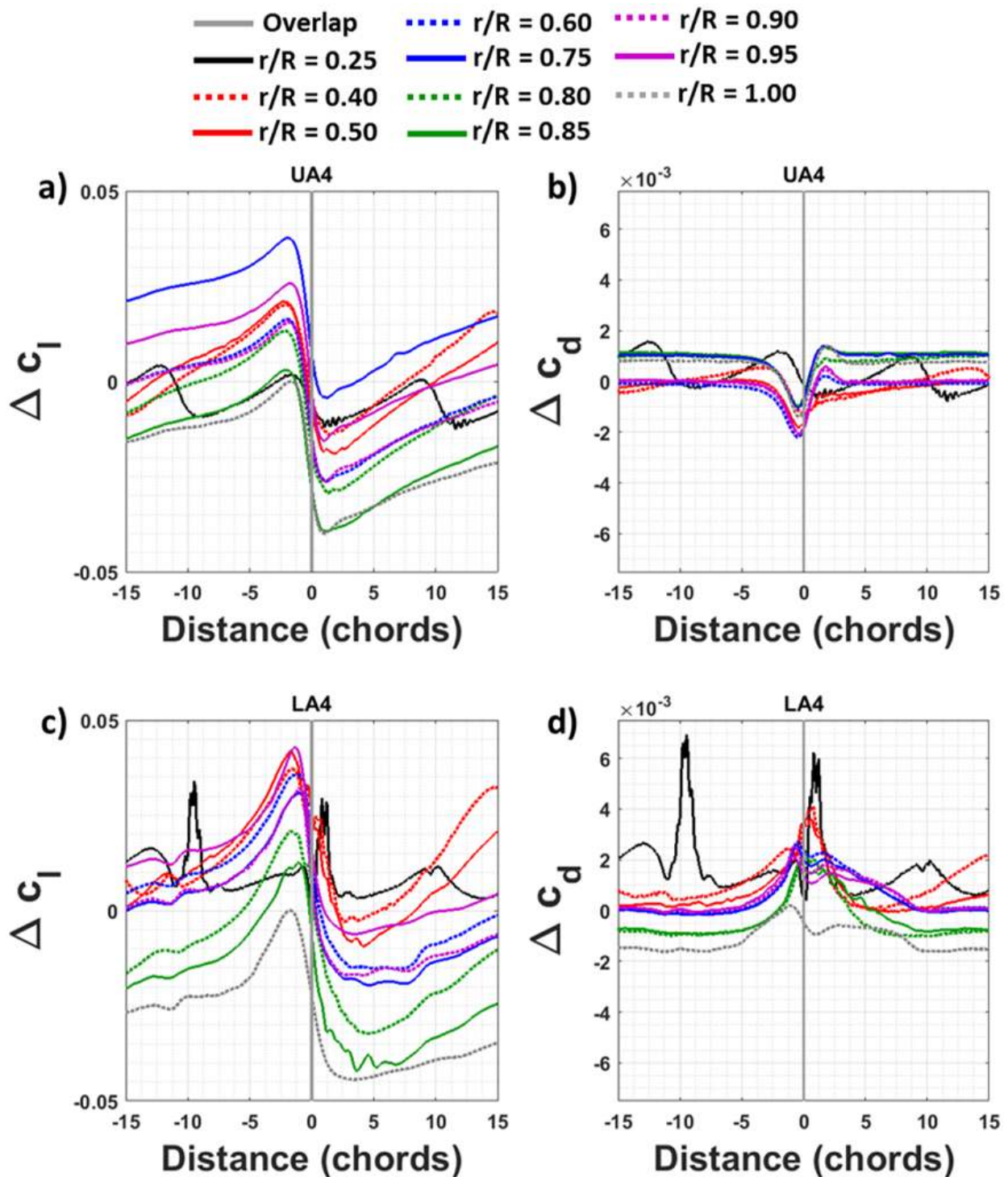


Figure 40. 2D representation of a modern coaxial rotor in hover: a) Δc_l and b) Δc_d for UA4, and c) Δc_l and d) Δc_d for LA4, versus distance to overlap ($r/R = 0.25$ through 1.00). Results shown for airfoil four (A4).

the modern coaxial rotor shows an increase before overlap and decrease after overlap for Δc_l versus distance and vice versa for Δc_d . The fluctuations in Δc_l and Δc_d are due to the blade crossing occurrences. Results for the modern single and coaxial rotors were stacked and analyzed to understand the acoustic signature difference between the two rotors.

3.9 Summary

A potential and compressible flow computational code was used to understand coaxial rotor specific aerodynamic phenomena in 2D. The effects due to thickness, circulation, compressibility, downwash, and shed vorticity were investigated. The potential code (VITS) was used to understand the flow field during a blade crossing event, where compressibility and downwash are not accounted for. VITS revealed that the lift of both the upper and lower airfoil increased before overlap, followed by a decrease in lift after overlap. Before overlap, the angle of attack of the upper airfoil increases because of the upwash from the lower airfoil, while the opposite occurs after overlap.

OVERFLOW 2.2k was used to model an isolated airfoil, two airfoils crossing, a single train of eight airfoils, and two trains of eight airfoils crossing. A Mach number sweep for an isolated airfoil was simulated to understand the fundamental aerodynamic effects. The crossing of two airfoils in 2D, offset vertically and traveling in opposite directions, was simulated while the angle of attack, airfoil thickness, vertical spacing between the airfoils, and Mach number (including transonic and compressible cases) were individually varied to isolate the effects of circulation, thickness, and compressibility. To dissect the effect of downwash and shed vorticity, an isolated airfoil, two airfoils crossing, a single train of eight airfoils, and two trains of eight airfoils crossing were simulated to isolate each effect. A vertical velocity was simulated to analyze downwash. In addition, the differences between viscid and inviscid solutions were compared to analyze shed vorticity to further understand the effect of shed vorticity from a blade crossing event.

The effect of circulation was explored by comparing results for three angles of attack with the same symmetrical airfoil, low speed, and separation distance in order to eliminate any large effects due to thickness or compressibility. Furthermore, three angles of attack with the same symmetrical airfoil and separation distance, but at compressible speeds, were compared. In terms of circulation for low- and high-speed conditions, when comparing angles of attack of -7° , 0° , and 7° , angles of attack of -7° and 7° resulted in a change in c_z (lift), c_x (drag), and c_m (moment) before and after overlap. Comparing -7° and 7° results showed equal results for c_x , but an equal and opposite result for c_z and c_m .

Thickness effects were explored by first comparing two different airfoils at a constant low speed, separation distance, and angle-of-attack flight condition. Thickness effects were further explored by comparing three different separation distances at a constant low speed with the same airfoil flight condition, which eliminated large effects of circulation and compressibility. Both comparisons were also explored at a compressible speed. Comparing the two airfoils revealed that at low- and high-speed conditions, thickness effects due to the airfoil were negligible. The same conclusion was true for separation distances above an S/c of 2 (or $S/D = 0.07$); modern-day coaxial rotors have an S/c greater than 2 to avoid thickness effects.

Effects of compressibility were explored by performing a speed sweep ($M = 0.50$ through 1.20) with the same symmetrical airfoil, angle of attack, and separation distance to eliminate any large effects of circulation. As the Mach number on the surface of the airfoil increased to 1.0, a large change in c_z , c_x , and c_m was observed because of compressibility and the onset formation of weak shocks.

The effect due to downwash resulted in all viscous and inviscid calculations seeing a decrease in lift. For all viscous simulations, the addition of downwash increased drag and decreased moment; the increase in drag is due to the additional force vector.

The single train of eight airfoils showed negligible difference compared to the isolated airfoil. A greater difference was observed when comparing the two trains of eight airfoils crossing, because of the presence of deposited shed vorticity at the location of overlap. Comparing the two airfoils crossing to the two trains of eight airfoils crossing, when more airfoils are ahead and behind each other the difference between the two becomes significant because of the presence of shed vorticity. By simulating viscous and inviscid y -vorticity contours, the deposited shed vorticity was pushed downward by the vertical downwash velocity; in turn, the deposited shed vorticity from the upper airfoils directly impacts the lower airfoils.

In conclusion, in terms of circulation, thickness, and compressibility effects, the prominent aerodynamic source at low-speed conditions was circulation when two airfoils are crossing in opposite directions. When downwash was introduced, the result due to shed vorticity became negligible for the upper airfoil, but the lower airfoil was introduced to the deposited vorticity from the upper airfoil. The addition of downwash reduced the angle of attack, thus minimizing circulation effects for positive angles of attack.

4 3D Coaxial Rotor Simulation

The performance of a helicopter is dependent on the power of the engine(s) and the lift/thrust that the rotor(s) produce. Compared to a single rotor, the addition of a second rotor results in two wakes interacting, and therefore further complicates the aerodynamic flow field. As discussed in Chapter 3, the 2D simulations for a hovering single rotor and coaxial rotors gave further insight into thickness, circulation, compressibility, shed vorticity, and downwash effects. However, 3D performance effects and forward flight were not explored. In this chapter, a combination of momentum theory and a hybrid CFD tool aided in uncovering aerodynamic and acoustic sources based on performance characteristics not revealed in the 2D simulations.

4.1 Rotor Unstructured Navier-Stokes (RotUNS) Performance Validation

Rotor Unstructured Navier-Stokes (RotUNS) operates within the RotCFD Integrated Design Environment (IDE) [61,62]. RotCFD offers a bridge between comprehensive rotorcraft analysis and CFD analysis. RotUNS is one of several flow solvers within RotCFD, which also includes a geometry module, a semi-automated grid generation module, a rotor module, and a flow visualization and analysis module, all integrated in one environment. Within the RotCFD IDE, grid generation and problem setup are quickly executed, facilitating parametric sweeps of rotor conditions and problem geometry. RotCFD balances ease of use and practical resource constraints with an accurate physical representation of the global flow field.

RotUNS uses 3D incompressible Unsteady Reynolds Averaged Navier-Stokes (URANS) equations and an unstructured grid [61,62]. Two options are available to model the rotor: actuator disk and discrete blade. Both options rely on user-provided tables of 2D airfoil coefficients for a range of angles of attack and Mach numbers. Using the computed velocity field and BEMT, the local angle of attack and the Mach number at each blade element section are computed and the aerodynamic coefficients are retrieved from the airfoil tables. For the discrete-blade model of the rotor, the section forces and moments are then converted to source terms that are added to the momentum equations at grid points where the blade intersects.

The discrete-blade model comprises an individual lifting line representing each blade, in contrast to the disk rotor model. The lifting-line changes location with time. In order to calculate the time-varying rotor sources, the instantaneous location of each rotor blade is found, followed by the calculation of the time-accurate rotor force that the blades exert on specific regions of the flow. Each rotor blade is divided into about 100 source locations, and the azimuth position of the blade is assumed to vary linearly with time. At each time step, the starting and ending azimuthal positions of a rotor blade are computed and used to find the coordinates of the blade sections and the intersections with the grid cells. The rotor sources are computed similar to the disk model and added to the momentum equations for the grid cell. The solution is then advanced in time.

All performance predictions presented in this chapter were calculated using CAMRAD II and the disk rotor model of RotUNS. The RotUNS calculated pressure fields were generated using the lifting-line (discrete-blade) rotor model to assess the effect of individual blades.

4.1.1 CAMRAD II

CAMRAD II [60] is a rotorcraft analysis tool that includes a combination of advanced technologies including steady calculations, multibody dynamics, nonlinear finite elements, and rotorcraft aerodynamics. The rotor structural dynamics model is based on beam theory. The rotor aerodynamics model is based on second-order lifting-line theory (steady 2D airfoil characteristics plus vortex wake), with unsteady aerodynamic forces from thin airfoil theory, and corrections for yawed flow and swept blades. In CAMRAD II, the rotors were trimmed to zero flapping while adjusting the collective pitch and the lateral and longitudinal cyclic of each rotor with a fixed shaft pitch angle. The HC1 rotor blades were modeled using 17 aerodynamic panels in CAMRAD II, with the panel width ranging from 8 percent R at the root to 3 percent R at the tip. Unlike the RotUNS blade model, which used the airfoil distribution shown in Figure 41, the CAMRAD II blade model used a constant NACA 0012 airfoil section. Additional details on the HC1 CAMRAD II model are available in reference [60].

4.2 Harrington Single Rotor 1 (HS1) and Coaxial Rotor 1 (HC1)

The performance and aerodynamics of the Harrington single rotor 1 (HS1) and coaxial rotor 1 (HC1) were predicted using RotUNS with the rotor disk model. Comparisons with the Harrington data serve to validate RotUNS for a coaxial rotor system. Although the experimental data for hover [13] and forward flight [16] are available, rotor control setting information is not. Disk model rotor calculations were explored to qualitatively understand the characteristics of the HS1 and HC1 flow fields.

4.2.1 Geometry description

The geometry for HS1 and HC1 is provided in Table 10, and the blade planform as modeled in RotUNS is shown in Figure 41. The difference between the blade geometry of the Harrington experiment [13] and Figure 41 is that the Harrington blades have a continuously varying nonlinear distribution of airfoil thickness. At this time, RotUNS does not allow a continuously varying airfoil thickness distribution, so nine NACA airfoils with varying thickness ratios were used to simulate the blades for HS1 and HC1 (see Fig. 41). The airfoil tables were interpolated at changing r/R locations to determine airfoil sectional c_l , c_d , and c_m as a function of angle of attack and Mach number. The airfoil tables were generated using RotCFD's airfoil table generator (AFTGen), which generates airfoil tables in standard C81 format using geometry and user-prescribed airfoil inputs. AFTGen was used for all RotUNS and BEMT calculations.

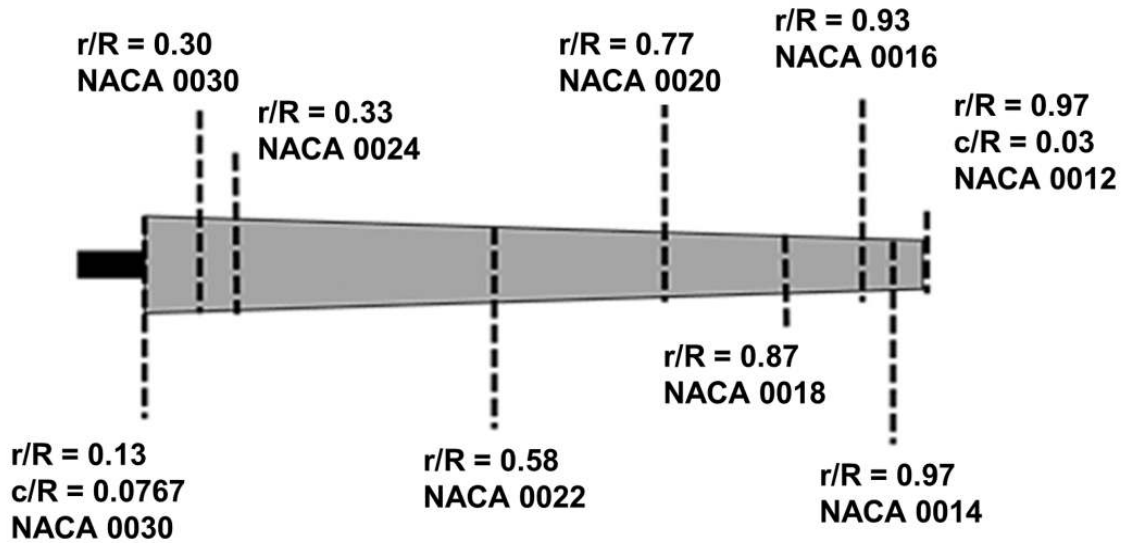


Figure 41. HS1 and HC1 blade planform geometry as modeled in RotUNS.

Table 10. HS1 and HC1 parameters [13].

Parameter	Harrington rotor 1
R , Radius (ft)	12.5
Number of blades (per rotor)	2
c , Chord (ft)	varying
Z , rotor separation (ft)	2.33
V_{tip} , Tip speed, hover (ft/sec)	500
Tip speed, forward flight (ft/sec)	469
Solidity	0.054
Solidity per rotor	0.027
Twist	None
Taper	linear distribution
Airfoils (thickness ratio)	nonlinear distribution
Cutout radius (r/R)	0.133
Hinge offset (r/R)	0.133
Upper rotor direction (HS1/HC1)	Clockwise
Lower rotor direction (HC1)	Counterclockwise

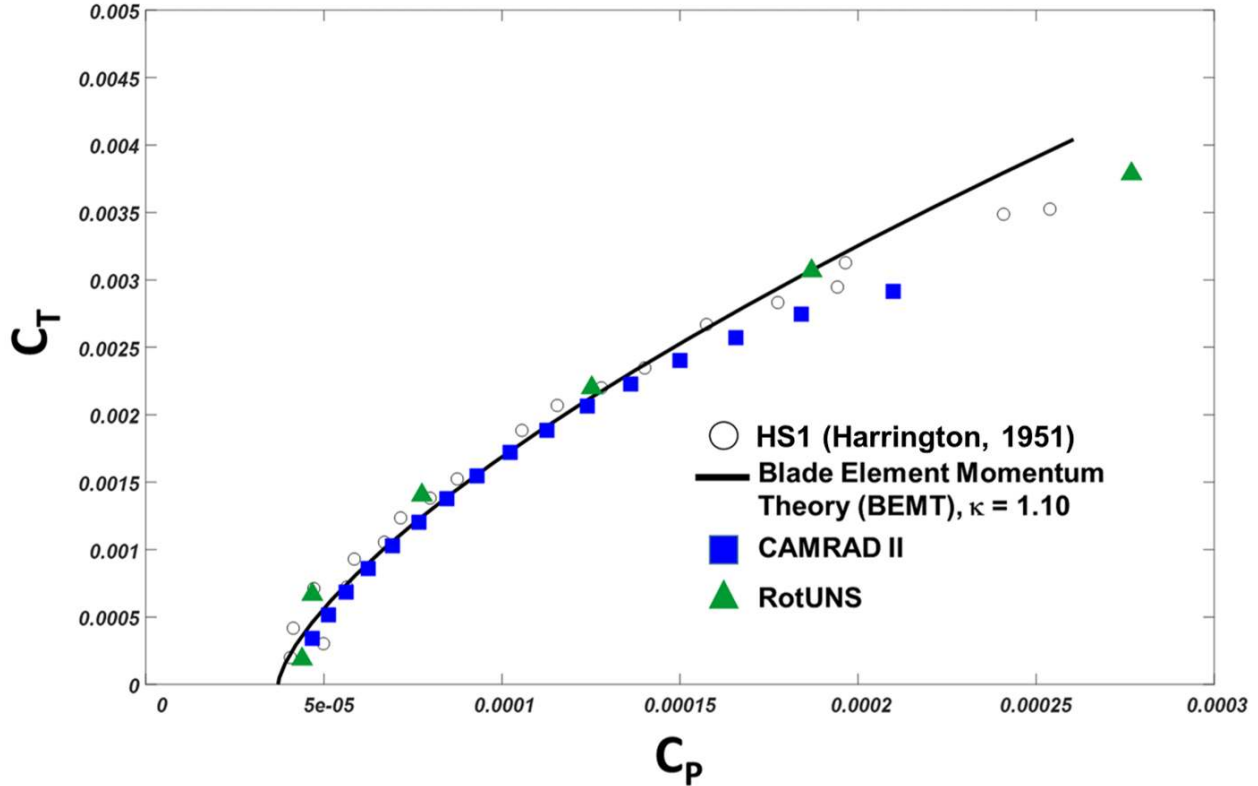


Figure 42. Performance of HS1 [13] in hover compared to BEMT, CAMRAD II, and RotUNS calculations.

4.3 HS1 Hover Performance

Figure 42 shows RotUNS, BEMT, and CAMRAD II hover calculations compared to measurements by Harrington [13] for the HS1 rotor for a collective pitch range from 1.5° to 9° . The BEMT predictions are based on Leishman's single-rotor blade element model [12]. In Figure 42, BEMT is underpredicting thrust for high values of power because of BEMT's assumptions [63]. The RotUNS and CAMRAD II calculations compare well with the Harrington [13] data.

4.4 HC1 Hover Performance

Figure 43 compares performance measurements [13] with predictions from RotUNS, RotUNS: Grid Adaption (GA), CAMRAD II, and the BEMT analysis for the HC1 system. Grid adaption, based on vorticity, was used for a few of the cases in anticipation of the complex interaction between the upper and lower rotor. The use of GA redefines and refines the mesh over time, allowing flow features to be captured with greater fidelity. In Figure 43, the BEMT calculations underpredicted the measurements and RotUNS calculations because of the BEMT input of κ_{int} and c_d . CAMRAD II calculations were closest to the experimental data compared to RotUNS and BEMT; this is due to the addition of section profile drag that was added as part of the shaft power calculation in CAMRAD II, resulting in calculations that closely match experimental data. The BEMT calculations for HC1 and HS1 at low collective settings closely match; as collective settings increase, RotUNS calculations compare better to the BEMT calculations [12].

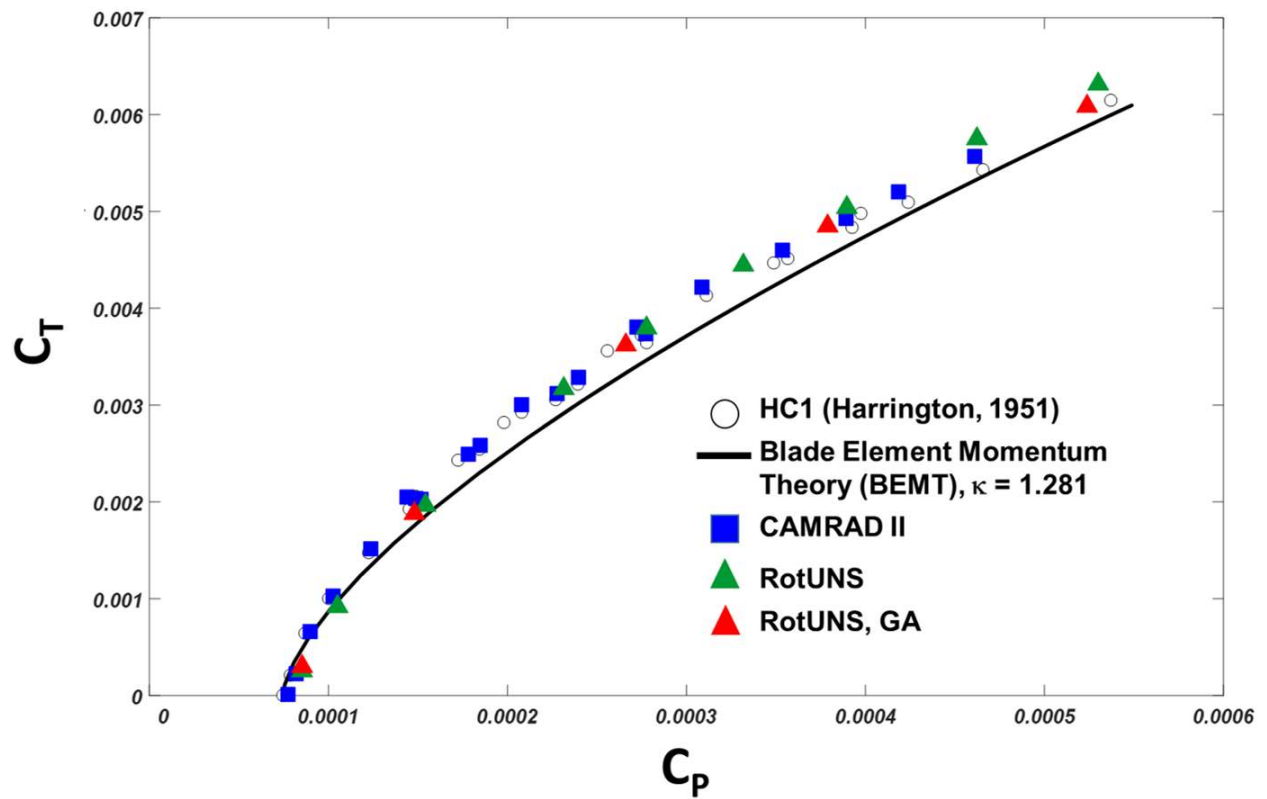


Figure 43. Performance of HC1 [13] in hover compared to BEMT, CAMRAD II, and RotUNS with and without grid adaption calculations.

Table 11. HC1 hover RotUNS rotor disk model control inputs (* denotes grid adaption (GA)).

θ_U ($^\circ$)	θ_L ($^\circ$)	% diff in Q
1.5	1.5	0.28
1.5*	1.5*	0.56
3.0	3.2	0.45
5.0	5.2	0.75
5.0*	5.0*	3.28
7.0	7.2	0.19
8.0	8.2	0.19
8.0*	8.0*	2.21
9.0	9.2	0.57
10.0	10.2	0.95
10.0*	10.0*	1.27
11.0	11.0	0.38
11.9	12.0	0.91
12.0*	12.0*	0.18

Collective settings for the upper and lower rotor were determined through an iterative process to achieve a torque-balanced solution. As shown in Table 11, torque balance was achieved for most of the cases by increasing the collective of the lower rotor by 0.2° compared to the upper rotor. Table 11 shows the percent torque difference between the upper and lower rotors; for the present work, a difference of < 1 percent was considered a balanced system. The thrust for the coaxial lower rotor is less than the thrust for the coaxial upper rotor because of the increased inflow to the lower rotor from the upper rotor [12].

The BEMT calculations used the same geometry assumptions as the RotUNS calculations, while using a coaxial interference-induced power factor from Leishman’s Case 4a [12,14]. Leishman’s Case 4a assumes that the rotors have balanced torque with the lower rotor operating in the slipstream of the upper rotor.

RotUNS with grid adaption shows an improvement at higher collective settings, but little or no change at lower thrust. Differences between Harrington’s data [13] and computational simulations can be due to blade modeling. The blades were not individually modeled, but rather the rotor was modeled as a disk with distributed momentum sources. Furthermore, the actual Harrington HS1 and HC1 had smooth airfoil (thickness-to-chord) transitions, unlike the geometry used by RotUNS and BEMT.

4.4.1 Rotor vertical separation distance variation

HC1 rotor performance was explored from 0.05 to $1.5 S/D$, where S is the vertical distance between the two rotors. Figure 44 reveals that as separation distance increases, the ratio between the thrust of the lower rotor (T_L) and the upper rotor (T_U) decreases, for balanced torque and constant total thrust coefficient, eventually becoming independent of the separation distance. Measurements by Ramasamy [9] for two different total thrust coefficients (and blade geometry) show similar trends, lending confidence in RotUNS prediction capability.

As previously mentioned, the RotUNS rotor collective pitch settings were determined through an iterative process to achieve a torque-balanced solution; the percent difference in torque for the calculations in Figure 44 is shown in Table 12.

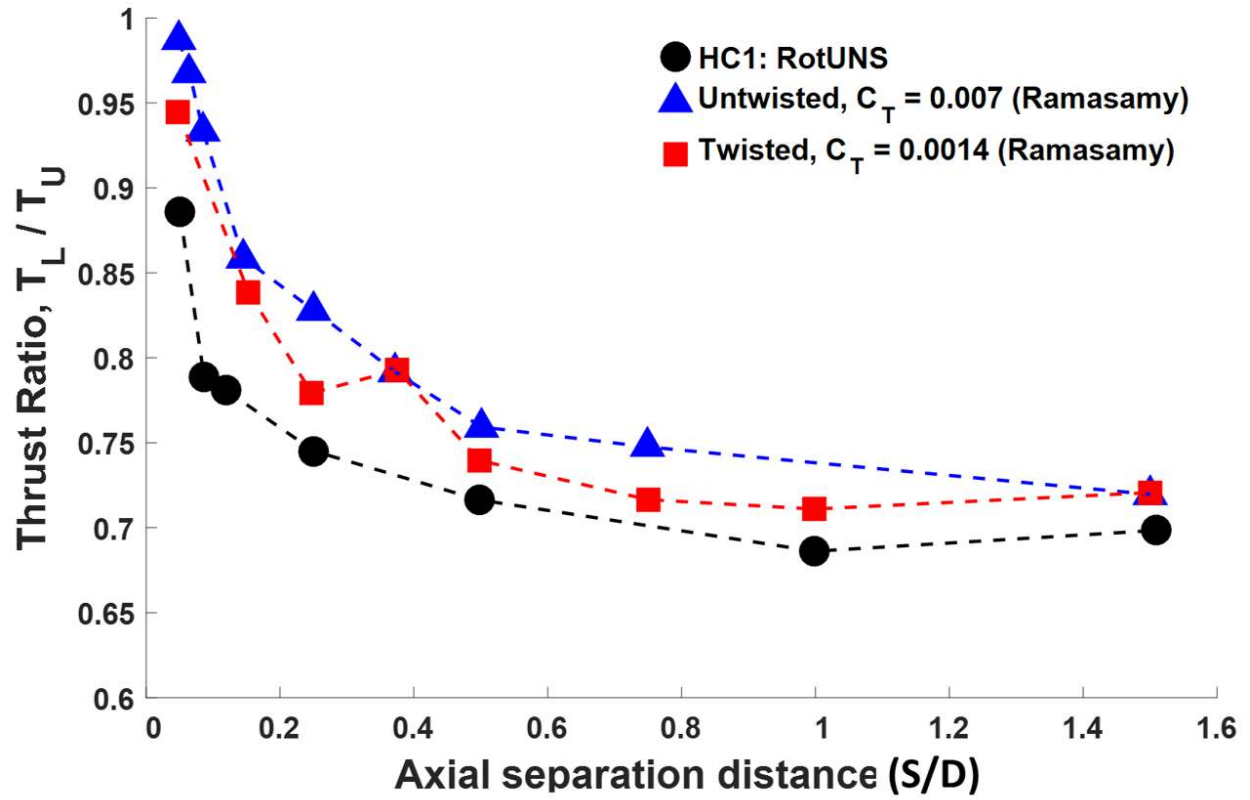


Figure 44. Thrust ratio versus rotor separation distance in hover comparing HC1 RotUNS rotor disk model calculations and Ramasamy’s experimental data [9] for twisted and untwisted blades.

Table 12. HC1 hover RotUNS rotor disk model control inputs for varying separation distance.

Z/D	θ_U (°)	θ_L (°)	% diff in Q
0.050	7.0	7.0	1.79
0.093	7.0	7.0	1.77
0.125	7.0	7.2	0.65
0.250	7.0	7.25	0.89
0.500	7.0	7.2	1.86
1.000	7.0	7.10	1.48
1.500	7.0	7.10	0.81

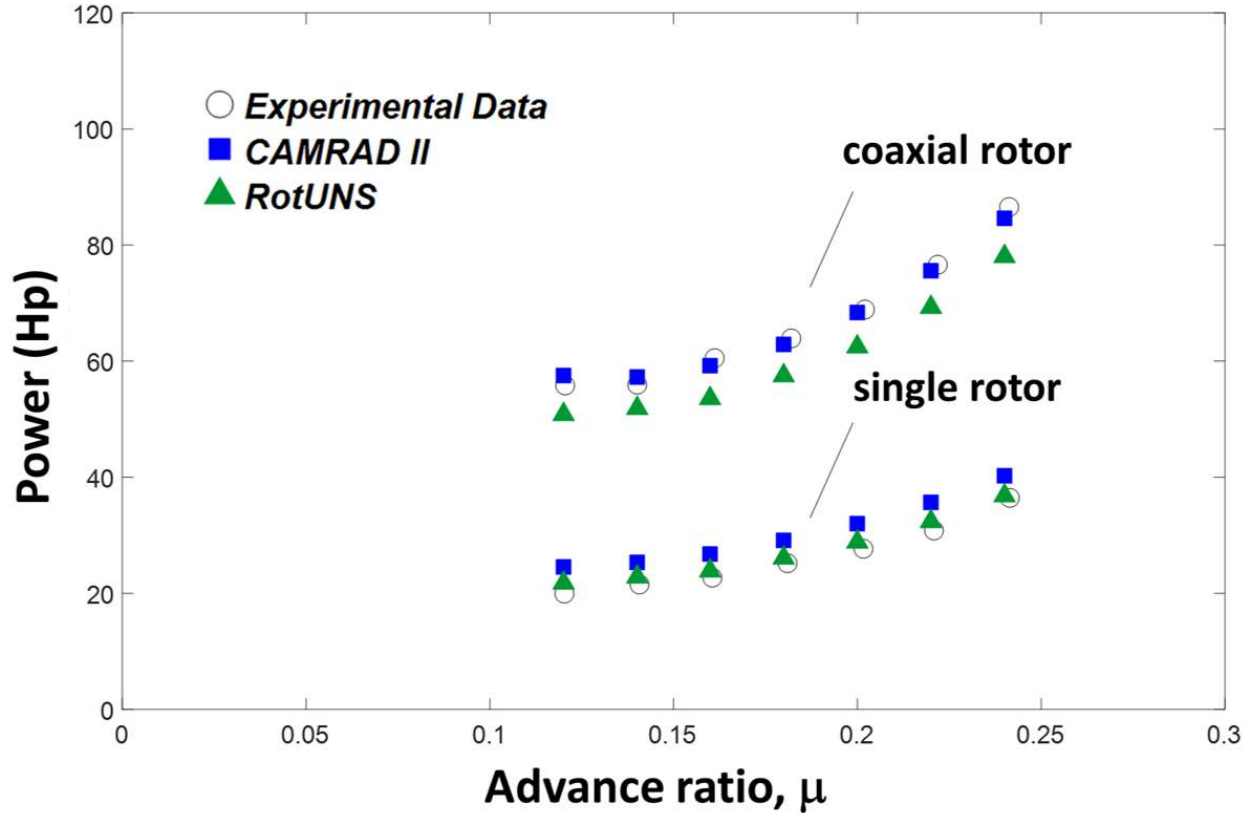


Figure 45. Measured performance of HS1 and HC1 [16] in forward flight compared to CAMRAD II and RotUNS calculations.

4.5 HS1 and HC1 Forward Flight Performance

Forward flight predictions required trim settings for the HC1 rotor. Here, RotUNS relied on trim control solutions provided by CAMRAD II [41]; the settings are provided in Table 13 and Table 14 for HS1 and HC1, respectively, for a trim target of balanced torque.

Figure 45 shows the measured forward flight performance of HS1 and HC1 [16] compared to CAMRAD II and RotUNS calculations. RotUNS calculations for HS1 are closer to the experimental data compared to CAMRAD II HS1 calculations, while CAMRAD II calculations for HC1 are closer to experimental data compared to RotUNS HC1 calculations. CAMRAD II and RotUNS percent error difference for HS1 and HC1 experimental data is shown in Table 15. Percent error was calculated using Equation 7. Compared to experimental HS1 data, CAMRAD II overpredicted more than RotUNS calculations. Compared to experimental HC1 data, RotUNS underpredicted while CAMRAD II correlated better.

$$\% \text{ error} = \frac{|\text{experimental} - \text{computational}|}{\text{experimental}} \times 100 \quad (7)$$

The two analysis used different airfoil distributions with RotUNS providing an airfoil thickness distribution that was more representative of the rotor [41]. For each airfoil, a C81Gen was used to

Table 13. HS1 forward flight RotUNS inputs using CAMRAD II control settings [41].

μ	α_s ($^\circ$)	θ ($^\circ$)	θ_{1s} ($^\circ$)	θ_{1c} ($^\circ$)
0.12	-2.18	7.31	-2.51	0.63
0.14	-2.87	7.50	-2.93	0.48
0.16	-3.66	7.82	-3.37	0.38
0.18	-4.53	8.27	-3.87	0.32
0.2	-5.48	8.83	-4.41	0.25
0.22	-6.49	9.51	-5.03	0.21
0.24	-7.57	10.33	-5.73	0.17

Table 14. HC1 forward flight RotUNS inputs using CAMRAD II control settings [41].

μ	α_s ($^\circ$)	θ ($^\circ$)	θ_{1s} ($^\circ$)	θ_{1c} ($^\circ$)
Lower rotor				
0.12	-2.16	7.98	-2.43	1.32
0.14	-2.85	8.03	-2.89	0.99
0.16	-3.64	8.27	-3.35	0.81
0.18	-4.51	8.67	-3.85	0.69
0.20	-5.47	9.19	-4.36	0.63
0.22	-6.46	9.85	-5.07	0.55
0.24	-7.53	10.65	-5.75	0.50
Upper rotor				
0.12	-2.16	8.07	-2.75	1.05
0.14	-2.85	8.08	-3.12	0.84
0.16	-3.64	8.31	-3.55	0.69
0.18	-4.51	8.69	-4.03	0.59
0.20	-5.47	9.21	-4.57	0.50
0.22	-6.46	9.87	-5.19	0.42
0.24	-7.53	10.68	-5.90	0.36

generate airfoil tables that were read by RotUNS, while CAMRAD II used an NACA 0012 airfoil table. Also, an increment to the section profile drag was added as part of the shaft power calculation in CAMRAD II. The computed torque from RotUNS for the upper and lower rotor torque for each advance ratio differed by less than 0.50 percent. In both RotUNS and CAMRAD II calculations the rotor shank ($r/R = 0$ to 0.133) was not modeled. Furthermore, CAMRAD II used a wake model, while RotUNS directly calculated the wake. Further investigation regarding the difference between HS1 and HC1 RotUNS and CAMRAD II calculations should be performed for both hover and forward flight, including induced drag, profile drag, and parasite drag differences.

4.6 Pressure Distribution Above and Below Rotor

As previously mentioned, the RotUNS discrete-blade option models the rotor blades as a lifting-line, therefore the flow field above and below the rotors are analyzed. A single rotor was analyzed first followed by a coaxial rotor for hover and forward flight. The Harrington rotor 1 was simulated with all rotors (single, upper/lower) set to a collective pitch of 7° .

Table 15. CAMRAD II and RotUNS percent error difference for HS1 and HC1 experimental data.

μ	HS1		HC1	
	CAMRAD II (%)	RotUNS (%)	CAMRAD II (%)	RotUNS (%)
0.12	22.69	9.32	3.00	8.88
0.14	17.71	6.17	2.21	7.27
0.16	18.01	5.02	2.27	11.55
0.18	15.66	3.61	1.65	10.16
0.20	15.89	4.48	0.70	9.19
0.22	15.76	5.06	1.29	9.45
0.24	10.77	1.26	2.33	9.91

The pressures above and below the rotor(s) are shown in Figures 46 through 49, which represent the absolute pressure normal to the surface at the closest flow-field grid point for HS1 and HC1. The figures simply illustrate the pressure change (lower or higher) as blades from the upper and lower rotors pass in opposite directions.

The absolute pressure below and above a single isolated rotor is shown in Figure 46 a) when the blades are at 0° ($B1$) and 180° ($B2$). A low pressure is evident above both blades and a high pressure below the blades, providing a positive upward thrust. Figure 46 b) shows the time histories of pressure just above and below blade $B1$ at $r/R = 0.85$ in the rotating frame; the pressure remains essentially constant throughout one revolution.

When a second rotor is introduced, the flow field becomes complex, as shown in Figures 47 through 49. The absolute pressure below and above each HC1 rotor is presented in Figures 47 and 48.

In Figure 47 the blades of the upper and lower rotor are not overlapped. The upper rotor blades are at 0° ($U1$) and 180° ($U2$) and the lower rotor blades are at 90° ($L1$) and 270° ($L2$). The presence of the lower rotor is shown at 90° and 270° in the upper rotor pressure contours, which reveal the influence of the pressure above the lower rotor. The same is also shown for the pressure above and below the lower rotor, where the pressure below the upper rotor is at 0° and 180° . For both the upper and lower rotors, a low pressure is shown at the location of the blades above and high pressure below the rotors, giving rise to a positive upward thrust.

In Figure 48 the upper and lower blades are overlapped at 45° ($U2$) and 135° ($U1$) for the upper rotor, and 45° ($L1$) and 135° ($L2$) for the lower rotor. In comparison to Figure 47 where the blades are not overlapped, a difference in pressure below and above is shown in Figure 48. When the blades are overlapped, the pressure above and below the upper rotor decreases. The opposite is shown for the lower rotor, where the pressure above and below increases.

The time histories of the pressure above and below the upper and lower rotor blades at an r/R of approximately 0.85 in the rotating frame are shown in Figure 49 for hover. The gray vertical line indicates the time of blade overlap. For both the upper and lower rotors, there is a change in pressure at the time of blade overlap. Blade two ($U2$) of the upper rotor experiences an overall decrease in pressure because of the low-pressure field generated from blade one ($L1$) of the lower rotor. Conversely, $L1$ experiences an increase in pressure because of the high-pressure field of $U2$. Comparing Figure 49 to Figure 46 b), an aerodynamic interaction is shown between the upper and lower rotor in the coaxial rotor system, unlike the single rotor.

The pressure above and below a rotor in forward flight at $\mu = 0.12$ is analyzed using the discrete-blade option of RotUNS. HS1 was analyzed first, followed by HC1. The control settings for HS1 and HC1 are shown in Tables 13 and 14.

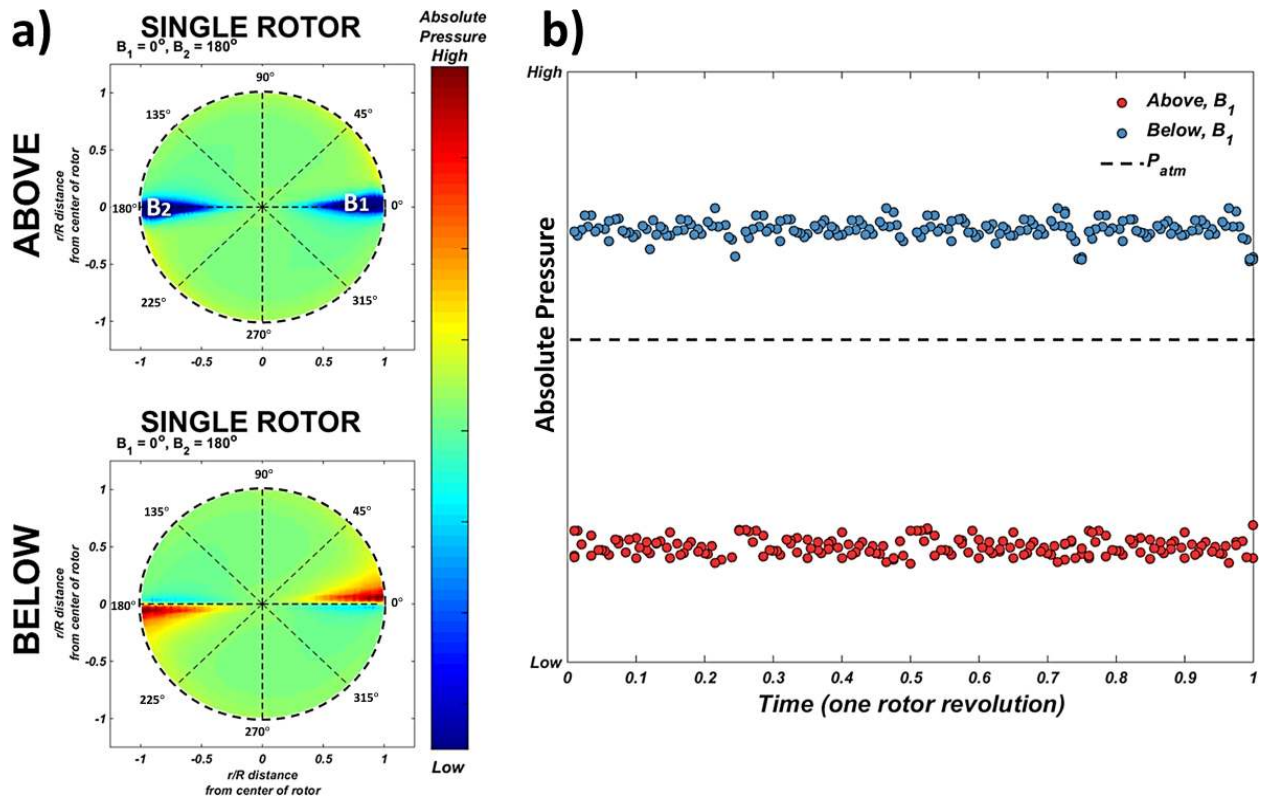


Figure 46. HS1 flow-field absolute pressures: a) below and above rotor, and b) time history (one revolution) at $r/R = 0.85$ in hover. RotUNS lifting-line (discrete blade) rotor model calculations.

Non-overlap

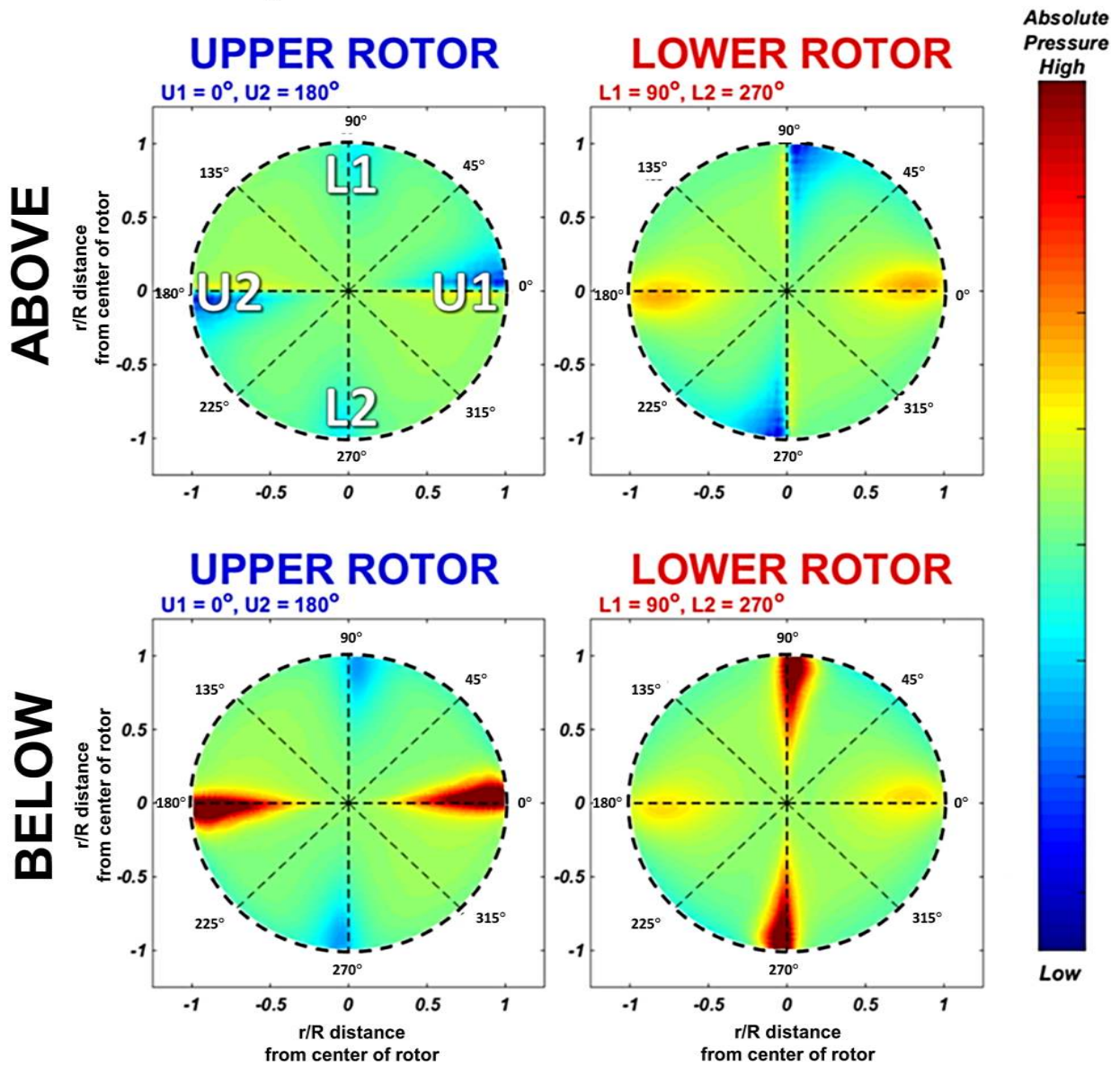


Figure 47. HC1 comparison of absolute pressure above and below upper and lower rotors at non-overlap. RotUNS lifting-line (discrete-blade) rotor model calculations are presented for hover.

Overlap

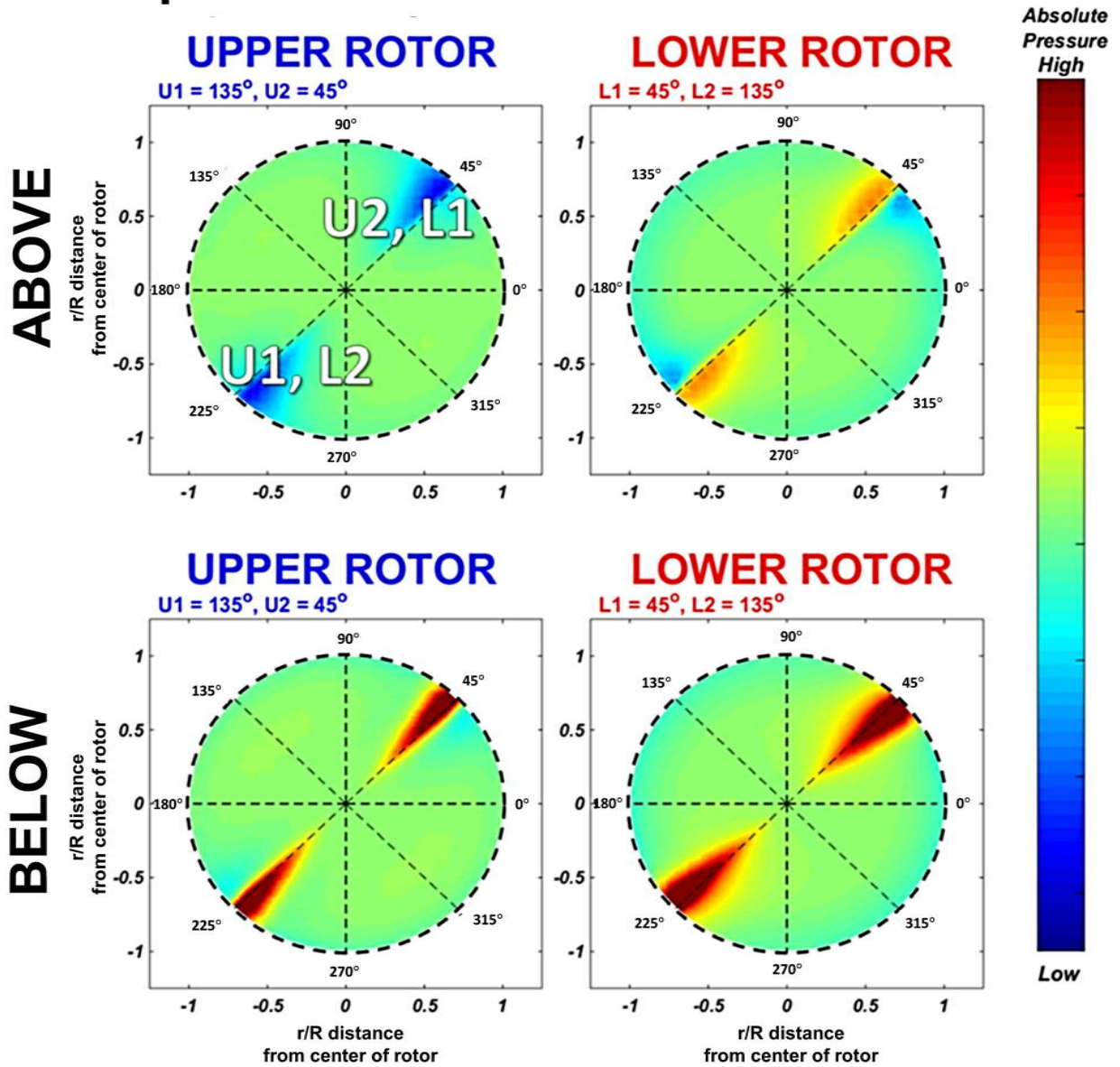


Figure 48. HC1 comparison of absolute pressure above and below upper and lower rotors at overlap. RotUNS lifting-line (discrete-blade) rotor model calculations are presented for hover.

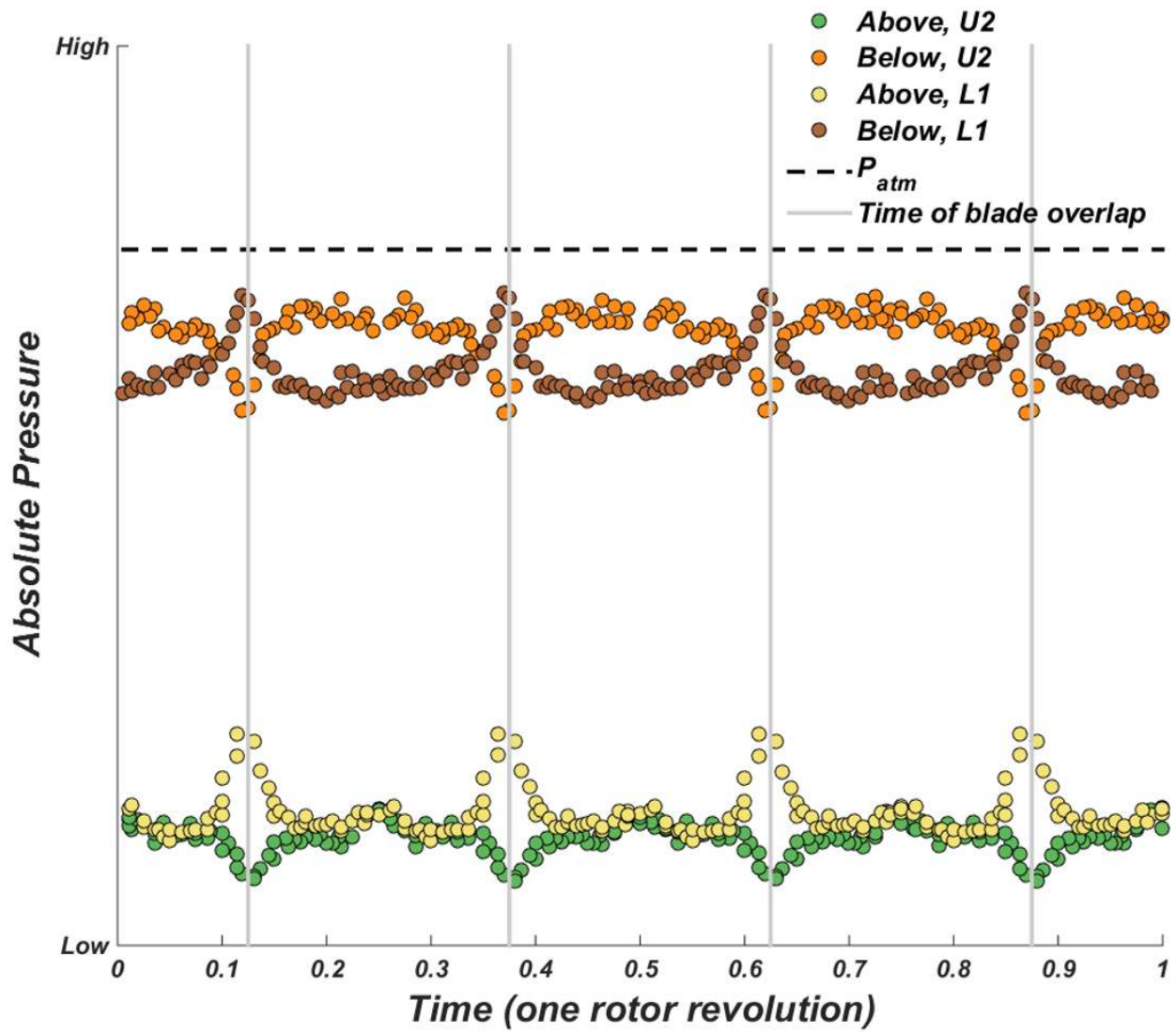


Figure 49. Time history (one revolution) at $r/R = 0.85$ for absolute pressure below and above $U2$ (upper rotor blade two) and $L1$ (lower rotor blade one) in hover.

The pressures above and below the rotor(s) are shown in Figures 50 through 52, which represent the absolute pressure normal to the plane of the rotor at the closest flow-field grid point for HC1.

In Figure 50 the blades of the upper and lower rotor are not overlapped. The upper rotor blades are at 0° ($U1$) and 180° ($U2$), and the lower rotor blades are at 90° ($L1$) and 270° ($L2$). The presence of the lower rotor is shown at 90° and 270° in the upper rotor pressure contours, which reveal the influence of the pressure above the lower rotor. The same is also shown for the pressure above and below the lower rotor, where the pressure below the upper rotor is at 0° and 180° . For the upper rotor, the blades ($U1$ and $U2$) experience a lower pressure above and higher pressure below, resulting in a positive upward thrust. A similar result is shown for $L1$ and $L2$.

In Figure 51 the upper and lower blades are overlapped at 225° ($U1$) and 45° ($U2$) for the upper rotor, and 45° ($L1$) and 225° ($L2$) for the lower rotor. Compared to Figure 50, the pressure above and below the upper rotor decreases when the blades overlap. The opposite is shown for the lower rotor, where the pressures above and below increase compared to the non-overlapped case (Fig. 50).

The 3D RotUNS HC1 calculations reveal that at the time of blade crossing the lower rotor blades enter a region of high pressure due to the high pressure below the upper rotor, and, in turn, an overall increase in absolute pressure on the lower rotor blades occurs. Also at the time of blade crossing, the upper rotor blades enter a region of lower pressure due to the low pressure above the lower rotor, and the upper rotor blades see an overall decrease in absolute pressure at this time. The conclusions from the 2D OVERFLOW blade crossing simulation are consistent with the 3D results.

Previously Barbely et al. [27] analyzed the pressure distribution above and below the upper and lower rotor in hover for HC1. The pressure above the lower rotor in forward flight and hover is shown in Figure 52 with the lower rotor blades at 90° and 270° . The pressure scales for the hover and forward flight cases are different. The pressure field in hover is symmetrical, while the forward flight cases is not.

4.6.1 Wake dissipation effects

Vortex diffusion is a critical issue with all computational simulations of rotor wakes. The projection of the rotor wakes must be tracked in order to understand information regarding possible BVIs. Using resolution enhancements in the grid, vortices can be preserved longer. Kim and Brown [18] conducted a computational investigation using the VTM developed by Brown coupled with a lifting-line representation of the blade. Without the use of grid adaption in RotUNS, the tip vortices are not discernible after approximately 120° of vortex age although the calculation represents 50 rotor revolutions. RotUNS was run with grid adaption (GA) for a small set of thrust/collective settings. The grid was automatically refined in areas of high vorticity and coarsened in areas of low vorticity.

The use of GA resulted in an improved agreement between rotor performance predictions and experimental data as compared to the RotUNS baseline grid results shown Figure 43. However, not all of the GA cases are as well torque-balanced as the baseline grid cases. In summary, the baseline grid is sufficient for performance predictions, but a detailed study of wake interactions requires grid adaption or a finer baseline grid to investigate possible BVIs.

4.7 Comparison of 2D and 3D Results

As shown in Figures 50 through 52, the pressure distribution above and below HS1 and HC1 further validates the change in aerodynamic loading on a blade when two rotor blades cross as

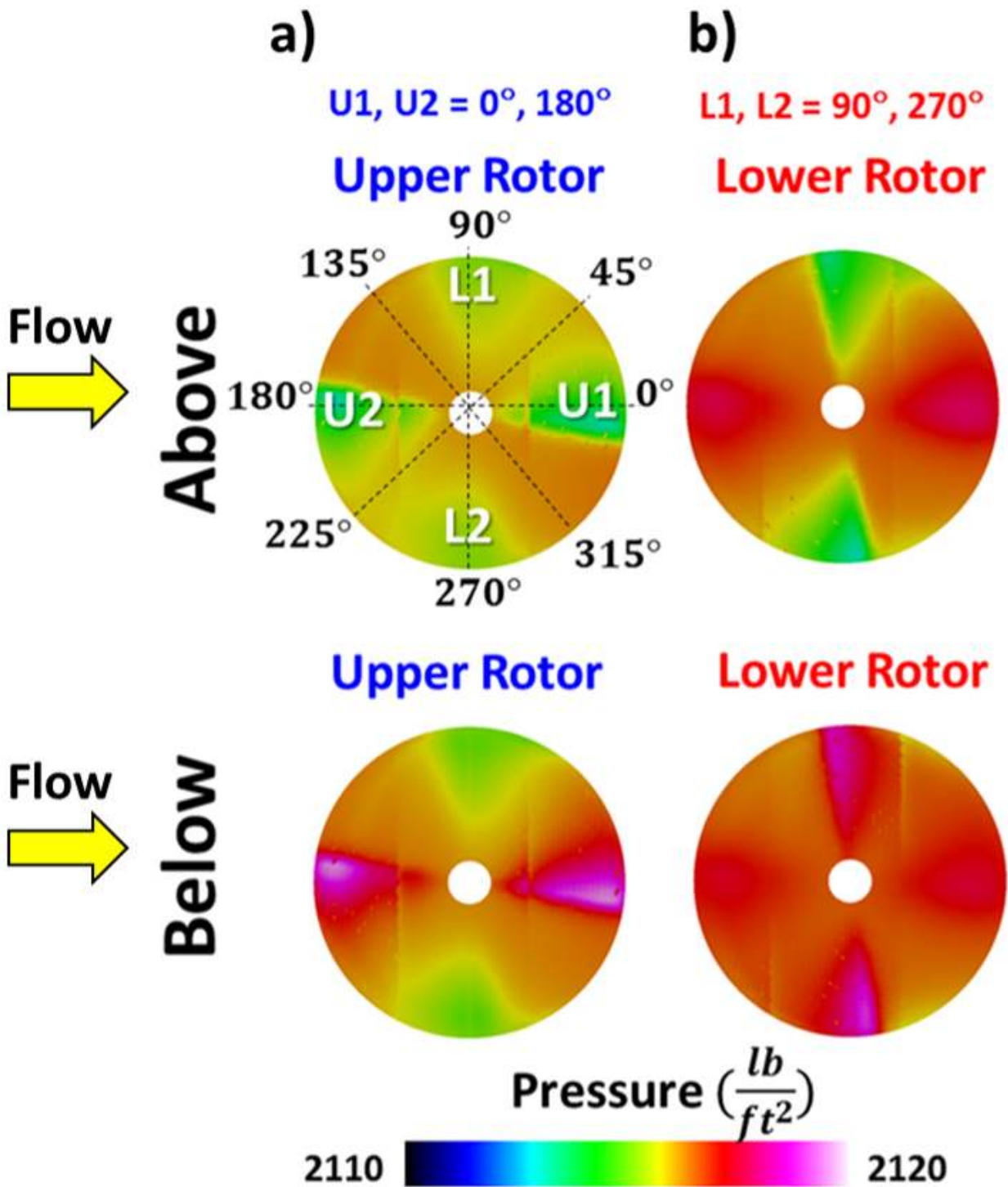


Figure 50. HC1 flow-field absolute pressures below and above rotor at two instances when blades are not overlapped, for a) upper rotor, where $U1, U2 = 0^\circ, 180^\circ$, and b) lower rotor, where $L1, L2 = 90^\circ, 270^\circ$. RotUNS forward flight lifting-line (discrete-blade) rotor model calculations in forward flight ($\mu = 0.12$).

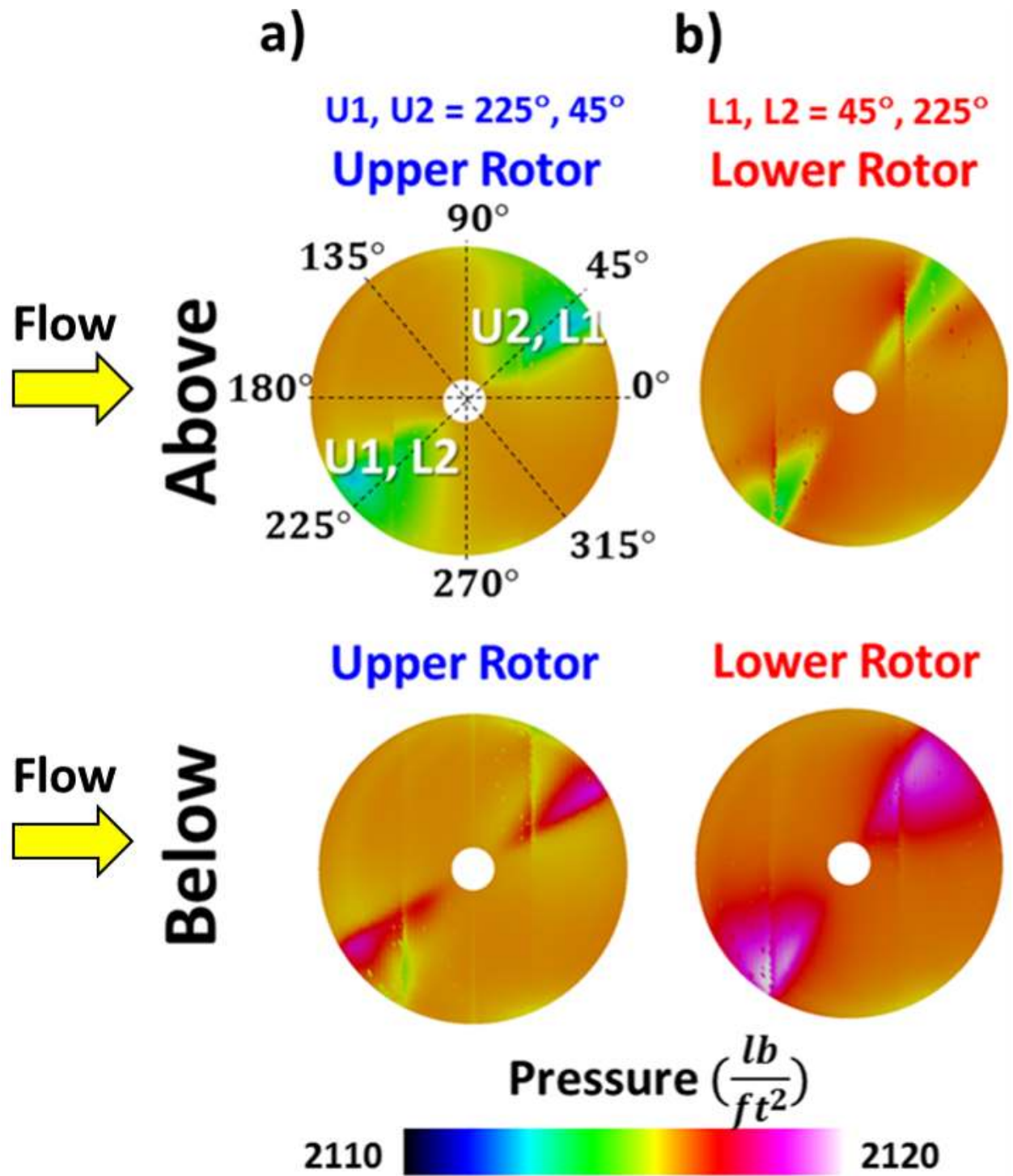
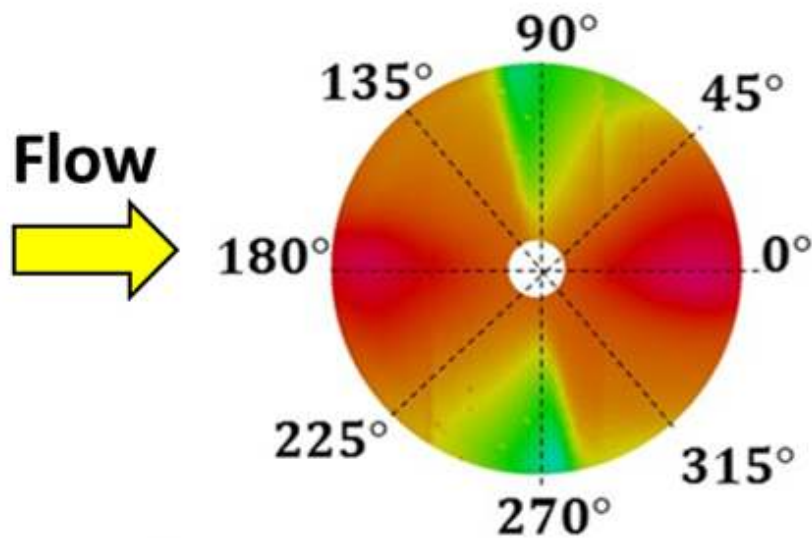


Figure 51. HC1 flow-field absolute pressures below and above rotor at two instances when blades are overlapped, for a) upper rotor, where $U1, U2 = 225^\circ, 45^\circ$, and b) lower rotor, where $L1, L2 = 45^\circ, 225^\circ$. RotUNS forward flight lifting-line (discrete-blade) rotor model calculations in forward flight ($\mu = 0.12$).

Lower Rotor Pressure Above $L1, L2 = 90^\circ, 270^\circ$

a) Forward Flight



b) Hover

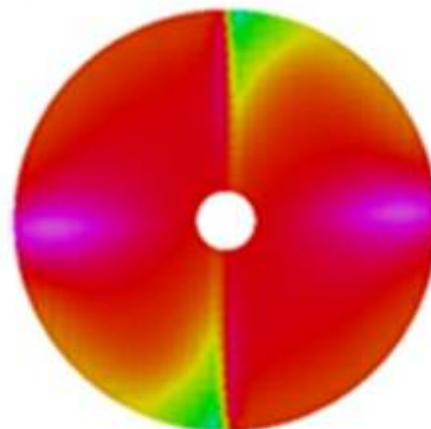


Figure 52. HC1 flow-field absolute pressures above lower rotor blades where $L1, L2 = 90^\circ, 270^\circ$ for a) forward flight, and b) hover. RotUNS lifting-line (discrete-blade) rotor model calculations.

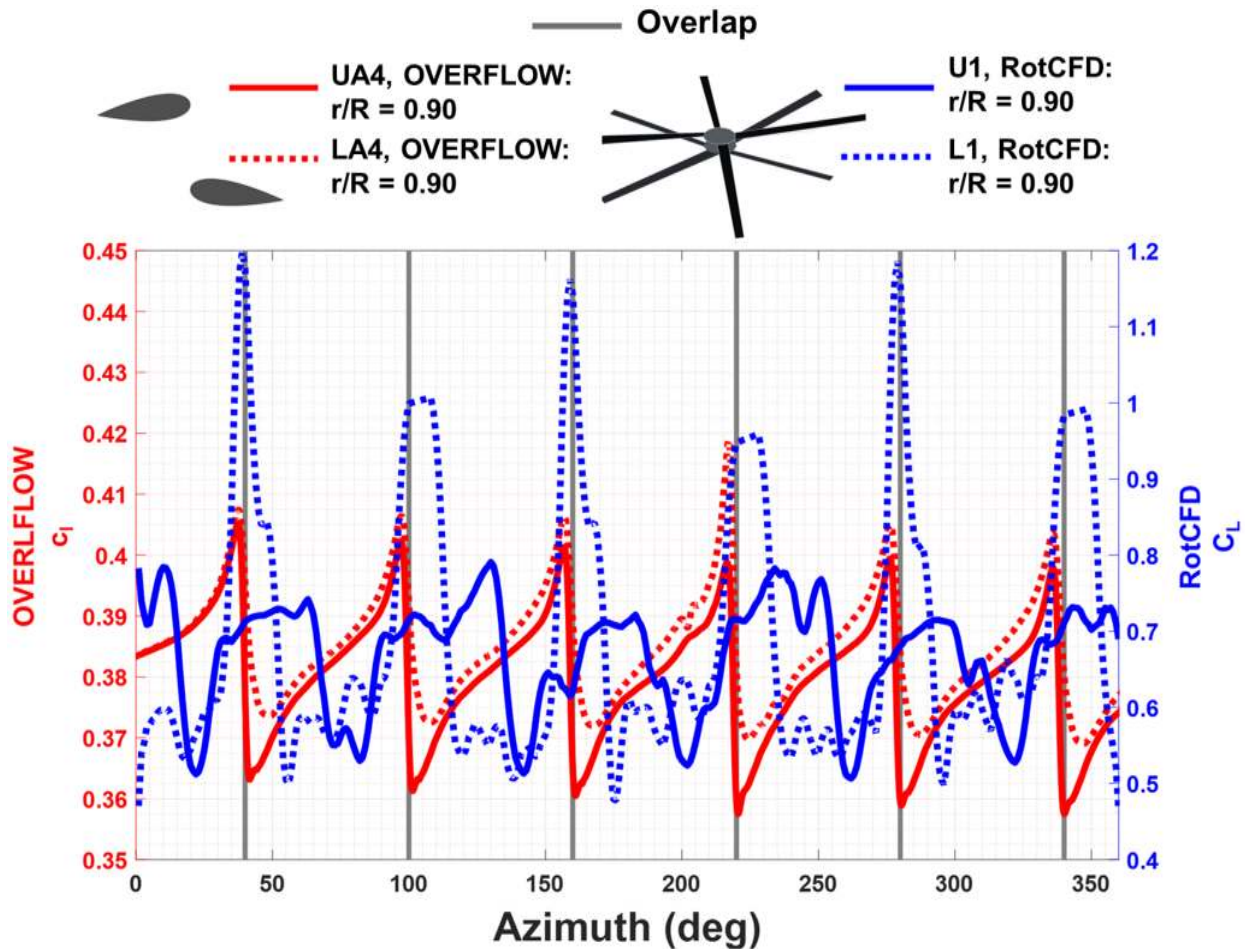


Figure 53. Comparison between 2D OVERFLOW and 3D RotCFD modern coaxial rotor in hover at $r/R = 0.90$ for upper rotor blade one (U1), lower rotor blade one (L1), upper airfoil four (UA4), and lower airfoil four (LA4) (OVERFLOW conditions: $M = 0.564$, $\alpha = 5.8^\circ$, $S/c = 4.0$ ($S = 2.0$ ft, $c = 0.5$ ft), and $D/c = 75.4$ ft. RotCFD conditions: $V_{tip} = 700$ ft/s, $\alpha = 5^\circ$, $S/c = 4.0$ ($S = 2.0$ ft, $c = 0.5$ ft), $C_T = 0.004$, $C_P = 0.0003$, and $\theta_U/\theta_L = 9^\circ$).

discussed in Chapter 3. RotUNS and 2D OVERFLOW hover results (Chapter 3) for the modern rotor design are compared (see Table 3) at a span location of $r/R = 0.90$. See Figure 53 for OVERFLOW c_l versus azimuth (y-axis on left in red) and RotCFD C_L versus azimuth (y-axis on right in blue). The 2D hover OVERFLOW results include shed vorticity and downwash effects. Both simulations show an increase in lift before overlap and a decrease in lift after overlap. Before overlap, the upper airfoil sees an increase in angle of attack because of the upwash from the lower airfoil. The angle of attack of the lower airfoil also increases because of the upwash from the upper airfoil and therefore an increase in lift is experienced by both airfoils, while the opposite occurs after time of overlap. Both LA4 and L1 see a larger change in lift before overlap compared to UA4 and U1. Differences between the two simulations result from the difference in airfoil/blade modeling; RotUNS models the blade as a lifting line, whereas 2D OVERFLOW models the blade r/R location as an airfoil. RotUNS is unable to model thickness effects, but is able to calculate performance characteristics unlike 2D OVERFLOW.

4.8 Summary

RotUNS has the ability to model a 3D coaxial rotor and provide insight into performance differences between a single and coaxial rotor in hover and forward flight. The 2D OVERFLOW simulation only modeled a hovering rotor, whereas 3D RotUNS expanded to forward flight. The 2D OVERFLOW calculations provided direct 2D information regarding the aerodynamics, whereas the 3D RotUNS performance calculations provided minimal insight into the rotor aerodynamics. RotUNS was validated and parametric studies were performed to understand the change in power and thrust. A new approach to understand the effect of BVI for coaxial rotors is discussed in the next chapter.

5 Blade Crossing and BVI Location Identification

Compared to a single main rotor, a coaxial rotor system results in aerodynamic interactions between the upper and lower rotors. Two of these interactions include blade crossings and additional BVI locations.

For a coaxial rotor, the time and location of a blade crossing occurrence is not always intuitive. As shown in Chapter 3, blade crossing affects the overall aerodynamic loading on a blade. As a result, the change in loading on a blade directly affects a change in loading noise. Furthermore, the time and location of the BVI becomes more complex because of the additional rotor blades, and therefore more difficult to predict.

A computational tool was developed to predict the time and location of blade crossings and the time, location, and interaction angle of a BVI occurrence. Information regarding blade overlap and BVI instances provides further insights to understanding coaxial aerodynamic and acoustic sources.

5.1 Blade Crossing Location Identification

Unlike a 2D simulation, the exact time of blade overlap of two contra-rotating rotors, with more than one blade each, requires careful accounting. The code RABBIT (RAPid Blade and Blade-vortex Interaction Timer) was developed to predict the time and location of blade overlap. RABBIT is a MATLAB code [64] that identifies the time and azimuth at which a reference blade of the upper (or lower) rotor crosses a lower (or upper) rotor blade. RABBIT aids in pinpointing locations of interest between, or in the plane of, the rotors.

The upper and lower rotors can have different parameters in RABBIT including RPM, number of blades, blade phase, reference blade, radius, and chord. Although a constant RPM and blade phasing were used for the upper and lower Harrington [13] coaxial rotor discussed in Chapter 2, results become less intuitive when the parameters for each rotor differ. For example, the reference blade is identified by first selecting the upper or lower rotor and then selecting the blade from that rotor. A blade crossing is recorded when a reference blade overlaps a blade from the other rotor. Figure 54 is an isometric view of the modern design coaxial rotor at $V_{tip} = 625$ ft/s, $\mu = 0.10$, $S = 2.0$ ft, and $\alpha_s = 7.00^\circ$. For the modern design coaxial rotor with three blades per rotor (rotating in opposite directions), RABBIT captures six overlaps of the reference blade in one rotor revolution.

As shown in Figure 54, the starting location for each blade is as follows: U_{ref} (upper rotor reference blade one, $U1$) is at 180° , $U2$ (upper rotor blade two) is at 60° , $U3$ (upper rotor blade three) is at 300° , $L1$ (lower rotor blade one) is at 240° , $L2$ (lower rotor blade two) is at 0° , and $L3$ (lower rotor blade three) is at 120° . The lower rotor blades overlap with U_{ref} in the following order for one revolution: $L3$ at 150° , $L2$ at 90° , $L1$ at 30° , $L3$ at 330° , $L2$ at 270° , and $L1$ at 210° .

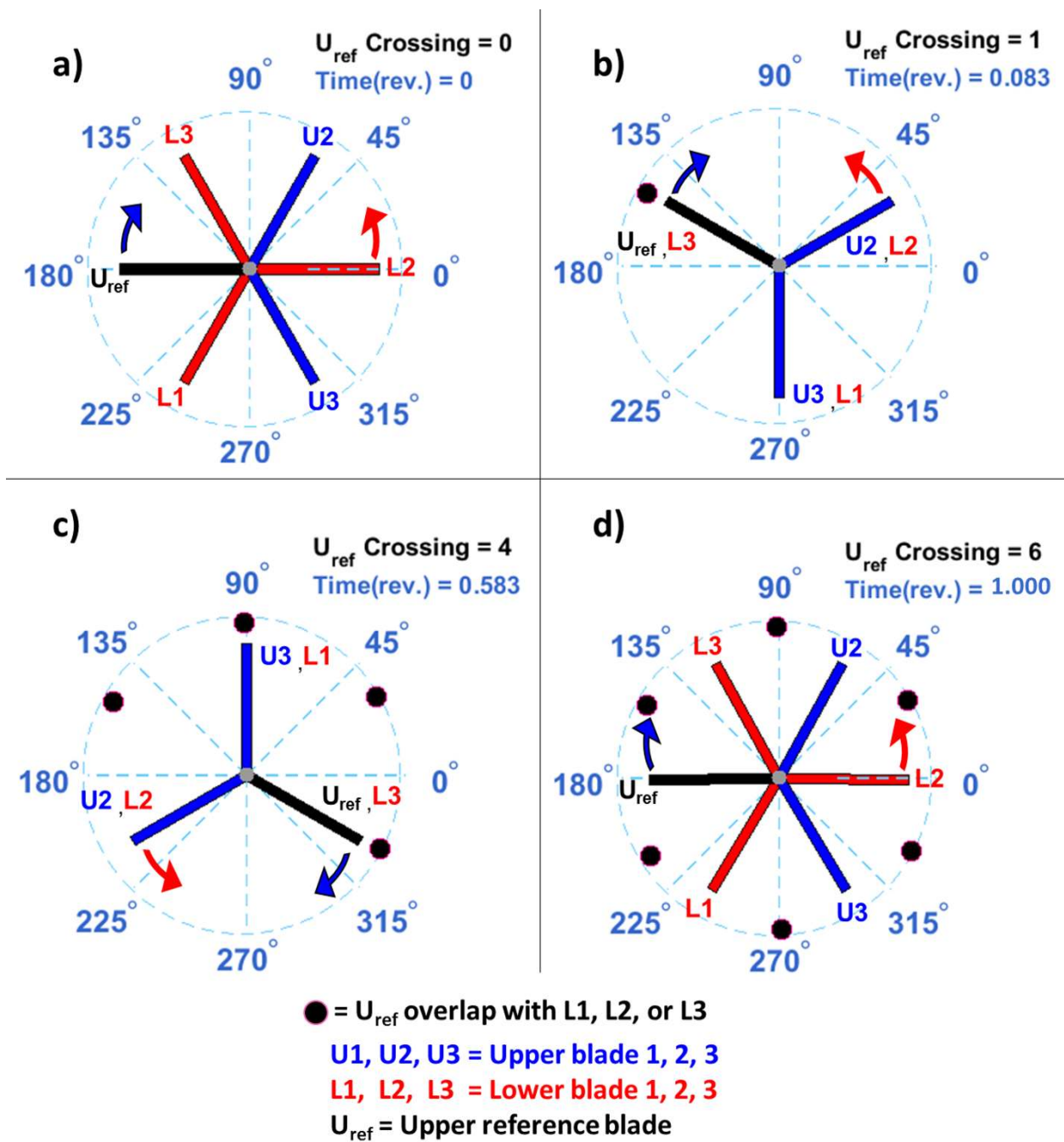


Figure 54. RABBIT's predictions for a six-bladed coaxial rotor blade crossing time and locations ($V_{tip} = 625$ ft/s, $\mu = 0.10$, $S = 2.0$ ft, and $\alpha_s = 7.00^\circ$).

For various unconventional coaxial configurations, RABBIT can predict blade crossings after one full revolution as shown in Figure 55. One full revolution is defined as the time it takes for the rotor with the lowest RPM to complete a revolution. Figure 55 a) shows an example of different spacing phase angles and two different radii and chord lengths for the upper and lower rotor. A coaxial rotor with varying RPM between the two rotors is calculated in Figure 55 b). A complex combination of Figures 55 a) and b) is shown in 55 c), where the number of blades, RPM, radius, chord, and phase angle are different between the upper and lower rotor. These unconventional coaxial configurations are for educational purposes and were designed to help debug RABBIT.

The time and location of blade crossing directly affect the acoustic signature. As shown in Chapter 3, the unsteady loading on the blade changes before, at, and after a blade crossing. The overall acoustic change is discussed in Chapter 5 by comparing a single and coaxial rotor in hover.

5.2 BVI Location Identification

For a finite wing, a tip vortex is generated because of the difference in pressure between the upper and lower surface of the wing. The air from the upper surface (low pressure) flows inboard toward the root, while the lower surface (high pressure) air flows toward the tip. A roll-up is caused by the joining of the upper and lower surface at the trailing edge. A number of small vortices are formed along the span of the wing and are rolled up into two large vortices at the wing tips [58]. Because of the conservation of vorticity, the bound circulation is trailed into the wake from the blade (root to tip) [53].

For a rotor blade, the circulation and lift are often highest at the tip, where the velocity on the blade is highest. The trailed vorticity from the rotor blade tip is generated by the radial variation of the bound circulation. A pictorial explanation of the generation of the tip vortex for a single rotor blade is shown in Figure 56 [53].

The strength of the blade tip vortices is governed by tip vortex core size (blade tip geometry) and bound circulation. The trajectory of the blade vortex provides the opportunity for a possible vortex and blade collision, resulting in unsteady loading. The interaction between a tip vortex and a rotor blade is known as a BVI [53]. The effect of a direct interaction between blade and tip vortices causes significant changes in blade loading and therefore noise. A vortex passing close to a rotor blade can also create a large change in loading. The strength of each interaction depends on the tip vortex strength, the local interaction angle between the blade and vortex, and the vertical distance between the blade and vortex [54]. For coaxial rotors, the lower rotor blades and the tip vortex from the upper rotor blades can create possible interactions [3].

As previously mentioned, RABBIT not only identifies the time and location of a blade crossing, but also the time, location, and angle of a BVI. The tip vortex trajectory model in RABBIT uses Beddoes' prescribed wake [63]. RABBIT's BVI identifier was validated using a single rotor blade study performed by Sim, George, and Yen [65]. Similar studies that identify BVI occurrences have been performed by others including Malovrh and Gandhi [66], where the wake was modeled as a free wake based on the Maryland Free Wake (MFW) algorithm. RABBIT was also validated for a coaxial rotor case using CAMRAD II.

5.3 Single Rotor BVI Location Identification

Simulations by RABBIT and Sim et al. [65] both incorporated Beddoes' prescribed wake model that uses a correction to the rigid wake based on the vortex element location. The three locations are when the vortex element is (1) within the rotor disk, (2) between the rotor disk and wake, and (3) in the rotor wake [65]. Beddoes' prescribed wake model is limited to advance ratios below

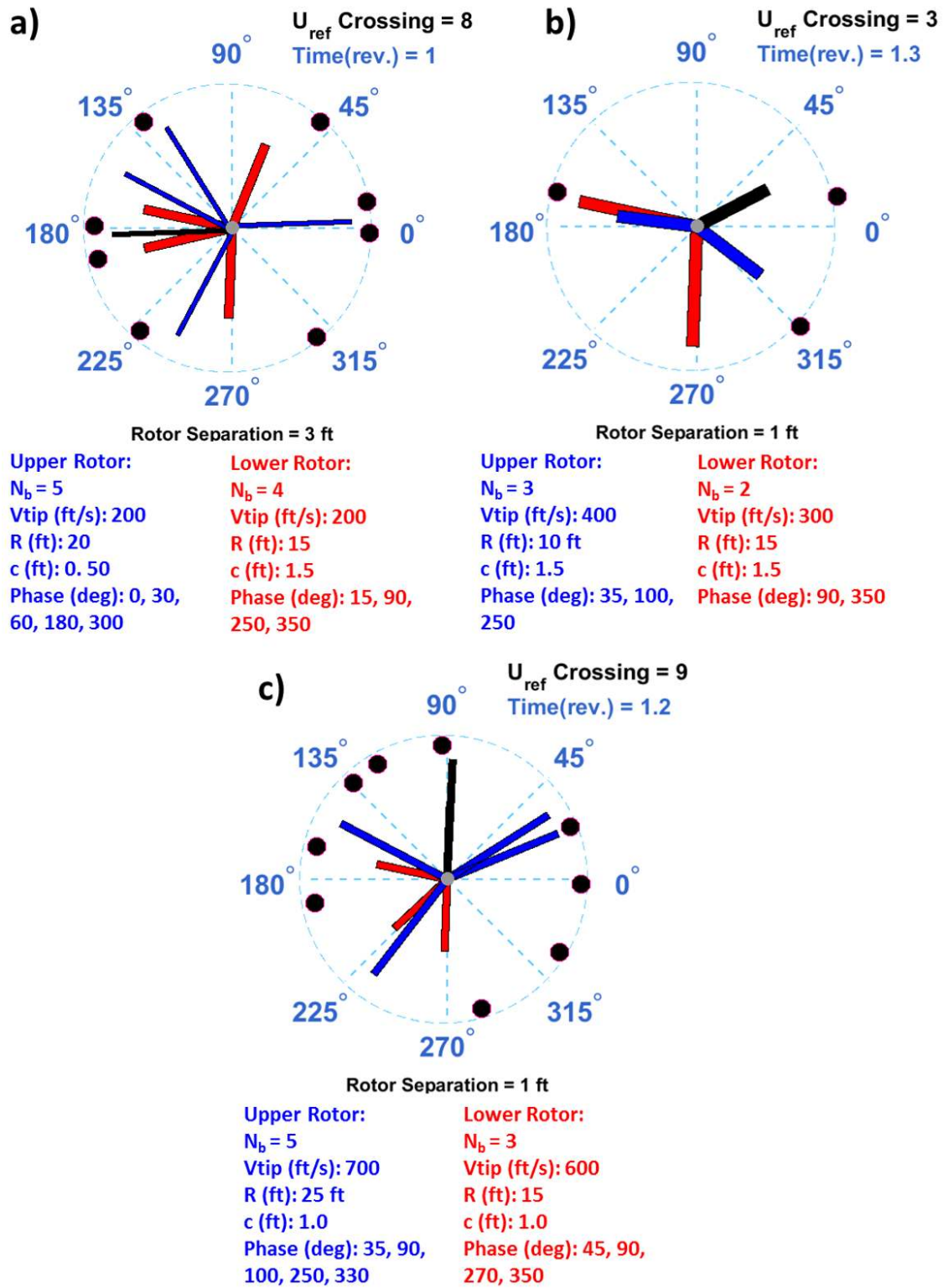


Figure 55. RABBIT's blade crossing predictions for three unconventional coaxial configurations.

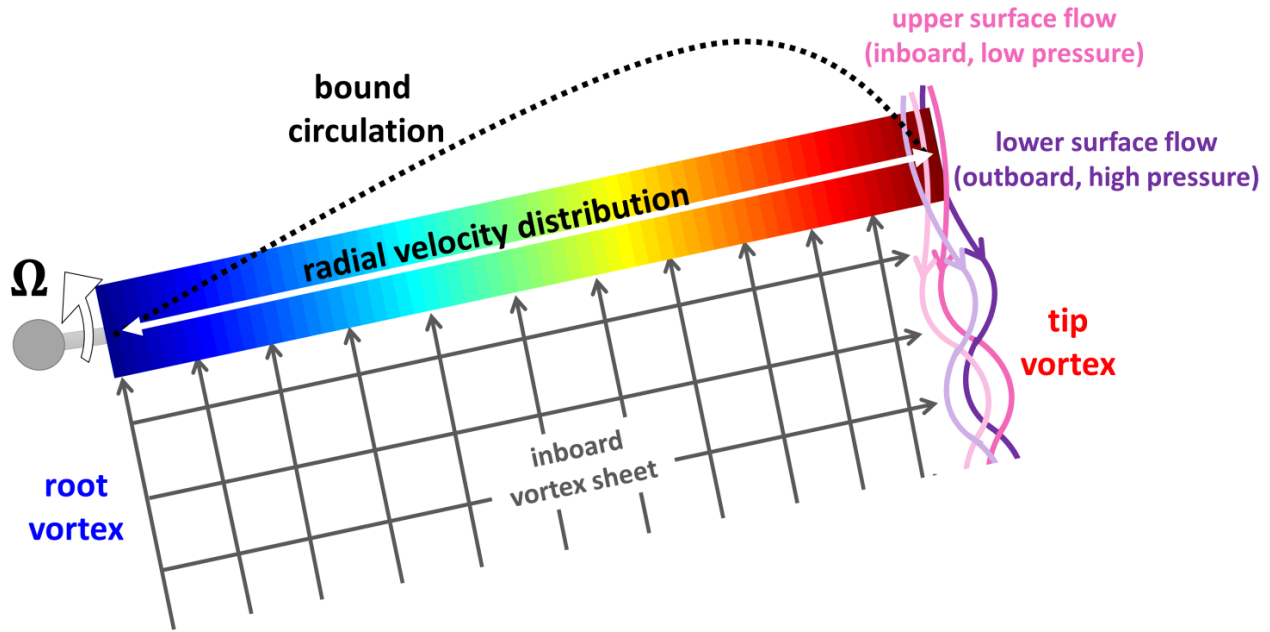


Figure 56. Pictorial representation of a blade tip vortex formation and the trailed and shed vorticity in wake.

0.15 [65]. Table 16 shows the operating conditions for the single rotor case study by Sim et al. [65] that was used to validate RABBIT for a single rotor.

Predictions from the Sim et al. [65] rotor case study were compared to RABBIT's predictions. In Figure 57 the rotor tip vortex wake displacements for X , Y , and Z , nondimensionalized by the rotor radius, are shown. Figure 57 c) includes Beddoes' wake as calculated by reference [65], and free-wake, rigid-wake, and experimental data provided by reference [65]. The rigid-wake model correlates least with experimental data, while the free wake and Beddoes' wake (RABBIT and Sim et al.) correlate equally as well. Discrepancy between RABBIT and Sim et al. for Z/R could be due to the difference in vortex wake discretization. Sim et al. modeled the vortex wake every degree, and RABBIT modeled the wake vortex every one-fifth of a degree.

Figure 58 shows the output from RABBIT after one rotor revolution and includes the location of BVIs and the tip vortex trajectory. Figure 59 shows a comparison of the identified BVI locations between Sim et al. and RABBIT. As shown in Figure 59, Sim et al. only provides BVI at $r/R = 0.90$. RABBIT's prediction for the blade azimuth angle versus r/R agrees with results from Sim et al. at $r/R = 0.90$; both analyses predict five different BVIs at 30° , 58° , 81° , 285° , and 315° .

The BVIs were calculated to determine the significance of each interaction for the case study. Important BVI strength factors include translating blade velocity (V_b), BVI angle (γ), miss distance (h), vortex strength (Γ), time (t), 2D lift curve slope ($c_{l\alpha}$), and chord (c). From this information, Sim et al. calculated a BVI impulse factor (\bar{I}) and the time rate of change of loading ($\frac{\partial F}{\partial t}$) as shown in reference [65]. The vortex strength (Γ) is calculated by assuming a core size of 5 percent of the chord [65]. The BVI impulse factor relates to the time rate of change of the blades' loading and is related to the magnitude of $\frac{\partial F}{\partial t}$ and noise intensity. Equations 9 through 11 are from Sim et al. [65].

The impulse factor is calculated from the translating blade velocity, BVI angle, and miss distance; see equation 8. The translating blade velocity is the velocity on the blade at the location of interaction and is determined by the radial and azimuthal position. The BVI angle is the angle at

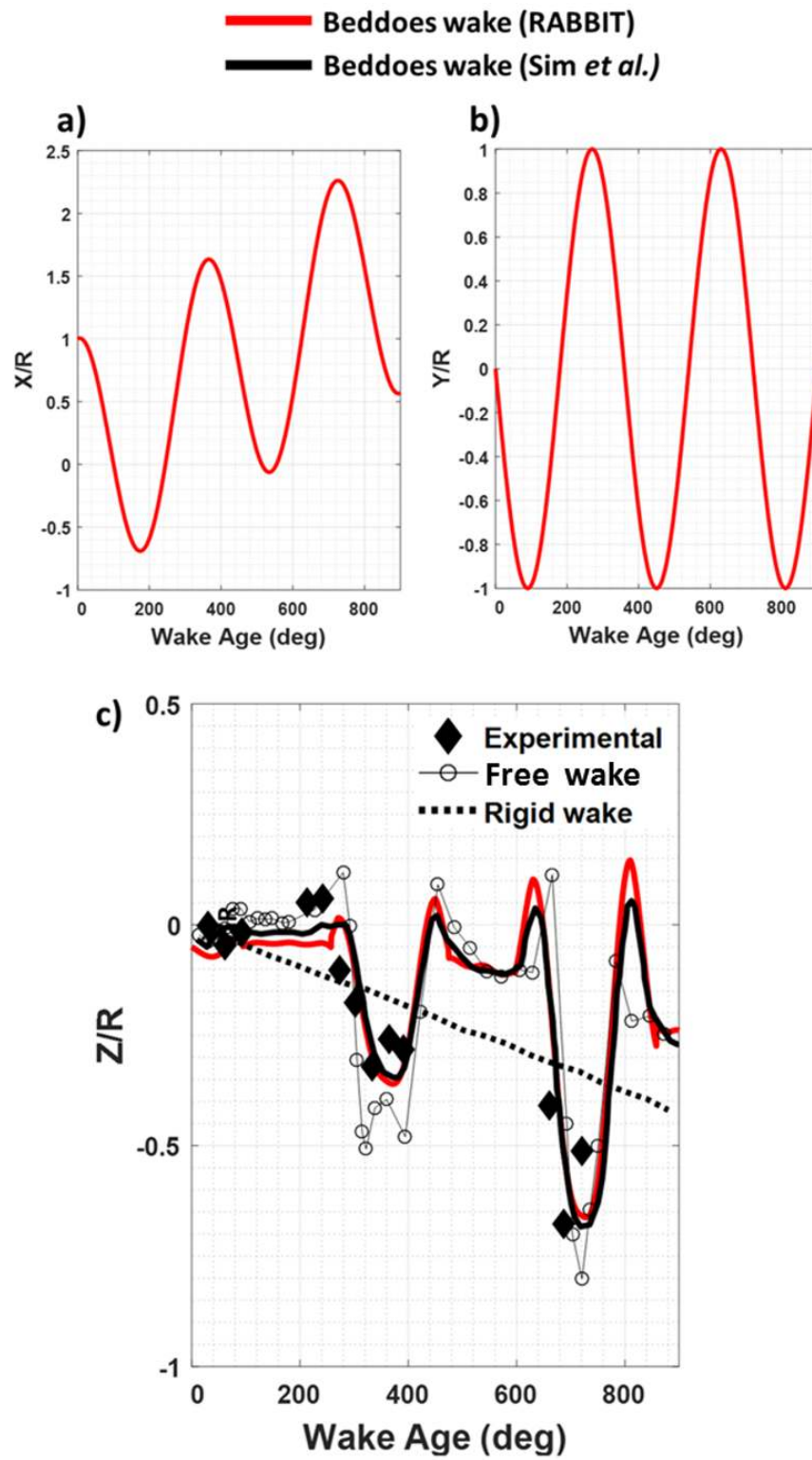


Figure 57. Rotor tip vortex wake displacement for a) X/R , b) Y/R , and c) Z/R .

Table 16. Operating conditions for single rotor case study.

Variable	Value	Units
R , Radius	3.28	ft
c , chord	0.328	ft
No. of blades	1	n/a
α_s , shaft angle	2.862	deg
Airfoils	NACA 0012	n/a
V_{tip} , tip speed	656.18	ft/s
χ_{TPP} , Skew angle	73.72	deg
Forward Velocity	65.68	ft/s
μ , Advance ratio	0.1000	n/a
μ_z , Rotor axial velocity ratio	0.0050	n/a
C_T , Thrust coefficient	0.0050	n/a

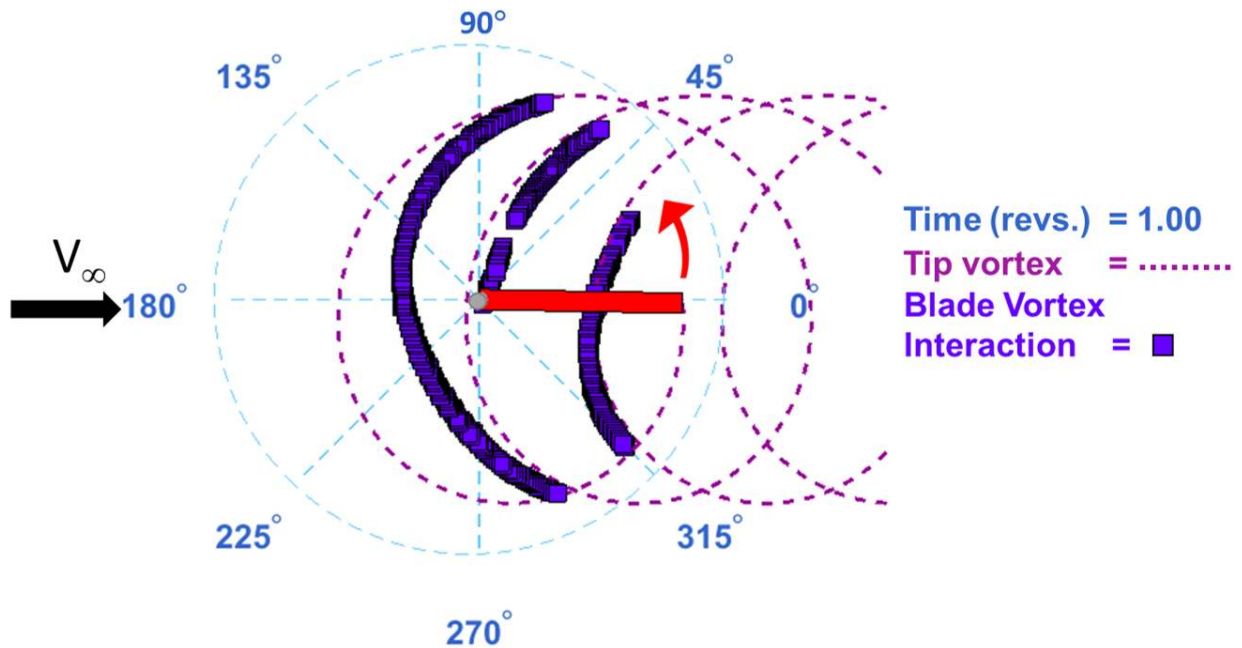


Figure 58. RABBIT output for single rotor case study.

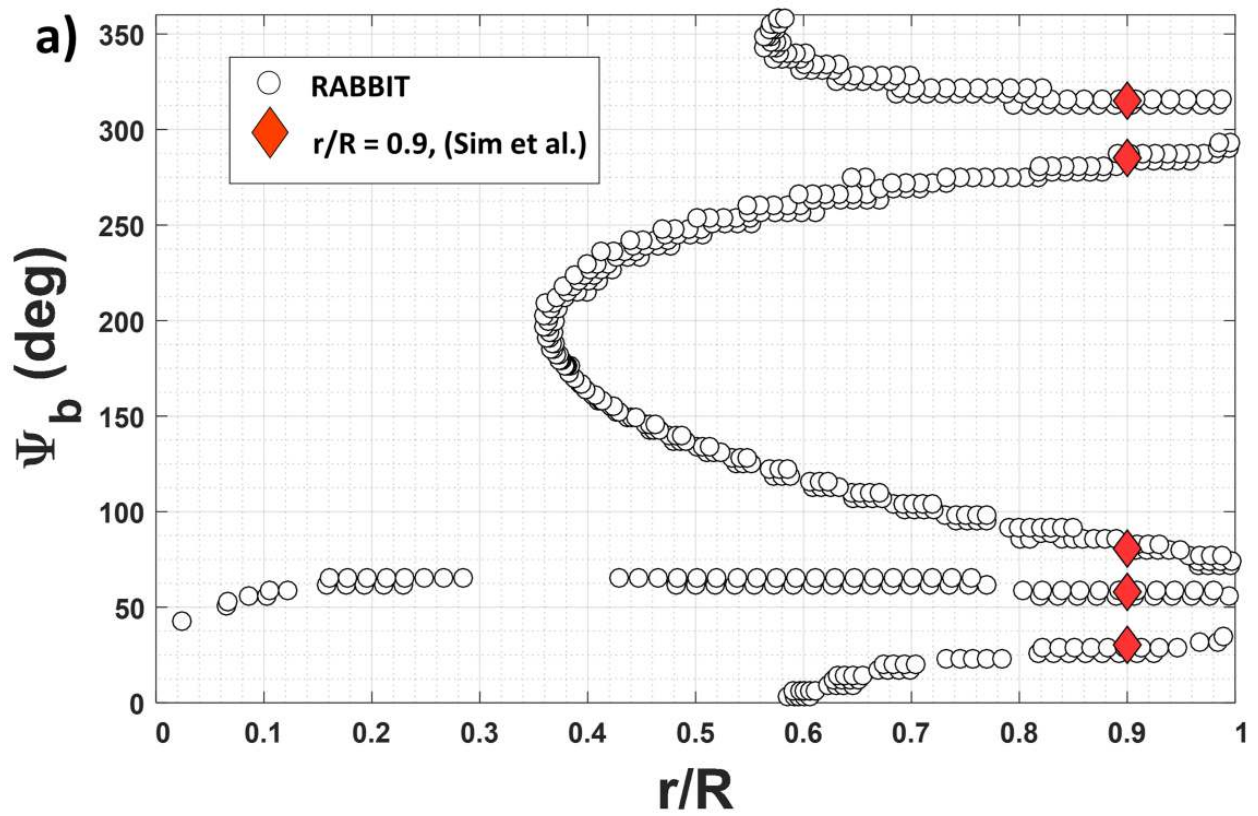


Figure 59. RABBIT and Sim et al. case study comparison of blade azimuth angle versus r/R locations.

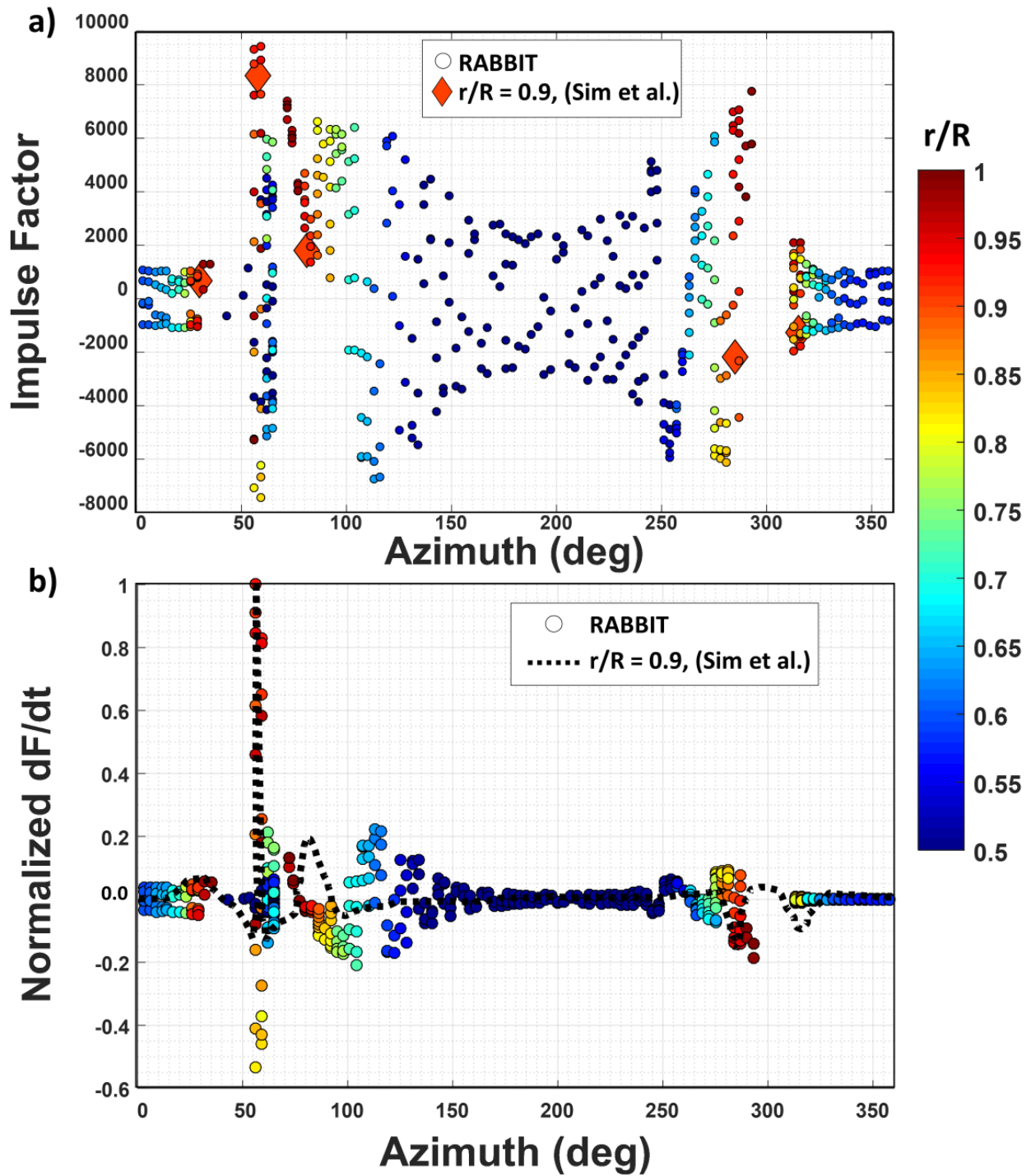


Figure 60. RABBIT and Sim et al. case study comparison of a) impulse factor versus azimuth angle, and b) normalized $\frac{\partial F}{\partial t}$ versus azimuth angle for r/R locations.

which the vortex hits the blade, and the miss distance is the vertical distance from the blade tip to the vortex. The product of the vortex strength factor ($\bar{\Gamma}$) and shape function (\bar{X}) are then used to calculate the time rate of change of loading ($\frac{\partial F}{\partial t}$); see equations 9 through 11 [65].

The impulse factor and $\frac{\partial F}{\partial t}$ normalized by maximum $\frac{\partial F}{\partial t}$ were calculated for the case study for all radial locations and shown in Figures 60 a) and b), respectively. For both the RABBIT and the Sim et al. calculations, the normalized $\frac{\partial F}{\partial t}$ resulted in the largest strength at 58° . RABBIT was able to calculate similar values for BVI locations at 30° , 58° , and 285° for $r/R = 0.90$ compared to Sim et al. but differed for BVI locations at 81° and 315° . Differences between the RABBIT and Sim et al. calculated impulse factor and normalized $\frac{\partial F}{\partial t}$ are due to differences in the Z/R wake (Fig. 57 c)) and vortex wake modeling, which directly influence the values of BVI angle and miss distance.

$$\bar{\Gamma} = \frac{V_b \cos \gamma}{h}, \quad (8)$$

$$\bar{\Gamma} = \frac{\Gamma}{2\pi h V_b} \quad (9)$$

$$\frac{\partial F}{\partial t} = (c_{l_\alpha} c) \left(\frac{1}{2} \rho V_b^2 \right) (\bar{\Gamma}) (\bar{X}) \frac{1 - \bar{X}^2}{(1 + \bar{X}^2)^2} \quad (10)$$

$$\text{where, } \bar{X} = \frac{V_b \cos(\gamma) t}{h} \quad (11)$$

5.4 Coaxial Rotor Blade Crossing and BVI Location Identification

RABBIT was validated against CAMRAD II [60] for a coaxial rotor by comparing an upper rotor tip vortex wake from each analysis, and comparing BVI locations and times with the lower rotor blades. RABBIT's Beddoes' wake model does not account for rotor-rotor wake interaction. CAMRAD II uses a nonuniform inflow free-wake geometry, different from the Beddoes' wake model, that accounts for rotor-rotor wake interaction. Only the upper tip vortex for the reference blade was modeled for simplicity.

A descent flight condition ($V_{tip} = 625$ ft/s, $\mu = 0.0867$, $C_T = 0.0025$, and $\alpha_S = 10.00^\circ$) for the modern design coaxial rotor was chosen to ensure a BVI location at the lower rotor. Figure 61 shows RABBIT's calculated blade crossing time and predicted BVI lower rotor location for upper reference blade one (U_{ref}) after one revolution.

RABBIT's capability to identify the location and time of a blade overlap was first validated against CAMRAD II. RABBIT and CAMRAD II predicted three distinct upper reference blade BVI instances with the lower rotor. Next, RABBIT's wake was compared to the wake from CAMRAD II for the same descent flight case. The wakes from each simulation were compared by overlaying the wakes and identifying possible BVIs. The two wakes are compared in Figure 62 at a time of 0.786 revolutions, where a BVI occurrence is identified at the lower rotor blade one with U_{ref} . The trajectory of the CAMRAD II tip vortex for the reference blade is compared to the RABBIT tip vortex for the same reference blade for each instance in time of a BVI occurrence, as shown in

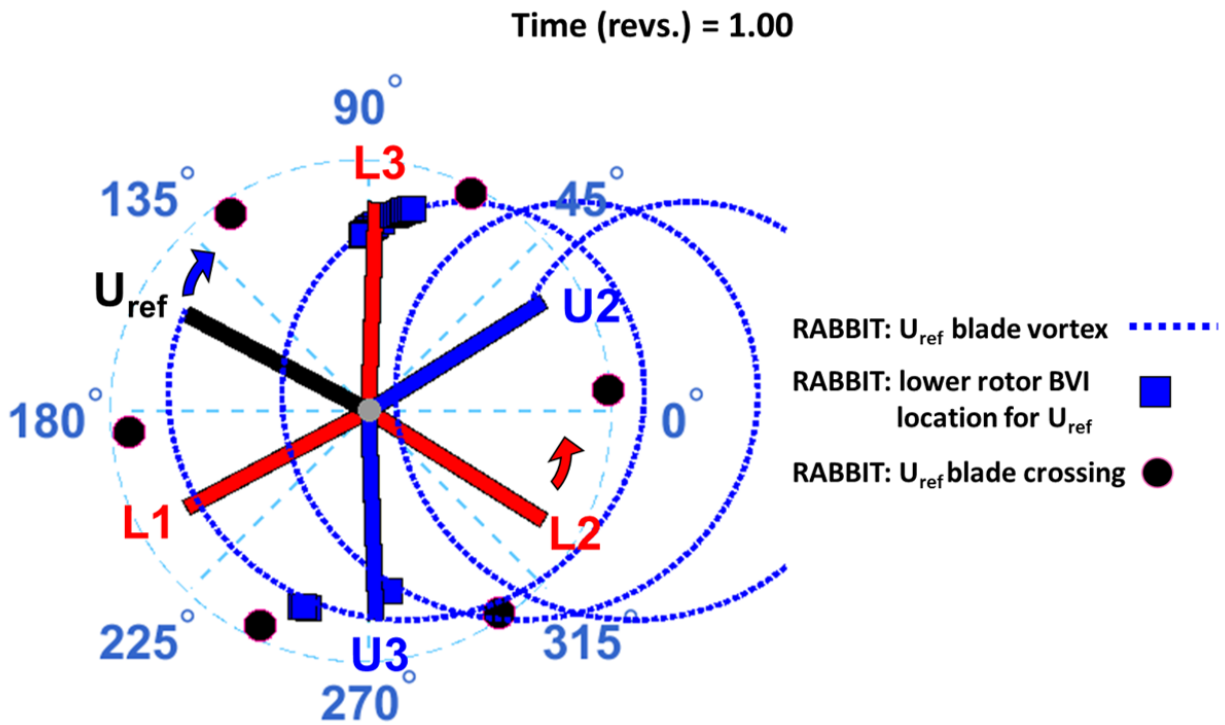


Figure 61. RABBIT blade crossing and lower rotor BVI predictions for a six-bladed (three upper/three lower) coaxial rotor ($V_{tip} = 625$ ft/s, $\mu = 0.0867$, $S = 2.0$ ft, $\chi_{TPP} = 89.6^\circ$, $C_T = 0.0025$, and $\alpha_S = 10.00^\circ$).

Figure 63. Although the wakes from RABBIT and CAMRAD II are different in shape, the location and time of all the BVI occurrences are the same. BVI location predictions for both RABBIT and CAMRAD II are at 91° , 250° , and 276° , at a span location greater than an r/R of 0.85. Because of the different shapes of the wakes, the values of BVI angle and miss distance are expected to vary slightly between RABBIT and CAMRAD II. The BVIs at 91° are the strongest, in terms of impulse factor and normalized $\frac{\partial F}{\partial t}$, compared to the BVIs at 250° and 276° , as shown in Figure 64. The BVI at 91° is the strongest because the interaction location is on the advancing side of the lower rotor, therefore the translating blade velocity is large compared to the BVI locations at 250° and 276° .

5.5 Summary

The computational tool RABBIT was developed to predict the time and location of blade crossings and the time, location, and interaction angle of BVIs. RABBIT's capabilities were validated using the Sim et al. case study for a single rotor with one blade. BVI location and strength were correctly predicted for the strongest BVI occurrence. CAMRAD II was used to validate RABBIT's blade crossing, and BVI location, time, and angle for a modern coaxial rotor.

6 Acoustic Prediction: Thickness and Loading Noise

The aerodynamics of a helicopter directly affect the aeroacoustics but lack information regarding time and radiation direction. Loads on a coaxial and single rotor in hover, along with thickness effects, were computed to study the time-varying acoustic pressure signature. The coaxial and single rotor acoustic signatures were compared for various observer locations to understand acoustic response differences.

The 2D loads computed in Chapter 3 were stacked to represent the spanwise loading of a rotor blade. A tip loss factor was introduced to account for zero loading at the tip of a 3D blade. The spanwise loading was then used as input to an acoustics solver to compute the noise at specified observer locations. Both thickness and loading noise were computed.

6.1 Aerodynamics Loads

OVERFLOW 2D results as shown in Chapter 3 (Fig. 39) were stacked together to represent the modern single rotor design in hover. A blade loading tip loss factor was applied to the loads for the single rotor and modern rotor design. Because of 3D flow effects, actual blade loading is zero at the tip [67]. The difference between blade element theory and actual loading on a rotor blade is shown in Figure 65. Prandtl's tip loss factor is directly applied to the calculated loads for each radial station as shown in equation 12.

$$F(r/R) = \frac{2}{\pi} \cos^{-1} \left(\exp \left(- \frac{N_b \sqrt{1 + \lambda^2}}{2 \lambda} (1 - r/R) \right) \right), \quad (12)$$

Figure 66 shows the aerodynamic loading for the modern single rotor design without tip loss (Figs. 66 a), b), and c)) and with a tip loss factor (Figs. 66 d), e), and f)). The total loss of lift from applying a tip loss factor must be added back to the total lift so that the overall lift remains the same [53]. The total lift difference with and without tip loss factor for the modern single rotor hover case is less than 0.50 percent in total F_Z . OVERFLOW 2D results for the modern coaxial rotor as shown in Chapter 3 (Fig. 40) are also stacked with an applied tip loss factor to the lift (see Fig. 67). The main difference between the modern single and coaxial rotor loading distribution is

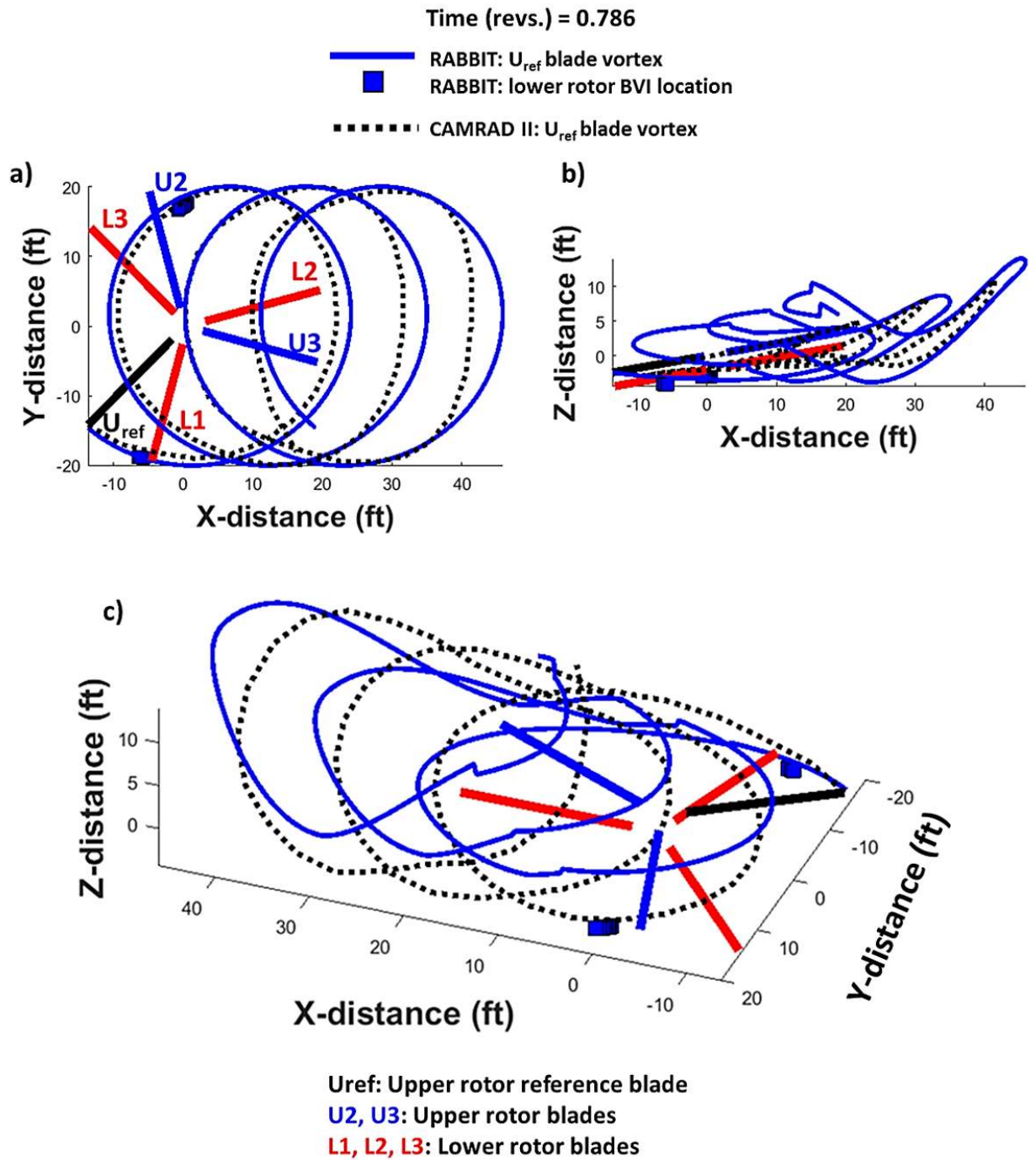


Figure 62. RABBIT versus CAMRAD II predictions for a six-bladed coaxial (three upper/three lower) rotor wake comparison at time of 0.786 revolutions (U_{ref}) ($V_{tip} = 625$ ft/s, $\mu = 0.0867$, $S = 2.0$ ft, $\chi_{TPP} = 89.6^\circ$, $C_T = 0.0025$, and $\alpha_S = 10.00^\circ$).

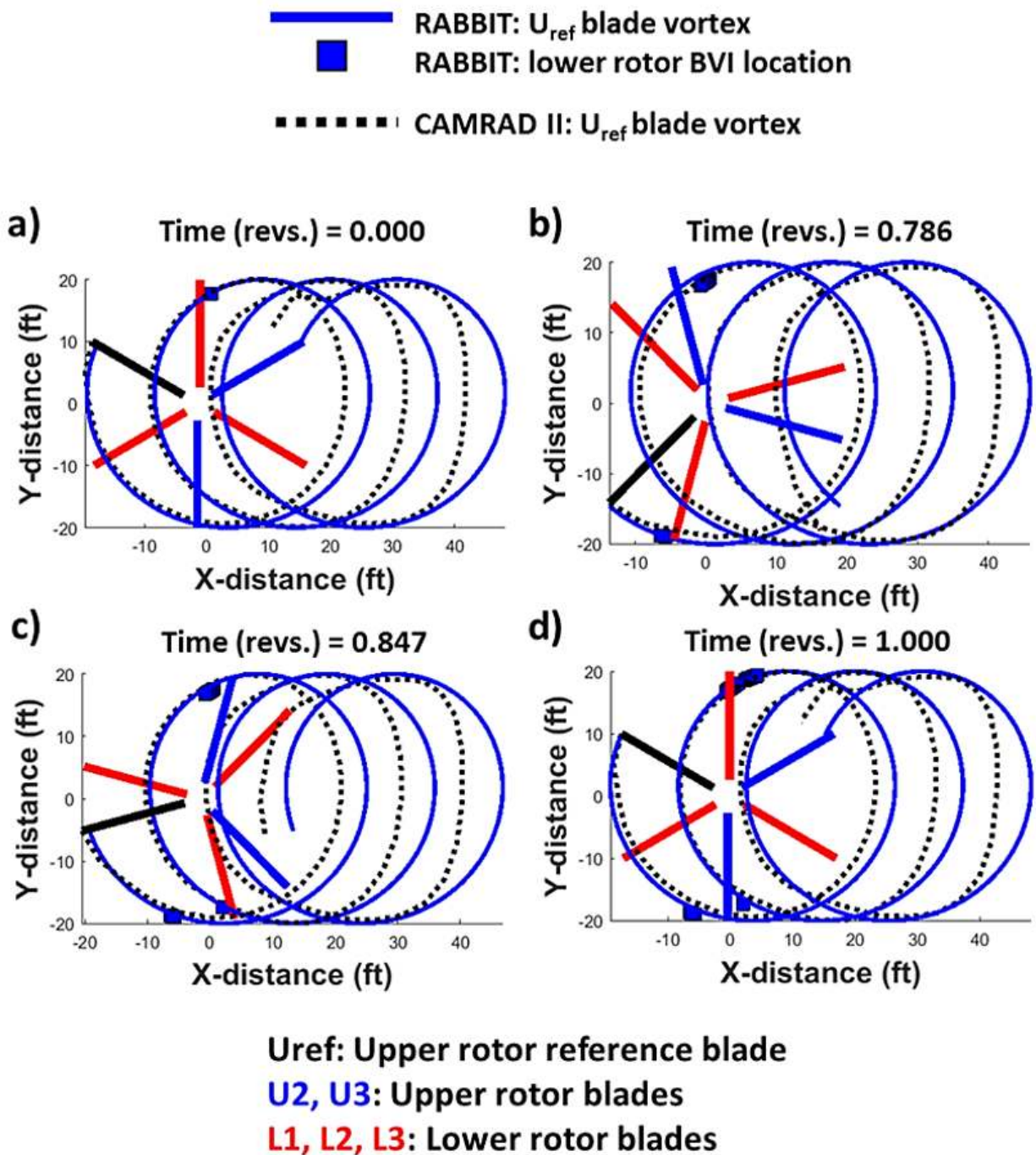


Figure 63. RABBIT versus CAMRAD II predictions for a six-bladed coaxial (three upper/three lower) rotor blade crossing time and BVI lower rotor locations for U_{ref} at time of a) 0.000, b) 0.786, c) 0.847, and d) 1.000 revolutions ($V_{tip} = 625$ ft/s, $\mu = 0.0867$, $S = 2.0$ ft, $\chi_{TPP} = 89.6^\circ$, $C_T = 0.0025$, and $\alpha_S = 10.00^\circ$).

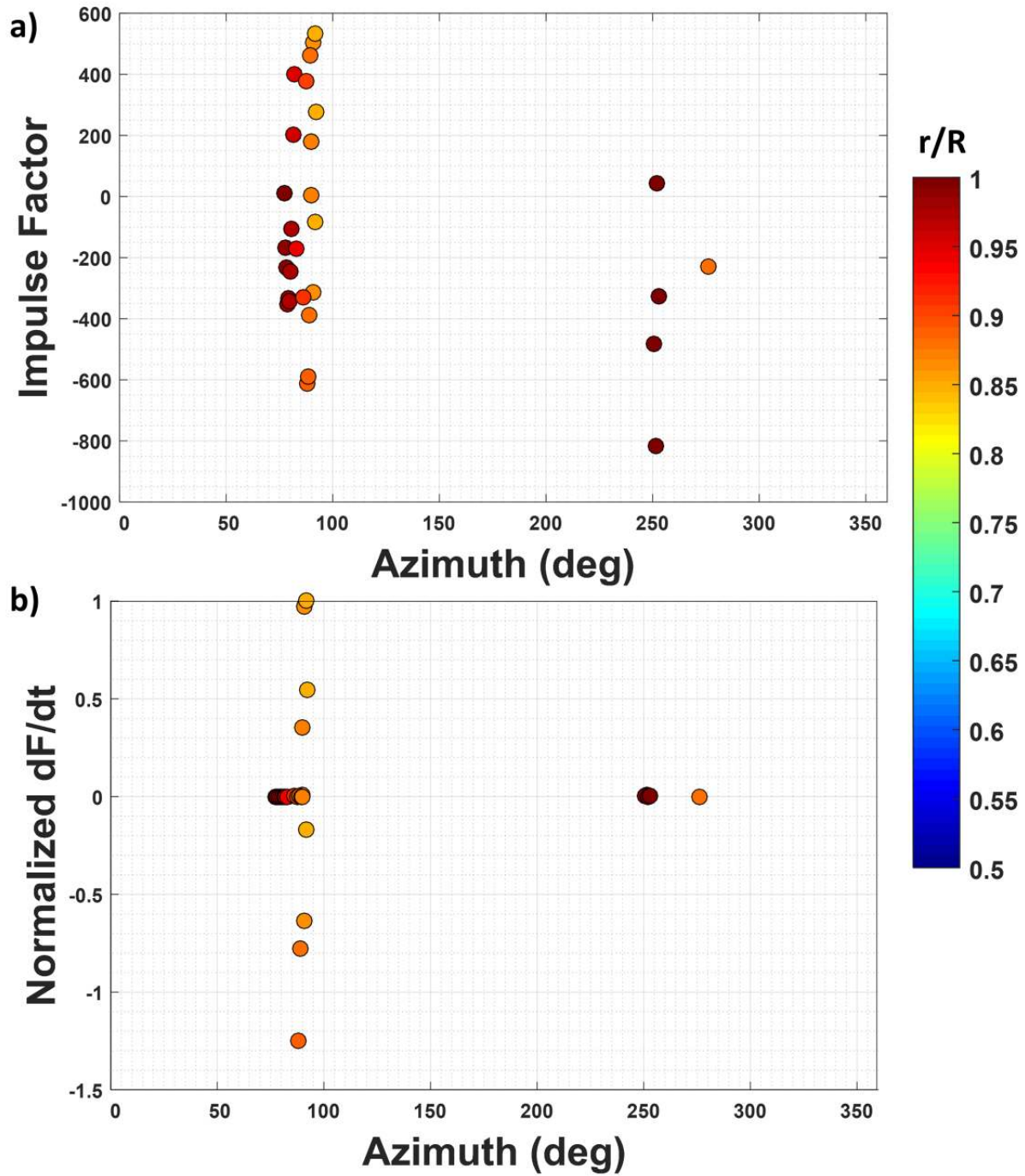


Figure 64. RABBIT modern coaxial lower rotor BVI predictions for U_{ref} for a) impulse factor versus azimuth angle, and b) normalized $\frac{\partial F}{\partial t}$ versus azimuth angle for r/R locations ($V_{tip} = 625$ ft/s, $\mu = 0.0867$, $S = 2.0$ ft, $\chi_{TPP} = 89.6^\circ$, $C_T = 0.0025$, and $\alpha_S = 10.00^\circ$).

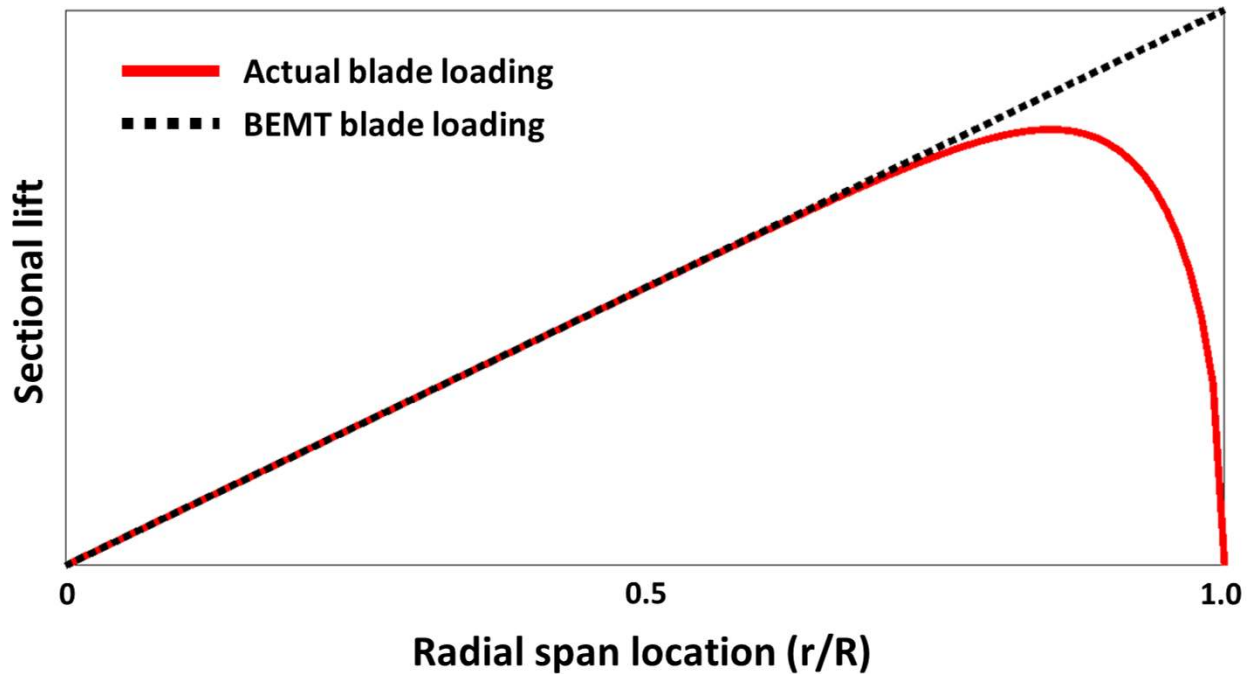


Figure 65. Rotor blade loading with and without tip loss.

the presence of pulses, due to blade overlap, for the modern coaxial rotor design. The increase and decrease in lift due to blade crossing can be seen at 45° , 105° , 165° , 225° , 285° , and 345° , which was predicted by RABBIT (Fig. 54).

6.2 Acoustic Predictions

The noise from the modern single and coaxial rotors was predicted using PSU-WOPWOP version 3.4.3 [50, 68]. The loads from the stacked OVERFLOW results shown in Figures 66 and 67 were used in the PSU-WOPWOP calculations to compute loading noise. Observers were placed around the rotor to understand differences in loading and thickness noise between a modern single and coaxial rotor. Differences in the acoustic pressure time history and overall sound pressure level (OASPL) are discussed.

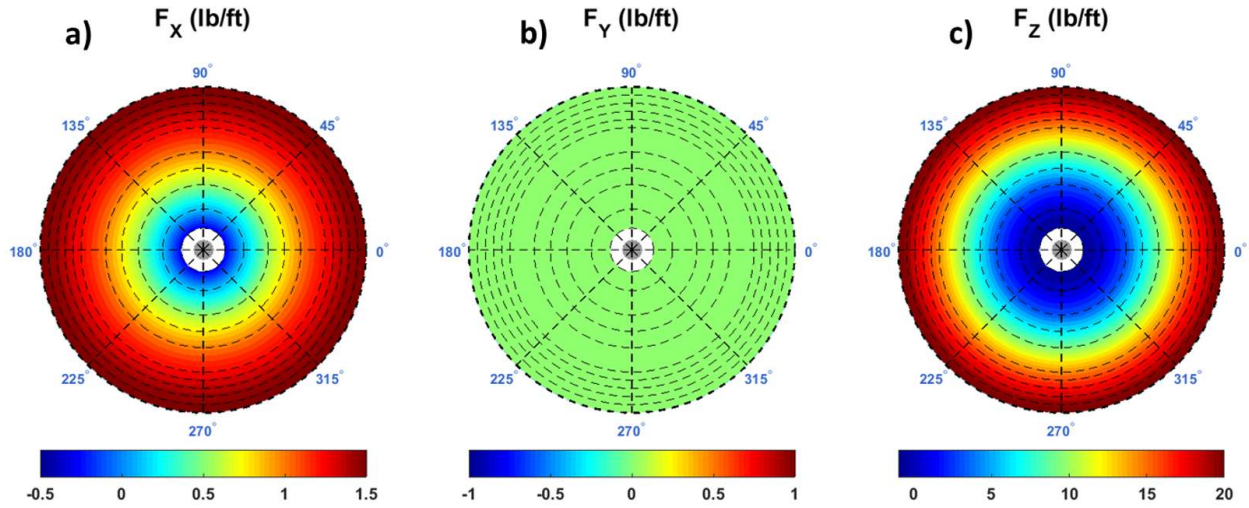
6.2.1 PSU-WOPWOP version 3.4.3

PSU-WOPWOP [50, 68] is a rotor noise prediction code that numerically solves Farassat's Formulation 1A of the Ffowcs Williams-Hawkings equation (see equations 4 through 6 in Chapter 2). Information regarding the rotor blade motion, blade surface geometry, and loading is needed to compute the acoustic pressure time history, along with the observer location. PSU-WOPWOP version 3.4.3 was used for all acoustic predictions in this study.

6.2.2 Observer locations

Multiple observers were placed around the modern single and coaxial rotor, where the origin was at the center of the hub for the modern single rotor and at the midpoint between the two rotors for the modern coaxial rotor. Observers were placed three rotor radii away at elevation angles

Without tip loss



With tip loss

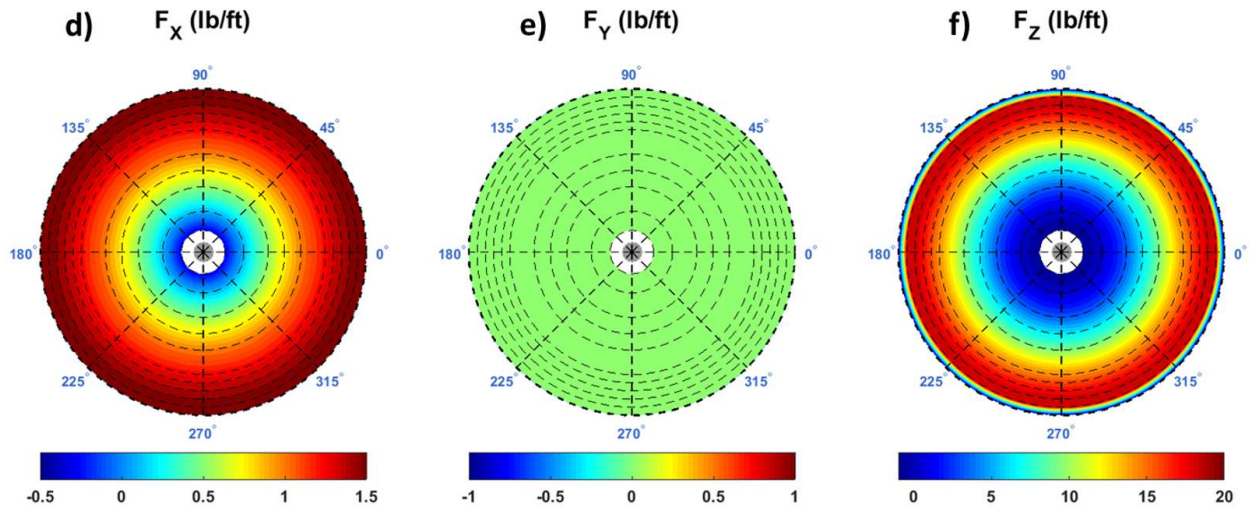


Figure 66. Stacked 2D OVERFLOW results for modern single rotor in hover without tip loss: a) F_X , b) F_Y , and c) F_Z , and with tip loss d) F_X , e) F_Y , and f) F_Z .

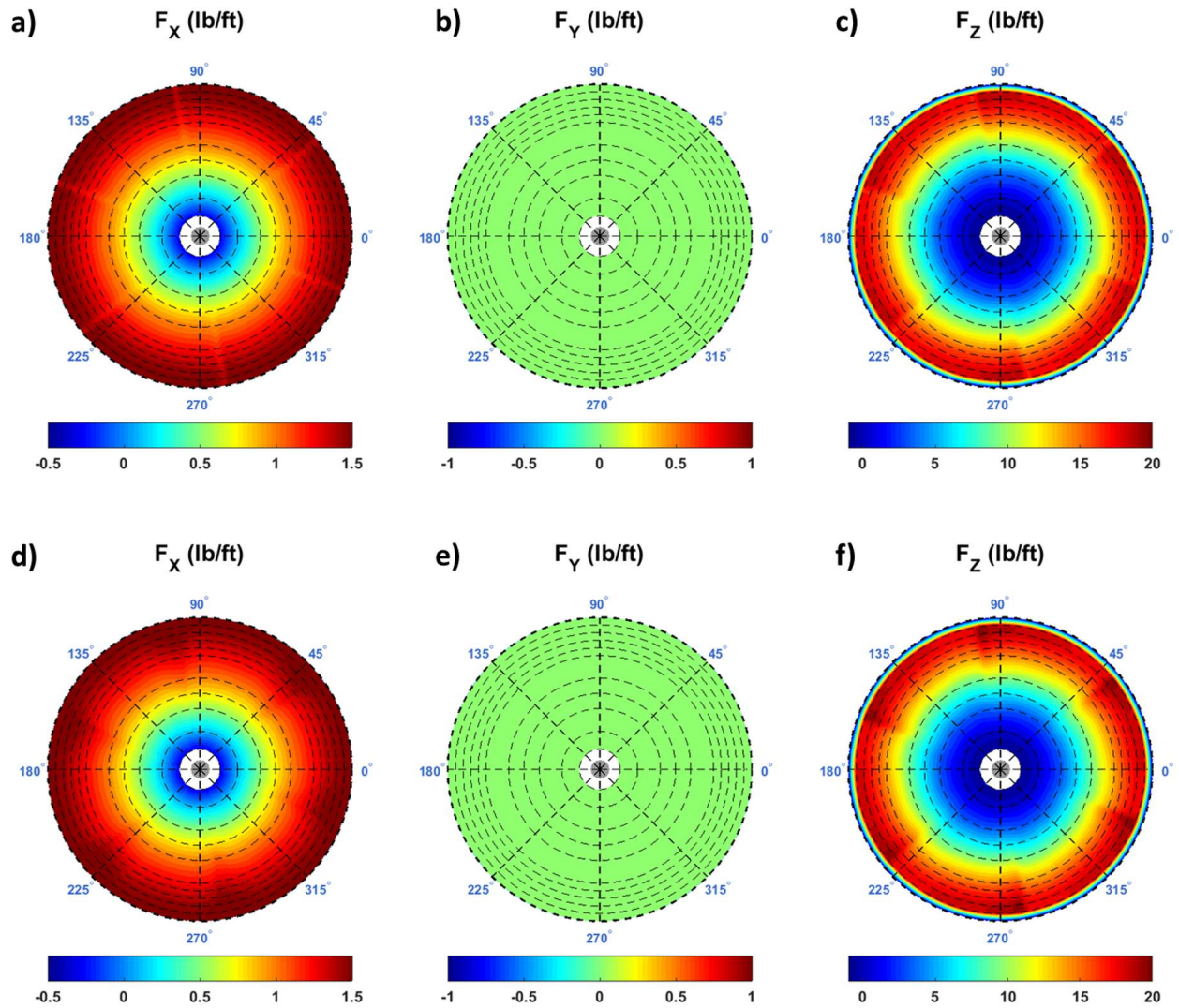


Figure 67. Stacked 2D OVERFLOW results for modern coaxial rotor in hover: upper rotor a) F_X , b) F_Y , and c) F_Z , and lower rotor d) F_X , e) F_Y , and f) F_Z .

Table 17. Modern single and coaxial rotor observer locations.

Observer #	X/R	Y/R	Z/R	Distance (Radii)	Directivity (deg)	Perspective
1	2.90	0.00	0.75	3.00	15	elevation
2	3.00	0.00	0.00	3.00	0	elevation
3	2.90	0.00	-0.75	3.00	-15	elevation
4	2.12	0.00	-2.12	3.00	-45	elevation
5	0.00	0.00	-3.00	3.00	-90	elevation
6	0.00	3.00	0.00	3.00	90	azimuth
7	2.12	2.12	0.00	3.00	45	azimuth
8	3.00	0.00	0.00	3.00	0	azimuth
9	2.12	-2.12	0.00	3.00	-45	azimuth
10	0.00	-3.00	0.00	3.00	-90	azimuth

of 15° , 0° , -15° , -45° , and -90° and azimuthal angles of 90° , 45° , 0° , -45° , and -90° (Table 17). Observers placed in-plane or near in-plane of the rotor are intended to capture thickness effects, while observers below the rotor are intended to capture the dominating loading noise. Observers 2 and 8 are directly in-plane of the rotor where thickness noise dominates, while observer 5 is directly below the rotor where loading noise dominates. General thickness and loading noise directivity are illustrated in Figure 68.

Loading (lift) noise dominates in the plane of the lift for the rotors, therefore loading noise is highest directly above and below the rotor because of the lifting force vector pointing in the direction of the observer location. Thickness noise (from drag) is highest in front of the rotor because of the motion of the blade, which is in the same plane as the drag force.

6.2.3 Modern single rotor acoustic predictions

For the modern single rotor in hover, acoustic pressure time histories and frequency spectra for the elevation observers (1 through 5) are shown in Figures 69 and 70, respectively. Acoustic pressure time histories and frequency spectra for the azimuthal observers (6 through 10) are shown in Figures 71 and 72, respectively.

Observers 1 through 5, at elevation angles of 15° to -90° , show thickness noise in front of the rotor between elevation angles of 15° to -15° (Figs. 69 a), b), and c) and Figs. 70 a), b), and c)). Note that the scale for thickness noise in Figures 69 and 70 is much smaller than the scale for loading noise. The three pulses in the thickness noise are due to the three blades. In Figures 71 and 72, observers 6 through 10 are placed in the plane of the rotor from 90° to -90° . Thickness noise OASPL (76.7 dB) is the same at observers 6 through 10, but the location of the blade pulses is shifted because of the different arrival times. Loading noise is highest when the observer is directly below the rotor (an elevation of -90° ; Figs. 69 e) and 70 e)).

6.2.4 Modern coaxial rotor acoustic predictions

Acoustic pressure time histories and frequency spectra predictions for the modern coaxial rotor in hover are shown in Figures 73 and 74, respectively, for observers 1 through 5 for elevation angles of 15° , 0° , -15° , -45° , and -90° , respectively. Figures 75 and 76 show corresponding results for observers 6 through 10 for azimuthal angles of 90° , 45° , 0° , -45° , and -90° , respectively.

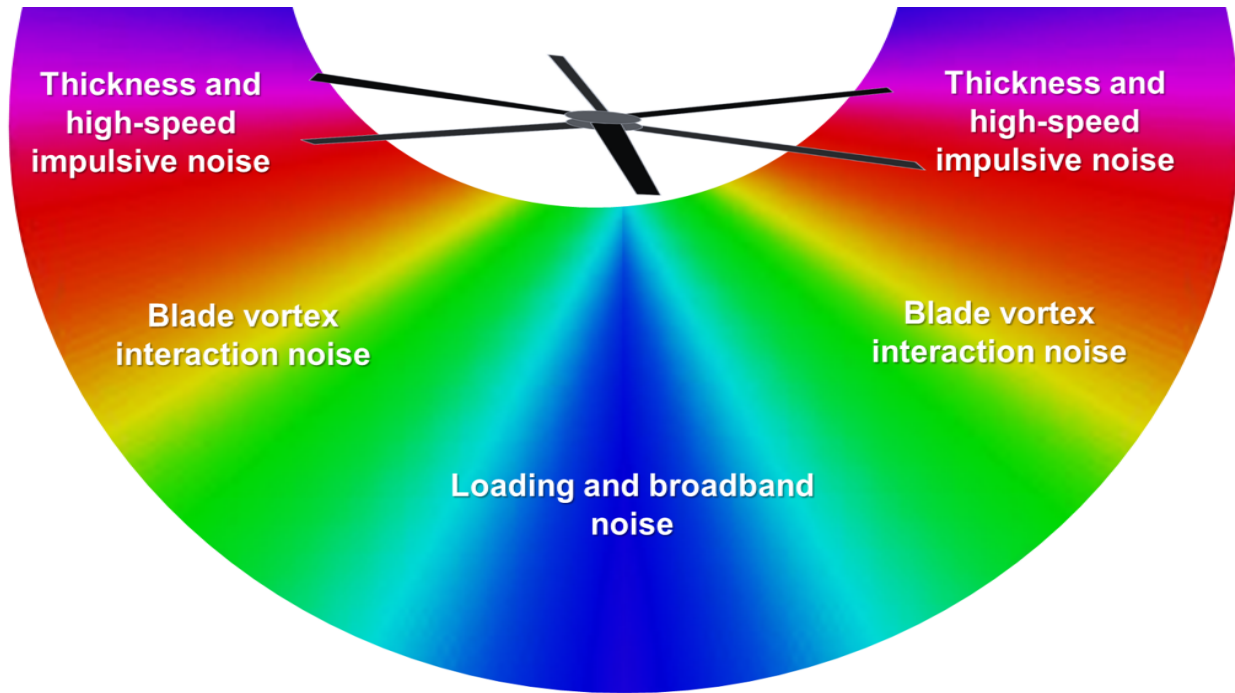


Figure 68. Rotor source noise directivity.

Figure 73 shows thickness noise in front of the rotor from an elevation angle of 15° to -15° . Only three pulses are shown in Figures 73 a) and b) because of the phase of the blades and observer location; in this case the noise from an upper and lower rotor blade arrives at observers 1 through 3 at the same time. For in-plane observers 6 through 10, Figure 75 a) shows six distinct pulses in the thickness noise prediction, whereas in Figure 75 c) only three pulses are shown because of the phase of the blades and observer location.

Loading noise for the modern coaxial rotor is largest directly below the rotor (Figs. 73 e) and 74 e)), similar to the single rotor. The effect on loading noise due to blade overlap is shown in Figure 73 e), where six large pulses are shown at 45° , 105° , 165° , 225° , 285° , and 345° .

6.2.5 Modern single versus coaxial rotor acoustic predictions

For the modern single and coaxial rotor, thickness, loading, and total noise in terms of OASPL (dB) are shown in Table 18, along with the differences for observers 1 through 10. Thickness, loading, and total acoustic time histories are compared between the modern single and coaxial rotor design in Figures 77 through 79.

For thickness noise, the modern coaxial rotor has a higher OASPL for all observers compared to the modern single rotor. As shown in Figures 77 a), b), c), d), and h), the pulses for the modern coaxial rotor are larger than the pulses for the modern single rotor. At observer locations 1, 2, 3, 4, and 8 (Figs. 77 a), b), c), d), and h)), the arrival times for the upper and lower rotor blades are the same, and coincide with the same arrival times as the single rotor blades. For these specific locations, the upper and lower rotor blades are added together. When the arrival times of the upper and lower rotor blades for the modern coaxial rotor do not coincide, six distinct pulses are shown in Figures 77 f), g), i), and j) for observers 6, 7, 9, and 10. The location of observer 5

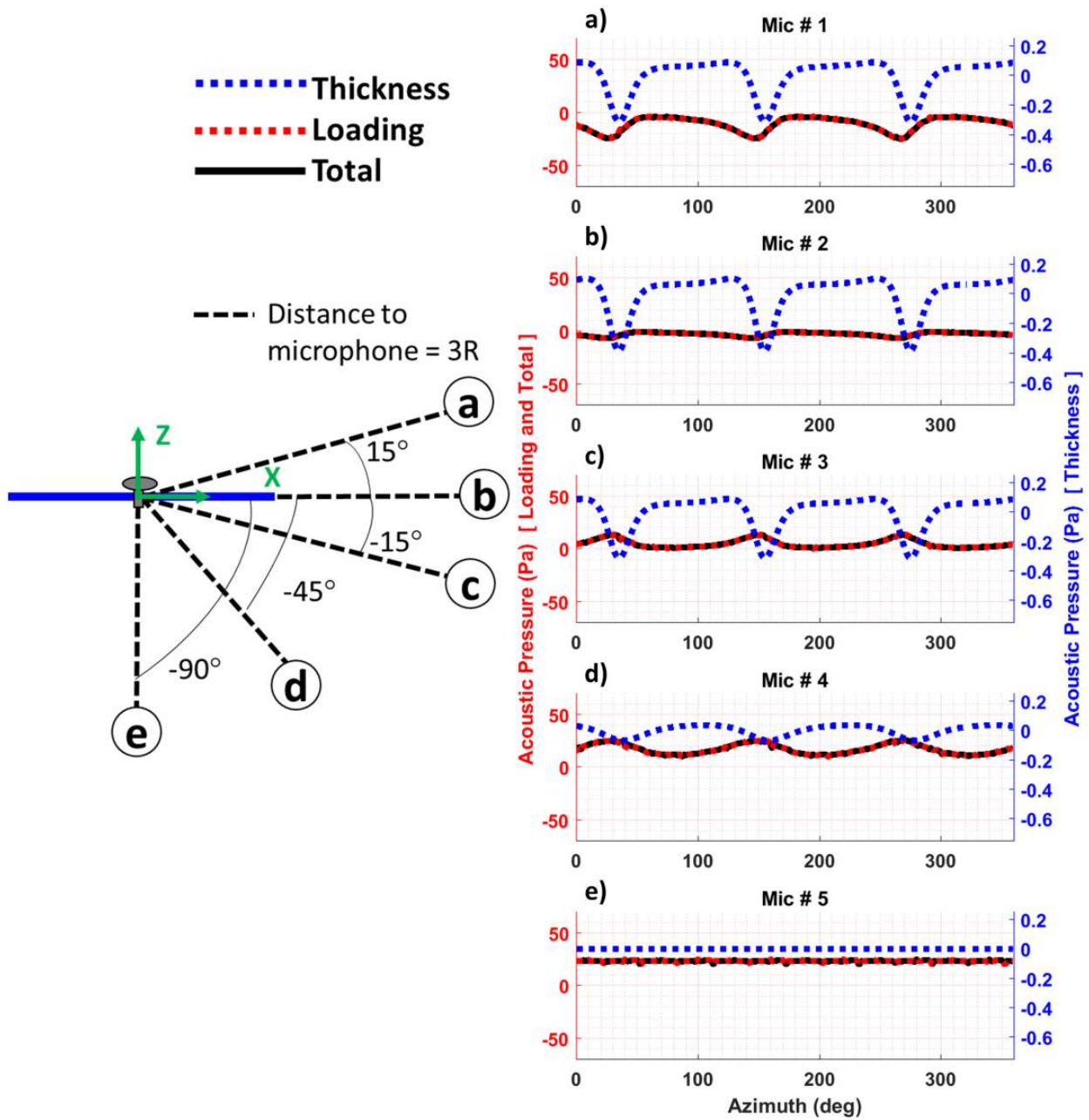


Figure 69. Elevation acoustic directivity in hover for modern single rotor acoustic pressure time history. Loading and total noise, left (red) y-axis; thickness noise, right (blue) y-axis.

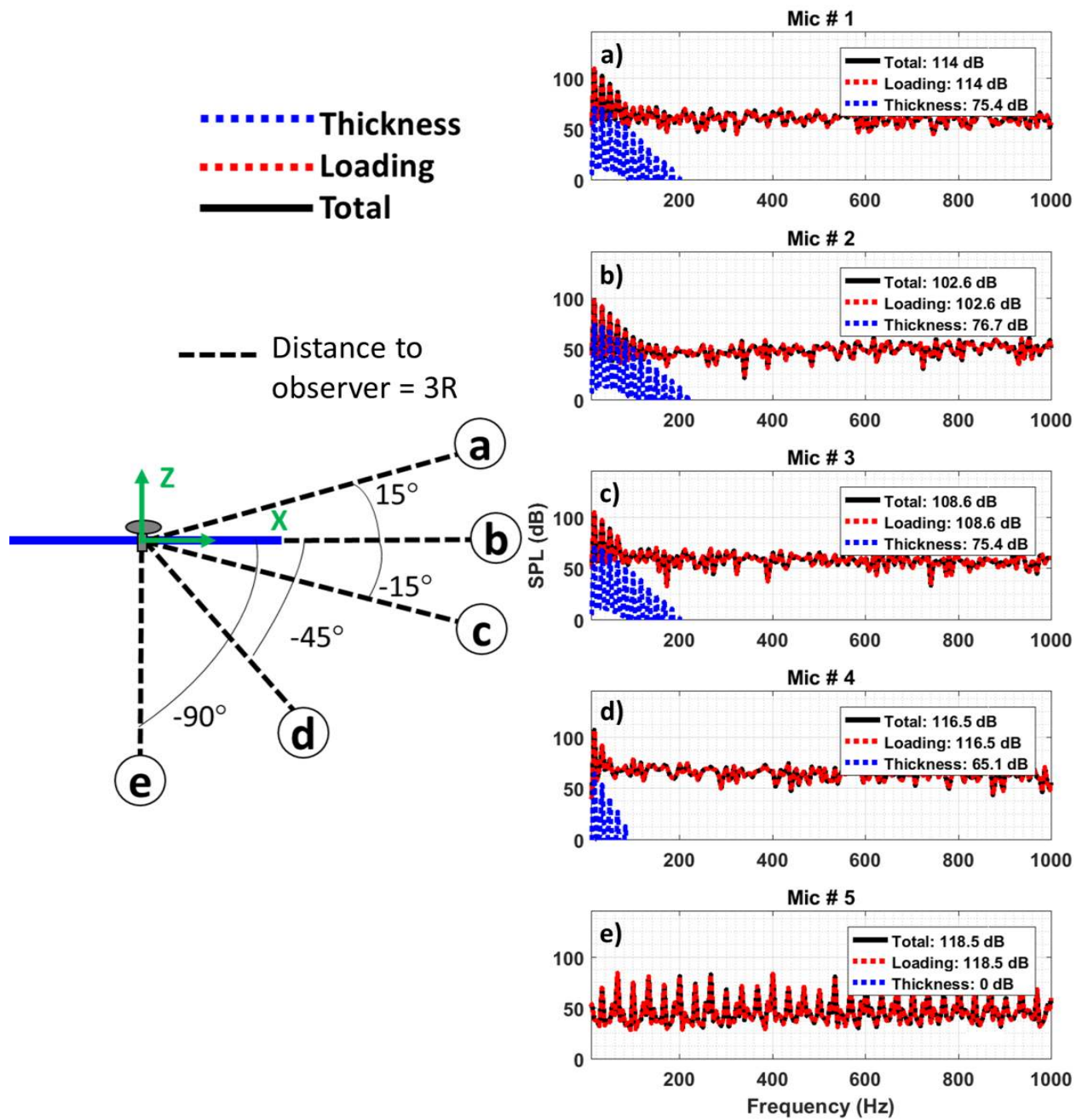


Figure 70. Elevation acoustic directivity in hover for modern single rotor frequency spectrum.

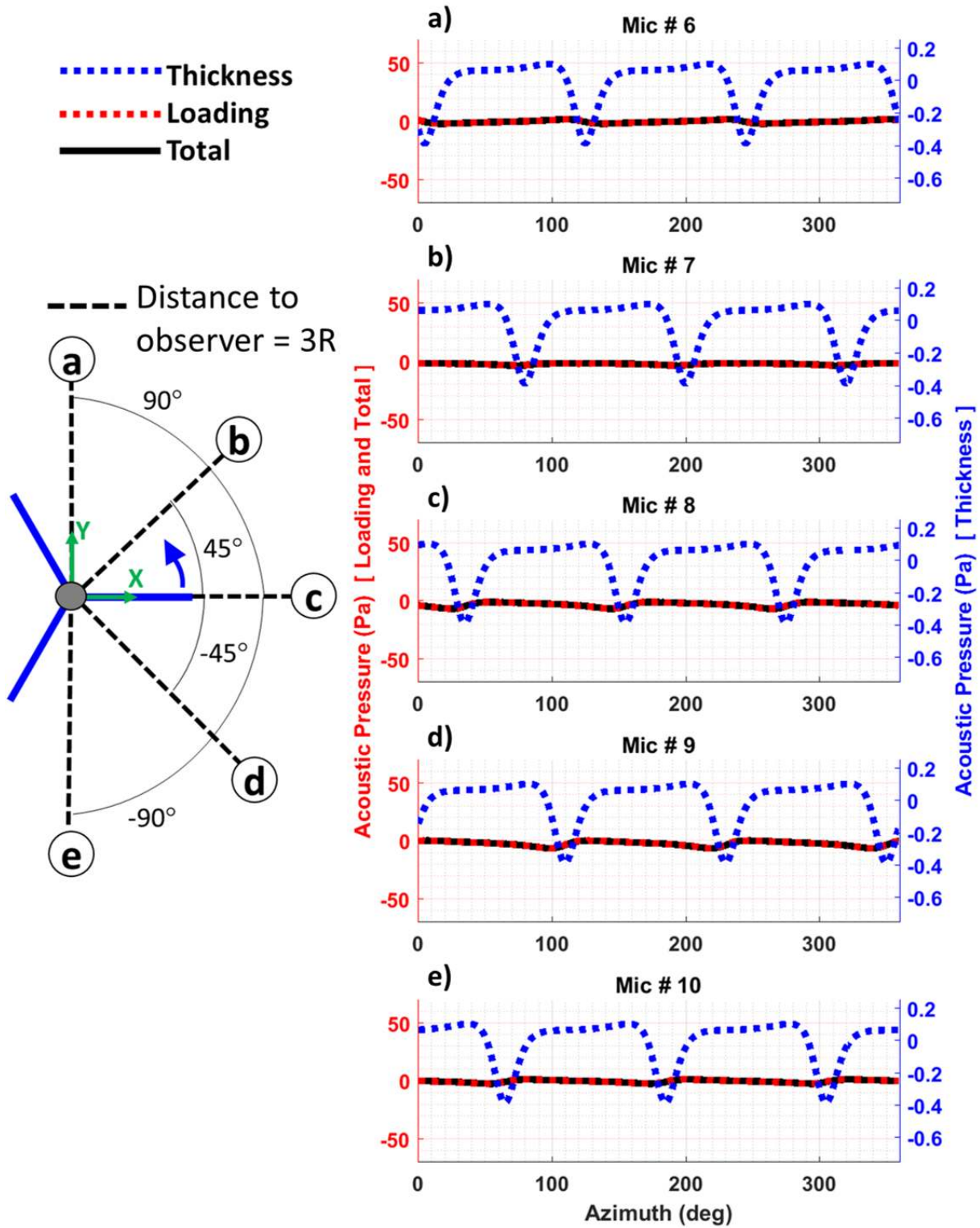


Figure 71. Azimuthal acoustic directivity in hover for modern single rotor acoustic pressure time history. Loading and total noise, left (red) y-axis; thickness noise, right (blue) y-axis.

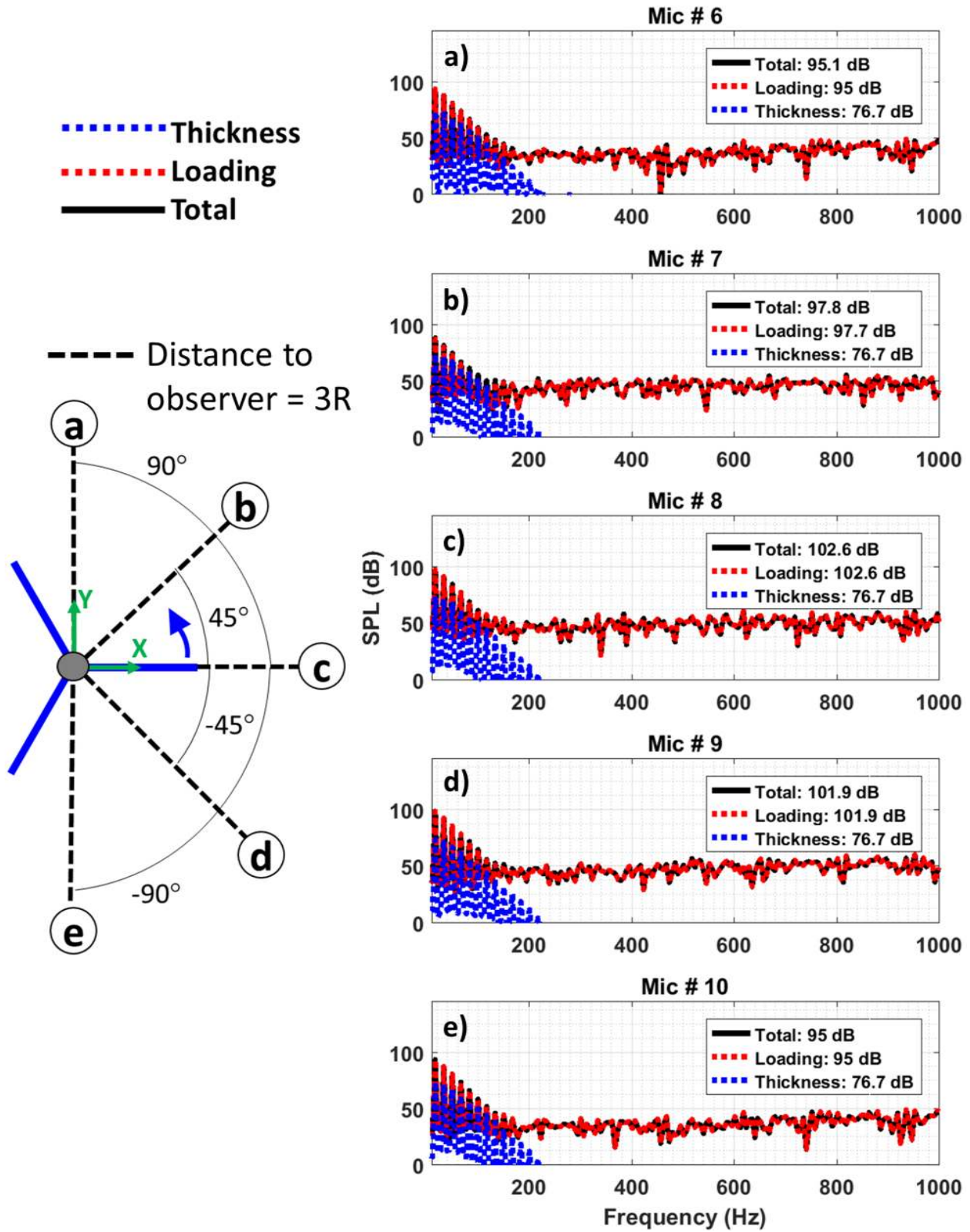


Figure 72. Azimuthal acoustic directivity in hover for modern single rotor frequency spectrum.

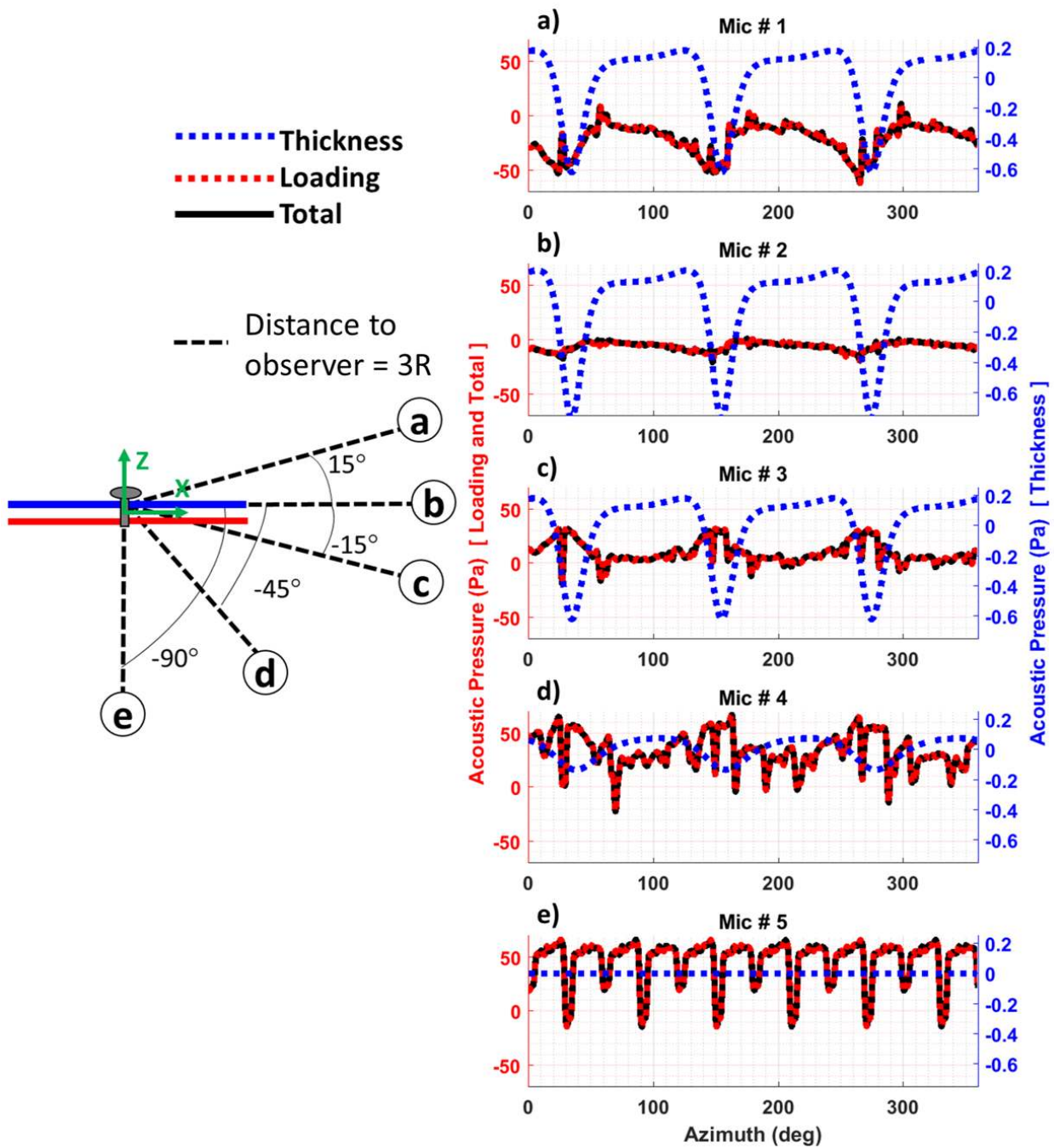


Figure 73. Elevation acoustic directivity in hover for modern coaxial rotor acoustic pressure time history. Loading and total noise, left (red) y-axis; thickness noise, right (blue) y-axis.

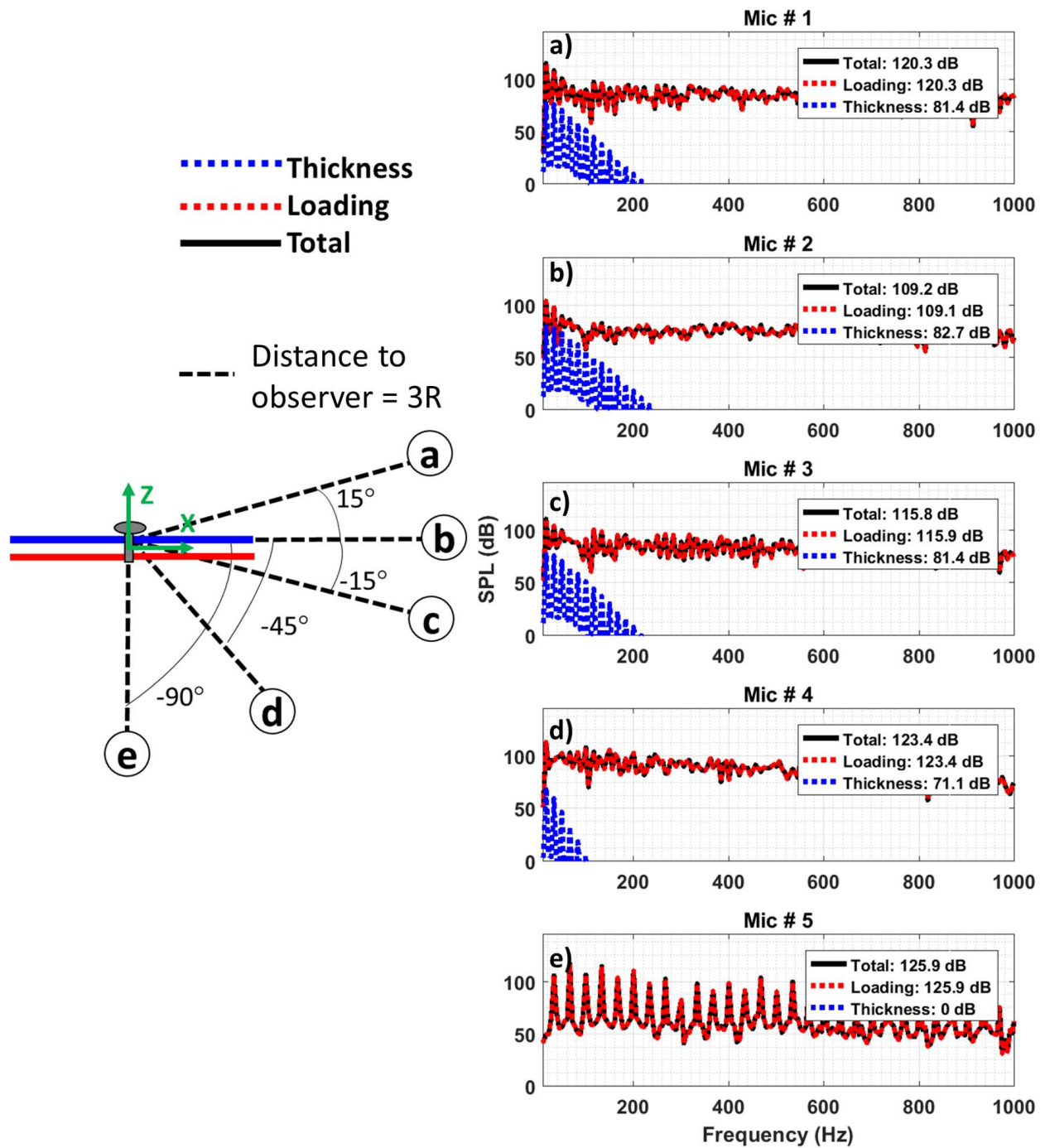


Figure 74. Elevation acoustic directivity in hover for modern coaxial rotor frequency spectrum.

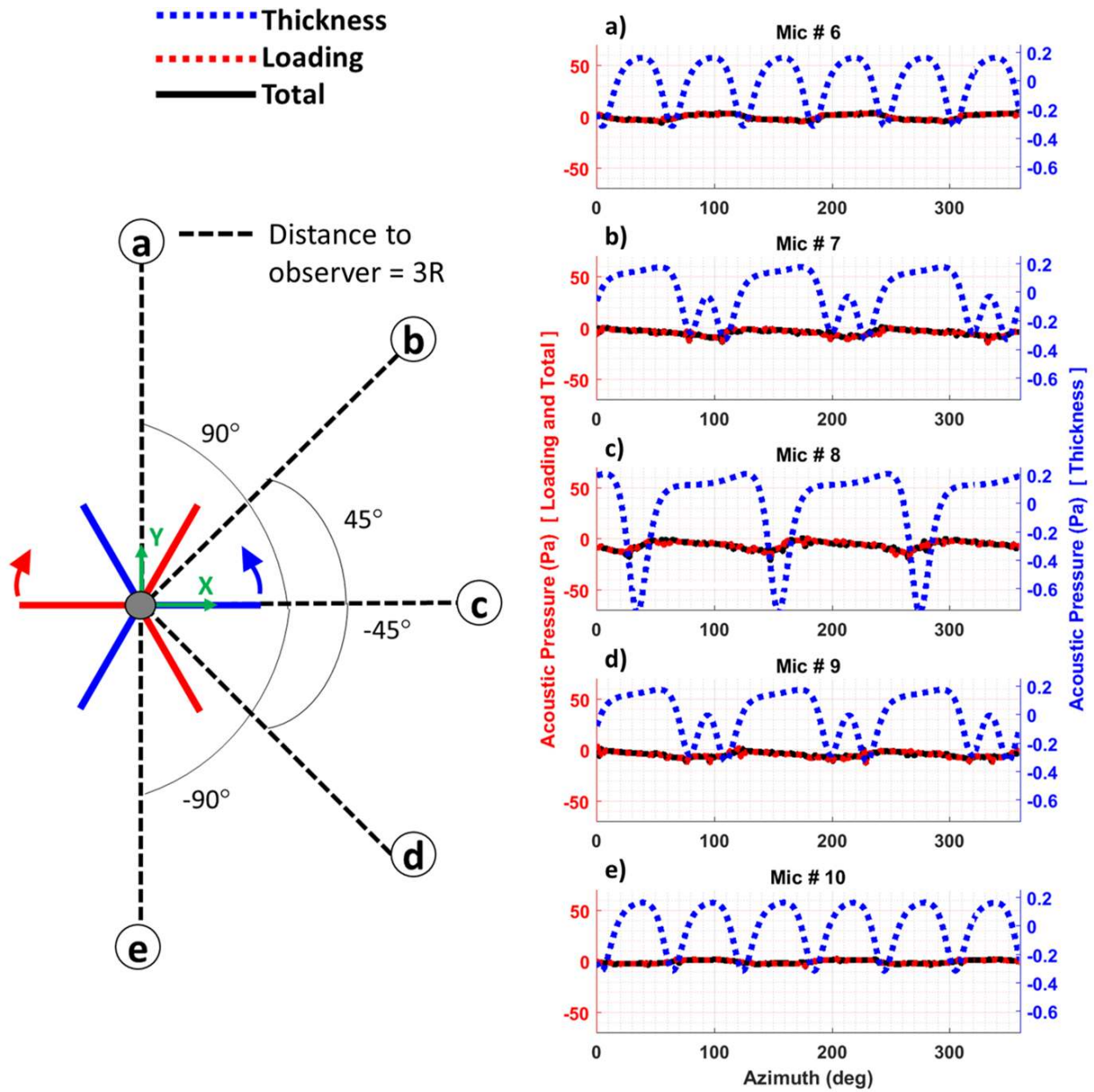


Figure 75. Azimuthal acoustic directivity in hover for modern coaxial rotor acoustic pressure time history. Loading and total noise, left (red) y-axis; thickness noise, right (blue) y-axis.

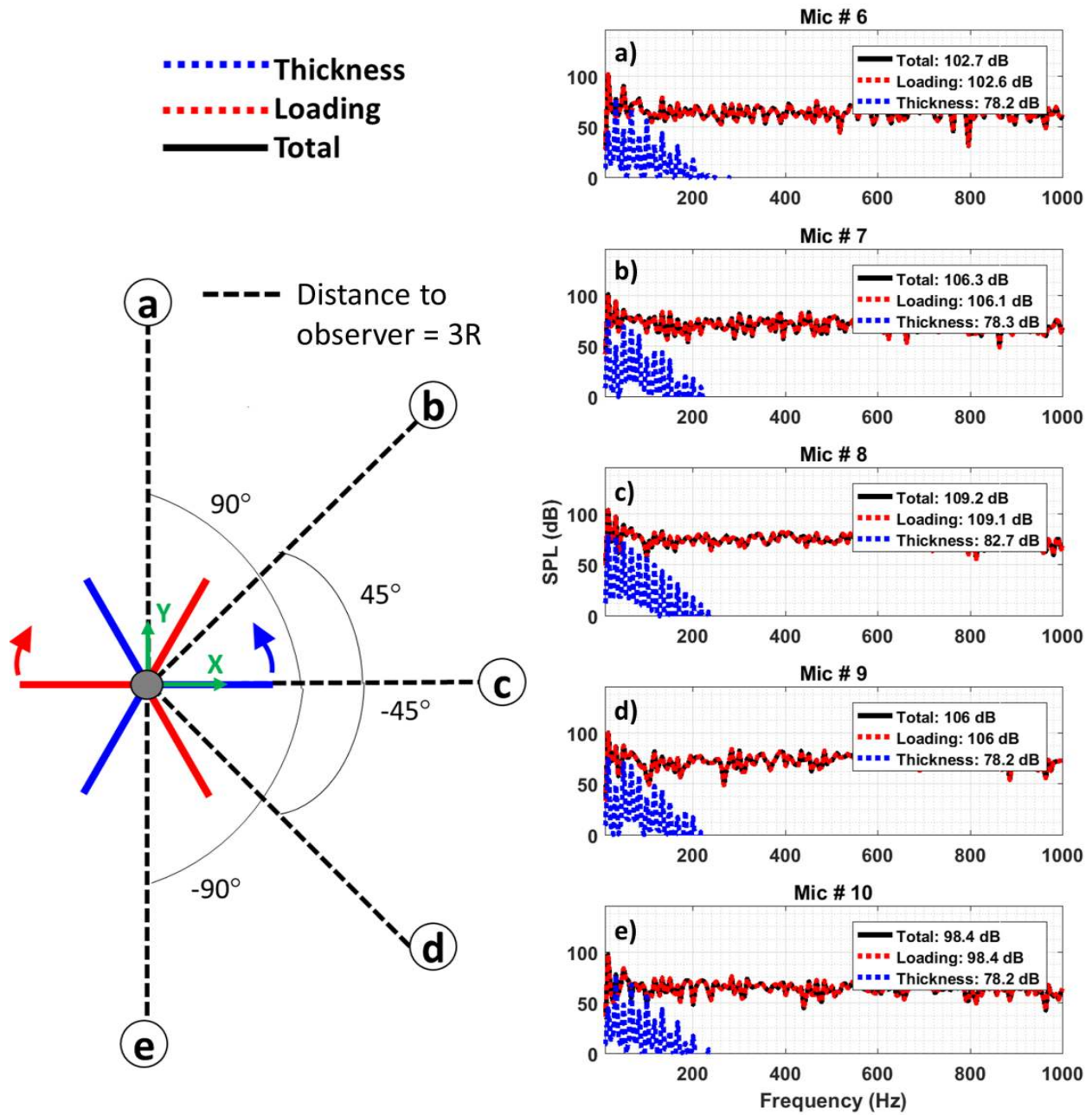


Figure 76. Azimuthal acoustic directivity in hover for modern coaxial rotor frequency spectrum.

(Fig. 77 e)) directly below the rotor results in no thickness noise. Observers 2 and 8 are collocated and experience the highest thickness noise OASPL.

Loading noise for the modern coaxial rotor is also higher compared to the modern single rotor. Comparing the modern single and coaxial rotor loading calculations, a clear difference between the two is shown in Figure 78 e) for observer 5. Observer 5, directly beneath the rotor, has the highest loading noise OASPL. The effect of blade overlap for the modern coaxial rotor compared to the modern single rotor is also evident in Figure 78 e). The additional pulses in the modern coaxial rotor acoustic loading time history are a direct result of blade overlap (Figs. 67 a) and d)).

Comparing the total noise for this particular configuration of a modern single and coaxial rotor resulted in a higher OASPL for all observers for the modern coaxial rotor. Increased OASPL for the modern coaxial rotor is due to the additional rotor, which results in additional aerodynamic effects for blade crossing occurrences.

6.3 Summary

Acoustic predictions for a modern single and coaxial rotor were performed using PSU-WOPWOP version 3.4.3. Adjusted for tip loss, blade aerodynamic loads constructed from stacked 2D OVERFLOW results were used to predict loading noise, while the geometry of the blades and blade motion were used for thickness noise calculations. Observers were placed around the modern single and coaxial rotor to capture thickness and loading noise effects. Overall noise was higher for the coaxial rotor compared to the single rotor for this particular configuration. Effects of the blade crossing occurrences in the loading time history were manifested in the loading noise of the coaxial rotor. For this configuration, loading noise calculations dominated compared to thickness noise calculations for the modern single and coaxial rotor.

7 Conclusions

Aerodynamic performance and aerodynamic noise sources of a coaxial, contra-rotating rotor (CACR) system in hover and edgewise flight were studied using various new and existing computational tools. The main aerodynamic difference between the single and coaxial rotor is the rotor wake interference, which has a larger influence on loading noise than on other noise sources. Having two rotors introduces two independent acoustic signals from two independent sources, which contributes to thickness noise. BVI is more complex because of the tip vortex from the upper rotor interacting with the lower rotor blades, providing more opportunities for BVI to occur. HSI noise can be avoided by slowing the rotor or flying at lower speeds in forward flight to avoid transonic flow on the rotors, but possible shock-shock interaction could occur between upper and lower rotor blades. Broadband noise was not explored, because of its expected minimal contribution to the overall sound.

Specific aerodynamic phenomena of coaxial rotors are identified along with their associated type of rotor source noise. Contributing design parameters and flight conditions are also discussed. Conclusions from this study are provided below.

- 2D potential flow simulations of two airfoils, separated vertically and traveling in opposite directions, were used to understand the aerodynamics of coaxial rotor blades before and after a blade crossing overlap. The lift of the upper and lower airfoil increases before overlap and decreases after overlap. The increase in lift of the upper airfoil is due to an increase in angle of attack caused by the upwash from the lower airfoil, while the angle of attack of the lower

Table 18. Modern coaxial and single rotor noise sources and differences for observers 1 through 10.

Thickness noise (dB)			
Observer	Coaxial rotor	Single rotor	Difference
1	81.39	75.37	6.02
2	82.72	76.71	6.01
3	81.37	75.37	6.00
4	71.11	65.11	6.00
5	0.00	0.00	0.00
6	78.23	76.72	1.51
7	78.31	76.72	1.59
8	82.72	76.71	6.01
9	78.23	76.72	1.51
10	78.23	76.71	1.52
Loading noise (dB)			
Observer	Coaxial rotor	Single rotor	Difference
1	120.27	113.96	6.31
2	109.14	102.58	6.56
3	115.86	108.64	7.22
4	123.36	116.47	6.89
5	125.88	118.48	7.40
6	102.64	94.96	7.68
7	106.13	97.66	8.47
8	109.14	102.58	6.56
9	105.95	101.90	4.05
10	98.38	94.96	3.42
Total noise (dB)			
Observer	Coaxial rotor	Single rotor	Difference
1	120.31	114.00	6.31
2	109.20	102.64	6.56
3	115.78	108.55	7.23
4	123.36	116.46	6.90
5	125.88	118.48	7.40
6	102.67	95.08	7.59
7	106.26	97.82	8.44
8	109.20	102.64	6.56
9	106.03	101.94	4.09
10	98.39	94.98	3.41

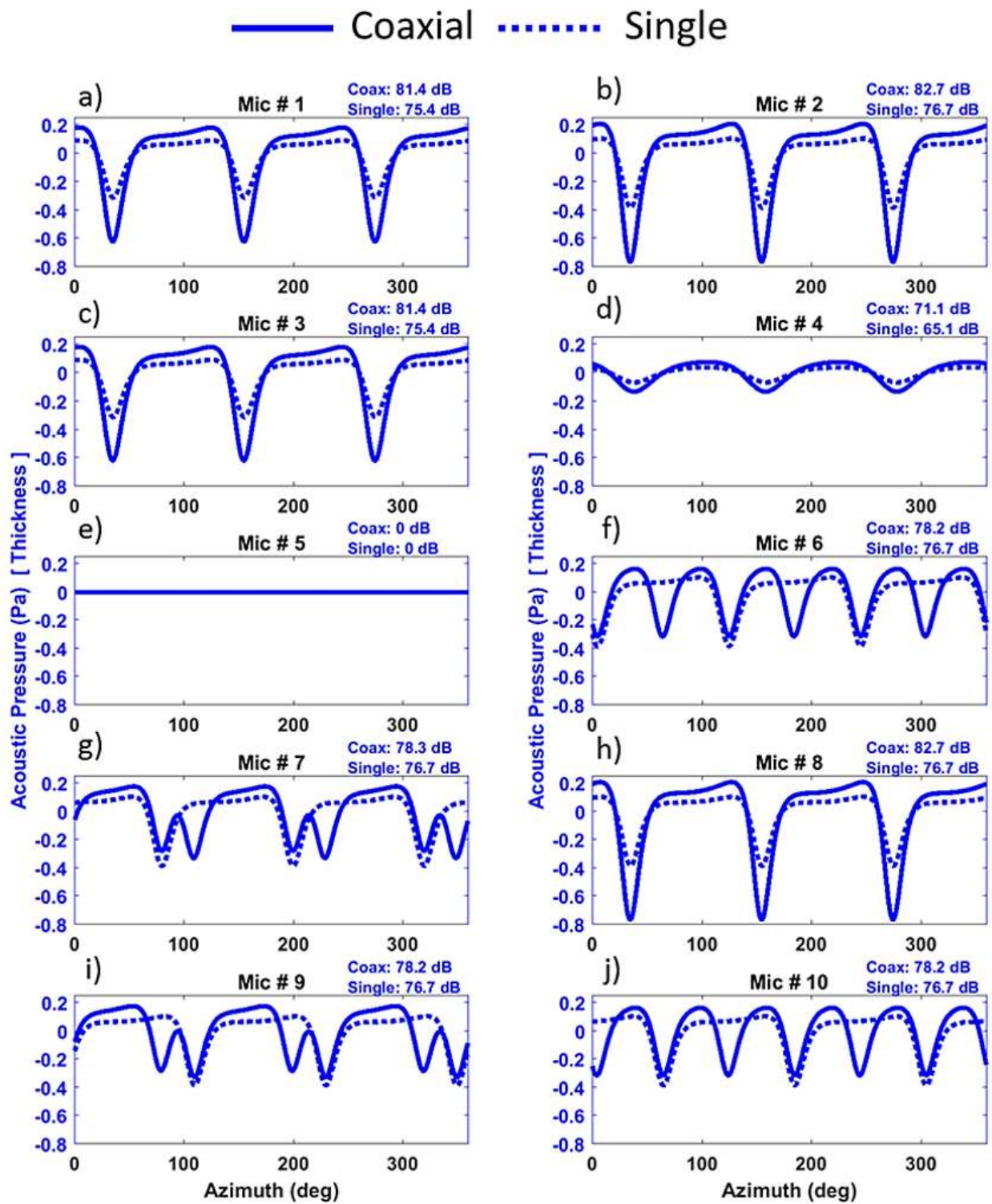


Figure 77. Modern single and coaxial rotor in hover. Thickness noise time history comparison for observers 1 through 10.

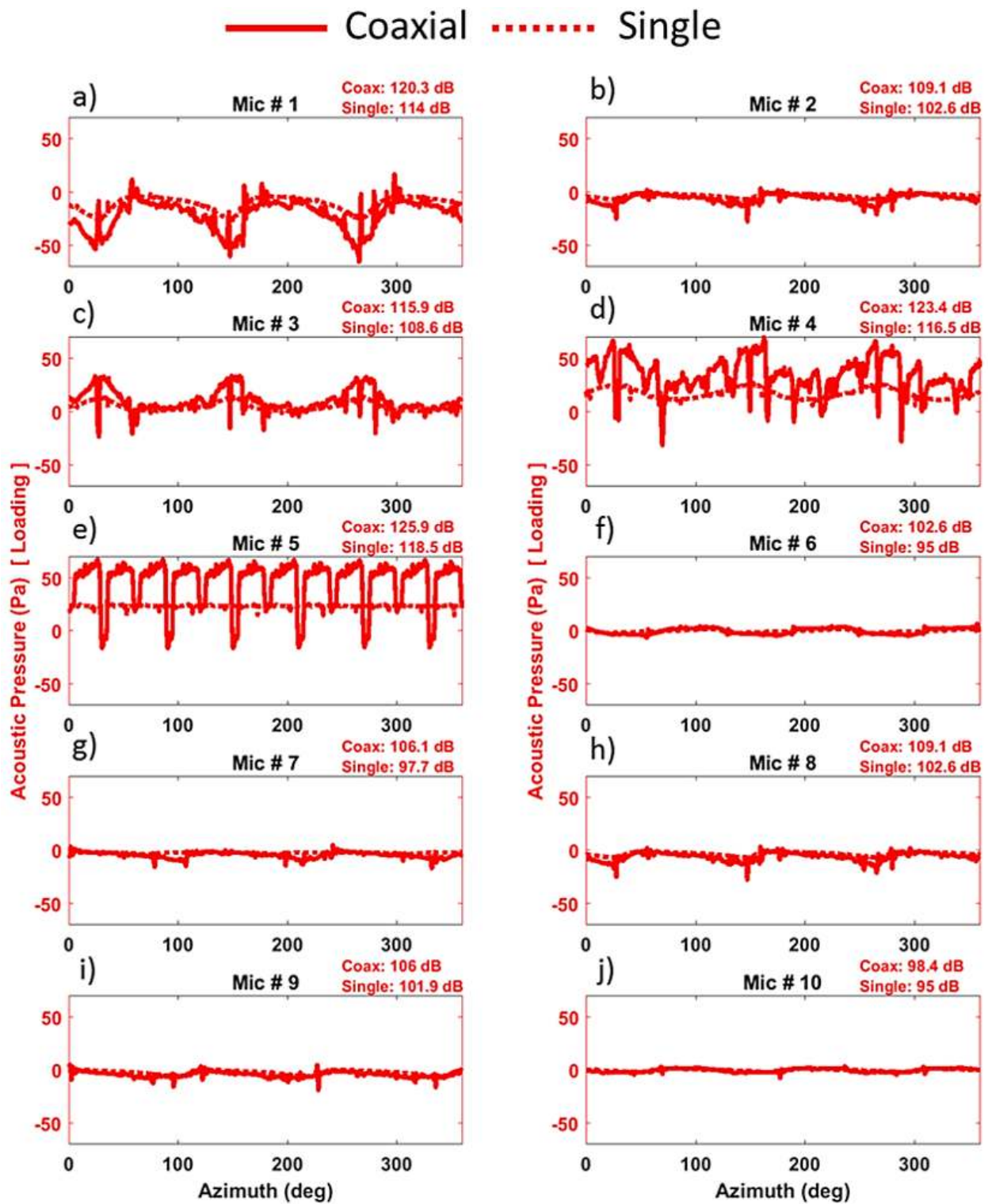


Figure 78. Modern single and coaxial rotor in hover. Loading noise time history comparison for observers 1 through 10.

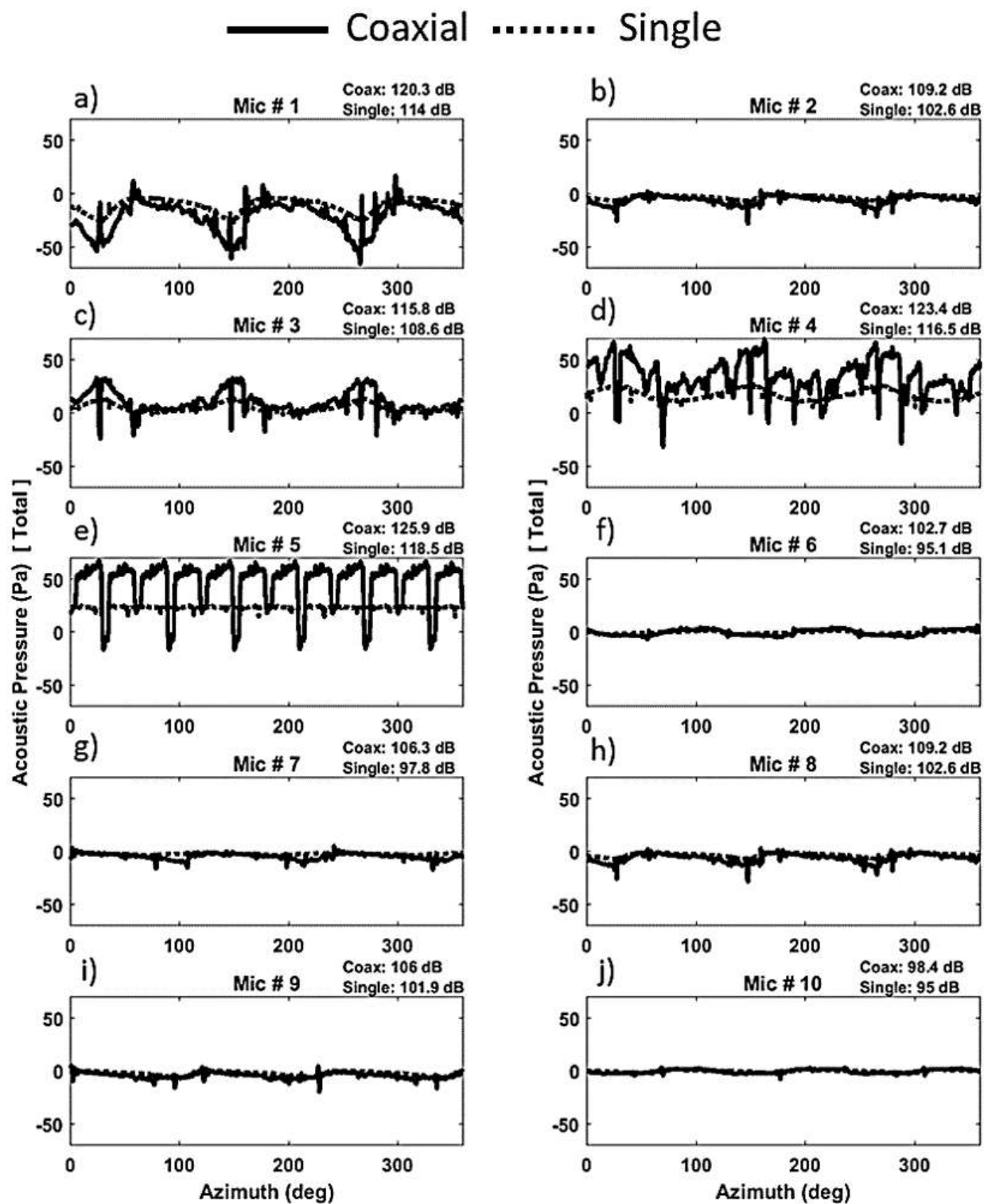


Figure 79. Modern single and coaxial rotor in hover. Total noise time history comparison for observers 1 through 10.

airfoil also increases because of the upwash from the upper airfoil. After overlap, the opposite phenomena occurs, where both the upper and lower airfoil experience a decrease in lift.

- 2D OVERFLOW results revealed that a separation distance greater than noise from two chords is required to minimize effects due to airfoil thickness. Furthermore, acoustic predictions revealed that thickness noise from a coaxial rotor is greater than noise from a single rotor, but the thickness noise of both rotor systems is negligible compared to loading noise. In addition, the presence of deposited shed vorticity from a crossing event was pushed downward when a vertical downwash velocity was simulated; in turn, the deposited shed vorticity from the upper airfoils directly impacts the lower airfoils. The presence of downwash reduced the angle of attack and therefore reduced effects due to circulation for positive angles of attack.
- Load calculations using 2D OVERFLOW and 3D RotUNS show significant effects when the upper and lower rotor blades of a coaxial rotor overlap. Blade crossing causes an increase in Mach number and absolute angle of attack. Reducing vertical separation distance can increase loading effects due to blade crossing occurrences. The code RABBIT was developed to identify the time and location of a blade crossing, and it is able to predict blade overlap for unconventional CACR designs. RABBIT accommodates varying blade phase angles and RPM, where time and location of crossing is less intuitive.
- RABBIT also predicts BVI locations and time along with BVI strength factors, giving designers the ability to quickly determine which flight conditions or design parameters to change in order to reduce BVI occurrences.
- To reduce the occurrence of HSI, it is suggested that the translating blade velocity not exceed Mach numbers that could result in rotor-shock interactions.

The aerodynamic phenomena investigated in this study provided insight into the complicated flow of contra-rotating rotor systems. Understanding the effect of various parameters on the different types of coaxial rotor noise sources enables designers to consider low-noise design options that will help improve the environment.

8 Future work

To continue exploring coaxial rotor aerodynamics and aeroacoustics sources, the following suggestions are made:

- The sharp fluctuations in blade loads during blade crossings are unique features of coaxial rotors, with strong implications for bending and torsional loads on the rotor. The work presented here is a starting point for investigating these loads, and providing design tools.
- The very strong loading noise source due to blade crossings is another unique feature of coaxial rotors compared to conventional rotors. This appears to be a problem that will generate strong interest in the acoustics community and demand innovations. Solutions may involve non-conventional blade designs.

References

1. Mosher, M. and Peterson, R. L., "Acoustic Measurements of a Full-Scale Coaxial Helicopter," AIAA Aeroacoustics Conference, Atlanta, GA, April 1983.
2. Wachspress, D. A. and Quackenbush, T. R., "Impact of Rotor Design on Coaxial Rotor Performance, Wake Geometry and Noise," American Helicopter Society 62nd Annual Forum, Phoenix, AZ, May 2006.
3. Kim, H. W., Duraisamy, K., and Brown, R. E., "Aeroacoustics of a Coaxial Rotor in Level Flight," American Helicopter Society 64th Annual Forum, Montreal, Canada, April 2008.
4. Kim, H. W., Duraisamy, K., and Brown, R. E., "Effect of Rotor Stiffness and Lift Offset on the Aeroacoustics of a Coaxial Rotor in Level Flight," American Helicopter Society 65th Annual Forum, Grapevine, TX, May 27–29, 2009.
5. Samokhin, V., Kotlyar, A., and Burtsev, B., "Acoustic Certification of Helicopter Ka-32a," 27th European Rotorcraft Forum, Moscow, Russia, Sept. 2001.
6. Boyd, D., Burley, C., and Conner, D., "Acoustic Predictions of Manned and Unmanned Rotorcraft Using the Comprehensive Analytical Rotorcraft Model for Acoustics (CARMA) Code System," American Helicopter Society International Specialists' Meeting on Unmanned Rotorcraft, Chandler, AZ, Jan. 2005.
7. Coleman, C. P., "A Survey of Theoretical and Experimental Coaxial Rotor Aerodynamic Research," NASA TP-3675, Mar. 1997.
8. Taylor, M. K., "A Balsa-Dust Technique for Air-Flow Visualization and Its Application to Flow Through Model Helicopter Rotors in Static Thrust," NACA TN-2220, Nov. 1950.
9. Ramasamy, M., "Measurements Comparing Hover Performance of Single, Coaxial, Tandem, and Tilt-Rotor Configurations," American Helicopter Society 69th Annual Forum, Phoenix, AZ, May 2013.
10. Cameron, C. G., Uehara, D., and Sirohi, J., "Transient Hub Loads and Blade Deformation of a Mach-Scale Coaxial Rotor in Hover," AIAA Science and Technology Forum and Exposition, SciTech, Orlando, FL, Jan. 2015.
11. Walsh, D., Weiner, S., Arifran, K., Lawrence, T., Wilson, M., Millott, T., and Blackwell, R., "High Airspeed Testing of the Sikorsky X2 Technology Demonstrator," American Helicopter Society 67th Annual Forum, Virginia Beach, VA, May 2011.
12. Leishman, J. G. and Ananthan, S., "An Optimum Coaxial Rotor System for Axial Flight," *Journal of the American Helicopter Society*, vol. 53, no. 4, pp. 366–381, 2008.
13. Harrington, R. D., "Full-Scale-Tunnel Investigation of the Static-Thrust Performance of a Coaxial Helicopter Rotor," NACA TN-2318, Mar. 1951.
14. Leishman, J. G. and Syal, M., "Figure of Merit Definition for Coaxial Rotors," *Journal of the American Helicopter Society*, vol. 53, no. 3, pp. 290–300, Jul. 2008.
15. Ho, J. C., Yeo, H., and Bhagwat, M., "Validation of Rotorcraft Comprehensive Analysis Performance Predictions for Coaxial Rotors in Hover," American Helicopter Society 71st Annual Forum, Virginia Beach, VA, May 2015.

16. Dingeldein, R. C., "Wind-Tunnel Studies of the Performance of Multirotor Configurations," NACA TN-3236, Aug. 1954.
17. Johnson, W., Moodie, A. M., and Yeo, H., "Design and Performance of Lift-Offset Rotorcraft for Short-Haul Missions," American Helicopter Society Aeromechanics Specialists' Conference, San Francisco, CA, Jan. 2012.
18. Kim, H. W. and Brown, R. E., "Computational Investigation of Small Scale Coaxial Rotor Aerodynamics in Hover," American Helicopter Society 62nd Annual Forum, Phoenix, AZ, May 2006.
19. Kim, H. W. and Brown, R. E., "Coaxial Rotor Performance and Wake Dynamics in Steady and Maneuvering Flight," American Helicopter Society 62nd Annual Forum, Phoenix, AZ, May 9-11, 2006.
20. Juhasz, O., Sya, M., Celi, R., Khromov, V., Rand, O., Ruzicka, G. C., and Strawn, R. C., "Comparison of Three Coaxial Aerodynamic Prediction Methods Including Validation With Model Test Data," Journal of the American Helicopter Society, vol. 59, no. 4, pp. 366-381, 2010.
21. McAlister, K. W., Tung, C., Rand, O., Khromov, V., and Wilson, J. S., "Experimental and Numerical Study of a Model Coaxial Rotor," American Helicopter Society 62nd Annual Forum, Phoenix, AZ, May 2006.
22. Schmaus, J. and Chopra, I., "Aeromechanics for a High Advance Ratio Coaxial Helicopter," American Helicopter Society 71st Annual Forum, Virginia Beach, VA, May 2015.
23. Arents, D. N., "An Assessment of the Hover Performance of the XH-59A Advancing Blade Concept Demonstration Helicopter," AMRDL, Fort Eustis, VA, Report USAAMRDL-TN-25, May 1977.
24. Singh, R. and Kang, H., "Computational Investigations of Transient Loads and Blade Deformations on Coaxial Rotor Systems," 33rd AIAA Applied Aerodynamics Conference, Dallas, TX, Jun. 2015.
25. Walsh, G. D., "A Preliminary Acoustic Investigation of a Coaxial Helicopter in High-Speed Flight," Ph.D. Thesis, Department of Aerospace Engineering, The Pennsylvania State University, State College, PA, 2016.
26. Walsh G., Brentner, K., Jacobellis, G., and Gandhi, F., "An Acoustic Investigation of a Coaxial Helicopter in High-Speed Flight," Proceedings of the AHS International 72nd Annual Forum, West Palm Beach, FL, May 16-19, 2016.
27. Barbely, N. L., Komerath, N. M., and Novak, L. A., "A Study of Coaxial Rotor Performance and Flow Field Characteristics," American Helicopter Society Aeromechanics Specialists' Conference, San Francisco, CA, Jan. 2016.
28. Barbely, N. L. and Komerath, N. M., "Coaxial Rotor Flow Phenomena in Forward Flight," SAE 2016 Aerospace Systems and Technology Conference, Hartford, CT, Sept. 2016.
29. Barbely, N. L. and Komerath, N. M., "Compressible 2D Flow Field Interaction of Two Contra-Rotating Blades," ASME 2016 International Mechanical Engineering Congress and Exposition, Phoenix, AZ, Nov. 11-17, 2016.

30. Schatzman, N. L., Komerath, N. M., and Romander, E., "Time-Varying Loads of Coaxial Rotor Blade Crossings," SAE 2017 Aerospace Systems and Technology Conference, Fort Worth, TX, Sept. 2017.
31. Singh, P. and Friedmann, P. P., "Application of Vortex Methods to Coaxial Rotor Wake and Load Calculations," 55th AIAA Aerospace Sciences Meeting, Grapevine, TX, Jan. 2017.
32. Singh, P. and Friedmann, P. P., "Modeling Coaxial Rotor Wakes in Forward Flight Using Viscous Vortex Particle Method With Refined Blade Loads," AHS International Technical Meeting, Aeromechanics Design for Transformative Vertical Flight, San Francisco, CA, Jan. 16–18, 2018.
33. Feil, R., Rauleder, J., Hajek, M., Cameron, C., and Sirohi, J., "Computational and Experimental Aeromechanics Analysis of a Coaxial Rotor System in Hover and Forward Flight," Proceedings of the 42nd European Rotorcraft Forum, Lille, France, 2016.
34. Schmaus, J. H., and Chopra, I., "Aeromechanics of Rigid Coaxial Rotor Models for Wind-Tunnel Testing," *Journal of Aircraft*, vol. 54, no. 4, 2017.
35. Cameron, C. G., Karpatne, A., and J. Sirohi, "Performance of a Mach-Scale Coaxial Counter-Rotating Rotor in Hover," *Journal of Aircraft*, vol. 53, no. 3, pp. 746–755, 2016.
36. Nagashima, T. and Nakanishi, K., "Optimum Performance and Wake Geometry of a Coaxial Rotor in Hover," *Vertica*, vol. 7, pp. 225–239, 1983.
37. Akimov, A., Butov, V., and Bourtsev, B., "Flight Investigation of Coaxial Rotor Tip Vortex Structure," American Helicopter Society 50th Annual Forum, Washington, D.C., June 1994.
38. Bagai, A., "Aerodynamic Design of the X2 Technology Demonstrator Main Rotor Blade," American Helicopter Society 64th Annual Forum, Montreal, Canada, April 2008.
39. Ruzicka, G. and Strawn, R., "Computational Fluid Dynamics Analysis of a Coaxial Rotor Using Overset Grids," American Helicopter Society Aeromechanics Specialists' Conference, San Francisco, CA, Jan. 2008.
40. Lim, J. W., McAlister, K. W., and Johnson, W., "Hover Performance Correlation for Full-Scale and Model-Scale Coaxial Rotors," American Helicopter Society 63rd Annual Forum, Virginia Beach, VA, May 2007.
41. Johnson, W., "Influence of Lift Offset on Rotorcraft Performance," NASA TP-215404, Nov. 2009.
42. Bohorquez, F., "Rotor Hover Performance and System Design of an Efficient Coaxial Rotary Wing Micro Air Vehicle," Ph.D. Thesis, Department of Aerospace Engineering, University of Maryland, College Park, MD, 2007.
43. Lakshminarayan, V. K. and Baeder, J. D., "Computational Investigation of Small Scale Coaxial Rotor Aerodynamics in Hover," 47th AIAA Meeting Including The New Horizons Forum and Aerospace Exposition, Orlando, FL, Jan. 2009.
44. Yeo H. and Johnson, W., "Investigation of Maximum Blade Loading Capability of Lift-Offset Rotors," American Helicopter Society 69th Annual Forum, Phoenix, AZ, May 2013.

45. Rajmohan, N., Zhao, J., and He, C., “A Coupled Vortex Particle/CFD Methodology for Studying Coaxial Rotor Configurations,” American Helicopter Society Aeromechanics Specialists’ Conference, San Francisco, CA, Jan. 2014.
46. Bhagwat, M. J., “Co-Rotating and Counter-Rotating Coaxial Rotor Performance,” AHS Technical Conference on Aeromechanics Design for Transformative Vertical Flight, San Francisco, CA, Jan. 2018.
47. Williams, F. J. and Hawkings, D. L., “Sound Generation by Turbulence and Surfaces in Arbitrary Motion,” *Philosophical Transactions of the Royal Society of London A: Mathematical, Physical and Engineering Sciences*, vol. 264, no. 1151, pp. 321–342, 1969.
48. Lighthill, M. J., “On Sound Generated Aerodynamically. I. General Theory,” *Royal Society of London A: Mathematical, Physical and Engineering Sciences*, vol. 211, no. 1107, pp. 564–587, 1952.
49. Farassat, F. and Succi, G. P., “The Prediction of Helicopter Discrete Frequency Noise,” *Tech. Rep.*, 1983, pp. 309–320.
50. Brentner, K. S. and Farassat, F., “Modeling Aerodynamically Generated Sound of Helicopter Rotors,” *Progress in Aerospace Sciences*, vol. 39, no. 2, pp. 83–120, 2003.
51. Pierce, A. D. and Beyer, R. T., *Acoustics: An Introduction to Its Physical Principles and Applications*. Melville, NY: Acoustical Society of America, 1991.
52. Martin, R. M., Marcolini, M. A., Splettstoesser, W. R., and Schultz, K. J., “Wake Geometry Effects on Rotor Blade-Vortex Interaction Noise Directivity,” NASA TP-3015, Nov. 1990.
53. Johnson, W., *Helicopter Theory*. Princeton, NJ: Princeton University Press, 1980.
54. Schmitz, F. H. and Yu, Y. H., “Helicopter Impulsive Noise: Theoretical and Experimental Status,” NASA TM-84390, 1983.
55. Brooks, T. F. and Burley, C. L., “Rotor Broadband Noise Prediction With Comparison to Model Data,” AIAA Paper 2001-2210, May 2001.
56. Harris, C. D., “Two-Dimensional Aerodynamic Characteristics of the NACA 0012 Airfoil in the Langley 8-Foot Transonic Pressure Tunnel,” NASA TM-81927, April 1981.
57. Sengupta, T. K., Bhole, A., and Sreejith, N. A., “Direct Numerical Simulation of 2D Transonic Flows Around Airfoils,” *Computers and Fluids*, vol. 88, pp. 19–37, 2013.
58. Bertin, J. J. and Smith, M. L., *Aerodynamics for Engineers*. Prentice-Hall, 1998, pp. 49–143.
59. Nichols, R. and Buning, P., “Users Manual for OVERFLOW 2.2,” NASA Langley Research Center, Hampton, VA, Aug. 2010.
60. Johnson, W., “CAMRAD-II: Comprehensive Analytical Model for Rotorcraft Aerodynamics and Dynamics,” Johnson Aeronautics, Palo Alto, CA, 2007.
61. Rajagopalan, R. G., Baskaran, V., Hollingsworth, A., Lestari, A., Garrick, D., Solis, E., and Hagerty, B., “RotCFD—A tool for Aerodynamic Interference of Rotors: Validation and Capabilities,” American Helicopter Society Aeromechanics Specialists’ Conference, San Francisco, CA, Jan. 2012.

62. Guntupalli, K., Novak, L. A., and Rajagopalan, R. G., “RotCFD: An Integrated Design Environment for Rotorcraft,” American Helicopter Society Aeromechanics Specialists’ Conference, San Francisco, CA, Jan. 2016.
63. Leishman, J. G., *Principles of Helicopter Aerodynamics*. New York, NY: Cambridge University Press, 2000.
64. MATLAB, Version 7.10.0 (r2010a). Natick, MA: The MathWorks Inc., 2010.
65. Sim, B. W., George, A. R., and Yen, S. J., “Blade-Vortex Interaction Noise Directivity Studies Using Trace Mach Number,” American Helicopter Society 2nd International Aeromechanics Specialists’ Conference, Bridgeport, CT, Oct. 11–13, 1995.
66. Malovrh, B. and Gandhi, F., “Sensitivity of Helicopter Blade-Vortex Interaction Noise and Vibration to Interaction Parameters,” *Journal of Aircraft*, vol. 42, no. 3, pp. 685–697, May 2005.
67. Bhagwat, M. J., “Effect of Blade Number on Induced Power in Hover,” *Journal of the American Helicopter Society*, vol. 56, no. 2, 2011.
68. Hennes, C., Lopes, L., Shirey, J., Erwin, J., and Brentner, K. S., “PSU-WOPWOP 3.3.3 Users Guide,” The Pennsylvania State University, University Park, PA, 2009.

For a copy of the following codes and input files please contact Dr. Natasha Lydia Schatzman (contact information below).

Chapter 3: Potential flow MATLAB code VITS (Vortex Interaction Tracking Simulation)

Chapter 4: Single and coaxial (HS1 and HC1) rotor blade momentum theory MATLAB code

Chapter 5: RABBIT (RApid Blade and Blade-vortex Interaction Timer) MATLAB code

Chapter 5: BVI impulse factor MATALB code

Chapter 6: PSU-WOPWOP input files for modern single and/or coaxial rotor

**Dr. Natasha Lydia Schatzman
NASA Ames Research Center
Email: Natasha.Schatzman@nasa.gov
Work phone: 650-604-5903**